TECHNISCHE UNIVERSITÄT MÜNCHEN

Lehrstuhl für Numerische Mechanik

Determination of Transport Parameters of Binary Electrolyte Solutions for the Use in Numerical Simulations

Andreas Josef Ehrl

Vollständiger Abdruck der von der Fakultät für Maschinenwesen der Technischen Universität München zur Erlangung des akademischen Grades eines

Doktor-Ingenieurs (Dr.-Ing.)

genehmigten Dissertation.

Vorsitzender: Univ.-Prof. Wolfgang Polifke, Ph. D.

Prüfer der Dissertation:

1. Univ.-Prof. Dr.-Ing. Wolfgang A. Wall
2. Univ.-Prof. Hubert A. Gasteiger, Ph. D.

Die Dissertation wurde am 08.10.2015 bei der Technischen Universität München eingereicht und durch die Fakultät für Maschinenwesen am 11.09.2017 angenommen.

Abstract

Nowadays, batteries are used as portable energy source in hand-held devices such as laptops, cameras and cell phones. In addition, advanced battery systems are also considered a key technology for the success of the German ”Energiewende”. However, the limited energy density and lifetime of current lithium ion batteries have to be improved further to fulfill all requirements. In this context, advanced numerical simulation tools are important for both the improvement of existing battery systems such as lithium ion batteries as well as the development of future battery systems such as lithium oxygen batteries. Computational methods can provide insight into physical and chemical aspects of battery systems, which are not or hardly achievable experimentally. The optimization of future battery designs is another important application for computer-based methods. For such numerical simulations, reproducibility and accuracy are key issues, which depend on appropriate physical models, boundary conditions, and accurately determined transport parameters, among other things.

In this work, two different physically-motivated ion-transport models for concentrated electrolyte solutions are introduced and related to each other. The first model is based on the Stefan-Maxwell approach, the second on non-equilibrium thermodynamics. Based on this comparison, a flexible computational approach based on the finite element method is developed which enables both the simulation of large realistic, geometrically resolved porous structures as well as the simulation of porous media homogenized by the volume averaging approach. The focus is in particular on galvanostatic boundary conditions for three-dimensional domains. The accuracy and the robustness of the proposed computational method is demonstrated by various numerical examples. Among others, a realistic three-dimensional porous structure is presented to accentuate the computational efficiency of the presented approach.

Similar simulation tools can be found in literature, whereas accurate and reliable transport parameters are scarce. Therefore, the focus of this work is on the development of accurate and at the same time as simple as possible experimental procedures for the determination of transport parameters required for predictive numerical simulations. In the considered models, ion-transport is described by three independent transport parameters and one thermodynamic quantity, namely the conductivity of electrolyte solution, the diffusion coefficient, the transference number of the reacting ionic species and the thermodynamic factor or, alternatively, the mean molar activity coefficient. For numerical simulations using the volume averaging approach, at least two additional geometrical parameters are required, namely porosity and tortuosity of the respective porous medium. For the direct determination of the mean molar activity coefficient, a novel method is introduced in this work. Resulting from the known activity coefficient, the transference number can be determined by concentration cell experiments. In addition, various known and unknown methods for the experimental determination of the transference number, the diffusion coefficient and the tortuosity are also discussed critically. The conductivity and the porosity are determined by standard methods.

In summery, the combined approach consisting of the development of a computational method for ion-transport in concentrated electrolyte solutions and the direct determination of the corresponding model parameters enables predictive simulations of ion-transport phenomena in advanced battery systems. The simulation of large geometrically resolved porous media al-

lows an investigation of the influence of the microstructure on the macroscopic behavior of a battery cell.

Zusammenfassung

Batterien werden heutzutage nicht nur als Energiequelle für tragbare Elektrogeräte wie zum Beispiel Laptops, Kameras und Handys eingesetzt, sondern auch als eine der entscheidenden Technologien für das Gelingen der deutschen Energiewende angesehen. Um dabei alle gestellten Anforderungen zu erfüllen, ist es erforderlich, die begrenzte Energiedichte und Lebensdauer von aktuellen Batteriesystemen weiter zu erhöhen. Hierbei spielen numerische Berechnungswerkzeuge zur Verbesserung bestehender Lithium-Ionen Batterien und zur Entwicklung von zukünftigen Batteriesystemen wie zum Beispiel der Lithium-Luft Batterie eine wichtige Rolle, da sie die Möglichkeit bieten, physikalisch-chemische Vorgänge zu untersuchen, die in Experimenten nur schwer oder gar nicht abgebildet werden können. Ein weiteres wichtiges Anwendungsfeld von numerischen Berechnungswerkzeugen ist die Optimierung von zukünftigen Batteriekonzepten. Hierfür sind Vergleichbarkeit und Genauigkeit eine Grundvoraussetzung, die unter anderem durch geeignete physikalische Modelle, Randbedingungen und genaue Materialparameter beeinflusst wird.

In der vorliegenden Arbeit werden zwei unterschiedliche, physikalische Ionentransportmodelle für konzentrierte Elektrolytlösungen vorgestellt und miteinander verglichen. Das erste Modell baut auf dem Stefan-Maxwell Ansatz auf und das zweite Modell auf der Nichtgleichgewichtssystematik der Thermodynamik. Ausgehend von diesem Vergleich wird ein Berechnungsverfahren auf Grundlage der Finiten Elemente Methode vorgestellt, das die Simulation von aufgelösten porösen Strukturen sowie die Simulation von porösen Strukturen, die mit dem Volumenmittelungsverfahren homogenisiert wurden, ermöglicht. Ein besonderes Augenmerk wird auf die Modellierung von galvanostatischen Randbedingungen für dreidimensionale Gebiete gelegt. Die Genauigkeit und Robustheit der numerischen Berechnungsverfahren wird in einer Vielzahl von numerischen Beispielen gezeigt. Die hohe Effizienz des vorgestellten Berechnungsverfahrens wird unter anderem durch die Simulation einer dreidimensionalen porösen Struktur verdeutlicht.

In der Literatur werden vergleichbare Berechnungswerkzeuge diskutiert, genaue und vertrauenswürdige Transportparameter für die zugrunde liegenden Modelle sind jedoch selten. Aus diesem Grund liegt der Schwerpunkt der Arbeit auf der Entwicklung von genauen, aber gleichzeitig möglichst einfachen Methoden zur Bestimmung von Transportparametern, die für voraussagende Simulationen nötig sind. Die verwendeten Ionentransportmodelle basieren auf drei Transportparametern und einer thermodynamischen Größe, nämlich der Konduktivität der Elektrolytlösungen, dem Diffusionskoeffizienten, der Übergangszahl der reagierenden Ionenart und dem Thermodynamikfaktor oder alternativ dem mittleren molaren Aktivitätskoeffizienten. Zwei zusätzliche geometrische Parameter, die Porosität und die Tortuosität, sind notwendig, wenn Berechnungsmethoden mit dem Volumenmittelungsverfahren eingesetzt werden. In der vorliegenden Arbeit wird eine neuartige Methode für die Bestimmung des mittleren molaren Aktivitätskoeffizienten vorgestellt. Die Übergangszahl kann dann aus dem bekannten Aktivitätskoeffizienten und Experimenten in einer Konzentrationszelle abgeleitet werden. Zusätzlich werden einige bekannte und neuartige Methoden zur Bestimmung der Übergangszahl, des Diffusionsko-

effizienten und der Tortuosität kritisch diskutiert. Die Konduktivität sowie die Porosität werden durch Standardmethoden bestimmt.

Die kombinierte Herangehensweise bestehend aus der Entwicklung eines Berechnungsverfahren für Ionentransport in konzentrierten Elektrolytlösungen und der direkten Bestimmung der zugehörigen Modellparameter ermöglicht voraussagende Simulationen von Ionentransportphänomenen in hochentwickelten Batteriesystemen. Die Simulation von großen, geometrisch aufgelösten porösen Medien ermöglicht außerdem die Untersuchung des Einflusses der Mikrostruktur auf das makroskopische Verhalten der Batterie.

Contents

Nomenclature

Abbreviations

A_k	chemical symbol of component k
e^-	symbol for an electron
BC	boundary condition
CV	cyclic voltammogram
ENC	electroneutrality condition
GMRES	Generalized minimal residual
Li	symbol for lithium
OCV	open circuit voltage
PGP	pulsed galvanostatic polarization
RE	reference electrode
REV	representative element volume
RT	room temperature
SSPP	steady-state potentiostatic polarization
WE	working electrode

Computational approach

$(.,.),\ (.,.)_\Omega$	inner product of $L^2(\Omega)$
$(.,.)_\Gamma$	inner product of $L^2(\Gamma)$
$(\dots)^{\mathrm{h}}$	finite element approximation to an arbitrary quantity
$(\dots)^{n+1}$	quantity at new time level
$(\dots)^{n+\alpha_{\mathrm{f}}},\ (\dots)^{n+\alpha_{\mathrm{m}}}$	quantity at intermediate time levels
$(\dots)^{n}$	quantity at previous time level

$\alpha_\mathrm{f},\ \alpha_\mathrm{m},\ \gamma$	parameters of the generalized-alpha scheme
$\mathcal{S}$	space of trial solution function
$\mathcal{T}$	space of test (weighting) function
ρ_∞	parameter of the ρ_∞-family
$H^1(\Omega)$	Sobolev space
$L^2(\Omega)$	space of square-integrable functions
N_i^h	shape function associated to node i
n_node	number of nodes in the computational domain

Domains and boundaries

$\boldsymbol{n}$	unit outer normal vector at a boundary
$V(t),\ S(t)$	arbitrary control volume $V(t)$ enclosed by the corresponding surface $S(t)$
$\bar{x}_0$	position vector defining the center of a REV
$\bar{x}_0^\mathrm{e}$	position vector defining the center of the electrolyte phase within the REV
$\boldsymbol{x}$	position vector
$\boldsymbol{x}'$	position vector within a REV
$\hat{x}_i$	component of position vector between arbitrary point x_i' within the REV and the center of the REV $x_{i,0}$
x_i	component of the position vector
Γ	boundary of domain Ω
$\Gamma_\mathrm{D},\ \Gamma_\mathrm{N},\ \Gamma_\mathrm{E}$	Dirichlet, Neuman and electrode boundary part
Ω	domain
$\overline{\Omega}$	closure of the domain Ω

Governing equations

$\dot{a}$	minimal distance between two ionic species $\left[\mathrm{nm}\right]$
A	area $\left[\mathrm{m}^2\right]$
$a(c)$	short notation for transport parameter and physical constants in the term describing the concentration overpotential

a_k	proportionality constant of component k expressing the secondary reference state $\left[\frac{\mathrm{dm}^3}{\mathrm{mol}}\right]$
$a_\pm$	proportionality constant of the salt expressing the secondary reference state $\left[\frac{\mathrm{dm}^3}{\mathrm{mol}}\right]$
$\boldsymbol{B}$	magnetic induction $\left[\frac{\mathrm{V\,s}}{\mathrm{m}^2}\right] = [T]$
c	equivalent concentration $\left[\frac{\mathrm{mol}}{\mathrm{dm}^3}\right] = [\mathrm{M}]$
c_k	concentration of component k $\left[\frac{\mathrm{mol}}{\mathrm{dm}^3}\right] = [\mathrm{M}]$
c_T	total concentration $\left[\frac{\mathrm{mol}}{\mathrm{dm}^3}\right] = [\mathrm{M}]$
$c_{k,0}$	initial concentration of component k $\left[\frac{\mathrm{mol}}{\mathrm{dm}^3}\right] = [\mathrm{M}]$
$\mathbb{D}_\pm$	dilute binary diffusion coefficient of a salt $\left[\frac{\mathrm{m}^2}{\mathrm{s}}\right]$
$\mathbb{D}_{kl}$	multi-component diffusion coefficient of species k and l $\left[\frac{\mathrm{m}^2}{\mathrm{s}}\right]$
$\mathcal{D}$	molecular diffusion coefficient of a binary electrolyte solution $\left[\frac{\mathrm{m}^2}{\mathrm{s}}\right]$
$\mathcal{D}_{kl}$	intermolecular diffusion coefficient of species k and l $\left[\frac{\mathrm{m}^2}{\mathrm{s}}\right]$
D_k	diffusion coefficient of component k $\left[\frac{\mathrm{m}^2}{\mathrm{s}}\right]$
D_el	diffusion coefficient of the electrolyte $\left[\frac{\mathrm{m}^2}{\mathrm{s}}\right]$
$D_{\pm,\mathrm{eff}}$	effective binary diffusion coefficient $\left[\frac{\mathrm{m}^2}{\mathrm{s}}\right]$
$D^*_{\pm,\mathrm{eff}}$	partial effective binary diffusion coefficient $\left[\frac{\mathrm{m}^2}{\mathrm{s}}\right]$
$D_\pm$	binary diffusion coefficient $\left[\frac{\mathrm{m}^2}{\mathrm{s}}\right]$
$\boldsymbol{D}$	electric displacement field $\left[\frac{\mathrm{A\,s}}{\mathrm{m}^2}\right]$
e	electronic charge $e = 1.602 \cdot 10^{-19}$ [C]
e	total energy density $\left[\frac{\mathrm{J}}{\mathrm{m}^3}\right]$
$\boldsymbol{E}$	electric field $\left[\frac{\mathrm{V}}{\mathrm{m}}\right]$
F	Faraday constant $F = 96485.3399$ $\left[\frac{\mathrm{A\,s}}{\mathrm{mol}}\right]$
$f_\pm$	mean molar activity coefficient of a binary salt $[-]$

f_k	molar activity coefficient of component k $[-]$
$\boldsymbol{H}$	magnetic field $\left[\frac{\mathrm{A}}{\mathrm{m}}\right]$
I	current $[\mathrm{A}]$
I	ionic strength $\left[\frac{\mathrm{mol}}{\mathrm{dm}^3}\right]$
I_0	initial current $[\mathrm{A}]$
i_n	normal component of current density $\boldsymbol{i}$ $\left[\frac{\mathrm{A}}{\mathrm{m}^2}\right]$
I_p	polarization current $[\mathrm{A}]$
I_S	steady-state current $[\mathrm{A}]$
$\boldsymbol{i}$	current density $\left[\frac{\mathrm{A}}{\mathrm{m}^2}\right]$
K_{kl}	friction coefficient for interaction of species k and l $\left[\frac{\mathrm{J\,s}}{\mathrm{m}^5}\right] = \left[\frac{\mathrm{kg}}{\mathrm{m}^3\,\mathrm{s}}\right]$
l	distance between the two electrodes $[\mathrm{m}]$
m	equivalent molality $\left[\frac{\mathrm{mol}}{\mathrm{kg}}\right]$
m	number of components dissolved in the solvent $[-]$
M_k	molar mass of component k $\left[\frac{\mathrm{kg}}{\mathrm{mol}}\right]$
n	number of transferred electrons e^- $[-]$
N_k	amount of substance of component k $[\mathrm{mol}]$
N_A	Avogadro constant $N_\mathrm{A} = 6.022 \cdot 10^{23}$ $\left[\mathrm{mol}^{-1}\right]$
N_M	MacMullin number $[-]$
$\boldsymbol{N}$	equivalent molar flux density $\left[\frac{\mathrm{mol}}{\mathrm{m}^2\,\mathrm{s}}\right]$
$\boldsymbol{N}_k$	molar flux density of component k due to diffusion and migration $\left[\frac{\mathrm{mol}}{\mathrm{m}^2\,\mathrm{s}}\right]$
$\boldsymbol{N}_k^\mathrm{B}$	molar flux density of component k with respect to the barycentric velocity $\boldsymbol{u}^\mathrm{B}$ $\left[\frac{\mathrm{mol}}{\mathrm{m}^2\,\mathrm{s}}\right]$
$\boldsymbol{N}_k^\mathrm{T}$	total molar flux density of component k due to convection, diffusion and migration
p	pressure $\left[\frac{\mathrm{N}}{\mathrm{m}^2}\right]$
$\boldsymbol{q}$	heat flux $\left[\frac{\mathrm{J}}{\mathrm{m}^2\,\mathrm{s}}\right] = \left[\frac{\mathrm{W}}{\mathrm{m}^2}\right]$
$\Delta_\mathrm{R}G$	reaction Gibbs energy k $\left[\frac{\mathrm{J}}{\mathrm{mol}}\right]$

R	entropy production rate $\left[\frac{\mathrm{J}}{\mathrm{m^3\,s}}\right]$
R	gas constant $R = 8.314472$ $\left[\frac{\mathrm{J}}{\mathrm{mol\,K}}\right]$
R	resistance $\left[\frac{\mathrm{V}}{\mathrm{A}}\right]$ = [Ω]
r_k	homogenous reaction rate of component k $\left[\frac{\mathrm{mol}}{\mathrm{m^3\,s}}\right]$
R_{el}	resistance of an electrolyte solution with separator $\left[\frac{\mathrm{V}}{\mathrm{A}}\right]$ = [Ω]
R_{HF}	high frequency resistance $\left[\frac{\mathrm{V}}{\mathrm{A}}\right]$ = [Ω]
R_{LF}	low frequency resistance $\left[\frac{\mathrm{V}}{\mathrm{A}}\right]$ = [Ω]
S	entropy $\left[\frac{\mathrm{J}}{\mathrm{K}}\right]$
s	entropy density $\left[\frac{\mathrm{J}}{\mathrm{K\,m^3}}\right]$
s	scan rate $\left[\frac{\mathrm{V}}{\mathrm{s}}\right]$
s_k	stoichiometric coefficient of component k $[-]$
$\left(1 + \frac{\partial \ln f_\pm}{\partial \ln c}\right) = \mathcal{X}$	thermodynamic factor of the salt $[-]$
T	temperature $[K]$
t_k	transference number of the component k $[-]$
T^*_{ji}	geometry coefficient $[-]$
t	time [s]
T_{end}	end time of simulation [s]
T_{I}	current interuption time [s]
U	internal energy [J]
U	open circuit potential [V]
u	internal energy density $\left[\frac{\mathrm{J}}{\mathrm{m^3}}\right]$
U_0	cell potential [V]
U'_0	formal potential used for the determination of the transference number [V]
U_{p}	polarization cell potential [V]
$U_{\mathrm{p,ox}}$, $U_{\mathrm{p,red}}$, $U_{\mathrm{p,1/2}}$	potential of the oxidation peak, the reduction peak and the have wave potential used for the determination of the transference number [V]
U_{Ref}	reference potential used for the determination of the transference number [V]

$\boldsymbol{u}$	velocity $\left[\frac{\mathrm{m}}{\mathrm{s}}\right]$
$\boldsymbol{u}^{\mathrm{B}}$	barycentric velocity of electrolyte solution $\left[\frac{\mathrm{m}}{\mathrm{s}}\right]$
$\boldsymbol{u}_k$	velocity of component k $\left[\frac{\mathrm{m}}{\mathrm{s}}\right]$
V	volume $\left[\mathrm{m}^3\right]$
w_k	mass fraction of component k $[-]$
z_k	charge number or valence of component k $[-]$
α	exponential factor in Archie's law $[-]$
α_{A}, α_{C}	anodic and cathodic constant in the Bulter-Volmer law $[-]$
β	constriction factor $[-]$
η	surface overpotential $[V]$
ε	porosity $[-]$
ε_0	relative permittivity $\varepsilon_0 = 8.854 \cdot 10^{-12}$ $\left[\frac{\mathrm{F}}{m}\right]$ = $\left[\frac{\mathrm{A\,s}}{\mathrm{V\,m}}\right]$
ε_{R}	relative permittivity $\left[\frac{\mathrm{F}}{m}\right]$ = $\left[\frac{\mathrm{A\,s}}{\mathrm{V\,m}}\right]$
ε_{a}	surface porosity $[-]$
γ	weighting factor for the surface concentration dependence of the Bulter-Volmer law $[-]$
$\gamma_{\pm}$	mean molal activity coefficient of a binary salt $[-]$
κ	conductivity of electrolyte solution $\left[\frac{S}{\mathrm{m}}\right]$
κ_k	conductivity of component k $\left[\frac{S}{\mathrm{m}}\right]$
κ_{eff}	effective conductivity of electrolyte solution $\left[\frac{S}{\mathrm{m}}\right]$
Λ_{m}	equivalent conductance $\left[\frac{S\,\mathrm{m}^2}{\mathrm{mol}}\right]$
$\hat{\mu}_+^{\mathrm{R}}$	electrochemical potential of the positive ionic species with respect to a lithium reference electrode $\left[\frac{\mathrm{J}}{\mathrm{mol}}\right]$
$\hat{\mu}_k$	electrochemical potential of component k $\left[\frac{\mathrm{J}}{\mathrm{mol}}\right]$
$\hat{\mu}_{\mathrm{el}}$	electrochemical potential of the electrolyte solution $\left[\frac{\mathrm{J}}{\mathrm{mol}}\right]$
μ^{θ}	standard chemical potential $\left[\frac{\mathrm{J}}{\mathrm{mol}}\right]$
μ_k	chemical potential of component k $\left[\frac{\mathrm{J}}{\mathrm{mol}}\right]$

μ_{el}	chemical potential of the electrolyte solution $\left[\frac{\mathrm{J}}{\mathrm{mol}}\right]$
$\mu_{\pm}$	chemical potential of a binary salt $\left[\frac{\mathrm{J}}{\mathrm{mol}}\right]$
μ_{cell}	standard chemical cell potential used for the determination of the thermodynamic factor $\left[\frac{\mathrm{J}}{\mathrm{mol}}\right]$
ν	dissociation number of the binary salt $[-]$
ν_k	dissociation number of component k $[-]$
Φ	electrostatic potential $[\mathrm{V}]$
$\Phi^{\ominus}$	electrostatic potential with respect to the negative ionic species $[\mathrm{V}]$
Φ^{R}	electrostatic potential with respect to a lithium reference electrode $[\mathrm{V}]$
Φ^{NP}	electrostatic potential within the electrolyte solution utilizing the Nernst-Planck approach $[\mathrm{V}]$
Φ^{n}	electrostatic potential with respect to an ionic species of the electrolyte solution $[\mathrm{V}]$
ρ	density of electrolyte solution $\left[\frac{\mathrm{kg}}{\mathrm{m}^3}\right]$
ρ_{e}	charge density of electrolyte solution $\left[\frac{\mathrm{A\,s}}{\mathrm{m}^3}\right]$
σ_{R}	relative conductivity $[-]$
$\overline{\tau}_{\mathrm{geo}}$	mean geometrical tortuosity $[-]$
τ	tortuosity $[-]$
τ_{el}	electric tortuosity $[-]$
τ_{geo}	geometrical tortuosity $[-]$
τ_{hyd}	hydraulic tortuosity $[-]$
τ_{path}	path length tortuosity $[-]$
$\Xi^{\mathrm{e,s}}$	ratio between the area $A^{\mathrm{e,s}}$ of the interface $\Gamma^{\mathrm{e,s}}$ and the volume V^{o} of the REV $[-]$

Operators

$\frac{\partial}{\partial t}$	partial time derivative
∇	spatial gradient operator
$\nabla\cdot$	divergence operator
d	total differential

Superscripts

$(\dots)^{\mathrm{e,e}}$	interface between electrolyte and electrolyte phase at the boundary of the representative element volume
$(\dots)^{\mathrm{e}}$	electrolyte phase within the representative element volume
$(\dots)^{\mathrm{e,s}}$	interface between electrolyte and solid phase within the representative element volume
$(\dots)^{\mathrm{o}}$	all phases within representative element volume
$(\dots)^{\mathrm{s}}$	solid phase within the representative element
$(\dots)^{\mathrm{R}}$	lithium reference electrode
$\overline{(\dots)}$	volumetric phase average of any quantity
$\overline{(\dots)}^{\mathrm{e}}$	volumetric intrinsic phase average of any quantity
$\widehat{(\dots)}$	deviation from the volumetric phase average
$\widetilde{(\dots)}^{\mathrm{e,s}}$	surface average of any quantity
A	anode
C	cathode

Subscripts

$+$	positive ionic species
$-$	negative ionic species
0	initial
0	solvent
A	anode
C	cathode
el	electrolyte
I	interface
i, j	index
k, l	index of electrolyte solution component
n	arbitrary reference species for the definition of the reference potential

r	index of electrochemical reaction
so	solid
S	steady-state

1 Introduction

Many devices of our daily life such as laptops and cell phones are powered and, therefore, also limited by the electric energy provided by batteries. Despite this fact, the battery has never been in the focus of public perception. This changed rapidly when the energy revolution, the so-called ”Energiewende”, started a few years ago. In this context, important keywords are electromobility and intermediate storage of electrical energy. Electromobility describes the usage of electric vehicles to satisfy our mobility needs. It does not only include vehicles, which are powered solely by batteries, but also hybrid vehicles which combine a combustion engine with an electric motor. Electromobility has a positive effect on the release of green house gases since the used electric energy can be produced with higher efficiency in conventional power plants than in combustion engines of cars and, more importantly, it enables alternative energy sources such as nuclear, solar or wind power. The increased fraction of green energy sources is the second important application for batteries in the energy revolution. Solar or wind power rely on renewable energy sources with the disadvantage of a fluctuating production rate. Therefore, it is necessary to develop flexible energy storage systems to balance energy consumption and production. Large scale battery systems are one potential system fulfilling the requirements.

The most basic functionality of a battery system is the conversion of stored chemical energy into electrical energy. A cylindrical battery configuration as shown in Fig. 1.1(a) is based on a coiled configuration of an elementary cell being the basic element of each battery system. The basic principle of an elementary cell is depicted in Fig. 1.1(b). An elementary cell consists of six components, namely two current collectors, a negative and a positive electrode separated

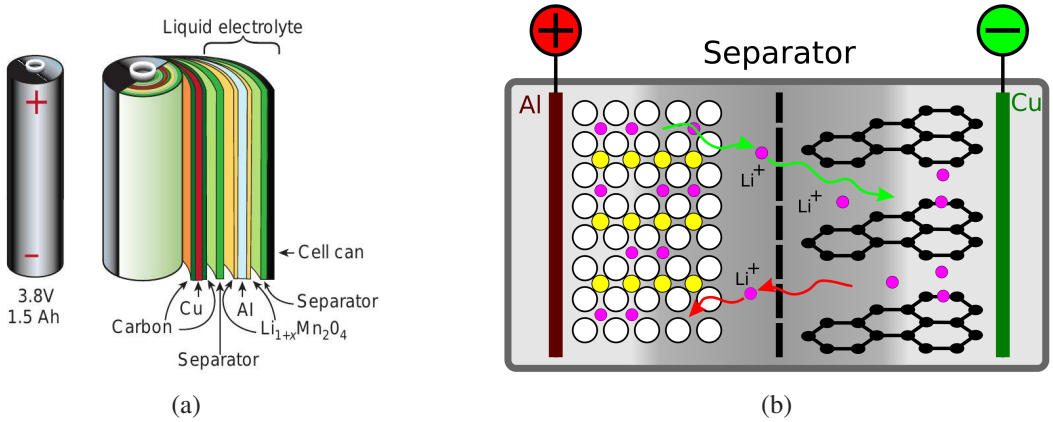

Figure 1.1: Basic principle of a cylindrical lithium ion battery consisting of a lithium manganese oxide (magenta, yellow and white dots) and a carbon (black rings) electrode: a) cylindrical battery configuration taken from [137] and b) an elementary cell taken from [39] including the path of lithium ions for charge (green arrows) and discharge (red arrows).

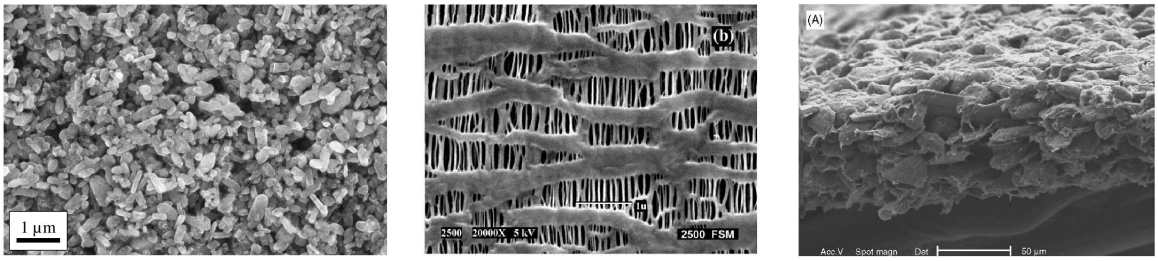

(a) Lithium iron phosphate [95]. (b) Separator CG2500 [8]. (c) Graphite [119].

Figure 1.2: Scanning electron microscope images of a) the cathode, b) the separator and c) the anode.

by an electrically isolating, porous separator and a lithium-based electrolyte solution. In standard lithium-ion batteries, the positive and the negative electrode consist of porous materials to increase the effective surface area and capacity of each electrode. The electrolyte solution fills the void space of both electrodes and the separator. In commercial cells, the negative electrode, being the anode during discharge, is usually made of graphite which is the soft form of carbon. An alternative material which is already employed in commercial cells is for example lithium titanate (LTO). For the positive electrode, being the cathode during discharge, different material compositions such as lithium cobalt oxide (LCO), lithium manganese oxide (LMO), lithium iron phosphate (LFP) or lithium nickel manganese cobald oxide (NMC) are used. For both cathode and anode, research into alternative materials continues as indicated, e.g, by Andre et al. [5] or Marom et al. [104]. Lithiumhexafluorophosphat ($LiPF_6$), dissolved in a mixture of various aprotic solvents is the most common electrolyte solution. Usually, various additives are added to the electrolyte solution to improve specific properties of the electrolyte solution. A detailed discussion of electrolyte solutions used in lithium-based rechargeable batteries is given, e.g., in Xu [156]. The last basic component of an elementary cell is the separator described best as a porous membrane which has to ensure ion-transport between anode and cathode but prevents electrical contact. A detailed review of commercial battery separators is given, e.g., in Arora and Zhang [8]. All aforementioned components are also discussed in detail, e.g., in Nazri and Pistoia [108] or Huggins [85]. Scanning Electron Microscope (SEM) images of typical cathode, separator and anode materials are provided in Fig. 1.2.

Basic principle of a rechargeable lithium ion cell At this point, a brief introduction to the basic operation principle of a rechargeable lithium ion cell consisting of graphite and LCO electrodes is given. Initially, a charged elementary cell with a lithiated graphite and delithiated LCO electrode is considered. The term lithiated describes the state of the electrode in which lithium ions are intercalated into the electrode material. In rechargeable lithium ion batteries, the insertion and the extraction of lithium ions to and from the electrodes are reversible. During discharge, lithium ions move through the electrolyte solution from the negative graphite electrode to the positive LCO electrode. At the graphite electrode, lithium ions are formed by the following anodic reaction:

$$LiC_6 \rightarrow Li^+ + e^- + C_6. \tag{1.1}$$

The lithium is extracted from the graphite and enters the electrolyte solution. The released electron e^- is transported from the electrode-electrolyte interface through the electrically-conducting graphite electrode to the current collector. This reaction is called oxidation. At the LCO cathode, the lithium ions available in the electrolyte solution next to the electrode-electrolyte interface are reduced and intercalated into the LCO cathode. The corresponding reaction can be written as

$$\mathrm{Li}_{(1-x)}\mathrm{CoO}_2 + x\ \mathrm{Li}^+ + x\ \mathrm{e}^- \rightarrow \mathrm{LiCoO}_2. \tag{1.2}$$

To close the cycle, the electrons e^- have to be transported through an external circuit from the negative to the positive electrode. By definition, oxidation always takes place at the anode and reduction at the cathode. Therefore, the nomenclature for the single components given in the beginning of this section is based on the discharge process. The oxidation and reduction given in Equ. (1.1) and (1.2) are often summarized in the corresponding redox reaction

$$x\ \mathrm{LiC}_6 + \mathrm{Li}_{(1-x)}\mathrm{CoO}_2 \rightleftarrows x\ \mathrm{C}_6 + \mathrm{LiCoO}_2.$$

The driving force for this reaction is a natural difference between the electrochemical potentials of the lithiated graphite electrode and the delithiated LCO electrode. The resulting electrochemical potential gradient within the electrolyte solution is also the driving force for the transport of lithium ions in the electrolyte solution. Since the electrochemical potential is influenced by the electrostatic potential and the concentration, among other things, ion-transport is often modeled by a diffusive and migrative process. A detailed discussion of the basic phenomenological transport mechanisms is given, e.g., in Bauer [18] or Newman and Thomas-Alyea [109, chap. 1]. Due to the delithiation of the anode and lithiation of the cathode, the electrochemical potential difference between the electrodes is decreased continuously until the the electrochemical potential difference is too small to act as driving force for the reaction. At this point, the elementary cell is discharged completely and has to be charged before it can be used again. During charging, the chemical processes are reversed by the application of an external power source.

To summarize, the discharge and charge process of an elementary cell can be split into three major physical phenomena, namely the lithium ion-transport through the electrolyte solution, the description of the reaction process at anode and cathode as well as the insertion (or intercalation) and extraction (or deintercalation) of lithium from the anode and cathode. The electron conduction in commercial anode and cathode materials is usually so fast that it can be neglected in most physically-motivated models.

Current issues of rechargeable battery systems are a limited energy density and lifetime as well as safety issues. An overview over these is given, e.g., by Wagner et al. [145] focusing on the needs of the electromobility or by Goodenough and Kim [71] giving a more general outlook. An up-to-date review on current research trends in lithium-based batteries is given, e.g., by Wagner et al. [146] or Scrosati and Garche [131]. In addition, alternative battery system such as lithium sulfur or lithium air batteries providing much higher theoretical energy densities are investigated as future alternatives to lithium ion batteries as discussed, e.g., by Armand and Tarascon [7]. The main issues of such alternative battery concepts are discussed, e.g., in Barchasz et al. [13] and Girishkumar et al. [68]. However, it will still take some time until these new concepts are used in commercial applications as emphasized by Girishkumar et al. [68, p. 2195]: "*Automotive propulsion batteries are just beginning the transition from nickel metal hybrid to Li-ion batteries*

after nearly 35 years of research and development on the latter. The transition to Li-air batteries (if successful) should be reviewed in terms of a similar development cycle."

Modeling of battery systems Computational methods can support the development of advanced battery systems since they can provide insight into physical and chemical aspects of battery systems, which are not or hardly achievable experimentally. Another important field of application for computer-based methods is the optimization of future battery designs. Therefore, it is not very surprising that various computational methods for simulating electrochemical systems are available in literature or commercial software tools to support the development and the design of battery systems. However, due to the large variety of computational methods and their general availability, it is important to distinguish strictly between different perspectives used for the development. In general, it is common to classify the computational methods with respect to the resolved length and time scale as it is discussed, e.g., by Ramadesigan et al. [124]. In battery applications, computational methods can be classified into four basic groups, namely the system level, the cell level and the geometrically resolved cell level as depicted in Fig. 1.1(a), Fig. 1.1(b) and Fig. 1.2, respectively. Beyond the geometrically resolved cell level, molecular dynamics and kinetic Monte Carlo methods are used to gain insight into physical and chemical phenomena such as the growth of the passivating Surface Electrolyte Interface (SEI) film as presented, e.g., by Methekar et al. [107], or the lithium diffusion within the active material as discussed, e.g., by Wagemaker et al. [144]. The predictability but also the computational costs of molecular dynamics and kinetic Monte Carlo methods are very high.

In contrast, computational methods used on system level exhibit usually a limited predictability combined with the advantage of low computational cost. Typical examples are empirical models which are based on experimental data and only marginally on physio-chemical principles. In this case, the model can hardly be applied to different operating conditions or applications based on different physio-chemical principles. Equivalent circuit models consisting of basic circuit elements such as resistances or capacitors are also very common on system level since they can be linked perfectly with experimental techniques such as impedance spectroscopy as it is done, e.g., in Hu et al. [84] or Ogihara et al. [117]. In the latter publication, the equivalent circuit model is used to describe physical phenomena on the cell level. However, the most common model on cell level are the so-called electrochemical engineering models which are based on fundamental physio-chemical principles such as ion-transport due to diffusion and migration resulting in an improved predictability compared, e.g., to equivalent circuit models. In these models, the porous structure of electrodes and separator is not resolved geometrically but modeled by so-called homogenization or volume averaging approaches. In this case, the effect of the porous medium is incorporated into the conservation laws by the introduction of additional geometrical parameters. Typical examples are for instance the cell model introduced by Fuller et al. [64] or simulation approaches as used, e.g., by Cai and White [34]. As indicated, e.g., by Albertus et al. [4], electrochemical engineering models are also combined with other computational approaches such as the equivalent circuit model to include effects which can hardly be described by more sophisticated models. On the geometrically resolved cell level, the porous structure of electrodes and separators are geometrically resolved which is the main difference to the approach used on the cell level. It is important to emphasize that an increased predictability due to a decreasing length scale also results in increased computational costs and in an increased

number of required model parameters. The determination of such physically-motivated parameters is a challenging task.

The computational methods described in this contribution focus on the cell level as well as on the geometrically resolved cell level. In addition, the focus is solely on ion-transport in binary electrolyte solution. Electrochemical reactions at electrodes are only considered in a very basic manner. The modeling of the intercalation process of lithium ions into the electrodes is not addressed at all in this work.

Objective and outline For all numerical simulations, reproducibility and accuracy are key issues, which depend on appropriate physical models, boundary conditions, and accurately determined transport parameters, among other things. In this context, two physically-motivated models for ion-transport in concentrated electrolyte solutions based on completely different physical principles are reviewed and related to each other. Based on this knowledge, a flexible computational approach for ion-transport in binary electrolyte solutions is introduced which enables both, simulations of large realistic, resolved porous structures as well as simulations of porous media homogenized by the volume averaging approach. Such a computational approach provides for example the opportunity to investigate the influence of the microstructure of the porous medium on the macroscopic behavior of the elementary cell. To account for the requirement to simulate complex realistic porous geometries, the Finite Element Method (FEM) is used as a discretization method. It has already been applied successfully to ion-transport in dilute electrolyte solutions by Bauer et al. [20]. In this work, the basic concept presented in Bauer et al. [20] is extended to concentrated electrolyte solutions whereas the stabilized finite element approach is not considered since convective transport can be neglected for most battery applications. The computational approach is implemented within the multi-physics computing platform BACI (Wall and Gee [147]) which is continuously developed and maintained by the Institute for Computational Mechanics at the Techischen Universität München.

Similar simulation tools can be found in literature, whereas accurate and reliable transport parameters are scarce. For example, two situations are frequently encountered: either the potential range of such transport parameters provided in literature is very broad or parameters are not reliable due to the fact that, e.g., important experimental procedures related to their determination are not specified. Therefore, it is the main objective of this work to develop accurate and at the same time as simple as possible experimental procedures for the determination of a complete set of transport parameters for binary electrolyte solutions required for predictive numerical simulations. In this context, experimental methods for the determination of geometrical parameters necessary for electrochemical engineering models are discussed as well. In this work, the development of a computational approach for ion-transport in concentrated electrolyte solutions and the experimental determination of the corresponding model parameters is seen as an interactive process which cannot be considered separately.

The entire project is embedded into the interdisciplinary energy storage research project ”Distributed stationary battery storage systems for the efficient use of renewable energies and support of grid stability” (EEBatt) supported by the Bavarian Ministry of Economic Affairs and Media, Energy, and Technology. The financial support as well as the successful cooperation within the ”Teilprojekt 2” are gratefully acknowledged. Parts of the numerical methods as well

as related experimental and numerical results presented in this thesis are published in Ehrl et al. [56–58], Roth et al. [127] and Landesfeind et al. [96, 97].

In section 2, two physically-motivated models for ion-transport in concentrated electrolyte solutions based on the Stefan-Maxwell approach and non-equilibrium thermodynamics are introduced and compared to each other. In addition, the connection of both models to the dilute solution theory based on the Nernst-Planck approach is derived which has not been addressed in literature so far. To circumvent the computationally costly spatial resolution of complex porous structures, the volume averaging approach for ion-transport in porous media is discussed in section 3. The validity of the volume averaging approach for ion-transport with concentration dependent transport parameters is also demonstrated. The determination of geometrical parameters, namely the porosity and the tortuosity of porous media, is addressed in section 4. In section 5, the theoretical background for the experimental determination of a complete set of transport parameters for ion-transport in aprotic, binary electrolyte solutions is discussed. As a complete set, three transport parameters, namely the conductivity of the electrolyte solution, the diffusion coefficient and the transference number and one thermodynamic quantity the so-called thermodynamic factor or, alternatively, the mean activity coefficient are considered. The presented methods include novel experimental procedures for the determination of the concentration dependent thermodynamic factor and the concentration dependent transference number. In addition, various known and unknown alternatives for the determination of the transference number are discussed critically. In section 6, the computational approach for ion-transport in concentrated electrolyte solutions based on the finite element method is introduced focusing in particular on the numerical modeling of galvanostatic boundary conditions. The computational approach is validated by various academic and realistic numerical examples in section 7. In addition, the experimental methods for the determination of transport parameters are partly validated and analyzed with respect to important design parameters. Finally, the applicability of the computational approach for realistic, porous geometries is demonstrated. In section 8, transport parameters of an exemplary electrolyte solution are determined experimentally utilizing the methods introduced in section 5. Finally, conclusions are drawn in section 9, before ending with a short outlook.

In appendix A the theoretical background of non-linear thermodynamics is introduced briefly. In appendix B and appendix C, more detailed mathematical derivations required in section 3 and section 5 are provided.

2 Mathematical modeling of concentrated binary electrolyte solutions

The most fundamental model for concentrated binary electrolyte solutions was introduced originally by Newman et al. [112]. It is based on a multi-component diffusion approach, the so-called Stefan-Maxwell approach, incorporating the influence of an electrostatic potential field. Often, this model is also called the 'Newman model'. A detailed discussion of the basic thermodynamic principles and of ion-transport in electrolyte solutions, in general, is given in Newman and Thomas-Alyea [109]. Besides, various electrochemical applications and practical examples are included in this textbook. The ion-transport model was extended for porous materials utilizing a homogenization approach in Newman and Tiedemann [111]. Up to now, this model is widely used in academic and industrial applications. It is also the standard model in commercial simulation software. A good summary of the model including some interesting applications is given, e.g., in Fuller et al. [63], Doyle [53] and Doyle et al. [54]. Over the years, the model was extended by various aspects such as a temperature dependence as discussed, e.g., by Gu and Wang [75], Cai and White [34], Song and Evans [134] or Botte et al. [28], transport of additional uncharged components, as e.g., in Albertus et al. [4], solvent effects, as e.g., in Liu and Monroe [100] and Georén and Lindbergh [67] or convection, as e.g., in Xue and Plett [157].

The model proposed by Latz and Zausch [99] is based on non-equilibrium thermodynamics. The main advantage of this approach is the inherent incorporation of thermal effects into the ion-transport equations. Similar approaches are presented, e.g., in Kontturi et al. [91] or Kjelstrup and Bedeaux [90]. A good overview over the topic is given in Landstorfer and Jacob [98]. A common model for dilute electrolyte solutions is the Nernst-Planck approach or the diffusion-migration equation, as it is also called. The second name is quite self-explanatory since the model is a reformulation of the Fick's law of diffusion, extended to the motion of charged particles. It was theoretically motivated by Planck and experimentally verified by Nernst. In the textbook by Kontturi et al. [91], the Nernst-Planck approach is derived from the framework of non-equilibrium thermodynamics, where in a first approximation the cross coefficients are neglected in the transport equations for charged components. A detailed discussion of the entire mathematical and numerical framework of the Nernst-Planck approach is given, e.g., in Bauer [18]. For binary electrolyte solutions, this model can also be reformulated to the form of the classical Fick's law of diffusion.

Based on thermodynamic considerations and the transition state theory, a variation of the Nernst-Planck equations for concentrated solutions is developed in Bazant et al. [22] and Ferguson and Bazant [61]. In contrast to the classical Nernst-Planck equations, the diffusion coefficients incorporate the ionic activity coefficient and are typically given as a function of the concentration. An similar approach is presented by Lai and Ciucci [93].

In section 2.1, some continuum-mechanical basics are introduced. Afterwards, the balance equations for mass and charge are presented in section 2.2 and section 2.3, respectively. The basic ideas of the concentrated solution theory based on the Stefan-Maxwell approach, the dilute solution theory based on the Nernst-Planck approach and the concentrated solution theory based on non-equilibrium thermodynamics are introduced in section 2.4, section 2.5 and section 2.6, and, more importantly, related to each other. This is necessary since the final equations of the different models show some significant differences. To understand these differences, the most important highlights of the respective derivations are illustrate in the following. The derivations are mostly based on binary electrolyte solutions since this is the most relevant case in battery research. Theoretically, it is not so complex to extend the models to multi-ion systems, but the main limiting factor is the determination of accurate and physically motivated transport parameters which are not only based on theoretical considerations. In addition, boundary and initial conditions for the ion-transport equations are specified in section 2.7.

2.1 Mathematical preliminaries

In the following, the behavior of electrochemical systems is investigated for the time interval $[0, T_{\text{end}}]$ in a polygonally shaped and bounded domain $\Omega \subset \mathbb{R}^d$, where $d \leq 3$ is the number of spatial dimensions. The domain Ω is filled with an electrolyte solution consisting of $k = 1, \ldots, \text{m}$ charged or uncharged components. The boundary of Ω is denoted by Γ and is assumed sufficiently smooth. The closure of Ω is defined as $\overline{\Omega} := \Omega \cup \Gamma$. To specify Boundary Conditions (BC) for each component k, a partition $\Gamma = \Gamma_{\text{D},c_k} \cup \Gamma_{\text{N},c_k} \cup \Gamma_{\text{E},c_k}$ is considered, where the three boundary regions are assumed pairwise disjoint. Appropriate boundary conditions are given as

$$\begin{aligned} c_k &= g_k && \text{on } \Gamma_{\text{D},c_k} \times (0, T_{\text{end}}), \\ -\boldsymbol{N}_k \cdot \boldsymbol{n} &= h_k && \text{on } \Gamma_{\text{N},c_k} \times (0, T_{\text{end}}), \\ -\boldsymbol{N}_k \cdot \boldsymbol{n} &= j_k && \text{on } \Gamma_{\text{E},c_k} \times (0, T_{\text{end}}), \end{aligned} \tag{2.1}$$

where c_k is the concentration of component k, $\boldsymbol{N}_k$ the molar flux density of component k and $\boldsymbol{n}$ the unit outer normal vector to the boundary. On Γ_{D,c_k}, Dirichlet boundary conditions are applied, where g_k represent prescribed ionic concentrations. The normal molar flux density on Γ_{N,c_k} is denoted as h_k. Electrode surfaces are represented by the boundary part Γ_{E,c_k}, which can be further subdivided into any number of anodic and cathodic parts. At electrode surfaces, the normal component j_k of the molar flux density corresponds to the rate of all electrochemical reactions $r = 1, \ldots, r_{\text{max}}$. Thus, the boundary condition reads

$$j_k := \begin{cases} 0 & \text{for inert ionic species,} \\ \sum_r -\frac{s_{r,k}}{n_r F} i_n & \text{for reactive ionic species,} \end{cases} \tag{2.2}$$

with n_r being the number of transferred electrons e^- in reaction r of the form

$$\sum_k s_{r,k} \mathrm{A}_k^{z_k} \rightleftarrows n_r e^-, \tag{2.3}$$

where $s_{r,k}$ is the stoichiometric coefficient of ionic species k in reaction r, F the Faraday constant, i_n the normal component of the current density $\boldsymbol{i}$ and $\mathrm{A}_k^{z_k}$ the chemical symbol of species k with the valence z_k. Initial conditions for c_k have to be specified,

$$c_k = c_{k,0} \qquad \text{in } \overline{\Omega} \times (0).$$

For the boundary conditions on the potential field Φ, the same spatial partition $\Gamma = \Gamma_{\mathrm{D},\Phi} \cup \Gamma_{\mathrm{N},\Phi} \cup \Gamma_{\mathrm{E},\Phi}$ is used as for the concentrations:

$$\begin{aligned} \Phi &= g_\Phi && \text{on } \Gamma_{\mathrm{D},\Phi} \times (0, T_\mathrm{end}), \\ -\boldsymbol{i} \cdot \boldsymbol{n} &= h_\Phi && \text{on } \Gamma_{\mathrm{N},\Phi} \times (0, T_\mathrm{end}), \\ -\boldsymbol{i} \cdot \boldsymbol{n} &= i_\mathrm{n} && \text{on } \Gamma_{\mathrm{E},\Phi} \times (0, T_\mathrm{end}). \end{aligned} \tag{2.4}$$

Since electrochemical reactions conserve mass and charge, the normal current density h_Φ at $\Gamma_{\mathrm{N},\Phi}$ is connected to the normal molar flux density h_k via $h_\Phi = F \sum_{k=0}^{m} z_k h_k$. Analogously, the normal current density i_n on $\Gamma_{\mathrm{E},\Phi}$ is related to j_k by Equ. (2.2). It is important to mention that not all theoretically possible combinations of BC and initial conditions are physically motivated or mathematically valid. For instance, the initial potential field Φ_0 is not independent of initial concentration fields $c_{k,0}$.

In this contribution, a macroscopic description of the electrochemical system is chosen, utilizing a continuum-mechanical approach. In literature (see, e.g., Newman and Thomas-Alyea [109], Kjelstrup and Bedeaux [90] or Kontturi et al. [91]), the continuum hypothesis is a generally accepted approximation for modeling electrochemical systems from an engineering perspective. A general introduction to continuum mechanics is given, e.g., in text books by Lai et al. [94] and Gurtin [76].

2.2 Mass conservation

In general, an electrolyte solution is a solvent where $m \geq 2$ ionic species and potentially additional neutral components are dissolved. In the context of concentrated solutions, the solvent is generally considered as the first component of the electrolyte solution and thus denoted by $k = 0$. For such a system, the basic principle of mass conservation is fulfilled for the total mass as well as for all charged and uncharged components of the electrolyte solution. In this contribution, the conservation laws are given only in local form applying to every point within the continuum. The generalized local form of the balance equation for arbitrary quantities such as mass or charge are derived from the conservation law in integral form with respect to a control volume $V(t)$ enclosed by the surface $S(t)$, as discussed e.g. by Kontturi et al. [91], Donea and Huerta [52] or Bauer [18]. The conservation of total mass is given by

$$\frac{\partial \rho}{\partial t} + \nabla \cdot (\rho \boldsymbol{u}) = 0, \tag{2.5}$$

where ρ denotes the density of the electrolyte solution including dissolved components, $\frac{\partial \rho}{\partial t}$ the partial time derivative of the density and $\boldsymbol{u}$ the velocity of the surface $S(t)$. In the following, the

velocity $\boldsymbol{u}$ is called reference velocity. From Equ. (2.5), it is clear that the only relevant transport mechanism for total mass is convection. If the density ρ of the electrolyte solution is approximately constant or the total time derivative $\frac{\mathrm{d}\rho}{\mathrm{d}t} = \frac{\partial\rho}{\partial t} + \boldsymbol{u} \cdot \nabla\rho$ is approximately zero, Equ. (2.5) reduces to $\nabla \cdot \boldsymbol{u} = 0$ and the electrolyte solution can be considered incompressible. This is also valid for chemical reactions since the total mass of the system is still conserved. Additionally, the charged and uncharged components in an electrolyte solution are also conserved according to

$$\frac{\partial c_k}{\partial t} + \nabla \cdot \underbrace{(c_k \boldsymbol{u} + \boldsymbol{N}_k)}_{\boldsymbol{N}_k^{\mathrm{T}} = c_k \boldsymbol{u}_k} = r_k. \tag{2.6}$$

Here, c_k is the concentration of component k in the electrolyte solution, r_k the reaction rate of component k and $\boldsymbol{N}_k$ the molar flux density of component k due to diffusion and migration. The definition of the total molar flux density $\boldsymbol{N}_k^{\mathrm{T}}$ also includes the convective transport of species k with respect to the reference velocity $\boldsymbol{u}$. As indicated in Equ. (2.6), the total molar flux density $\boldsymbol{N}_k^{\mathrm{T}}$ can also be expressed as a 'convective' transport of species k with the component velocity $\boldsymbol{u}_k$. This definition is of particular importance in the Stefan-Maxwell approach. The reaction rate r_k is only non-zero if component k is involved in a homogeneous chemical reaction. Since the aforementioned conditions for incompressibilty are usually fulfilled for electrolyte solutions, Equ. (2.5) and Equ. (2.6) can also be formulated in convective form, as it is shown here for Equ. (2.6):

$$\frac{\partial c_k}{\partial t} + \boldsymbol{u} \cdot \nabla c_k + \nabla \cdot \boldsymbol{N}_k = r_k. \tag{2.7}$$

Mathematically, an arbitrary choice of the reference velocity is possible. However, this is not recommended from a physical point of view. A common definition for the reference velocity is the solvent velocity $\boldsymbol{u} \equiv \boldsymbol{u}_0$. This definition is called Hittorf's reference frame. For a binary electrolyte solution, the choice of the solvent velocity $\boldsymbol{u}_0$ as reference velocity gives

$$\begin{aligned} c_0 \boldsymbol{u}_0 &= \boldsymbol{N}_0^{\mathrm{T}} = c_0 \boldsymbol{u}_0 + \boldsymbol{N}_0 \\ c_1 \boldsymbol{u}_1 &= \boldsymbol{N}_1^{\mathrm{T}} = c_1 \boldsymbol{u}_0 + \boldsymbol{N}_1 \\ c_2 \boldsymbol{u}_2 &= \boldsymbol{N}_2^{\mathrm{T}} = c_2 \boldsymbol{u}_0 + \boldsymbol{N}_2. \end{aligned}$$

Therefore, the molar flux density $\boldsymbol{N}_0$ of the solvent with respect to the solvent velocity $\boldsymbol{u}_0$,

$$\boldsymbol{N}_0 = c_0 \boldsymbol{u}_0 - c_0 \boldsymbol{u}_0 = 0, \tag{2.8}$$

has to be zero, whereas the molar flux densities $\boldsymbol{N}_1$ and $\boldsymbol{N}_2$ of the remaining components $k = 1, 2$ are defined as

$$\boldsymbol{N}_{1,2} = c_{1,2} \left(\boldsymbol{u}_{1,2} - \boldsymbol{u}_0 \right). \tag{2.9}$$

Especially for very concentrated solutions and ionic liquids, the choice of the solvent velocity $\boldsymbol{u}_0$ as reference velocity may be problematic since the solvent velocity of the electrolyte is also

influenced by the remaining components of the electrolyte solution. Therefore, it is useful to introduce an alternative definition for the reference velocity. The concentration c_k in Equ. (2.6) can also be expressed in terms of the mass fraction w_k and the molar mass M_k of component k,

$$c_k = \rho \frac{w_k}{M_k},$$

which gives, when inserted into Equ. (2.6) and multiplied by M_k,

$$\frac{\partial(\rho w_k)}{\partial t} + \nabla \cdot (\rho w_k \boldsymbol{u}_k) = M_k r_k.$$

Summation over all m component conservation equations results in the total mass conservation given in Equ. (2.5) since $\sum_{k=0}^{m} w_k = 1$ by definition, $\sum_{k=0}^{m} M_k r_k = 0$ due to mass conservation for homogeneous reactions and

$$\rho \boldsymbol{u} \equiv \rho \boldsymbol{u}^{\mathrm{B}} = \rho \sum_{k=0}^{m} w_k \boldsymbol{u}_k. \tag{2.10}$$

Equ. (2.10) gives the definition of the barycentric velocity $\boldsymbol{u}^{\mathrm{B}} = \sum_{k=0}^{m} w_k \boldsymbol{u}_k$ as reference velocity $\boldsymbol{u}$. In contrast to the solvent velocity $\boldsymbol{u}_0$, the barycentric velocity can be used generally in the conservation law for linear momentum (Navier-Stokes equation). For dilute solutions, the barycentric velocity $\boldsymbol{u}^{\mathrm{B}} = w_0 \boldsymbol{u}_0 + \sum_{k=1}^{m} w_k \boldsymbol{u}_k \approx \boldsymbol{u}_0$ can be approximated by the solvent velocity $\boldsymbol{u}_0$ if the mass fraction of the solvent is approximately one. A detailed explanation of the basic principle of reference velocities, additional definitions and their implications are given in Kontturi et al. [91] and Newman and Thomas-Alyea [109].

2.3 Electric charge conservation

In a continuum approach, an electrolyte solution is usually considered to be locally electrically neutral:

$$\sum_{k} z_k c_k = 0. \tag{2.11}$$

Here, the charge number of component k is denoted by z_k, which is zero for neutral components, positive for cations and negative for anions. The validity of the ElectroNeutrality Condition (ENC) can be justified, e.g., by the model of Debye-Hückel. In this model, the Debye length describes the extent of the ionic atmosphere around a central cation or anion in an electrolyte solution. Usually, the Debye length is in the order of Ångström to nanometer and hence can be neglected in a macroscopic model. A detailed derivation of the Debye-Hückel theory is given, e.g., in Wright [153]. In Kontturi et al. [91], electroneutrality is justified by the high energy required for charging a macroscopic system. For an electrically neutral electrolyte solution, electric charge conservation is derived from the general law of conservation (see, e.g., Kontturi et al. [91]). Multiplication of Equ. (2.6) by Fz_k and summation over all components k of the

electrolyte gives

$$\frac{\partial}{\partial t}\left[F\sum_{k=0}^{m}(z_k c_k)\right] + \nabla\cdot\left(F\sum_{k=0}^{m}(z_k c_k)\boldsymbol{u} + F\sum_{k=0}^{m}(z_k \boldsymbol{N}_k)\right) = 0. \tag{2.12}$$

Using charge density

$$\rho_\mathrm{e} \equiv F\sum_{k=0}^{m} z_k c_k,$$

and the electric current density

$$\boldsymbol{i} = F\sum_{k=0}^{m} z_k \boldsymbol{N}_k, \tag{2.13}$$

Equ. (2.12) becomes to the electric charge conservation as given, e.g., in Kontturi et al. [91]

$$\frac{\partial \rho_\mathrm{e}}{\partial t} + \nabla\cdot\boldsymbol{i} = 0. \tag{2.14}$$

Due to the ENC, the convective term of the total molar flux density cancels out in Equ. (2.12). Therefore, it is clear, that the electric current density is always based on molar flux densities which do not include convective transport. Additionally, uncharged components as the solvent or neutral components ($z_k = 0$) do not contribute to the electric charge conservation, the charge density and the current density. As a result of the ENC, the charge density in the electric charge conservation is by definition zero. Hence, Equ. (2.14) simplifies to

$$\nabla\cdot\boldsymbol{i} = 0. \tag{2.15}$$

2.4 Concentrated solution theory based on Stefan-Maxwell approach

2.4.1 Stefan-Maxwell approach

The most famous model for concentrated solutions, which is widely used in literature and in many industrial applications, is based on the Stefan-Maxwell approach. The following derivation is inspired by Newman and Thomas-Alyea [109] and Kontturi et al. [91].

In general, the Stefan-Maxwell approach is based on particle dynamics where all components of an electrolyte solution are assumed to be independent particles interacting with each other. As long as the collision between particles can be considered elastic, conservation of momentum and energy is generally valid. For such a case, the diffusion processes in multi-

component systems such as electrolyte solutions can be characterized by

$$c_k \nabla \hat{\mu}_k = \sum_l K_{kl}(\boldsymbol{u}_l - \boldsymbol{u}_k), \tag{2.16}$$

where $\hat{\mu}_k$ denotes the electrochemical potential of component k as introduced in appendix A.4. The component velocities of species k and l are denoted by $\boldsymbol{u}_k$ and $\boldsymbol{u}_l$, respectively, as introduced in Equ. (2.6). The friction coefficient associated with components k and l is given by K_{kl}. A more detailed derivation of this equation is given, e.g., in Kontturi et al. [91, chap. 2.4]. Alternatively, the friction coefficient K_{kl} can also be expressed in terms of an intermolecular diffusion coefficient $\mathcal{D}_{kl}$:

$$K_{kl} = RT \frac{c_k c_l}{c_\mathrm{T}} \frac{1}{\mathcal{D}_{kl}}, \tag{2.17}$$

where

$$c_\mathrm{T} = \sum_{k=0}^{m} c_k \tag{2.18}$$

is the total concentration of all electrolyte components. For the friction coefficients K_{kl} as well as for the intermolecular diffusion coefficients $\mathcal{D}_{kl}$, Onsager's reciprocal theorem

$$K_{kl} = K_{lk} \qquad \text{and} \qquad \mathcal{D}_{kl} = \mathcal{D}_{lk} \tag{2.19}$$

is valid. As described in Newman and Thomas-Alyea [109, chap. 12.1], the theorem is a consequence of Newton's third law of motion. The physical meaning of Equ. (2.16) is the balance between driving force and the frictional force:

$$\text{driving force} + \text{frictional force} = 0.$$

Here, the driving force is the gradient of the electrochemical potential times the concentration and the frictional force is given by the movement of the components relative to each other multiplied by a friction coefficient. Summation over all k components of the electrolyte solution gives

$$\sum_k c_k \nabla \hat{\mu}_k = \sum_k \sum_l K_{kl}(\boldsymbol{u}_l - \boldsymbol{u}_k). \tag{2.20}$$

In the absence of pressure and temperature gradients, the term on the left hand side of this equation is equal to zero as a result of the Gibbs-Duhem equation (A.6). In this special case, all frictional forces on the right hand side have to balance. This implication will be clearer when the special case of a binary electrolyte is considered.

Stefan-Maxwell equations for binary electrolyte solutions The restriction to binary electrolyte solutions in the following has mainly two reasons. In a battery system, the electrolyte solution is usually based on a single salt with additional substances to improve specific prop-

erties, but the amount of additives is generally so small that the electrochemical behavior of the electrolyte solution is not influenced significantly. As a consequence, the assumption of a binary electrolyte solution is justified in quite many cases. The second reason is that an accurate determination of all transport parameters for a multi-component electrolyte solution is quite challenging. Therefore, it may be favorable to approximate a multi-component electrolyte solution by a binary electrolyte solution with additional components modeled to be electrochemically inert. Of course, such an approach may not be possible for all electrolyte solutions as, e.g., for ionic liquids.

In general, a binary electrolyte solution is a solvent in which an arbitrary, neutral salt $\mathrm{A}_{\nu_+}\mathrm{B}_{\nu_-}$ consisting of the charged components A^{z_+} and B^{z_-} is dissolved. The neutral salt has to fulfill the condition

$$\nu_+ z_+ + \nu_- z_- = 0. \tag{2.21}$$

For such an electrolyte solution, Equ. (2.16) can be written as

$$c_+ \nabla \hat{\mu}_+ = K_{0+}(\boldsymbol{u}_0 - \boldsymbol{u}_+) + K_{+-}(\boldsymbol{u}_- - \boldsymbol{u}_+), \tag{2.22}$$
$$c_- \nabla \hat{\mu}_- = K_{0-}(\boldsymbol{u}_0 - \boldsymbol{u}_-) + K_{+-}(\boldsymbol{u}_+ - \boldsymbol{u}_-), \tag{2.23}$$
$$c_0 \nabla \hat{\mu}_0 = K_{0+}(\boldsymbol{u}_+ - \boldsymbol{u}_0) + K_{0-}(\boldsymbol{u}_- - \boldsymbol{u}_0). \tag{2.24}$$

Here, Onsager's reciprocal theorem given in Equ. (2.19) is already applied to simplify the notation. For binary electrolytes, the subscripts k and l in Equ. (2.16) are replaced by $+$ for the cation, $-$ for the anion and 0 for the electrolyte solution. Based on Hittorf's reference frame defined in section 2.2 and Equ. (2.9), the molar flux density of the positive and negative ionic species in a binary electrolyte solution can be written as

$$\boldsymbol{N}_+ = c_+(\boldsymbol{u}_+ - \boldsymbol{u}_0) = -c_+(\boldsymbol{u}_0 - \boldsymbol{u}_+), \tag{2.25}$$
$$\boldsymbol{N}_- = c_-(\boldsymbol{u}_- - \boldsymbol{u}_0) = -c_-(\boldsymbol{u}_0 - \boldsymbol{u}_-). \tag{2.26}$$

Additionally, it is possible to express the current density $\boldsymbol{i}$ from Equ. (2.13) in terms of the component velocities $\boldsymbol{u}_k$,

$$\begin{aligned} \boldsymbol{i} &= F\left(z_+ \boldsymbol{N}_+ + z_- \boldsymbol{N}_-\right) \\ &= F z_+ c_+ (\boldsymbol{u}_+ - \boldsymbol{u}_0) + F z_- c_- (\boldsymbol{u}_- - \boldsymbol{u}_0) \\ &= F z_+ c_+ (\boldsymbol{u}_+ - \boldsymbol{u}_-), \end{aligned} \tag{2.27}$$

where the ENC given in Equ. (2.11) for binary electrolyte solutions is used in the form $z_+ c_+ = -z_- c_-$. As a result, the Stefan-Maxwell equations given in Equ. (2.22) – Equ. (2.24) for binary electrolyte solutions can also be expressed in terms of the molar flux densities $\boldsymbol{N}_+$ and $\boldsymbol{N}_-$ as

well as the current density $\boldsymbol{i}$

$$c_+ \nabla \hat{\mu}_+ = -K_{0+} \frac{\boldsymbol{N}_+}{c_+} - K_{+-} \frac{\boldsymbol{i}}{F z_+ c_+}, \tag{2.28}$$

$$c_- \nabla \hat{\mu}_- = -K_{0-} \frac{\boldsymbol{N}_-}{c_-} + K_{+-} \frac{\boldsymbol{i}}{F z_+ c_+}, \tag{2.29}$$

$$c_0 \nabla \hat{\mu}_0 = +K_{0+} \frac{\boldsymbol{N}_+}{c_+} + K_{0-} \frac{\boldsymbol{N}_-}{c_-}. \tag{2.30}$$

At this point, the advantage of using Hittorf's reference frame becomes particularly clear. In this reference frame, the electrochemical potential is expressed in terms of the molar ionic fluxes and current density without an additional contribution of the mean molar flux $\boldsymbol{N}_0$ of the solvent. In contrast, for the barycentric velocity $\boldsymbol{u}^{\mathrm{B}}$ as a reference frame, Equ. (2.28) – Equ. (2.30) read as

$$c_+ \nabla \hat{\mu}_+ = -K_{0+} \frac{\boldsymbol{N}_+^{\mathrm{B}}}{c_+} + K_{0+} \frac{\boldsymbol{N}_0^{\mathrm{B}}}{c_0} - K_{+-} \frac{\boldsymbol{i}}{F z_+ c_+}, \tag{2.31}$$

$$c_- \nabla \hat{\mu}_- = -K_{0-} \frac{\boldsymbol{N}_-^{\mathrm{B}}}{c_-} + K_{0-} \frac{\boldsymbol{N}_0^{\mathrm{B}}}{c_0} + K_{+-} \frac{\boldsymbol{i}}{F z_+ c_+}, \tag{2.32}$$

$$c_0 \nabla \hat{\mu}_0 = +K_{0+} \frac{\boldsymbol{N}_+^{\mathrm{B}}}{c_+} - K_{0+} \frac{\boldsymbol{N}_0^{\mathrm{B}}}{c_0} + K_{0-} \frac{\boldsymbol{N}_-^{\mathrm{B}}}{c_-} - K_{0-} \frac{\boldsymbol{N}_0^{\mathrm{B}}}{c_0}. \tag{2.33}$$

The summation of Equ. (2.28) – (2.30) and Equ. (2.31) – (2.33) fulfill the Gibbs-Duhem relation derived from Equ. (A.6) naturally

$$c_+ \nabla \hat{\mu}_+ + c_- \nabla \hat{\mu}_- + c_0 \nabla \hat{\mu}_0 = 0, \tag{2.34}$$

if the temperature T and the pressure p are constant within the electrolyte solution. The assumption of a constant pressure is only valid for an electrolyte solution which is at rest $\boldsymbol{u}_0 = \boldsymbol{u}^B = 0$ since pressure gradients are directly connected to the existence of a flow field as a result of the Navier-Stokes equations.

Connection between current density and electrochemical potentials Based on the definitions of the current density in Equ. (2.13) and the molar flux densities in Equ. (2.28) and (2.29), a relation between the current density and the electrochemical potentials $\hat{\mu}_+$ and $\hat{\mu}_-$ of the charged components is given as

$$\frac{1}{z_+^2 c_+^2 F^2} \left(1 + \frac{K_{+-}}{K_{0+}} + \frac{K_{+-}}{K_{0-}} \right) F \, \boldsymbol{i} = - \left(\frac{1}{K_{0+}} \frac{\nabla \hat{\mu}_+}{z_+} + \frac{1}{K_{0-}} \frac{\nabla \hat{\mu}_-}{z_-} \right). \tag{2.35}$$

The velocity reference frame is not relevant for the current flow since it is only influenced by the movement of the positive ionic species relative to the negative ionic species as shown in Equ. (2.27). This is in line with the fact that the flux contributions of the solvent in Equ. (2.31) and (2.32) cancel out if these equations are used instead of Equ. (2.28) and (2.29).

Equation (2.35) can be further reformulated to

$$\begin{aligned}&\frac{1}{z_+^2 c_+^2 F^2}\left(\frac{K_{0+}K_{0-}+K_{+-}(K_{0+}+K_{0-})}{K_{0+}+K_{0-}}\right) F\,\boldsymbol{i}\\ &=-\left(\frac{K_{0-}}{K_{0+}+K_{0-}}\frac{\nabla\hat{\mu}_+}{z_+}+\frac{K_{0+}}{K_{0+}+K_{0-}}\frac{\nabla\hat{\mu}_-}{z_-}\right),\end{aligned} \tag{2.36}$$

giving the current density of a binary electrolyte solution as a function of the electrochemical potentials:

$$\frac{F}{\kappa}\,\boldsymbol{i}=-\left(t_+\frac{\nabla\hat{\mu}_+}{z_+}+t_-\frac{\nabla\hat{\mu}_-}{z_-}\right). \tag{2.37}$$

Here, κ denotes the conductivity of the electrolyte solution while t_+ and t_- are the transference numbers of the positive and negative ionic species, respectively. A comparison of Equ. (2.36) and Equ. (2.37) gives

$$\frac{1}{\kappa}=\frac{1}{z_+^2 c_+^2 F^2}\left(\frac{K_{0+}K_{0-}+K_{+-}(K_{0+}+K_{0-})}{K_{0+}+K_{0-}}\right) \tag{2.38}$$

and

$$t_+=\frac{K_{0-}}{K_{0+}+K_{0-}}, \tag{2.39}$$

$$t_-=\frac{K_{0+}}{K_{0+}+K_{0-}}. \tag{2.40}$$

The transference numbers of the positive and negative ionic species are related by

$$t_++t_-=1. \tag{2.41}$$

Molar flux and current density based on the chemical potential of the salt For a binary electrolyte solution, it is convenient to replace the electrochemical potentials of the ionic species by the chemical potential of the salt as defined in Equ. (A.10). To do so, Equ. (2.37) has to be reformulated using Equ. (2.41),

$$\frac{1}{z_+}\nabla\hat{\mu}_+=-\frac{F}{\kappa}\boldsymbol{i}+\frac{t_-}{z_+}\left(\nabla\hat{\mu}_+-\frac{z_+}{z_-}\nabla\hat{\mu}_-\right).$$

Using the ENC given in Equ. (2.11) in the form $\frac{z_+}{z_-}=-\frac{\nu_-}{\nu_+}$ and the definition of the chemical potential $\mu_\pm$ of a salt given in Equ. (A.10), the electrochemical potential of the positive ionic species can be written as

$$\nabla\hat{\mu}_+=-\frac{z_+F}{\kappa}\boldsymbol{i}+\frac{t_-}{\nu_+}\nabla\mu_\pm. \tag{2.42}$$

Analogously, the electrochemical potential of the negative ionic species can be expressed as

$$\nabla\hat{\mu}_- = -\frac{z_- F}{\kappa}\boldsymbol{i} + \frac{t_+}{\nu_-}\nabla\mu_\pm. \tag{2.43}$$

These two relations can be used together with Equ. (2.28) and (2.29) to compute the molar flux density of the positive ionic species

$$\boldsymbol{N}_+ = -\frac{c_+^2}{\nu_+}\frac{1}{K_{0+}+K_{0-}}\nabla\mu_\pm + \frac{t_+}{z_+ F}\boldsymbol{i} \tag{2.44}$$

and the molar flux density for the negative ionic species

$$\boldsymbol{N}_- = -\frac{c_-^2}{\nu_-}\frac{1}{K_{0+}+K_{0-}}\nabla\mu_\pm + \frac{t_-}{z_- F}\boldsymbol{i}.$$

The conservation equation for the positive ionic species discussed in section 2.2 can finally be written as

$$\frac{\partial c_+}{\partial t} + \nabla\cdot\left(c_+\boldsymbol{u}_0 - \frac{c_+^2}{\nu_+}\frac{1}{K_{0+}+K_{0-}}\nabla\mu_\pm + \frac{t_+}{z_+ F}\boldsymbol{i}\right) = r_+ \tag{2.45}$$

and the conservation equation for the negative ionic species as

$$\frac{\partial c_-}{\partial t} + \nabla\cdot\left(c_-\boldsymbol{u}_0 - \frac{c_-^2}{\nu_-}\frac{1}{K_{0+}+K_{0-}}\nabla\mu_\pm + \frac{t_-}{z_- F}\boldsymbol{i}\right) = r_-. \tag{2.46}$$

As a result of the ENC given in Equ. (2.11), it is sufficient for binary electrolyte solutions to solve only for a single ionic component. The corresponding concentration of the second ionic component is automatically determined by the ENC. In literature (see, e.g., Landstorfer and Jacob [98]) this approach is called a strong enforcement of the ENC. Similar conservation equations could be derived for the barycentric velocity as a reference. However, in this case, an additional condition for the determination of the molar fluxes density $\boldsymbol{N}_0$ is necessary.

Convective effects in battery applications In an electrolyte solution, a velocity field can be introduced essentially by three different mechanisms, namely by forced convection, natural convection and volume effects. First, forced convection can be excluded for most battery applications since a battery is a closed system. Second, natural convection does not play a major role for electrolyte solutions filling a porous medium as it is indicated by experimental results presented in section 8.5.1. The small distance between the electrodes and the porous medium minimize the development of a velocity field as a result of density gradients within the electrolyte solution. For applications without a porous medium and larger distance between the two electrodes, a velocity field as result of buoyancy effects has to be included as an potential transport mechanism. In this case, the transport equations given in Equ. (2.45) and (2.46) are limited in their applications since the non-uniform pressure field violate the Gibbs-Duhem equation (2.34). Under such circumstances, the more general version of the Gibbs-Duhem equation (A.3) has to be considered for the derivation of the transport equations. The pressure field within the electrolyte solution can

be determined, e.g., by solving the Navier-Stokes equations utilizing the barycentric velocity $\boldsymbol{u}^{\mathrm{B}}$ as reference velocity.

Third, a velocity field within the electrolyte solution can also develop as a result of volumetric effects. Concentration variations of the positive and negative ionic species can lead to an significant driving force for solvent diffusion to keep the local volume of electrolyte solution constant. In a three-dimensional structure, this results in a complex transport of solvent and charged components potentially inducing pressure and flow fields. Such conditions require a coupled approach combining the ion-transport equations with the Navier-Stokes equation and an additional closing condition as emphasized, e.g., by Liu and Monroe [100]. In contrast, the volume conservation as applied, e.g., in Nyman et al. [115] or a kinematic condition as used in Liu and Monroe [100] is sufficient as an additional closing condition for one-dimensional models. In this context, different definitions for transference number are possible. The transference number t_+ used in this contribution is defined with respect to the solvent velocity. Other definitions for the transference number with respect to, e.g., the barycentric velocity or the laboratory are presented, e.g., in Nyman et al. [115] or Newman and Thomas-Alyea [109].

In the following, only the mass balance of the positive and the negative ionic species are considered for modeling the ion-transport in concentrated binary electrolyte solution. Volumetric effects are neglected assuming $\boldsymbol{u}_0 = 0$ since a consistent modeling of solvent effects in three-dimensional domains is too elaborate within the Stefan-Maxwell approach. In addition, the available models describing the volumetric effect are still discussed controversially in scientific community. In battery applications, this approach is commonly used in literature, not only in older publications but also in recent models as introduced, e.g., by Ferguson and Bazant [61] or Latz and Zausch [99]. As a result of this assumption, it is not necessary to distinguish between different transference number definitions.

Transport parameters In the literature, transport parameters are usually not given as a function of the friction coefficients K_{kl} but as a function of the intermolecular diffusion coefficients $\mathcal{D}_{kl}$. Based on Equ. (2.17), the conductivity and transference numbers defined in Equ. (2.38) – Equ. (2.40) can equivalently be written as

$$\frac{1}{\kappa} = -\frac{1}{z_+ z_- c_{\mathrm{T}}} \frac{RT}{F^2} \left(\frac{c_0 t_-}{c_+ \mathcal{D}_{0-}} + \frac{1}{\mathcal{D}_{+-}} \right), \tag{2.47}$$

$$t_+ = \frac{z_+ \mathcal{D}_{0+}}{z_+ \mathcal{D}_{0+} - z_- \mathcal{D}_{0-}} \qquad \text{and} \qquad t_- = \frac{-z_- \mathcal{D}_{0-}}{z_+ \mathcal{D}_{0+} - z_- \mathcal{D}_{0-}}. \tag{2.48}$$

The molecular diffusion coefficient $\mathcal{D}$ for a binary electrolyte solution is defined as

$$\mathcal{D} = \frac{(z_+ - z_-)\mathcal{D}_{0+}\mathcal{D}_{0-}}{z_+ \mathcal{D}_{0+} - z_- \mathcal{D}_{0-}}, \tag{2.49}$$

which is related to the frictional coefficients K_{0+} and K_{0-} by the relation

$$\frac{c_+^2}{\nu_+} \frac{1}{K_{0+} + K_{0-}} = \frac{1}{RT} \frac{c_{\mathrm{T}}}{c_+ c_0} \frac{\nu_+}{\nu} \mathcal{D}. \tag{2.50}$$

As a result, ion-transport in a binary electrolyte solution can be described by three independent transport parameters, namely the conductivity, the transference number of one ionic species and the molecular diffusion coefficient. Additional parameters are the solvent concentration c_0 and the total concentration c_T defined in Equ. (2.18).

2.4.2 Electrical state of the electrolyte solution

So far, equations for the molar flux densities $\boldsymbol{N}_+$ and $\boldsymbol{N}_-$ have been derived based on the chemical potential $\mu_\pm$ of the salt and the current density $\boldsymbol{i}$. Additionally, it has been shown in section A that the chemical potential $\mu_\pm$ of the salt can be correlated to the concentration c and, hence, does not depend on the electrical state of the electrolyte solution at all. However, the current density $\boldsymbol{i}$ is not only influenced by the chemical potential of the salt but also by the electrochemical potentials $\hat{\mu}_+$ and $\hat{\mu}_-$ and, therefore, by the electrical state of the electrolyte solution, as it can be seen in Equ. (A.9), Equ. (2.42) and Equ. (2.43). Therefore, it is necessary to introduce an additional variable describing the electrical state of the electrolyte solution including a reference value since Equ. (2.42) and Equ. (2.43) contain only the gradients of the electrochemical potentials $\hat{\mu}_+$ and $\hat{\mu}_-$ making the absolute level of the electrical state mathematically arbitrary. This is also clear from an experimental point of view. The electrostatic potential of an electrode can only be measured with respect to a second electrode such as a counter electrode or a reference electrode. The same holds true for the electrostatic potential at an arbitrary point $\boldsymbol{x}$ within the electrolyte solution.

a) Electrochemical potential The first option to describe the electrical state of an electrolyte solution is the electrochemical potential of an arbitrarily picked ionic species. Here, the electrochemical potential $\hat{\mu}_+$ of the positive ionic species is chosen which gives according to Equ. (2.42)

$$\boldsymbol{i} = -\frac{\kappa}{z_+ F}\nabla\hat{\mu}_+ + \frac{\kappa}{z_+ F}\,\frac{t_-}{\nu_+}\nabla\mu_\pm.$$

In this equation, the chemical potential $\mu_\pm$ of the salt is given by Equ. (A.14) with the equivalent concentration c as introduced in Equ. (A.11). Additionally, it is common in the literature to replace the transference number of the negative ionic species by the transference number of the positive ionic species by means of Equ. (2.41). Thus, the current density can also be expressed as

$$\boldsymbol{i} = -\frac{\kappa}{z_+ F}\nabla\hat{\mu}_+ + \frac{\nu}{z_+\nu_+}\,\frac{RT}{F}\,\kappa\left(1 + \frac{\partial \ln f_\pm}{\partial \ln c}\right)(1 - t_+)\,\nabla \ln c, \tag{2.51}$$

which depends only on the equivalent concentration c, the electrochemical potential $\hat{\mu}_+$ and various transport parameters. It is important to emphasize that the definition of the electrochemical potential $\hat{\mu}_+$ is not just a different form of the electrostatic potential Φ but also includes the concentration of the positive ionic species as can be seen in Equ. (A.9) and Equ. (A.12).

As reference state, the electrochemical potential $\hat{\mu}_+^{\mathrm{R}}$ is defined with respect to a lithium reference electrode:

$$\hat{\mu}_+^{\mathrm{R}} \equiv \hat{\mu}_+ - \mu_{\mathrm{Li}}. \tag{2.52}$$

As result of this definition, the chemical potential $\hat{\mu}_+$ in Equ. (2.51) can be replaced by the chemical potential $\hat{\mu}_+^{\mathrm{R}}$ defined with respect to reference electrode since $\nabla\hat{\mu}_+^{\mathrm{R}} = \nabla\hat{\mu}_+$. The same concept is used, e.g, by Latz and Zausch [99].

b) Electrostatic potential with respect to a reference electrode The most widely used concept for describing the electrical state of the electrolyte solution is the introduction of suitable reference electrodes to define the electrostatic potential Φ. For battery applications, the electrical state of the electrolyte solution is usually define with respect to a lithium reference electrode since the most common salts are based on lithium. This concept is experimentally inspired since the electrostatic potential is often measured with respect to a lithium reference electrode. For binary electrolyte solutions consisting of a single anion and cation, the general form of an electrochemical reaction given in Equ. (2.3) can be simplified to

$$s_+\mathrm{A}_+^{z_+} + s_-\mathrm{A}_-^{z_-} + s_0\mathrm{A}_0 + s_{\mathrm{so}}\mathrm{A}_{\mathrm{so}} \rightleftarrows ne^-, \tag{2.53}$$

where M_0 and M_{S} denote chemical symbol of the solvent and the material of the reference electrode, respectively. Both substances may take part in the surface reaction on the reference electrode. As stated in Hamann and Vielstich [78, 4.1.2], the current flow through the reference electrode has to be negligibly small. This means that the electrochemical reaction can be considered to be in equilibrium resulting in $\Delta_{\mathrm{R}}G = 0$ as explained in section A.6. According to Equ. (A.16) and with

$$\hat{\mu}_{\mathrm{e}^-} = z_{\mathrm{e}^-}F\Phi, \tag{2.54}$$

as given in Newman and Thomas-Alyea [109, chap. 8.1], Equ. (2.53) can be written as

$$(s_+\nabla\hat{\mu}_+ + s_-\nabla\hat{\mu}_-) + s_0\nabla\hat{\mu}_0 = -nF\nabla\Phi^{\mathrm{R}}, \tag{2.55}$$

where the absolute values of the electrochemical potential are already expressed by their gradients. Since the electrochemical potential of the reference electrode is a constant, its gradient vanishes and does not appear in Equ. (2.55). The term $(s_+\nabla\hat{\mu}_+ + s_-\nabla\hat{\mu}_-)$ is reformulated by adding and subtracting $\frac{n}{z_-}\nabla\hat{\mu}_-$ leading to

$$\begin{aligned} s_+\nabla\hat{\mu}_+ + s_-\nabla\hat{\mu}_- &= \frac{s_+}{\nu_+}\left(\nu_+\nabla\hat{\mu}_+ + \nu_-\nabla\hat{\mu}_-\right) - \frac{n}{z_-}\nabla\hat{\mu}_- \\ &= \frac{s_+}{\nu_+}\nabla\mu_\pm - \frac{n}{z_-}\nabla\hat{\mu}_-, \end{aligned} \tag{2.56}$$

where the electroneutrality condition $s_+z_+ + s_-z_- = -n$ for the surface reaction is used.

In the absence of pressure and temperature gradients, the Gibbs-Duhem equation (2.34) gives

$$\nabla\hat{\mu}_0 = -\frac{c}{c_0}\nabla\mu_{\pm}. \tag{2.57}$$

Inserting Equ. (2.57) and Equ. (2.56) into Equ. (2.55) results in

$$-F\nabla\Phi^{\mathrm{R}} = \left(\frac{s_+}{\nu_+ n} - \frac{s_0 c}{c_0 n}\right)\nabla\mu_{\pm} - \frac{1}{z_-}\nabla\hat{\mu}_-. \tag{2.58}$$

Equ. (2.58) relates the electrostatic potential Φ^{R} of reference electrode to the the electrochemical potentials $\mu_{\pm}$ and $\hat{\mu}_-$ of the salt and of the negative ionic species dissolved in the electrolyte solution, respectively. Replacing the electrochemical potential of the negative ionic species according to Equ. (2.43), the well-known equation for the electric potential Φ^{R} (see, e.g., Newman and Thomas-Alyea [109, chapter 12.4]) is established:

$$\boldsymbol{i} = -\kappa\nabla\Phi^{\mathrm{R}} - \frac{1}{F}\,\kappa\,\frac{1}{\nu_+ z_+}\left(\frac{z_+ s_+}{n} + t_+ - \frac{c}{c_0}\,\frac{s_0\nu_+ z_+}{n}\right)\nabla\mu_{\pm}.$$

The gradient $\nabla\mu_{\pm}$ of the chemical potential $\mu_{\pm}$ can be replaced according to Equ. (A.14) leading to

$$\boldsymbol{i} = -\kappa\nabla\Phi^{\mathrm{R}} + \frac{RT}{F}\,\kappa\,\frac{\nu}{\nu_+ z_+}\left(1 + \frac{\partial\ln f_{\pm}}{\partial\ln c}\right)\left(-\frac{z_+ s_+}{n} - t_+ + \frac{c}{c_0}\,\frac{s_0\nu_+ z_+}{n}\right)\nabla\ln c.$$

This equation is valid for an arbitrary reference electrode. In battery science, the most common reference electrode is the lithium reference electrode with the formal surface reaction $\mathrm{Li} \rightleftarrows \mathrm{Li}^+ + e^-$. In this case, Equ. (2.55) simplifies to

$$-1\,\nabla\hat{\mu}_+ + 0\,\nabla\hat{\mu}_- + 0\,\nabla\hat{\mu}_0 = -z_+ F\,\nabla\Phi^{\mathrm{R}}, \tag{2.59}$$

where $s_+ = -1$, $s_- = 0$, $s_0 = 0$ and $-n = s_+ z_+ + s_- z_-$. Hence, the equation for the electric potential with respect to a lithium reference electrode reads as

$$\boldsymbol{i} = -\kappa\nabla\Phi^{\mathrm{R}} + \frac{\nu}{z_+\nu_+}\,\frac{RT}{F}\,\kappa\left(1 + \frac{\partial\ln f_{\pm}}{\partial\ln c}\right)(1 - t_+)\,\nabla\ln c. \tag{2.60}$$

For a lithium reference electrode, Equ. (2.58) can also be motivated physically by an equivalent formulation for the lithium surface reaction:

$$\mathrm{Li} + \mathrm{M}^- \rightleftarrows \mathrm{LiM} + e^-.$$

Here, the lithium surface reaction $\mathrm{Li} \rightleftarrows \mathrm{Li}^+ + e^-$ is extended by the negative ionic species M^- dissolved in the electrolyte solution where the negative and positive ionic species are considered as a neutral ion pair as discussed in section A.5. As a result, the surface reaction in terms of the gradient can also be characterized by

$$-F\nabla\Phi^{\mathrm{R}} = -\nabla\mu_{\pm} + \nabla\hat{\mu}_-,$$

which corresponds to Equ. (2.58).

For a lithium reference electrode, it is also possible to relate Equ. (2.51) to Equ. (2.60) if the lithium surface reaction given in Equ. (2.59) is used to replace the electrochemical potential $\hat{\mu}_+$ by the electrostatic potential $z_+F\Phi^{\mathrm{R}}$ of the reference electrode as indicated, e.g. in Nyman et al. [115]:

$$\hat{\mu}_+ \equiv F\Phi^{\mathrm{R}}.$$

This means that the formulation with respect to electrochemical potential of an arbitrary ionic specis is equivalent to the formulation using the electrostatic potential if both are defined with respect to the same reference electrode.

c) Electrostatic potential with respect to a reference species According to Newman and Thomas-Alyea [109], the reference potential can also be defined with respect to a reference species n

$$\hat{\mu}_n = RT \ln c_n + z_n F \Phi^n$$

which gives for the electrochemical potential of any other species

$$\hat{\mu}_k = RT \ln c_k + z_k F \Phi^n + RT \left(\ln f_k - \frac{z_k}{z_n} \ln f_n \right) + RT \left(\ln a_k - \frac{z_k}{z_n} \ln a_n \right). \tag{2.61}$$

Here, Φ^n denotes the electrostatic potential with respect to the reference species n. The proportionality constants a_k and a_n result from the definition for the chemical potential given in Equ. (A.12). Both definitions can be motivated by the internal energy given in Equ. (A.8):

$$\begin{aligned}
\mathrm{d}\, u =& T\, \mathrm{d}\, s + \sum_{k=1}^{n} \Big[\left(\mu_k + z_k F \Phi^n \right) \mathrm{d}\, c_k \Big] \\
=& T\, \mathrm{d}\, s + \sum_{k=1}^{n-1} \Big[\left(RT \ln c_k + z_k F \Phi^n + RT \ln f_k + RT \ln a_k \right) \mathrm{d}\, c_k \Big] \\
& + \left(RT \ln c_n + z_n F \Phi^n \right) \mathrm{d}\, c_n + \left(RT \ln f_n + RT \ln a_n \right) \underbrace{\sum_{k=1}^{n-1} \left(-\frac{z_k}{z_n} \mathrm{d}\, c_k \right)}_{\mathrm{d}\, c_n} \\
=& \sum_{k=1}^{n-1} \left[\left(RT \ln c_k + z_k F \Phi^n + RT \left(\ln f_k - \frac{z_k}{z_n} \ln f_n \right) + RT \left(\ln a_k - \frac{z_k}{z_n} \ln a_n \right) \right) \mathrm{d} c_k \right] \\
& + \left(RT \ln c_n + z_n F \Phi^n \right) \mathrm{d}\, c_n + T\, \mathrm{d}\, s \\
=& T\, \mathrm{d}\, s + \sum_{k=1}^{n-1} \hat{\mu}_k \, \mathrm{d}\, c_k + \hat{\mu}_n \, \mathrm{d}\, c_n.
\end{aligned}$$

In the absence of temperature and pressure gradients, the gradient of Equ. (2.61) reduces to

$$\nabla\hat{\mu}_k = RT\nabla \ln c_k + z_k F\nabla\Phi^n + RT\left(\nabla \ln f_k - \frac{z_k}{z_n}\nabla \ln f_n\right). \tag{2.62}$$

The gradients of the proportionality constants a_k and a_n are zero since these depend only on the pressure and the temperature. If the negative ionic species is used as reference ($n = \ominus$), Equ. (2.62) can be inserted in Equ. (2.37) describing the current density as a function of the electrochemical potentials, resulting in

$$\boldsymbol{i} = -\kappa\nabla\Phi^{\ominus} + \frac{\nu}{\nu_+ z_+}\,\frac{RT}{F}\kappa\left[\left(\frac{\nu_-}{\nu} - t_+\right)\nabla \ln c - t_+\nabla \ln f_\pm\right] \tag{2.63}$$

In this definition, the potential $\Phi^{\ominus}$ is defined with respect to the reference species, and thus, does not involve any influence of electrodes.

2.4.3 Cell potential

As shown in the previous section, the used reference state directly influences the structure of the current equation as derived for Equ. (2.51), Equ. (2.60) and Equ. (2.63). It was also demonstrated that the formulation using the electrochemical potential of an ionic species given in Equ. (2.51) and the formulation using the electrostatic potential given in Equ. (2.60) are equivalent if both are defined with respect to the same reference electrode. This has to be also demonstrated for the remaining formulation given in Equ. (2.63) since the final cell potential has to be the same for all formulations. The cell potential must not depend on the choice of the reference potential. In this section, the connection between the equations for the current density and the cell potential is shown and it is demonstrated that all definitions are equivalent.

Definition of cell potential The simplest cell is used for the demonstration that the cell potential is independent of the choice of the reference potential. The same concept can also be applied to more complex cell configuration. As shown schematically in Fig. 2.1, the cell consists of two copper deflectors α and α', two lithium electrodes β and β' separated by an $LiClO_4$ electrolyte solution γ. The transition region describes an electrolyte solution with a variable salt concentration. According to Newman and Thomas-Alyea [109, chap. 2.4],

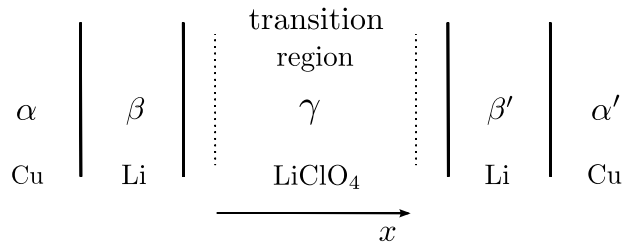

Figure 2.1: Basic cell setup consisting of two copper deflectors α and α', two lithium electrodes β and β' separated by an electrolyte solution γ.

the cell potential U can be expressed as

$$FU = z_{e^-} F(\Phi_{\mathrm{so}}\big|_{\alpha} - \Phi_{\mathrm{so}}\big|_{\alpha'}) = \hat{\mu}_{e^-}\big|_{\alpha} - \hat{\mu}_{e^-}\big|_{\alpha'}.$$

Here, the cell potential U is the difference between the electrochemical potentials of the electrons in phases α and α' which is also related to the difference in the electrostatic potentials Φ_{so}. Assuming thermodynamic equilibrium between adjacent phases, the cell potential can also be expressed as the difference between the electrochemical potentials of the electrons in the lithium phases β and β':

$$FU = \hat{\mu}_{e^-}\big|_{\beta} - \hat{\mu}_{e^-}\big|_{\beta'}. \tag{2.64}$$

As a result of the electrochemical reactions at the electrode surface, the electrochemical potential of the electrons is related to the electrochemical potentials of the products and educts of the reactions. As shown in section section A.6, the lithium reaction $\mathrm{Li} \rightleftarrows \mathrm{Li}^+ + e^-$ can be characterized in terms of electrochemical potentials according to

$$\hat{\mu}_{\mathrm{Li}}\big|_{\beta} = \hat{\mu}_{+}\big|_{\beta|\gamma} + \hat{\mu}_{e^-}\big|_{\beta}, \qquad \text{and} \qquad \hat{\mu}_{\mathrm{Li}}\big|_{\beta'} = \hat{\mu}_{+}\big|_{\beta'|\gamma} + \hat{\mu}_{e^-}\big|_{\beta'}.$$

Here, the reaction Gibbs energy $\Delta_{\mathrm{R}}G$ is zero which corresponds to an equilibrium between the adjacent phases. Thus, the cell potential between the two lithium electrodes can be written as

$$FU = \hat{\mu}_{\mathrm{Li}}\big|_{\beta} - \hat{\mu}_{+}\big|_{\beta|\gamma} - \left(\hat{\mu}_{\mathrm{Li}}\big|_{\beta'} - \hat{\mu}_{+}\big|_{\gamma|\beta'}\right).$$

Since the phases β and β' are identical, the electrochemical potentials of lithium cancel out. Additionally, the current flow across the electrode is zero as a result of the assumed equilibrium state between the phases. In this case, the cell potential is given by

$$FU = \hat{\mu}_{+}\big|_{\gamma|\beta'} - \hat{\mu}_{+}\big|_{\beta|\gamma}. \tag{2.65}$$

Thus, the cell potential U is proportional to the difference between the electrochemical potentials of the lithium ions in the vicinity of the electrodes.

Now, the cell potentials associated with the three different reference potentials are compared for a lithium cell consisting of two lithium electrodes and an electrolyte solution. The system is modeled by a one-dimensional approximation to allow for analytical integration along a one-dimensional path. Although there is no current flow across the considered electrodes, the current density $\boldsymbol{i}$ in Equ. (2.51), Equ. (2.60) and Equ. (2.63) is not dropped at this point since there could be current flow due to the presence of additional electrodes.

a) Electrochemical potential At this point, it becomes clear why the electrochemical potential $\hat{\mu}_+$ is the most natural choice to define the electrical state of the electrolyte solution. The right hand side of Equ. (2.65) is directly given by Equ. (2.51) if $\hat{\mu}_+$ is isolated and integrated along a

one-dimensional path as shown in Fig. 2.1:

$$U = -\int_{\beta|\gamma}^{\gamma|\beta'} \frac{1}{\kappa}\boldsymbol{i}\,\mathrm{d}\,x + \frac{RT}{F}\frac{1}{\nu_+}\left[\nu \ln \frac{c\big|_{\gamma|\beta'}}{c\big|_{\beta|\gamma}} - \nu\int_{\beta|\gamma}^{\gamma|\beta'} t_+\,\mathrm{d}\ln c \right. \\ \left. +\nu \ln \frac{f_\pm\big|_{\gamma|\beta'}}{f_\pm\big|_{\beta|\gamma}} - \nu\int_{\beta|\gamma}^{\gamma|\beta'} t_+\,\mathrm{d}\ln f_\pm\right]. \tag{2.66}$$

b) Electrostatic potential with respect to a reference electrode According to Equ. (2.64) and Equ. (2.54), the cell potential U between two lithium electrodes can be written as

$$U = \Phi^{\mathrm{R}}\big|_{\gamma|\beta'} - \Phi^{\mathrm{R}}\big|_{\beta|\gamma}.$$

which is the equivalent to Equ. (2.64) assuming equilibrium between the different phases. The steps leading from Equ. (2.64) to Equ. (2.65) are already included in the definition of electrostatic potential Φ^{R}. Isolation of the electrostatic potential Φ^{R} in Equ. (2.60) and the subsequent integration along a one-dimensional path gives the same result as in Equ. (2.66).

c) Electrostatic potential with respect to a reference species According to Equ. (2.61) and Equ. (A.13), the electrochemical potential $\hat{\mu}_{\mathrm{Li}^+}$ of the lithium ions can be written as

$$\hat{\mu}_+ = RT\ln c_+ + z_+F\Phi^{\ominus} + RT\frac{\nu}{\nu_+}\ln f_\pm + RT\frac{1}{\nu_+}\ln \underbrace{\left(a_+^{\nu_+}a_-^{\nu_-}\right)}_{a_\pm}.$$

Inserting this relation into Equ. (2.65) gives

$$FU = z_+F\left(\Phi^{\ominus}\big|_{\gamma|\beta'} - \Phi^{\ominus}\big|_{\beta|\gamma}\right) + RT\left[\ln\frac{c\big|_{\gamma|\beta'}}{c\big|_{\beta|\gamma}} + \frac{\nu}{\nu_+}\ln\frac{f_\pm\big|_{\gamma|\beta'}}{f_\pm\big|_{\beta|\gamma}} + \frac{1}{\nu_+}\ln\frac{a_\pm\big|_{\gamma|\beta'}}{a_\pm\big|_{\beta|\gamma}}\right], \tag{2.67}$$

whereas the last term is equal to zero for constant temperature and pressure fields. The potential difference $\Phi^{\ominus}\big|_{\gamma|\beta'} - \Phi^{\ominus}\big|_{\beta|\gamma}$ is given by the integrated form of Equ. (2.63):

$$\Phi^{\ominus}\big|_{\gamma|\beta'} - \Phi^{\ominus}\big|_{\beta|\gamma} = -\int_{\beta|\gamma}^{\gamma|\beta'} \frac{1}{\kappa}\boldsymbol{i}\,\mathrm{d}\,x + \frac{RT}{F}\frac{1}{\nu_+z_+}\left[\nu_- \ln\frac{c\big|_{\gamma|\beta'}}{c\big|_{\beta|\gamma}} - \int_{\beta|\gamma}^{\gamma|\beta'} \nu t_+\,\mathrm{d}\ln c \right. \\ \left. -\int_{\beta|\gamma}^{\gamma|\beta'} \nu t_+\,\mathrm{d}\ln f_\pm\right]. \tag{2.68}$$

Combining Equ. (2.67) and Equ. (2.68) with $z_+ = 1$ gives the same cell potential as before:

$$U = -\int_{\beta|\gamma}^{\gamma|\beta'} \frac{1}{\kappa}\boldsymbol{i}\,\mathrm{d}\,x + \frac{RT}{F}\frac{1}{\nu_+}\left[\nu \ln \frac{c\big|_{\gamma|\beta'}}{c\big|_{\beta|\gamma}} - \nu\int_{\beta|\gamma}^{\gamma|\beta'} t_+\,\mathrm{d}\ln c + \nu \ln \frac{f_\pm\big|_{\gamma|\beta'}}{f_\pm\big|_{\beta|\gamma}} - \nu\int_{\beta|\gamma}^{\gamma|\beta'} t_+\,\mathrm{d}\ln f_\pm\right] \tag{2.69}$$

Compared to the previous definitions, the electrostatic potential $\Phi^{\ominus}$ with respect to the negative ionic species includes only the potential drop in the electrolyte solution due to current flow and variations in the concentration. The potential drop at the electrodes the so-called Nernst potential is not considered in this definition and has to be added separately.

2.4.4 Final system of ion-transport equations

Mass conservation for the positive ionic species given in Equ. (2.45) can be reformulated to

$$\frac{\partial c_+}{\partial t} + \nabla\cdot\left[-\frac{c_+^2}{\nu_+}\frac{1}{RT}\frac{c_\mathrm{T}}{c_+\,c_0}\frac{\nu_+}{\nu}\mathcal{D}\nabla\mu_\pm + \frac{t_+}{z_+F}\boldsymbol{i}\right] = r_+, \tag{2.70}$$

where the definition of the molar flux density given in Equ. (2.44) and the definition of the molecular diffusion coefficient $\mathcal{D}$ given in Equ. (2.50) are used. Mass conservation for the negative ionic species can be expressed accordingly. In Equ. (2.70), the diffusive molar flux density depends on the chemical potential $\mu_\pm$ of the salt. Inserting the gradient of the chemical potential $\mu_\pm$ of the salt

$$\nabla\mu_\pm = \nu RT\left(1 + \frac{\partial \ln f_\pm}{\partial \ln c}\right)\frac{1}{c_+}\nabla c_+$$

given in Equ. (A.14) into Equ. (2.70) yields

$$\frac{\partial c_+}{\partial t} + \nabla\cdot(-D_\pm\,\nabla c_+) + \nabla\cdot\left(\frac{t_+}{z_+F}\boldsymbol{i}\right) = r_+,$$

where the binary diffusion coefficient $D_\pm$ is defined as

$$D_\pm \equiv \frac{c_\mathrm{T}}{c_0}\,\mathcal{D}\left(1 + \frac{\partial \ln f_\pm}{\partial \ln c}\right)$$

with the ThermoDynamic Factor (TDF)

$$\left(1 + \frac{\partial \ln f_\pm}{\partial \ln c}\right) = \mathcal{X}. \tag{2.71}$$

This definition is equivalent to the definition used in Newman and Thomas-Alyea [109, chap. 12.2]:

$$D_{\pm} = \frac{c_{\mathrm{T}}}{c_0}\,\mathcal{D}\left(1 + \frac{\mathrm{d}\ln\gamma_{\pm}}{\mathrm{d}\ln m}\right)\left(1 - \frac{\mathrm{d}\ln c_0}{\mathrm{d}\ln c}\right),$$

where $\gamma_{\pm}$ denotes the mean molal activity coefficient and m the molality. This equation can be derived from Equ. (2.70) with

$$\nabla\mu_{\pm} = RT\nu\nabla\ln m\gamma_{\pm}$$

and

$$m = \frac{c}{c_0 M_0}.$$

In many textbooks, the concentration of the positive ionic species is replaced by the equivalent concentration $c = \frac{c_+}{\nu_+} = \frac{c_-}{\nu_-}$ giving the well-known ion-transport equation for concentrated binary electrolyte solutions:

$$\frac{\partial c}{\partial t} + \nabla\cdot\left(-D_{\pm}\,\nabla c\right) + \nabla\cdot\left(\frac{t_+}{\nu_+ z_+ F}\boldsymbol{i}\right) = \frac{r_+}{\nu_+}. \tag{2.72}$$

As explained in Chap. 2.4.2, all three equations for the current density $\boldsymbol{i}$ utilizing different definitions for the electrical state of the electrolyte solution are equivalent. In the following, the classical definition based on a lithium reference electrode is applied:

$$\boldsymbol{i} = -\kappa\nabla\Phi^{\mathrm{R}} + \frac{\nu}{z_+\nu_+}\,\frac{RT}{F}\,\kappa\left(1 + \frac{\partial\ln f_{\pm}}{\partial\ln c}\right)(1 - t_+)\,\nabla\ln c. \tag{2.73}$$

The system of equation is closed by the conservation of charge

$$\nabla\cdot\boldsymbol{i} = 0. \tag{2.74}$$

2.5 Nernst-Planck approach for dilute electrolyte solutions

The Nernst-Planck approximation is the classical approach to model ion-transport in dilute electrolyte solutions. Due to its wide-ranging dissemination, this model has already been discussed in many contributions. In Kontturi et al. [91, chap. 2.3], the ion-transport equations based on the Nernst-Planck approximation are derived from a non-linear thermodynamic framework, for instance. In Bauer [18], an overview of the entire system of ion-transport equations for dilute electrolyte solutions is given. In the following, a short review of the Nernst-Planck model is given and a comparison with the concentrated solution theory based on the Stefan-Maxwell equations is drawn.

In the Nernst-Planck approach, the molar flux density of component k is given as

$$\boldsymbol{N}_k = -D_k \nabla c_k - \frac{F}{RT} z_k D_k c_k \nabla \Phi^{\mathrm{NP}}, \tag{2.75}$$

consisting of a diffusion and a migration term. Here, D_k denotes the diffusion coefficient of component k and Φ^{NP} the electrostatic potential within the electrolyte solution. As in all previous approaches, convective transport has been neglected. The motivation for this approach is given in section 2.4.1. Hence, the mass conservation equation (2.7) can be written as follows for component $k \in [1, ..., m]$:

$$\frac{\partial c_k}{\partial t} + \nabla \cdot \left(-D_k \nabla c_k - \frac{F}{RT} D_k z_k c_k \nabla \Phi^{\mathrm{NP}}\right) = r_k. \tag{2.76}$$

The most prominent option for closing the system of equations is to apply the electroneutrality condition given in Equ. (2.11). Alternatively, the system can also be closed by enforcing the conservation of charge. A detailed discussion of the various options to close the system of equations is given in Bauer [18].

Alternative formulation of the Nernst-Planck approach The electrochemical system described by the Nernst-Planck approach can also be characterized by the conductivity κ of the electrolyte solution, the transference numbers t_k and the scalar multi-component diffusion coefficient $\mathbb{D}_{kl}$. The basic definition of the current density given in Equ. (2.13) can be reformulated using Equ. (2.75)

$$\boldsymbol{i} = -\underbrace{\sum_k^m \left(\frac{F^2}{RT} D_k z_k^2 c_k\right)}_{\kappa} \nabla \Phi^{\mathrm{NP}} - F \sum_k^m (z_k D_k \nabla c_k), \tag{2.77}$$

where the definition of the conductivity κ has already been applied. This equation can also be expressed using the transference numbers $t_k = \frac{\kappa_k}{\kappa}$

$$\boldsymbol{i} = -\kappa \nabla \Phi^{\mathrm{NP}} - \frac{RT}{F} \kappa \sum_k^m \frac{t_k}{z_k} \nabla \ln c_k. \tag{2.78}$$

The transference number t_k in this equation equals the ratio of the component-based conductivity κ_k to the overall conductivity κ of the electrolyte solution as indicated in Equ. (2.79).

In a next step, Equ. (2.77) can be used to eliminate the electrostatic potential Φ^{NP} in the mass conservation equation (2.76) giving the alternative formulation

$$\frac{\partial c_k}{\partial t} + \nabla \cdot \left[- D_k \nabla c_k - \frac{1}{z_k F} \underbrace{\frac{\frac{F^2}{RT} D_k z_k^2 c_k}{\kappa}}_{t_k = \kappa_k / \kappa} \left(-\boldsymbol{i} - F \sum_l^m (z_l D_l \nabla c_l) \right) \right] = r_k. \tag{2.79}$$

As a result, Equ. (2.79) can be formulated as

$$\frac{\partial c_k}{\partial t} + \nabla \cdot \left[-D_k \nabla c_k + \frac{t_k}{z_k} \left(\sum_{l \neq k}^{m} (z_l D_l \nabla c_l) + z_k D_k \nabla c_k \right) \right] + \nabla \cdot \frac{t_k \boldsymbol{i}}{z_k F} = r_k. \tag{2.80}$$

Using the ENC (2.11) to replace the second concentration c_k, the multi-component diffusion coefficient $\mathbb{D}_{kl}$ can be introduced to describe the diffusive transport in the component-based mass conservation:

$$\frac{\partial c_k}{\partial t} - \nabla \cdot \left[\sum_{l}^{m} \underbrace{\left(D_k \delta_{kl} + \frac{t_k}{z_k} (D_k - D_l) z_l \right)}_{\mathbb{D}_{kl}} \nabla c_i \right] + \nabla \cdot \frac{t_k \boldsymbol{i}}{z_k F} = r_k. \tag{2.81}$$

As before, the system of equations can be closed by either the electroneutrality condition (2.11) or condition Equ. (2.15) for conservation of charge.

So far, the ion-transport system has been described by m component-based mass conservation equations. Owing to electroneutrality, the ion-transport system can also be described by only $m - 1$ ion-transport equations since the concentration c_m can be expressed as a linear combination of the remaining $m - 1$ concentrations:

$$z_m c_m = - \sum_{k}^{m-1} z_k c_k.$$

By eliminating component m, Equ. (2.81) and Equ. (2.78) simplify to the Charge-conservation-Nernst-Planck (CNP) model which is derived in Bauer [18]. The CNP model has to be closed the conservation of charge given in Equ. (2.15). This approach is called a strong enforcement of the electroneutrality condition. In contrast, if m component-based mass conservation equations are closed by the electroneutrality condition, the electroneutrality condition is enforced weakly. An example for a weak enforcement of the electroneutrality condition is the Nernst-Planck approach presented in Bauer [18].

Binary electrolyte solution So far, the ion-transport model for dilute solutions has been derived for an arbitrary number of components. However, the system can also restricted to a binary electrolyte solution as it is done for the concentrated solution theory. For a binary electrolyte solution, the mass conservation equation for the positive ionic species given in Equ. (2.81) can be reformulated to

$$\frac{\partial c_+}{\partial t} - \nabla \cdot (\mathbb{D}_{\pm} \nabla c_+) + \nabla \cdot \frac{t_+ \boldsymbol{i}}{z_+ F} = r_+, \tag{2.82}$$

where $\mathbb{D}_{\pm}$ denotes the dilute binary diffusion coefficient resulting from the multi-component diffusion coefficient $\mathbb{D}_{kl}$. Additionally, Equ. (2.78) can be expressed as

$$\boldsymbol{i} = -\kappa \nabla \Phi^{\mathrm{NP}} - \frac{RT}{F} \kappa \left(\frac{t_+}{z_+} + \frac{t_-}{z_-} \right) \nabla \ln c_+. \tag{2.83}$$

For binary electrolyte solutions, the conductivity κ defined in Equ. (2.77) is given as

$$\kappa = \frac{F^2}{RT}(z_+ D_+ - z_- D_-) z_+ c_+,$$

the transference numbers t_+ and t_- defined in Equ. (2.79) as

$$t_+ = \frac{D_+ z_+^2 c_+}{(z_+ D_+ - z_- D_-) z_+ c_+} = \frac{z_+ D_+}{(z_+ D_+ - z_- D_-)},$$
$$t_- = \frac{D_- z_-^2 c_-}{(z_+ D_+ - z_- D_-) z_+ c_+} = \frac{-z_- D_-}{(z_+ D_+ - z_- D_-)},$$

and the dilute binary diffusion coefficient $\mathbb{D}_\pm$ defined in Equ. (2.81) as

$$\mathbb{D}_\pm = \frac{(z_+ - z_-) D_+ D_-}{(z_+ D_+ - z_- D_-)}.$$

These transport parameters exhibit a strong similarity with the transport parameters Equ. (2.47) – Equ. (2.50) used in the concentrated solution theory which is already indicated in Newman and Thomas-Alyea [109, chap. 12.5].

Comparison with concentrated solution theory derived from the Stefan-Maxwell approach Based on Equ. (2.82), Equ. (2.83) and Equ. (2.15), the final system of equations for a binary electrolyte solution can be written as

$$\begin{aligned} &\frac{\partial c}{\partial t} - \nabla \cdot (\mathbb{D}_\pm \nabla c) + \nabla \cdot \left(\frac{t_+ \boldsymbol{i}}{\nu_+ z_+ F} \right) = \frac{r_+}{\nu_+}, \\ &\boldsymbol{i} = -\kappa \nabla \Phi^{\mathrm{NP}} + \frac{\nu}{z_+ \nu_+} \frac{RT}{F} \kappa \left(\frac{\nu_-}{\nu} - t_+ \right) \nabla \ln c, \\ &\nabla \cdot \boldsymbol{i} = 0, \end{aligned} \tag{2.84}$$

where $c_+ = \nu_+ c$ is used to express the equations using the equivalent concentration c. These equations are equivalent to those in concentrated solution theory given in Equ. (2.72), Equ. (2.63) and Equ. (2.74) since $\ln f_\pm$ defined in Equ. (2.63) approaches zero and the ratio c_0/c_T unity for dilute solutions. Additionally, the definitions of the transport parameters based on the Nernst-Planck approach resemble the definitions of the transport parameters for concentrated electrolyte solutions given in Equ. (2.47) – Equ. (2.50) if the diffusion coefficients D_k of the ionic species are interpreted as the molecular diffusion coefficient $\mathcal{D}_k$. In Equ. (2.47) for the conductivity κ, the cross diffusion coefficient $\mathcal{D}_{+-}$ is negligibly small for dilute solutions, since it describes the friction between positive and negative ions. Finally, the electrostatic potential Φ^{NP} used in the Nernst-Planck approach is equivalent to the electrostatic potential $\Phi^{\ominus}$ defined with respect to negative ionic species. As for the electrostatic potential $\Phi^{\ominus}$, the Nernst potential describing the potential drop at the electrodes is not included in the formulation and has to be considered separately as it is done, e.g., in Bruce and Vincent [31].

2.6 Ion-transport based on non-equilibrium thermodynamics

An alternative model for ion-transport within electrolyte solutions has been proposed by Latz and Zausch [99]. In this contribution, the complete derivation is based on the general principles of non-equilibrium thermodynamics. Therefore, the proposed model is thermodynamically consistent which ensures, e.g., a strictly positive entropy production. Additionally, thermal effects can be incorporated consistently into the framework which is a significant advantage compared to the Stefan-Maxwell approach discussed in section 2.4. A similar approach is taken, e.g., by Kjelstrup and Bedeaux [90].

As in the Stefan-Maxwell approach, the binary electrolyte solution is considered electrically neutral. In addition, convective transport effects are assumed to be negligibly small. As a result of both, the concentration of the solvent can be eliminated as an independent variable utilizing the mass conservation:

$$M_0 \,\mathrm{d}\, c_0 + M_+ \,\mathrm{d}\, c_+ + M_- \,\mathrm{d}\, c_- = 0. \tag{2.85}$$

Here, M_0, M_+ and M_- denote the molar mass of the solvent, the positive and the negative ionic species.

A total energy density of a polarizable system in an external electromagnetic field can be described by the thermodynamic relation given in Henjes and Liu [80]

$$\mathrm{d}\, e = T \,\mathrm{d}\, s + \mu_+ \,\mathrm{d}\, c_+ + \mu_- \,\mathrm{d}\, c_- + \mu_0 \,\mathrm{d}\, c_0 + \boldsymbol{E} \cdot \,\mathrm{d}\, \boldsymbol{D} + \boldsymbol{H} \cdot \,\mathrm{d}\, \boldsymbol{B}. \tag{2.86}$$

Here, e denotes the total energy density, s the entropy density, $\boldsymbol{E} = -\nabla\Phi$ the electric field, $\boldsymbol{D}$ the electric displacement field, $\boldsymbol{H}$ the magnetic field and $\boldsymbol{B}$ the magnetic induction. Unlike in the Stefan-Maxwell approach, the chemical potential μ_k and the electrostatic potential Φ are independent in this formulation. Equ. (2.86) can reformulated to

$$\mathrm{d}\, e = T \,\mathrm{d}\, s + \mu_\mathrm{e} \,\mathrm{d}\, c_+ + \boldsymbol{E} \cdot \,\mathrm{d}\, \boldsymbol{D} + \boldsymbol{H} \cdot \,\mathrm{d}\, \boldsymbol{B},$$

with the chemical potential μ_el of the electrolyte solution

$$\begin{aligned} \mu_\mathrm{el} \,\mathrm{d}c_+ &\equiv \mu_+ \,\mathrm{d}c_+ + \mu_- \,\mathrm{d}c_- + \mu_0 \,\mathrm{d}c_0 \\ &= \left[\mu_+ + \frac{\nu_-}{\nu_+}\mu_- - \frac{\mu_0}{M_0}\left(M_+ + \frac{\nu_-}{\nu_+}M_-\right)\right] \mathrm{d}c_+ = \left[\frac{1}{\nu_+}\mu_\pm - \frac{\mu_0}{\nu_+}\frac{M_\pm}{M_0}\right] \mathrm{d}c_+, \end{aligned} \tag{2.87}$$

where $M_\pm = \nu_+ M_+ + \nu_- M_-$, Equ. (2.85), Equ. (2.11) and Equ. (2.21) are used. The advantage of this formulation is that the chemical potential of the solvent is incorporated naturally into the definition of the chemical potential μ_el of the electrolyte solution. At this point, it is assumed that solvent diffusion does not induce a velocity and pressure field within the electrolyte solution. In the original contribution, the chemical potential μ_el of the electrolyte solution is defined slightly different since an alternative definition of the equivalent concentration $c = c_+ = -\frac{\nu_- z_-}{\nu_+ z_+} c_-$ and the notational simplification $\nu_+ = \nu_- = 1$ are used. The chemical potential $\mu_\pm$ is based on the same definition as given in Equ. (A.10). The electric field $\boldsymbol{E}$, the electric displacement $\boldsymbol{D}$,

the magnetic field $\boldsymbol{H}$ and the magnetic induction $\boldsymbol{B}$ are related to the current density $\boldsymbol{i}$ via

$$\boldsymbol{E} \cdot \frac{\partial \boldsymbol{D}}{\partial t} + \boldsymbol{H} \cdot \frac{\partial \boldsymbol{B}}{\partial t} = -\nabla \cdot (\boldsymbol{E} \times \boldsymbol{H}) - \boldsymbol{i} \cdot \boldsymbol{E}.$$

This equation is derived from the Maxwell equations as explained, e.g., in Jackson [86, chap. 6.7]. Additionally, the conservation of mass (section 2.2), of charge (section 2.3) and of entropy

$$\frac{\partial s}{\partial t} = -\nabla \cdot \frac{\boldsymbol{q}}{T} + \frac{R}{T}$$

are used to formulate the equations for the molar flux density, heat density and current density. Here, R denotes the entropy production rate. A more detailed derivation is given in Latz and Zausch [99]. As a result, the ion-transport equation can be written as

$$\frac{\partial c}{\partial t} + \nabla \cdot (-D_{\text{el}} \nabla c) + \nabla \cdot \left(\frac{t_+}{\nu_+ z_+ F} \boldsymbol{i} \right) = 0, \tag{2.88}$$

where the additional stoichometry coefficient ν_+ in the third term results from the alternative definition of the equivalent concentration $c = \frac{c_+}{\nu_+} = \frac{c_-}{\nu_-}$ and D_{el} denotes the diffusion coefficient of the electrolyte solution. The current density is given as

$$\boldsymbol{i} = -\kappa \nabla \Phi - \frac{1}{z_+ F} \kappa \, t_+ \frac{\partial \mu_{\text{el}}}{\partial c} \nabla c. \tag{2.89}$$

The conservation equations for the heat density and the temperature dependency are not considered in the present work.

Comparison with concentrated solution theory derived from the Stefan-Maxwell approach
The mass conservation equation (2.88) has the same form as Equ. (2.72), whereas Equ. (2.89) shows significant differences to all formulations presented in section 2.4.2. As suggested by Latz and Zausch [99], the electrostatic potential Φ can also be expressed using the electrochemical potential $\hat{\mu}_{\text{el}} \equiv \mu_{\text{el}} + z_+ F \Phi$ of the electrolyte solution giving

$$\boldsymbol{i} = -\kappa \frac{\nabla \hat{\mu}_{\text{el}}}{z_+ F} + \frac{1}{z_+ F} \, \kappa \, (1 - t_+) \, \frac{\partial \mu_{\text{el}}}{\partial c} \nabla c. \tag{2.90}$$

In the original publication, the electrochemical potential φ is defined as $\varphi = \frac{\hat{\mu}_{\text{el}}}{z_+ F}$. The term $\frac{\partial \mu_{\text{el}}}{\partial c} \nabla c$ can be reformulated to

$$\begin{aligned} \frac{\partial \mu_{\text{el}}}{\partial c} \nabla c = \nabla \mu_{\text{el}} &= \frac{1}{\nu_+} \left[\nabla \mu_\pm - \frac{M_\pm}{\nu_+ M_0} \nabla \mu_0 \right] \\ &= \frac{1}{\nu_+} \left[1 + \frac{c}{c_0} \frac{M_\pm}{M_0} \right] \nabla \mu_\pm, \end{aligned} \tag{2.91}$$

using Equ. (2.87) and the Gibbs-Duhem equation (2.34)

$$\nabla \mu_0 = -\frac{c}{c_0} \nabla \mu_{\pm}.$$

As a result, Equ. (2.89) can also be expressed as

$$\boldsymbol{i} = -\kappa \frac{\nabla \hat{\mu}_{\mathrm{el}}}{z_+ F} + \frac{\nu}{\nu_+ z_+} \frac{RT}{F} \kappa \left[1 + \frac{c}{c_0} \frac{M_{\pm}}{M_0}\right] \left(1 + \frac{\partial \ln f_{\pm}}{\partial \ln c}\right) (1 - t_+) \nabla \ln c. \tag{2.92}$$

Here, the gradient of the chemical potential $\nabla \mu_{\pm}$ is replaced by Equ. (A.14). The formulation is only valid in the absence of temperature and pressure gradients. A similar reformulation for the chemical potential of the active material is shown, e.g., in Christensen and Newman [41, Equ. 6]. As in section 2.4.2, the electrochemical potential $\hat{\mu}_{\mathrm{el}}$ of the electrolyte solution is related to the chemical potential μ_{el} of a lithium reference electrode

$$\hat{\mu}_{\mathrm{el}}^{\mathrm{R}} \equiv \hat{\mu}_{\mathrm{el}} - \mu_{\mathrm{Li}}$$

giving

$$\nabla \hat{\mu}_{\mathrm{el}}^{\mathrm{R}} = \nabla \hat{\mu}_{\mathrm{el}},$$

since the chemical potential μ_{Li} of lithium is constant.

If the influence of the solvent on the electrochemical potential of the electrolyte is neglected in Equ. (2.91), the equation for the current given in Equ. (2.92) is equivalent to the formulation given in Equ. (2.51). In this case, only the electrochemical potentials of the positive and negative ionic species are considered as a driving force for the ionic species. However, the used incorporation of the solvent into the mass balance per volume given in Equ. (2.85) is also a simplification since the variation of the electrolyte density ρ_{el} is neglected in Equ. (2.85). The consideration of density or, actually, volumetric effect would result in a coupled approach combining the ion-transport equations with the Navier-Stokes equations. This would also require the incorporation of total differential of the pressure $\mathrm{d}\, p$ into Equ. (2.86). Compared to the Stefan-Maxwell approach, the thermodynamically motivated approach is much more powerful since temperature effects can be incorporated consistently within the framework as it is shown in Latz and Zausch [99].

2.7 Initial and boundary conditions

The mathematical description of the governing equations and boundary conditions has already been given in section 2.1. In this section, the physical interpretation of the mathematical description is presented. In general, most electrochemical applications can be divided into three different classes, which can be distinguished based on the applied initial and boundary conditions. The first class comprises all potential-controlled applications as, e.g., potential step or potential sweep methods. In the case of a potential-controlled experiment, an electrostatic potential difference is applied between two electrodes resulting in a variable current flow across the

surface of the electrodes. Additionally, no-flux conditions are applied to all remaining boundaries and a homogeneous initial concentration field is assumed in the beginning. The second class comprises current-controlled applications which are current-controlled such as a galvanostatic experiments. In such applications, a constant current flow across the electrodes is prescribed resulting in a variable electrostatic cell potential. As in the first class, no-flux boundary conditions are applied to the remaining boundaries and a homogeneous initial concentration profile is assumed. The last class comprises applications where no-flux conditions are applied to all boundaries inclusive electrodes and a non-homogeneous initial concentration field is applied resulting in a non-homogeneous potential field within the electrolyte solution. The most famous representative of this class is the concentration cell. Besides, all relaxation experiments based on galvanostatic or potentiostatic polarization can be included into this class.

In a potential-controlled simulation, the potential difference can be described via Dirichlet conditions on the potential. In case of a current-controlled simulation, the current flow density can be converted into an equivalent molar flux density by

$$\boldsymbol{i} = z_+ F \boldsymbol{N}_+ \tag{2.93}$$

and applied via a Neumann condition. In both cases, the kinetic behavior of the electrodes is ignored completely. Alternatively, potential- and current-controlled applications can also incorporate kinetic models like the well-known Butler-Volmer law. There are many different formulations of the Butler-Volmer law available in the literature. However, in all formulations, the surface overpotential η introduced in section A.6 is assumed to be the driving force for an electrochemical reaction (see, e.g., Newman and Thomas-Alyea [109, chap. 8]). It describes the deflection of the chemical potential from the equilibrium potential with zero net reaction rate since forward and backward reactions are in balance. Additionally, physical phenomena as, e.g., double layer charging on electrode surfaces can be considered.

Electrode kinetics As described in appendix A.6, the surface overpotential η is the driving force for a reversible electrochemical reaction. Therefore, the correct description of the surface overpotential is of central importance when modeling electrochemical cells. Irreversible reactions such as the formation of the Solid Electrolyte Interface (SEI) or parasitic side reactions are not considered in this work.

The overpotential defined in Equ. (A.17) is related to the electrochemical potentials $\hat{\mu}_k$ of all components k participating in the electrochemical reaction. The electrochemical potential $\hat{\mu}_{e^-}$ of the electrons can be approximated by the electrostatic potential Φ_{so} in the solid phase. This can be derived from the phase equilibrium between a solid and a liquid phase as demonstrated, e.g., in Newman and Thomas-Alyea [109, chap. 2.4]. As a result, Equ. (A.17) can be reformulated to

$$\eta = \Phi_{\text{so}} + \frac{s_{\text{so}}}{nF}\mu_{\text{so}} + \sum_i \frac{s_i}{nF}\hat{\mu}_i, \tag{2.94}$$

where the charge number $z_- = -1$ of electrons has been used. Here, the subscript i stands for all dissolved, charged and uncharged components participating in the electrochemical reaction. The chemical potential $\mu_{\text{so}} = \sum_j \frac{s_j}{nF}\mu_j$ includes all chemical potentials of solid, uncharged components, which are part of the electrode. For instance, the chemical potential μ_{so} depends on the

State Of Charge (SOC) since the composition of the active material changes due to lithiation or de-lithiation. As stated by Latz and Zausch [99], the overpotential can be defined as the "*deviation of the electrochemical potential from the chemical equilibrium between active particle, the solid phase, and electrolyte*". From an alternative point of view, the term $\left(\Phi_{\text{so}} + \frac{s_{\text{so}}}{nF}\mu_{\text{so}}\right)$ can be seen as the electrochemical potential of the solid and the terms $\sum_i \left(\frac{s_i}{nF}\hat{\mu}_i\right)$ can be regarded as the electrochemical potential of the electrolyte. Usually, the chemical potential of lithium is included as a reference, which gives

$$\eta = \Phi_{\text{so}} - U_0 + \frac{1}{nF}\mu_{\text{Li}} + \sum_i \frac{s_i}{nF}\hat{\mu}_i, \tag{2.95}$$

where $U_0 \equiv \frac{1}{nF}\left(\mu_{\text{Li}} - s_{\text{so}}\mu_{\text{so}}\right)$ denotes the open circuit potential with respect to lithium reference electrode.

In general, the definition of the overpotential given in Equ. (2.94) can be used with all definitions describing the electrical state of electrolyte solution given in section 2.4.2. In the following, a binary electrolyte solution consisting of a dissolved lithium salt and lithium electrodes are assumed giving

$$\eta = \Phi_{\text{so}} - U_0 + \frac{1}{nF}\left(\mu_{\text{Li}} - \hat{\mu}_+\right). \tag{2.96}$$

The term $\frac{1}{nF}\left(\mu_{\text{Li}} - \hat{\mu}_+\right) = -\Phi^{\text{R}}$ defines the electrostatic potential with respect to a lithium reference electrode as used for Equ. (2.60). Additionally, the definition $\hat{\mu}_+^{\text{R}} \equiv \hat{\mu}_+ - \mu_{\text{Li}}$ introduced in Equ. (2.52) for Equ. (2.51) is also included. The surface overpotential can also be defined based on an ionic species as reference. In this case, the inclusion of the chemical potential μ_{Li} as done in Equ. (2.94) and (2.95) is not necessary. However, in this case, it is more elaborate to define the chemical potential of the solid.

The simplest electrode reaction is the deposition or dissolution of a metal M_{so} represented by the electrochemical reaction

$$s_{\text{so}}M_{\text{so}} + s_+M_+ \rightleftarrows ne^-.$$

It can be modeled by the Butler-Volmer law

$$i_n = i_0\left(\frac{c_k}{c_{k,0}}\right)^{\gamma}\left[\exp\left(\frac{\alpha_{\text{A}}F}{RT}\eta\right) - \exp\left(-\frac{\alpha_{\text{C}}F}{RT}\eta\right)\right]. \tag{2.97}$$

A detailed derivation of the Butler-Volmer law is given, e.g., in Wittmann [152] or Newman and Thomas-Alyea [109]. The involved parameters are the exchange current density i_0, some reference concentration $c_{k,0}$ of the reactive ionic species, an exponent γ for weighting the surface concentration dependency, an anodic constant α_{A}, and a cathodic constant α_{C}. In battery science, the most famous representative of this type of the electrochemical reaction is the reaction

$$\text{Li} \rightleftarrows \text{Li}^+ + e^-. \tag{2.98}$$

In this special case, the open circuit potential is zero by definition,

$$U_0 = \frac{1}{nF}\mu_{\mathrm{Li}} - \frac{1}{nF}\mu_{\mathrm{Li}} = 0,$$

and Equ. (2.95) simplifies to

$$\eta = \Phi_{\mathrm{so}} - \frac{1}{z_+ F}\left(\hat{\mu}_+ - \mu_{\mathrm{Li}}\right)$$

where the relation $n = z_+$ resulting from Equ. (2.59) is used. In this manuscript, only the Butler-Volmer law for the deposition or dissolution of lithium on the lithium electrode is used since all experiments discussed in the following are based on two lithium electrodes. More complex reaction models are discussed, e.g., in Wittmann [152], Bard and Faulkner [14] or Newman and Thomas-Alyea [109]. In Willman [151], a numerical method is developed for the incorporation of double layer charging into electrode boundary conditions.

3 Ion-transport in porous media

As discussed in section 1, there are two different approaches for modeling and simulating electrochemical phenomena in battery systems. The three-dimensional porous structure of electrodes and separators filled with an electrolyte solution can be resolved geometrically resulting in a very detailed model. However, these models are computationally very expensive and usually to large to be applicable to the entire battery system. Alternatively, the porous microstructure can also be modeled by a homogeneous continuum on the macroscopic level. In this case, the influence of the microstructure is incorporated by additional geometrical parameters such as the porosity ε and the tortuosity τ.

In literature, there are different models available describing the transfer from the microscopic conservation laws to the macroscopic level. One of the most famous approaches is the volume averaging method explained, e.g., in Whitaker [149] or Bear and Bachmat [23]. Often, this method is also called averaged-field or mean-field theory. The basic idea of the method is the integration of the microscopic partial differential equations over a Representative Element Volume (REV) giving the macroscopic transport equations. Applying this method to ion-transport results in the so-called homogenized ion-transport equations. Originally, these equations were introduced in Newman and Tiedemann [111] and Newman et al. [112]. However, in most of the publications, Doyle et al. [54] and Fuller et al. [64] are cited as reference for the homogenized ion-transport equations. Nevertheless, an actual derivation is missing in all these publications. In Lai and Ciucci [93], the volume averaging method is applied to the so-called generalized Poisson-Nernst-Planck equations. Apart from the used alternative ion-transport model, the obtained macroscopic equations are equivalent to homogenized ion-transport equations given in Newman and Tiedemann [111]. However, the volume average of terms including concentration dependent transport parameters are also not discussed in this publication. A review of the homogenized ion-transport equations including a theoretical motivation is given in Landstorfer and Jacob [98]. Nowadays, the homogenized ion-transport equations are the standard model for battery applications in science and industry.

An alternative approach for the transformation of the microscopic conservation laws to the macroscopic level is used, e.g., in Ciucci and Lai [44]. In that contribution, the homogenization theory in combination with an asymptotic expansion of the transport equations is used to derive a multi-scale system for ion-transport in porous media. In addition to the macroscopic equations, a microscale problem has to be solved at each point of the domain. The introduction of additional assumptions such as a periodical three-dimensional spherical microstructure leads to the same equations as introduced by Newman and Tiedemann [111]. In this publication it is also emphasized that micro-macro formulations may not be applicable for thin electrodes with 'large' microscopic features. In Hori and Nemat-Nasser [83], it is shown in the context of structural mechanics that the homogenization theory and the volume averaging method 'can be related to each other, even though they are based on different concepts' (see Hori and Nemat-Nasser

[83, p. 680]). At this point it is important to emphasize that the term homogenized ion-transport equations is not connected exclusively to the homogenization theory but is generally used for the macroscopic description of ion-transport in porous media. Alternative multi-scale approaches are introduced for the modeling of stress-induced ion-transport as, e.g., in Salvadori et al. [130] or Golmon et al. [69]. In general, alternative approaches with interesting features may be available in different communities, since the modeling of transport processes in porous media is necessary in many engineering fields as, e.g., the oil industry, bio-mechanics and so on (see, e.g., Adler [2, chap. 2.2]).

In this section, the mathematical framework for the volume averaging of the ion-transport equations is presented taking also account for concentration dependent transport parameters. This is necessary since constant transport parameters are usually assumed for the derivation of the homogenized ion-transport equations although the transport parameters are concentration dependent in reality. For that purpose, the mathematical approach introduced by Bear and Bachmat [23] is explained in detail and extended to transport equations with variable transport parameters. In this contribution, the focus is on ion-transport in the separator since experiments for the determination of transport parameters are based on a cell without a porous electrode. However, for the sake of completeness, the derivation of the homogenized ion-transport equations for electrodes is also included.

3.1 Volume averaging method

The basic concept of the homogenization approach presented, e.g., in Bear and Bachmat [23] is the averaging of the quantities of interest over a Representative Element Volume (REV) at the microscopic level and transferring the mean values to to the macroscopic level.

3.1.1 Basic definitions

In Fig. 3.1 an exemplary REV within a porous medium is shown including basic notations. A porous medium consisting of two phases is considered as an example for the homogenization of a porous microstructure. The extension to more than two phases is mostly a technical issue. The domain Ω° of the REV is a subset of the domain Ω occupied by the porous medium. Here, the domain Ω° of the REV consists of an electrolyte phase Ω^{e} and a solid phase Ω^{s}. The boundary between the electrolyte phase and solid phase is denoted by $\Gamma^{\mathrm{e,s}}$ with the respective surface area $A^{\mathrm{e,s}}$. The boundary $\Gamma^{\mathrm{e,e}}$ denotes the part of the REV intersecting the electrolyte phase. The corresponding area is $A^{\mathrm{e,e}}$. Quantities defined on the electrolyte phase are indicated by $()^{\mathrm{e}}$ and quantities defined on the solid phase by $()^{\mathrm{s}}$. For instance, the volumes of the electrolyte and solid phase are denoted by V^{e} and V^{s} and the volume of the REV by V°. The center of the REV is defined by $\boldsymbol{x}_0$ and the center of the electrolyte phase volume by $\boldsymbol{x}_0^{\mathrm{e}}$. The location of the points at the macroscopic level are denoted by $\boldsymbol{x}$ and the location of the points at the microscopic level within the REV by $\boldsymbol{x}'$. Both location vectors are part of the same coordinate system. The ratio

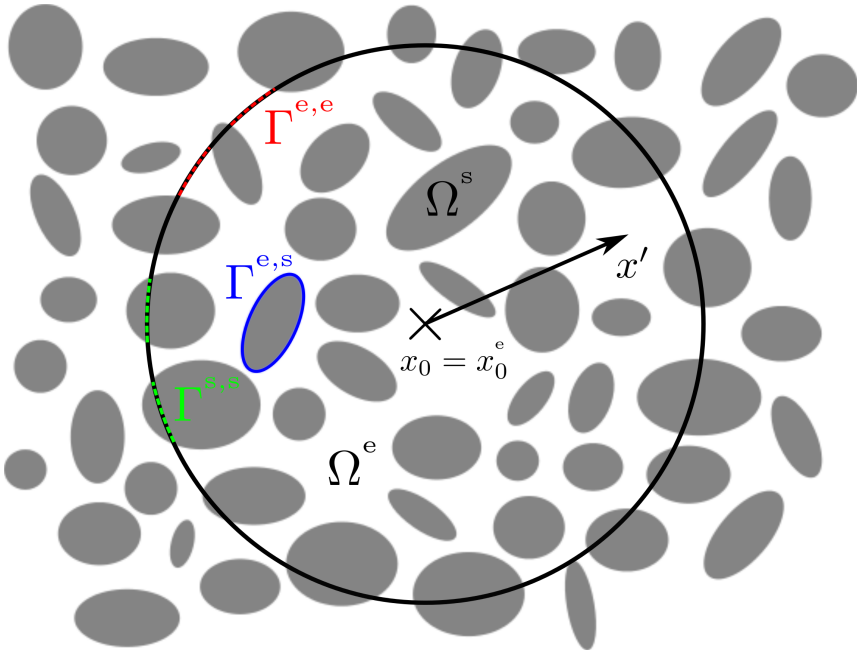

Figure 3.1: Two-dimensional sketch of a porous microstructure with a spherical Representative Element Volume (REV).

between electrolyte volume V^{e} and the volume of the REV V° defines the porosity ε:

$$\varepsilon = \frac{V^{\mathrm{e}}}{V^{\circ}}.$$

The exact size of the volume V° is strongly influenced by the dimensions and the characteristic of the underlying microstructure and by the models objectives. However, the basic requirement for the homogenization approach is the fulfillment of the condition

$$\left.\frac{\partial \varepsilon(\boldsymbol{x}_0, V)}{\partial V}\right|_{V=V^{\circ}} = 0$$

at each point $\boldsymbol{x} = \boldsymbol{x}_0$ within the macroscopic domain Ω. This equation simply states that the porosity has to be independent from the position $\boldsymbol{x}_0$ and from the size V° of the REV. In reality, this condition will only be fulfilled approximately. A detailed discussion about the exact definition of the REV size is given e.g. in Bear and Bachmat [23, chap. 1.2.2].

For the definition of the volumetric average of the concentration $\bar{c}$, the concentration c is integrated over the domain Ω^{e} and afterwards divided by the total volume V° of the domain Ω°. This gives the volumetric phase average $\bar{c}$ of the concentration c with respect to the volume V°

$$\bar{c}(\boldsymbol{x}, t) = \frac{1}{V^{\circ}} \int_{\Omega^{\mathrm{e}}} c(\boldsymbol{x}', t; \boldsymbol{x}) \, \mathrm{d}\, V.$$

Here, the integral is based on the subdomain Ω^{e}, since the considered quantity c is only a property of the electrolyte phase. The notation $c(\boldsymbol{x}', t; \boldsymbol{x})$ indicates that the concentration field $c(\boldsymbol{x}', t)$ within the REV centered at an arbitrary point $\boldsymbol{x}$ of the macroscopic domain Ω is considered for the averaging process. All points within the REV are described by the position vector $\boldsymbol{x}'$. In general, the notation $\overline{(\dots)}$ is the volumetric average of any quantity inside the brackets. Alternatively, the quantity c can also be averaged with respect to the volume filled by the electrolyte V^{e}, which results in

$$\bar{c}^{\,\mathrm{e}}(\boldsymbol{x}, t) = \frac{1}{V^{\mathrm{e}}} \int_{\Omega^{\mathrm{e}}} c(\boldsymbol{x}', t; \boldsymbol{x}) \, \mathrm{d}\, V,$$

where $\bar{c}^{\,\mathrm{e}}$ denotes the volumetric intrinsic phase average of $c(\boldsymbol{x}, t)$. The notation $\overline{(\dots)}^{\mathrm{e}}$ is the volumetric intrinsic phase average of any quantity within the brackets. In general, the volumetric phase average and volumetric intrinsic phase average are related by the porosity ε

$$\overline{(\dots)} = \varepsilon \overline{(\dots)}^{\mathrm{e}}. \tag{3.1}$$

Equivalently, the volumetric phase average $\overline{\Phi}$ of the potential Φ is defined as

$$\overline{\Phi}(\boldsymbol{x}, t) = \varepsilon \overline{\Phi}^{\mathrm{e}} = \frac{V^{\mathrm{e}}}{V^{\mathrm{o}}} \frac{1}{V^{\mathrm{e}}} \int_{\Omega^{\mathrm{e}}} \Phi(\boldsymbol{x}', t; \boldsymbol{x}) \, \mathrm{d}\, V = \frac{1}{V^{\mathrm{o}}} \int_{\Omega^{\mathrm{e}}} \Phi(\boldsymbol{x}', t; \boldsymbol{x}) \, \mathrm{d}\, V.$$

The same formalism can also be applied for all other quantities such as the velocity $\boldsymbol{u}$.

3.1.2 Volume average of the ion-transport equations

To obtain the macroscopic conservation laws, the conservation law for mass

$$\begin{aligned} &\frac{1}{V^{\mathrm{o}}} \int_{\Omega^{\mathrm{e}}} \frac{\partial c(\boldsymbol{x}', t; \boldsymbol{x})}{\partial t} \, \mathrm{d}\, V + \\ &+ \frac{1}{V^{\mathrm{o}}} \int_{\Omega^{\mathrm{e}}} \nabla \cdot \Big(c(\boldsymbol{x}', t; \boldsymbol{x}) \, \boldsymbol{u}(\boldsymbol{x}', t; \boldsymbol{x}) + \boldsymbol{N}(\boldsymbol{x}', t; \boldsymbol{x}) \Big) \, \mathrm{d}\, V = 0 \end{aligned} \tag{3.2}$$

and current

$$\frac{1}{V^{\mathrm{o}}} \int_{\Omega^{\mathrm{e}}} \nabla \cdot \boldsymbol{i}(\boldsymbol{x}', t; \boldsymbol{x}) \, \mathrm{d}\, V = 0$$

at the microscopic level are integrated over an REV. Despite the fact that convective transport is usually neglected in battery applications, it is included in Equ. (3.2) to give a complete overview over the homogenized macroscopic conservation laws. Both conservation equations can also be written in terms of the short notation, which gives

$$\varepsilon \, \overline{\frac{\partial c}{\partial t}}^{\mathrm{e}} + \varepsilon \, \overline{\nabla \cdot (c \boldsymbol{u} + \boldsymbol{N})}^{\mathrm{e}} = 0 \tag{3.3}$$

and

$$\varepsilon \overline{\nabla \cdot \boldsymbol{i}}^{\,\mathrm{e}} = 0. \tag{3.4}$$

Here, Equ. (3.1) is used to transform the volumetric phase average to the volumetric intrinsic phase average. On the macroscopic level, the dependencies of the variables on position $\boldsymbol{x}$ and time t are omitted to simplify the notation. In the following, the mathematical framework for the reformulation of Equ. (3.3) and Equ. (3.4) is presented. A detailed overview including theoretical considerations is given in Bear and Bachmat [23]. The final averaging rules for the time derivative

$$\varepsilon \overline{\frac{\partial c}{\partial t}}^{\,\mathrm{e}} = \frac{\partial \varepsilon \bar{c}^{\,\mathrm{e}}}{\partial t} - \Xi^{\mathrm{e,s}} \widetilde{(c \boldsymbol{u}_{\mathrm{I}}^{\mathrm{e,s}} \cdot \boldsymbol{n})}^{\,\mathrm{e,s}}, \tag{3.5}$$

for the product of two non-constant quantities

$$\varepsilon \overline{c \boldsymbol{u}}^{\,\mathrm{e}} = \varepsilon (\bar{c}^{\,\mathrm{e}} \bar{\boldsymbol{u}}^{\,\mathrm{e}} + \overline{\hat{c}\, \hat{\boldsymbol{u}}}^{\,\mathrm{e}}) \tag{3.6}$$

and for the spatial derivative

$$\varepsilon \overline{\nabla \cdot \boldsymbol{N}}^{\,\mathrm{e}} = \nabla \cdot (\varepsilon \overline{\boldsymbol{N}}^{\,\mathrm{e}}) + \Xi^{\mathrm{e,s}} \widetilde{(\boldsymbol{N} \cdot \boldsymbol{n})}^{\,\mathrm{e,s}}, \tag{3.7}$$

are shown exemplarily for the concentration c. As shown in Fig. 3.1, the boundary between the electrolyte phase and solid phase is denoted by $\Gamma^{\mathrm{e,s}}$ with the respective surface area $A^{\mathrm{e,s}}$ The velocity of the boundary between the electrolyte and the solid phase is denoted by $\boldsymbol{u}_{\mathrm{I}}$. The deviation from the concentration $c(\boldsymbol{x}, t)$ at a point $\boldsymbol{x}'$ within a REV centered at $\boldsymbol{x}$ from its intrinsic phase average $\bar{c}^{\,\mathrm{e}}$ over that REV is denoted by $\hat{c}(\boldsymbol{x}', t; \boldsymbol{x})$:

$$\hat{c}(\boldsymbol{x}', t; \boldsymbol{x}) \equiv c(\boldsymbol{x}', t; \boldsymbol{x}) - \bar{c}^{\,\mathrm{e}}.$$

An important implication of this definition is that the volumetric intrinsic phase average $\overline{\hat{c}}$ of $\hat{c}$ is zero

$$\overline{\hat{c}}(\boldsymbol{x}, t) = \frac{1}{V^{\mathrm{e}}} \int_{\Omega^{\mathrm{e}}} \Big(c(\boldsymbol{x}', t; \boldsymbol{x}) - \bar{c}^{\,\mathrm{e}}(\boldsymbol{x}, t) \Big)\, \mathrm{d}\, V = 0$$

since $\bar{c}^{\,\mathrm{e}}$ is constant in the corresponding REV. The notation $\widetilde{(\ldots)}^{\,\mathrm{e,s}}$ is the surface average of any quantity

$$\widetilde{(\ldots)}^{\,\mathrm{e,s}} = \frac{1}{A^{\mathrm{e,s}}} \int_{\Gamma^{\mathrm{e,s}}} (\ldots)\, \mathrm{d}\, A$$

and $\Xi^{\mathrm{e,s}}$ for ratio between the area $A^{\mathrm{e,s}}$ of the interface $\Gamma^{\mathrm{e,s}}$ and the volume V^{o} of the REV:

$$\Xi^{\mathrm{e,s}} = \frac{A^{\mathrm{e,s}}}{V^{\mathrm{o}}}.$$

The averaging rules given in Equ. (3.5) – Equ. (3.7) can be applied to Equ. (3.3) and Equ. (3.4) resulting in

$$\frac{\partial \varepsilon \bar{c}_k^{\,\mathrm{e}}}{\partial t} - \Xi^{\mathrm{e,s}} \widetilde{(c\, \boldsymbol{u}_{\mathrm{I}}^{\mathrm{e,s}} \cdot \boldsymbol{n})}^{\mathrm{e,s}} + \nabla \cdot \left(\varepsilon \bar{c}^{\,\mathrm{e}} \bar{\boldsymbol{u}}^{\,\mathrm{e}} + \varepsilon \overline{\hat{c}\, \hat{\boldsymbol{u}}}^{\,\mathrm{e}} \right) + \nabla \cdot \left(\varepsilon \overline{\boldsymbol{N}}^{\,\mathrm{e}} \right) + \Xi^{\mathrm{e,s}} \widetilde{(\boldsymbol{N} \cdot \boldsymbol{n})}^{\mathrm{e,s}} = 0, \tag{3.8}$$

and

$$\nabla \cdot \left(\varepsilon \bar{\boldsymbol{i}}^{\,\mathrm{e}} \right) + \Xi^{\mathrm{e,s}} \widetilde{(\boldsymbol{i} \cdot \boldsymbol{n})}^{\mathrm{e,s}} = 0. \tag{3.9}$$

In the following, all terms of Equ. (3.8) and Equ. (3.9) are discussed with respect to battery applications:

a) First term in Equ. (3.8) $\left[\frac{\partial \varepsilon \bar{c}_k^{\,\mathrm{e}}}{\partial t} \right]$
Under normal operation conditions, the porosity ε of a separator is always constant. This is not true for electrodes since the solid phase may change its volume due to the expansion of the active material as a result of lithium intercalation. Since the volumetric expansion of most of the active materials is negligible small (few percents with respect to the original volume) and does not happen rapidly, it is usually valid to assume a constant porosity for electrodes, too. An example for an active material with a potentially time-dependent porosity is silicon since the volumetric change is about 400% as mentioned, e.g., in Chakraborty et al. [40]. An additional physical phenomenon introducing a time-dependent porosity is the growth of a Surface Interface Layer (SEI). However, this effect can also be neglected for most of the applications since the SEI is usually in the order of nanometer.

b) Second term in Equ. (3.8) $\left[\Xi^{\mathrm{e,s}} \widetilde{(c\, \boldsymbol{u}_{\mathrm{I}}^{\mathrm{e,s}} \cdot \boldsymbol{n})}^{\mathrm{e,s}} \right]$
This term can be neglected for a separator since the interface between electrolyte and solid $\Gamma^{\mathrm{e,s}}$ is fixed in space and time, i.e., $\boldsymbol{u}_{\mathrm{I}}^{\mathrm{e,s}} = 0$. Assuming the same operating conditions as in item *a*), this also valid for electrodes.

c) Third term in Equ. (3.8) $\left[\nabla \cdot (\varepsilon \bar{c}^{\,\mathrm{e}} \bar{\boldsymbol{u}}^{\,\mathrm{e}}) \right]$
This term is also zero since convective flow is usually negligible small in battery applications as explained in section 2 which means $\boldsymbol{u} = 0$.

d) Forth term in Equ. (3.8) $\left[\nabla \cdot (\varepsilon \overline{\hat{c}\, \hat{\boldsymbol{u}}}^{\,\mathrm{e}}) \right]$
In literature, this term is called dispersive flux. Bear and Bachmat [23] describes the dispersive fluxes as a macroscopic flux of the concentration c, relative to the transport with the average velocity $\bar{\boldsymbol{u}}^{\,\mathrm{e}}$ of the electrolyte phase. The modeling of this term may be quite complex. However, this term is also zero as long as the convective velocity is neglected.

e) Fifth term in Equ. (3.8) $\left[\nabla \cdot \left(\varepsilon \overline{\boldsymbol{N}}^{\,\mathrm{e}} \right) \right]$
The volume average of the molar flux density will be discussed in detail in the following sections.

f) Sixth term in Equ. (3.8) $\left[\Xi^{\mathrm{e,s}}\widetilde{(\boldsymbol{N}\cdot\boldsymbol{n})}^{\mathrm{e,s}}\right]$
This term describes the molar flux density across the interface $\Gamma^{\mathrm{e,s}}$ within a REV resulting, e.g., from the electrochemical reaction of lithium ions at the surface of the active material. This term is zero for porous media with a non-reactive surface such as a separator.

g) First term in Equ. (3.9) $\left[\nabla\cdot\left(\varepsilon\,\overline{\boldsymbol{i}}^{\mathrm{e}}\right)\right]$
The volume average of the current density will be discussed in detail in the following sections.

h) Second term in Equ. (3.9) $\left[\Xi^{\mathrm{e,s}}\widetilde{(\boldsymbol{i}\cdot\boldsymbol{n})}^{\mathrm{e,s}}\right]$
This term describes the current flow across interface $\Gamma^{\mathrm{e,s}}$ within a REV and is related to term 6. by

$$\widetilde{(\boldsymbol{N}\cdot\boldsymbol{n})}^{\mathrm{e,s}} = \frac{1}{\nu_+ z_+ F}\widetilde{(\boldsymbol{i}\cdot\boldsymbol{n})}^{\mathrm{e,s}}. \tag{3.10}$$

As mentioned already in item *f*), this term is zero for a porous medium without a reactive surface $\Gamma^{\mathrm{e,s}}$ such as a separator. Note, that the equivalent molar flux is defined as $\boldsymbol{N} = \frac{\boldsymbol{N}_+}{\nu_+}$.

As a result, the general macroscopic ion transport equations given in Equ. (3.8) and Equ. (3.9) can be simplified for standard battery applications to

$$\begin{aligned}\varepsilon\frac{\partial\overline{c}^{\mathrm{e}}}{\partial t} + \nabla\cdot\varepsilon\overline{\boldsymbol{N}}^{\mathrm{e}} + \Xi^{\mathrm{e,s}}\widetilde{(\boldsymbol{N}\cdot\boldsymbol{n})}^{\mathrm{e,s}} &= 0,\\ \nabla\cdot\left(\varepsilon\,\overline{\boldsymbol{i}}^{\mathrm{e}}\right) + \Xi^{\mathrm{e,s}}\widetilde{(\boldsymbol{i}\cdot\boldsymbol{n})}^{\mathrm{e,s}} &= 0,\end{aligned}$$

where the assumptions given in items *a*) – *d*) are used. For a porous medium with a non-reactive surface, Equ. (3.8) and Equ. (3.9) simplify even more

$$\begin{aligned}\varepsilon\frac{\partial\overline{c}^{\mathrm{e}}}{\partial t} + \nabla\cdot\varepsilon\overline{\boldsymbol{N}}^{\mathrm{e}} &= 0,\\ \nabla\cdot\left(\varepsilon\,\overline{\boldsymbol{i}}^{\mathrm{e}}\right) &= 0,\end{aligned} \tag{3.11}$$

since the source terms describing the effect of the surface reaction are also zero as described in item *f*) and *h*).

3.2 Volume average of the molar flux and current density

3.2.1 Constant transport parameters on micro- and macroscale

So far, the standard averaging rules are applied to the ion transport equations. In a next step, an averaging rule for the molar flux and current density is introduced. The volumetric intrinsic

phase average of the molar flux density $\boldsymbol{N}$ (see Equ. (2.44)) is defined as

$$\overline{\boldsymbol{N}}^{\mathrm{e}} = -\overline{D_{\pm}(c)\,\nabla c}^{\mathrm{e}} + \frac{1}{\nu_+ z_+ F}\,\overline{t_+(c)\,\boldsymbol{i}}^{\mathrm{e}}. \tag{3.12}$$

Equivalently, the volumetric intrinsic phase average of the current density can be written as

$$\overline{\boldsymbol{i}}^{\mathrm{e}} = -\overline{\kappa(c)\nabla\Phi^{\mathrm{R}}}^{\mathrm{e}} + \underbrace{\frac{RT}{z_+F}\,\frac{\nu}{\nu_+}\,\Lambda_{\mathrm{m}}(c)\,\left[1+\frac{\mathrm{d}\ln f_{\pm}(c)}{\mathrm{d}\ln c}\right]\,(1-t_+(c))}_{a(c)}\,\nabla c}^{\mathrm{e}}\,, \tag{3.13}$$

where the concentration dependent transport parameters in the second term are summarized in the variable $a(c)$. For the following derivation, the equivalent conductance $\Lambda_{\mathrm{m}} = \frac{\kappa}{c}$ as defined in Newman and Thomas-Alyea [109, p. 285] is used to simplify the second term. Here, the potential Φ^{R} is defined with respect to a lithium reference electrode. The superscript $^{\mathrm{R}}$ is dropped in the following. In these equations, it is the main challenge to derive an averaging rule for the volumetric intrinsic phase average of the molar flux density $\overline{\boldsymbol{N}}^{\mathrm{e}}$ and of the current density $\overline{\boldsymbol{i}}^{\mathrm{e}}$ which transfers the volumetric intrinsic phase average from the form $\overline{\nabla(\ldots)}^{\mathrm{e}}$ into the form $\nabla\overline{(\ldots)}^{\mathrm{e}}$, considering concentration dependent transport parameters.

For this purpose, an alternative averaging rule is derived for the spatial gradient in Bear and Bachmat [23, chap. 2.3.5], utilizing the quasi-stationary form of the time-dependent diffusion problem with a constant diffusion coefficient $D_{\pm}$ on the microscopic level

$$\frac{\partial^2 c}{\partial (x_i)^2} = 0. \tag{3.14}$$

The spatial derivation $\frac{1}{x_i} = \frac{1}{x_i'}$ are equal since the same coordinate systems are used on the micro- and the macroscale. Additional approximations are

$$\int_{\Gamma^{\mathrm{e,e}}} \frac{\partial c}{\partial x_j}\hat{x}_j n_i \,\mathrm{d}\,A \approx \frac{1}{A^{\mathrm{e,e}}}\int_{\Gamma^{\mathrm{e,e}}} \frac{\partial c}{\partial x_j}\,\mathrm{d}\,A \int_{\Gamma^{\mathrm{e,e}}} \hat{x}_j n_i \,\mathrm{d}\,A \tag{3.15}$$

and

$$\frac{1}{A^{\mathrm{e,e}}}\int_{\Gamma^{\mathrm{e,e}}} \frac{\partial c}{\partial x_j}\,\mathrm{d}\,A \approx \frac{1}{V^{\mathrm{e,e}}}\int_{\Omega^{\mathrm{e}}} \frac{\partial c}{\partial x_j}\,\mathrm{d}\,V \approx \frac{\partial}{\partial x_j}\left(\frac{1}{V^{\mathrm{e,e}}}\int_{\Omega^{\mathrm{e}}} c\,\mathrm{d}\,V\right), \tag{3.16}$$

where $\hat{x}_j$ denotes the position vector $(x_j' - x_{j,0})$ between an arbitrary point x_j' within the REV and the center of the REV $x_{j,0}$. As depicted in Fig. 3.1, $\Gamma^{\mathrm{e,e}}$ is the boundary of the electrolyte phase Ω^{e} within the REV and $A^{\mathrm{e,e}}$ the associated surface area. In the following, the Einstein notation is used instead of the matrix notation. In the approximation given in Equ. (3.15), the surface integral is split into a physically motivated term and a geometrically motivated term. Since the surface integral is split into two surface integrals, the term has to be scaled additionally with the inverse of the area $A^{\mathrm{e,e}}$. The second approximation given in Equ. (3.16) is actually a combination of two approximations. The first is the equality between the surface integral and the volume integral. The second is the extraction of the spatial derivative from inside the integral.

Both approximation of Equ. (3.16) can be motivated by the linear behavior of the concentration field within the REV. An approximately linear behavior of any macroscopic quantity within a REV is a basic requirement of the volume averaging method as stated in Bear and Bachmat [23, chap. 1.2.3]. Unfortunately, a theoretical explanation for the approximation in Equ. (3.15) is not given in Bear and Bachmat [23].

As a result of Equ. (3.14) – Equ. (3.16), the alternative averaging rule for spatial derivatives can be written as

$$\overline{\frac{\partial c}{\partial x_j}}^{\mathrm{e}} = T^*_{ji}\frac{\partial \overline{c}^{\mathrm{e}}}{\partial x_i} + \frac{\Xi^{\mathrm{e,s}}}{\varepsilon}\frac{1}{A^{\mathrm{e,s}}}\int_{\Gamma^{\mathrm{e,s}}} \hat{x}_j \frac{\partial c}{\partial x_i} n_i \,\mathrm{d}\, A, \tag{3.17}$$

where the geometry coefficient T^*_{ji}

$$T^*_{ji} = \frac{1}{V^{\mathrm{e}}}\int_{\Gamma^{\mathrm{e,e}}} \hat{x}_j n_i \,\mathrm{d}\, A \tag{3.18}$$

is a fundamental property of the geometrical configuration of the electrolyte phase within REV. A more detailed derivation is given in Bear and Bachmat [23, chap. 2.3.5]. As explained in Bear and Bachmat [23, chap. 2.3.6] the tensor T^*_{ji} simplifies for an isotropic porous medium with a spherical REV to

$$T^*_{ji} = \frac{\varepsilon_{\mathrm{a}}}{\varepsilon}\delta_{ij}, \tag{3.19}$$

where ε_{a} denotes the surface porosity. The same relation is also valid for a cubical REV with an edge length l. For simple geometries as shown in Fig. 3.2, the geometry coefficient T_{ij} can be interpreted as the inverse of the path length tortuosity $1/\tau_{\mathrm{path}}$ which describes the elongation of the path l' trough the porous medium with respect to a direct connection l as explained, e.g., in Holzer et al. [82]:

$$T^*_{11} = \varepsilon_{\mathrm{a}}\varepsilon^{-1}\delta_{11} = \frac{A^{\mathrm{e,e}}}{A^{\mathrm{o}}}\left(\frac{V^{\mathrm{e}}}{V^{\mathrm{o}}}\right)^{-1} = \frac{2A_{\mathrm{cross}}t}{2ht}\,\frac{lht}{A_{\mathrm{cross}}l't} = \frac{l}{l'} = \frac{1}{\tau_{\mathrm{path}}}.$$

An identical result can be derived for an isotropic three-dimensional porous medium which is penetrated by channels with a constant cross section A_{cross} as shown in Bear and Bachmat [23, chap. 2.3.6]. Considering the complexity of a realistic porous medium with intersecting channels of varying cross section, it becomes clear that the path length tortuosity τ_{path} is a very rough approximation for the microstructure of a REV.

The second term on rhs in Equ. (3.17) includes information about the fluxes across the interface $\Gamma^{\mathrm{e,s}}$ as well as geometrical information about the microstructure of the REV $\hat{x}_j$. The geometrical information about the microstructure as well as a different scaling factor are the main differences to the term resulting from the averaging rule given in Equ. (3.7). This term is zero if the concentration gradient normal to the interface $\Gamma^{\mathrm{e,s}}$ is zero as it is the case for a non-reactive interfaces. This is not the case for electrodes but in many publications, this term does not show up at all as, e.g., in Lai and Ciucci [93] or Landstorfer and Jacob [98].

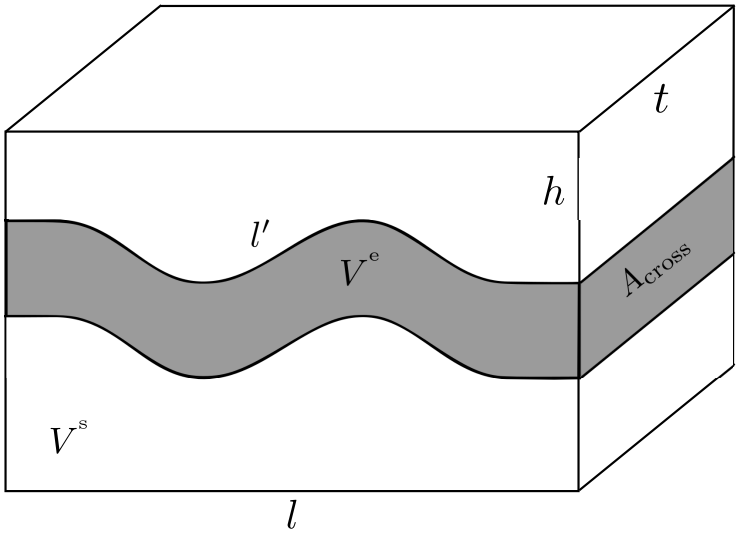

Figure 3.2: Sketch of a three-dimensional medium with the dimensions $l \times h \times t$ penetrated by a single channel filled with electrolyte solution.

3.2.2 Constant transport parameters on microscale and variable transport parameters on macroscale

The main differences between the derivation in Bear and Bachmat [23, chap. 2.3.5] and the balance equations considered in this contribution are the concentration dependent transport parameters within the volumetric intrinsic phase average and an additional volumetric coupling between the concentration and the potential field.

In a first step, it is shown that Equ. (3.17) can also be used for a system with variable transport parameters. For this, it has to be assumed that the transport parameters are constant within a REV to use the approximation given in Equ. (3.17) but variable on the macroscale. This simply means that the transport parameter can vary between different REVs. In the following, it is demonstrated that the assumption of constant transport parameters within the REV is valid for certain condition. This will be discussed based on the diffusive term of Equ. (3.12). The diffusive molar flux density can be reformulated utilizing Equ. (3.6)

$$\overline{D_{\pm}(c)\,\frac{\partial c}{\partial x_i}}^{\mathrm{e}} = \overline{D_{\pm}(c)}^{\mathrm{e}}\,\overline{\frac{\partial c}{\partial x_i}}^{\mathrm{e}} + \overline{\hat{D}_{\pm}(c)\,\widehat{\frac{\partial c}{\partial x_i}}}^{\mathrm{e}} \,,$$

which includes the volumetric intrinsic phase average of the concentration dependent diffusion coefficient, the volumetric intrinsic phase average of the concentration gradient and a term with the deviations from the volumetric intrinsic phase average of both. In general, it is possible to approximate the diffusion coefficient at each position $\boldsymbol{x}'$ within the electrolyte phase of the REV

as Taylor series evaluated at the volumetric center of electrolyte phase $\boldsymbol{x}_0^{\mathrm{e}}$

$$D_{\pm}(c(\boldsymbol{x}',t))|_{\boldsymbol{x}_0^{\mathrm{e}}} = D_{\pm}(c(\boldsymbol{x}_0^{\mathrm{e}},t)) + \sum_{i=1}^{3}\left[\frac{\partial D_{\pm}(c(\boldsymbol{x}_0^{\mathrm{e}},t))}{\partial x_i}(x_i' - x_{i,0}^{\mathrm{e}})\right] + \ldots = \\ = D_{\pm}(c(\boldsymbol{x}_0^{\mathrm{e}},t)) + \sum_{i=1}^{3}\left[\frac{\partial D_{\pm}(c(\boldsymbol{x}_0^{\mathrm{e}},t))}{\partial c(\boldsymbol{x}_0^{\mathrm{e}},t)}\,\frac{\partial c(\boldsymbol{x}_0^{\mathrm{e}},t)}{\partial x_i}(x_i' - x_{i,0}^{\mathrm{e}})\right] + \ldots. \quad (3.20)$$

Note, that the center $\boldsymbol{x}_0$ of the REV does not have to coincide with the center $\boldsymbol{x}_0^{\mathrm{e}}$ of the electrolyte phase within the REV. Equivalently, the concentration

$$c(\boldsymbol{x}',t)\Big|_{\boldsymbol{x}_0^{\mathrm{e}}} = c(\boldsymbol{x}_0',t) + \sum_{i=1}^{3}\left[\frac{\partial c(\boldsymbol{x}_0^{\mathrm{e}},t)}{\partial x_i}(x_i' - x_{i,0}^{\mathrm{e}}) + \frac{1}{2}\,\frac{\partial^2 c(\boldsymbol{x}_0^{\mathrm{e}},t)}{\partial x_i^2}(x_i' - x_{i,0}^{\mathrm{e}})^2\right] + \ldots$$

and the concentration gradient

$$\frac{\partial c(\boldsymbol{x}',t)}{\partial x_i}\Big|_{\boldsymbol{x}_0^{\mathrm{e}}} = \frac{\partial c(\boldsymbol{x}_0^{\mathrm{e}},t)}{\partial x_i} + \frac{\partial^2 c(\boldsymbol{x}_0^{\mathrm{e}},t)}{\partial x_i^2}\,(x_i' - x_{i,0}^{\mathrm{e}}) + \ldots \quad (3.21)$$

can also be formulated as a Taylor series evaluated at the center of the electrolyte phase. All terms are linear within the REV if higher order terms are neglected which is the standard approach for the volume averaging method as stated in Bear and Bachmat [23, p. 28]. This approximation is sufficiently accurate as long as the size of REV is adequate with respect to arising concentration gradients. Using the linearized diffusion coefficient $D_{\pm}(c(\boldsymbol{x}',t))|_{\boldsymbol{x}_0^{\mathrm{e}}}$ and concentration gradient $\frac{\partial c(\boldsymbol{x}',t)}{\partial x_i}\Big|_{\boldsymbol{x}_0^{\mathrm{e}}}$ as basis for the volumetric intrinsic phase average of the diffusion coefficient $\overline{D_{\pm}(c)}^{\mathrm{e}}$, it is possible to write

$$\overline{D_{\pm}(c)}^{\mathrm{e}} = \frac{1}{V^{\mathrm{e}}}\int_{\Omega^{\mathrm{e}}}\left(D_{\pm}(c(\boldsymbol{x}_0^{\mathrm{e}},t)) + \sum_{i=1}^{3}\left[\frac{\partial D_{\pm}(c(\boldsymbol{x}_0^{\mathrm{e}},t))}{\partial c(\boldsymbol{x}_0^{\mathrm{e}},t)}\,\frac{\partial c(\boldsymbol{x}_0^{\mathrm{e}},t)}{\partial x_i}(x_i' - x_{i,0}^{\mathrm{e}})\right]\right)\mathrm{d}\,V,$$

where terms including $(x_i' - x_{i,0}^{\mathrm{e}})^2$ are also neglected. This can be reformulated to

$$\overline{D_{\pm}(c)}^{\mathrm{e}} = \frac{1}{V^{\mathrm{e}}}\int_{\Omega^{\mathrm{e}}} D_{\pm}(c(\boldsymbol{x}_0^{\mathrm{e}},t))\,\mathrm{d}\,V + \\ \sum_{i=1}^{3}\left[\frac{\partial D_{\pm}(c(\boldsymbol{x}_0^{\mathrm{e}},t))}{\partial c(\boldsymbol{x}_0^{\mathrm{e}},t)}\,\frac{\partial c(\boldsymbol{x}_0^{\mathrm{e}},t)}{\partial x_i}\,\frac{1}{V^{\mathrm{e}}}\underbrace{\int_{\Omega^{\mathrm{e}}}(x_i' - x_{i,0}^{\mathrm{e}})\,\mathrm{d}\,V}_{\Upsilon}\right],$$

where the integral Υ is approximately zero if the center $\boldsymbol{x}_0$ of the REV is on the same position as the center $\boldsymbol{x}_0^{\mathrm{e}}$ of the electrolyte phase within the REV as indicated in Fig. 3.1. This condition is approximately fulfilled if the electrolyte phase is equivalently distributed over the REV. As a result, the volumetric intrinsic phase average of the diffusion coefficient at the point $\boldsymbol{x}$ of the macroscopic domain Ω is equivalent to the diffusion coefficient at the center of the electrolyte

phase of the respective REV

$$\overline{D_{\pm}(c)}^{\mathrm{e}} \approx \frac{1}{V^{\mathrm{e}}} \int_{\Omega^{\mathrm{e}}} D_{\pm}(c(\boldsymbol{x}_0^{\mathrm{e}}, t))\, \mathrm{d}\, V = D_{\pm}(c(\boldsymbol{x}_0^{\mathrm{e}}, t)) = D_{\pm}(c). \tag{3.22}$$

As long as both conditions, the linear fields within a REV and $\boldsymbol{x}_0^{\mathrm{e}} = \boldsymbol{x}_0$, are fulfilled exactly, Equ. (3.22) is not just an approximation but also exact. The deviation from the volumetric intrinsic phase average of the diffusion coefficient is defined as

$$\hat{D}_{\pm}(c) = D_{\pm}(c) - \overline{D_{\pm}(c)}^{\mathrm{e}},$$

which gives in the context of linear approximations for the diffusion coefficient and the concentration field

$$\hat{D}_{\pm}(c) = \sum_{i=1}^{3} \left[\frac{\partial D_{\pm}(c(\boldsymbol{x}_0^{\mathrm{e}}, t))}{\partial c(\boldsymbol{x}_0^{\mathrm{e}}, t)} \frac{\partial c(\boldsymbol{x}_0^{\mathrm{e}}, t)}{\partial x_i} (x_i' - x_{i,0}^{\mathrm{e}}) \right]. \tag{3.23}$$

This term is also a measure for the accuracy of the linear approximation if the real diffusion coefficient $D_{\pm}(c)$ is used instead of the linearized diffusion coefficient. Equivalently, the deviation from the volumetric intrinsic phase average of the concentration gradient can be written as

$$\widehat{\frac{\partial c}{\partial x_i}} = \sum_{i=1}^{3} \frac{\partial^2 c(\boldsymbol{x}_0^{\mathrm{e}}, t)}{\partial x_i^2} (x_i' - x_{i,0}^{\mathrm{e}}). \tag{3.24}$$

As a result of Equ. (3.23) and Equ. (3.24), the term

$$\overline{\hat{D}_{\pm}(c)\, \widehat{\frac{\partial c}{\partial x_i}}}^{\mathrm{e}} = \frac{1}{V^{\mathrm{e}}} \int_{\Omega^{\mathrm{e}}} \left(\hat{D}_{\pm}(c) \widehat{\frac{\partial c}{\partial x_i}} \right) \mathrm{d}\, V \approx 0 \tag{3.25}$$

can be neglected as a result of the product $(x_i' - x_{i,0}^{\mathrm{e}})(x_j' - x_{j,0}^{\mathrm{e}})$ being small. Therefore, it is valid to write

$$\overline{D_{\pm}(c)\, \frac{\partial c}{\partial x_i}}^{\mathrm{e}} = D_{\pm}(c)\, \overline{\frac{\partial c}{\partial x_i}}^{\mathrm{e}},$$

if the concentration field and the connected diffusion coefficient can be approximated linearly inside the REV with a sufficient accuracy and if the electrolyte phase is equivalently distributed over the REV resulting in

$$\boldsymbol{x}_0^{\mathrm{e}} = \boldsymbol{x}_0. \tag{3.26}$$

Note, that the first condition is fulfilled best for small REV, whereas the REV has to be sufficiently large for the volume averaging in order to be representative. It is possible that both requirements cannot be satisfied simultaneously.

The same approach can also be used for the remaining concentration dependent transport parameters present in Equ. (3.12) and Equ. (3.13). Therefore, it is generally valid to approximate the volumetric intrinsic phase average of the transport parameters by their value at the volumetric center of the REV $\boldsymbol{x}_0^{\mathrm{e}}$ without neglecting substantial effects. This also means that it is valid to approximated the transport parameters within a REV as constant for certain condition and variable on the macroscale. However, this also means that partial differential equation given in Equ. (3.14) used for the derivation of Equ. (3.17) is still an approximation.

3.2.3 Variable transport parameter on micro- and macroscale

Here, the derivation of Bear and Bachmat [23] is extended to multi-field problems with variable transport parameters such as the considered ion-transport problem. The volumetric coupling of two fields is discussed briefly in the section 'coupled fluxes' in Bear and Bachmat [23, chap. 2.6.6]. The derivation is shown exemplarily for the current equation given in Equ. (3.11) in combination with the charge conservation given in Equ. (3.13). After some reformulations, the same framework can also be applied for the fluxes given in Equ. (3.12) in combination with mass conservation given in Equ. (3.13).

As demonstrated in section B, the same approach as in Bear and Bachmat [23] can be used to derived the following averaging rule:

$$\overline{a(c)\frac{\partial c}{\partial x_j}}^{\mathrm{e}} - \overline{\kappa(c)\frac{\partial \Phi}{\partial x_j}}^{\mathrm{e}} = \frac{\Xi^{\mathrm{e,s}}}{\varepsilon}\widetilde{\hat{x}_j i_i n_i}^{\mathrm{e,s}} + T^*_{ji}\left(\widetilde{a(c)\frac{\partial c}{\partial x_i}}^{\mathrm{e,e}} - \widetilde{\kappa(c)\frac{\partial \Phi}{\partial x_i}}^{\mathrm{e,e}}\right). \tag{3.27}$$

Compared to Equ. (3.17), the areal intrinsic phase average on $\Gamma^{\mathrm{e,e}}$ is not yet converted to a volumetric intrinsic phase average. In addition, the conservation law in form of

$$\frac{\partial}{\partial x_i}\left(a(c)\frac{\partial c}{\partial x_i} - \kappa(c)\frac{\partial \Phi}{\partial x_i}\right) = 0,$$

is used at the microscopic level within the REV which is a more general formulation than Equ. (3.17) since the volumetric coupling between the concentration and the potential field as well as concentration dependent transport parameters within the REV are considered. If the transport parameters are constant within the entire macroscopic domain, the approximation given in Equ. (3.17) can be used to simplify Equ. (3.27)

$$a\overline{\frac{\partial c}{\partial x_j}}^{\mathrm{e}} - \kappa\overline{\frac{\partial \Phi}{\partial x_j}}^{\mathrm{e}} = \frac{\Xi^{\mathrm{e,s}}}{\varepsilon}\widetilde{\hat{x}_j i_i n_i}^{\mathrm{e,s}} + T^*_{ji}\left(a\frac{\partial \bar{c}^{\mathrm{e}}}{\partial x_i} - \kappa\frac{\partial \overline{\Phi}^{\mathrm{e}}}{\partial x_i}\right), \tag{3.28}$$

which has the same form as the averaging rule for a single field given in Equ. (3.17). This demonstrates that the averaging rules are generally applicable to multi-field problems. However, the general problem of concentration dependent transport parameters is still not solved yet.

In the following, an argumentation is presented which allows to convert the surface integral to a volume integral and to extract the spatial derivative from inside the integral. It is demon-

strated based on the areal intrinsic phase average of the concentration term $\widetilde{a(c)\frac{\partial c}{\partial x_i}}^{\mathrm{e,e}}$. Both quantities can be written as their volumetric intrinsic phase averages and their derivations evaluated only along the boundary $\Gamma^{\mathrm{e,e}}$

$$a(c)\Big|_{\Gamma^{\mathrm{e,e}}} = \overline{a(c)}^{\mathrm{e}} + \widehat{a(c)}^{\mathrm{e}}\Big|_{\Gamma^{\mathrm{e,e}}},$$
$$\frac{\partial c}{\partial x_i}\Big|_{\Gamma^{\mathrm{e,e}}} = \overline{\frac{\partial c}{\partial x_i}}^{\mathrm{e}} + \widehat{\frac{\partial c}{\partial x_i}}^{\mathrm{e}}\Big|_{\Gamma^{\mathrm{e,e}}}.$$

Both relation can be inserted in the areal intrinsic phase average of the concentration term in Equ. (3.28), which gives

$$\begin{aligned}
\widetilde{a(c)\frac{\partial c}{\partial x_i}}^{\mathrm{e,e}} =& \frac{1}{A^{\mathrm{e,e}}}\int_{\Gamma^{\mathrm{e,e}}}\left(a(c)\Big|_{\Gamma^{\mathrm{e,e}}}\frac{\partial c}{\partial x_i}\Big|_{\Gamma^{\mathrm{e,e}}}\right)\mathrm{d}\,A \\
=& \overline{a(c)}^{\mathrm{e}}\,\overline{\frac{\partial c}{\partial x_i}}^{\mathrm{e}}\,\frac{1}{A^{\mathrm{e,e}}}\int_{\Gamma^{\mathrm{e,e}}}\mathrm{d}\,A + \overline{\frac{\partial c}{\partial x_i}}^{\mathrm{e}}\,\frac{1}{A^{\mathrm{e,e}}}\int_{\Gamma^{\mathrm{e,s}}}\widehat{a(c)}^{\mathrm{e}}\Big|_{\Gamma^{\mathrm{e,e}}}\mathrm{d}\,A + \\
& \overline{a(c)}^{\mathrm{e}}\,\frac{1}{A^{\mathrm{e,e}}}\int_{\Gamma^{\mathrm{e,e}}}\widehat{\frac{\partial c}{\partial x_i}}^{\mathrm{e}}\Big|_{\Gamma^{\mathrm{e,e}}}\mathrm{d}\,A + \frac{1}{A^{\mathrm{e,e}}}\int_{\Gamma^{\mathrm{e,e}}}\widehat{a(c)}^{\mathrm{e}}\Big|_{\Gamma^{\mathrm{e,e}}}\widehat{\frac{\partial c}{\partial x_i}}^{\mathrm{e}}\Big|_{\Gamma^{\mathrm{e,e}}}\mathrm{d}\,A. \qquad (3.29)
\end{aligned}$$

At this point, all terms including the deviation from the volumetric intrinsic phase average are neglected which results in the following approximation

$$\widetilde{a(c)\frac{\partial c}{\partial x_i}}^{\mathrm{e,e}} \approx \overline{a(c)}^{\mathrm{e}}\,\overline{\frac{\partial c}{\partial x_i}}^{\mathrm{e}}, \qquad (3.30)$$

where

$$\frac{1}{A^{\mathrm{e,e}}}\int_{\Gamma^{\mathrm{e,e}}}\mathrm{d}\,A = 1.$$

The approximation given in Equ. (3.30) simply states that the areal intrinsic phase average of the current flow as a result of a concentration gradient is the same as the current flow resulting from the volumetric intrinsic phase average of the transport parameter $a(c)$ and of the concentration gradient. Assuming constant transport parameters, this approximation is the same as the first approximation in Equ. (3.16). This approximation can also be motivated by the first order Taylor series for transport parameters as well as for concentration and potential gradients within a REV. This approach is comparable to the diffusion coefficient and the concentration gradient given in Equ. (3.20) and Equ. (3.21), respectively. Following the approach presented earlier, the deviations from the volumetric intrinsic phase average can be formulated accordingly to Equ. (3.23) and Equ. (3.24). In this case, the fourth term on rhs of Equ. (3.29) is negligible small due to the

product between $(x_i' - \overset{\mathrm{e}}{x}_{i,0})(x_j' - \overset{\mathrm{e}}{x}_{j,0})$. The second term can be written as

$$\begin{aligned}\overline{\frac{\partial c}{\partial x_i}}^{\mathrm{e}} \frac{1}{A^{\mathrm{e,e}}} \int_{\Gamma^{\mathrm{e,e}}} \widehat{a(c)}^{\mathrm{e}} \Big|_{\Gamma^{\mathrm{e,e}}} \mathrm{d}\, A &= \overline{\frac{\partial c}{\partial x_i}}^{\mathrm{e}} \frac{1}{A^{\mathrm{e,e}}} \int_{\Gamma^{\mathrm{e,e}}} \sum_i^3 \left[\frac{\partial a(c(\overset{\mathrm{e}}{x}_{i,0}, t))}{\partial c(\overset{\mathrm{e}}{x}_{i,0}, t)} \frac{\partial c(\overset{\mathrm{e}}{x}_{i,0}, t)}{\partial x_i} (x_i' - \overset{\mathrm{e}}{x}_{i,0}) \right] \mathrm{d}\, A \\ &= \overline{\frac{\partial c}{\partial x_i}}^{\mathrm{e}} \frac{1}{A^{\mathrm{e,e}}} \sum_i^3 \left[\frac{\partial a(c(\overset{\mathrm{e}}{x}_{i,0}, t))}{\partial c(\overset{\mathrm{e}}{x}_{i,0}, t)} \frac{\partial c(\overset{\mathrm{e}}{x}_{i,0}, t)}{\partial x_i} \underbrace{\int_{\Gamma^{\mathrm{e,e}}} (x_i' - \overset{\mathrm{e}}{x}_{i,0}) \mathrm{d}\, A}_{\approx 0} \right].\end{aligned}$$

The surface integral over $\Gamma^{\mathrm{e,e}}$ of the spherical REV can be approximated by zero as long as the areal center $\boldsymbol{x}_0^{\mathrm{A}}$ of the outer electrolyte surface of the REV is the same as the volumetric center $\overset{\mathrm{e}}{\boldsymbol{x}}_0$ of electrolyte phase and as the volumetric center $\boldsymbol{x}_0$ of the REV:

$$\boldsymbol{x}_0^{\mathrm{A}} = \overset{\mathrm{e}}{\boldsymbol{x}}_0 = \boldsymbol{x}_0. \tag{3.31}$$

This condition is fulfilled for an electrolyte phase which is distributed equivalently over the REV. The same argumentation can also be used for the third term of Equ. (3.29). Note that the third term would also be present for problems with constant transport parameters. Therefore, the equivalent conditions are required for the original approximation given in Equ. (3.16). As a result, the approximation postulated in Equ. (3.30) is valid for the presented conditions.

As long as the approximation Equ. (3.30) is valid, it is possible to write the volumetric intrinsic phase average of the concentration gradient as

$$\overline{\frac{\partial c}{\partial x_i}}^{\mathrm{e}} = \frac{\partial \bar{c}^{\mathrm{e}}}{\partial x_i}, \tag{3.32}$$

since the areal intrinsic phase average of the gradient at $\Gamma^{\mathrm{e,e}}$ is equivalent to the volumetric intrinsic phase average of the gradient at $\Gamma^{\mathrm{e,e}}$. This means, that the volumetric intrinsic phase average of the gradient is constant over the entire REV and it is possible to extract the spatial derivative from the integral. This can also be demonstrated if the linear approximation of the concentration and concentration gradient is used in the respective definitions:

$$\begin{aligned}\frac{\partial \bar{c}^{\mathrm{e}}}{\partial x_i} =& \frac{\partial}{\partial x_i} \left[\frac{1}{V^{\mathrm{e}}} \int_{\Omega^{\mathrm{e}}} c \,\mathrm{d}\, V \right] \\ =& \frac{\partial}{\partial x_i} \left[\frac{1}{V^{\mathrm{e}}} \int_{\Omega^{\mathrm{e}}} c(\boldsymbol{x}_0', t) + \sum_i^3 \left[\frac{\partial c(\overset{\mathrm{e}}{\boldsymbol{x}}_0, t)}{\partial x_i} (x_i' - \overset{\mathrm{e}}{x}_{i,0}) \right] \mathrm{d}\, V \right] \\ =& \frac{\partial}{\partial x_i} \left[\frac{1}{V^{\mathrm{e}}} \int_{\Omega^{\mathrm{e}}} c(\boldsymbol{x}_0', t) \,\mathrm{d}\, V \right] = \frac{\partial c(\boldsymbol{x}_0', t)}{\partial x_i}\end{aligned}$$

and

$$\overline{\frac{\partial c}{\partial x_i}}^{\mathrm{e}} = \frac{1}{V^{\mathrm{e}}} \int_{\Omega^{\mathrm{e}}} \frac{\partial c}{\partial x_i} \mathrm{d}\, V = \frac{\partial c(\boldsymbol{x}_0', t)}{\partial x_i}.$$

For both reformulations, it is assumed like before that the areal center of the outer electrolyte surface of the REV is the same as the volumetric center of electrolyte volume. As a result, Equ. (3.27) can be written as

$$\overline{a(c)\frac{\partial c}{\partial x_j}}^{\mathrm{e}} - \overline{\kappa(c)\frac{\partial \Phi}{\partial x_j}}^{\mathrm{e}} = \frac{\Xi}{\varepsilon}^{\mathrm{e,s}}\widetilde{\hat{x}_j i_i n_i}^{\mathrm{e,s}} + T^*_{ji}\, a(c)\frac{\partial \bar{c}^{\mathrm{e}}}{\partial x_i} - T^*_{ji}\,\kappa(c)\frac{\partial \overline{\Phi}^{\mathrm{e}}}{\partial x_i}, \tag{3.33}$$

where Equ. (3.30) and Equ. (3.32) are used. In addition, the volumetric intrinsic average of the transport parameters is replaced by the value at the center of the respective REV as demonstrated in Equ. (3.22) for the diffusion coefficient. Compared to the original derivation giving Equ. (3.17), the transport parameters do not have to be constant within the REV. Instead, it is required that the areal center of the outer electrolyte surface of the REV is the same as the volumetric center of the REV as indicated in Equ. (3.31). However, the original approximation also requires the same conditions as explained before. Unfortunately, there is not justification for the approximation given in Equ. (3.15) which is also used in this derivation.

3.3 Summary

In this section, the theoretical derivation of the volume averaging method is shown for multi-field problems with variable transport parameters. Two different approaches are presented where the following conditions have to be fulfilled:

- The primary fields as well as the connected transport parameters can be approximated linearly within the REV with a sufficient accuracy. This is also one of the basic requirements for volume averaging method, in general.
- The volumetric center $\boldsymbol{x}_0$ of the REV has to be equal to the volumetric center $\boldsymbol{x}_0^{\mathrm{e}}$ of the electrolyte phase within the REV and to the areal center $\boldsymbol{x}_0^{\mathrm{A}}$ of the outer surface of the electrolyte phase.
- The splitting of the integral into two integrals given in Equ. (3.15) has to be valid.

In section section 3.2.2, the assumption of constant transport parameters within a REV is motivated. For this purpose, condition Equ. (3.26) would be enough but the approximation given in Equ. (3.16) requires Equ. (3.31) as a condition. The second approach is presented in section 3.2.3. In this approach, it is not required anymore that the transport parameters are constant within the REV. Therefore, it is the most general approach.

Note, that the linear approximation within a REV is fulfilled best for small REV, whereas the REV has to be sufficiently large for the volume averaging in order to be representative.

Homogenized ion-transport equations for separators Based on the framework presented in section 3.1, the ion-transport equations given in Equ. (2.72)–Equ. (2.74) can be written as

$$\varepsilon \frac{\partial \overline{c}^{\,\mathrm{e}}}{\partial t} + \nabla \cdot \Big[-\varepsilon\, T^*_{ji}\, D_{\pm}(c)\, \nabla \overline{c}^{\,\mathrm{e}} + \frac{t_+(c)}{\nu_+ z_+ F}\, \overline{\boldsymbol{i}} \Big] = 0 \tag{3.34}$$

$$\overline{\boldsymbol{i}} = -\varepsilon\, T^*_{ji}\, \kappa(c) \nabla \overline{\Phi}^{\,\mathrm{e}} + \frac{RT}{z_+ F}\, \frac{\nu}{\nu_+} \varepsilon\, T^*_{ji}\, \kappa(c) \left[1 + \frac{\mathrm{d} \ln f_{\pm}(c)}{\mathrm{d} \ln c} \right] (1 - t_+(c))\, \frac{1}{c} \nabla \overline{c}^{\,\mathrm{e}} \tag{3.35}$$

$$\nabla \cdot \overline{\boldsymbol{i}} = 0. \tag{3.36}$$

Since a separator consists only of non-reactive surfaces, additional terms resulting from the volume averaging approach does not have to be considered in the macroscopic conservation laws.

Homogenized ion-transport equations for electrodes The ion-transport equations for an electrolyte solution shown in Equ. (2.72)–Equ. (2.74) can also be written as

$$\frac{\partial \varepsilon \overline{c}^{\,\mathrm{e}}}{\partial t} + \nabla \cdot \Big[-\varepsilon\, T^*_{ji}\, D_{\pm}(c)\, \nabla \overline{c}^{\,\mathrm{e}} + \frac{\overline{t}_+(c)}{\nu_+ z_+ F}\, \overline{\boldsymbol{i}} \Big] + \Xi^{\mathrm{e,s}} \widetilde{(\boldsymbol{N} \cdot \boldsymbol{n})}^{\,\mathrm{e,s}} = 0 \tag{3.37}$$

$$\overline{\boldsymbol{i}} = -\varepsilon\, T^*_{ji}\, \kappa(c) \nabla \overline{\Phi}^{\,\mathrm{e}} + \frac{RT}{z_+ F}\, \frac{\nu}{\nu_+} \varepsilon\, T^*_{ji}\, \kappa(c) \left[1 + \frac{\mathrm{d} \ln f_{\pm}(c)}{\mathrm{d} \ln c} \right] (1 - t_+(c))\, \frac{1}{c} \nabla \overline{c}^{\,\mathrm{e}} \tag{3.38}$$

$$\nabla \cdot \left(\varepsilon\, \overline{\boldsymbol{i}}^{\,\mathrm{e}} \right) + \Xi^{\mathrm{e,s}} \widetilde{(\boldsymbol{i} \cdot \boldsymbol{n})}^{\,\mathrm{e,s}} = 0. \tag{3.39}$$

where reactive-surface reactions are included in volume averaging approach. If the additional surface term resulting from the volume averaging method (see Equ. (3.17) and Equ. (3.33)) can be neglected, the ordinary ion-transport equation for porous electrodes are obtained. If it is justified to neglect the term resulting from the volume averaging method, has to be considered in a separate project since the focus of this contribution is not on the modeling of electrodes but on the determination of transport parameters.

In the literature, the mass conservation is usually formulated differently. For that reason, Equ. (3.37) is reformulated by Equ. (3.39) giving well-known formulation for electrodes

$$\frac{\partial \varepsilon \overline{c}^{\,\mathrm{e}}}{\partial t} - \nabla \cdot \Big[\varepsilon\, T^*_{ji}\, D_{\pm}(c)\, \nabla \overline{c}^{\,\mathrm{e}} \Big] + \frac{\nabla t_+(c) \cdot \overline{\boldsymbol{i}}}{\nu_+ z_+ F} - \frac{(1 - t_+(c))}{\nu_+ z_+ F} \nabla \cdot \overline{\boldsymbol{i}} = 0.$$

4 Geometrical parameters for homogenized porous media

4.1 Overview of geometrical parameters used in the literature

The volume averaging approach for porous media introduced in section 3 is a macroscopic description of a porous medium where the influence of the microstructure is modeled by additional geometrical parameters, namely the porosity ε and the geometry coefficient T_{ji}^*. The porosity ε is a well-defined property of a porous medium, which can be determined easily in experiments. In contrast, the geometry coefficient T_{ji}^* is based on a non-intuitive mathematical derivation. Therefore, it is quite natural that many different definitions and methods were introduced over the years equipping the geometry coefficient T_{ji}^* with a more intuitive geometrical or experimental interpretation. This interpretation is strongly influenced by the application, e.g., fluid flow or scalar transport in porous media. It is exactly this large variety of different definitions and methods which makes it so difficult to compare different tortuosities available in the literature with each other. In the following, the most important definitions used in battery applications are introduced. In addition, a comprehensive overview of the recent research in this field is provided. The result presented in this section are also published partly in Landesfeind et al. [97].

As explained in Holzer et al. [82], the effect of a porous microstructure on the macroscopic conservation laws can be described by the relative conductivity

$$\sigma_{\mathrm{R}} = \frac{\kappa_{\mathrm{eff}}}{\kappa}, \tag{4.1}$$

which relates the effective conductivity κ_{eff} as a macroscopic property of the porous medium to the electrolyte conductivity κ, as indicated in Fig. 4.1(a) and Fig. 4.1(b). The conductivity is the natural choice for this description since it can be determined easily by experiments. However, the conductivity κ and the diffusion coefficient $D_{\pm}$ are exchangeable, as pointed out in Holzer et al. [82, p. 2936], as long as both transport mechanisms are influenced by the same microstructure parameters. This assumption is quite credible since both the conductivity and the diffusion coefficient are based on the mobility of the ionic species. The MacMullin number N_{M} as defined, e.g., in Patel et al. [119] is the reciprocal of the relative conductivity

$$N_{\mathrm{M}} = \frac{1}{\sigma_{\mathrm{R}}} = \frac{\kappa}{\kappa_{\mathrm{eff}}}.$$

Sometimes, the MacMullin number is called the formation factor as, e.g., in Holzer et al. [82]. The relative conductivity or the MacMullin number are the basis for many empirical laws intending to describe the influence of the microstructure on the macroscopic conservation laws in

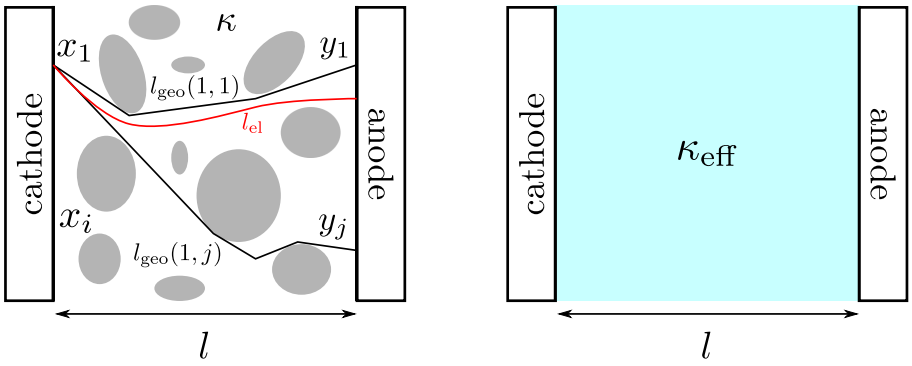

(a) Microscopic perspective. (b) Macroscopic perspective.

Figure 4.1: Microscopic and macroscopic perspectives of a porous medium including various definitions for the path length as well as the conductivity κ and the effective conductivity κ_{eff}.

terms of the porosity ε and additional parameters. One of the most famous empirical laws was introduced by Archie [6]:

$$\sigma_{\text{R}} = \varepsilon^{\alpha}, \tag{4.2}$$

where a power law relationship with exponent α between the porosity ε of sandstone and the specific conductivity σ_{R} is used. Other empirical laws are given, e.g., in the review by Shen and Chen [133] or in Barrande et al. [15]. As mentioned in Holzer et al. [82, p. 2936], these empirical laws hold "*only for a series of samples from the same geological formation, because these rocks have similar microstructures*". For a different type of microstructure, the exponent α may be quite different. Therefore, Archie's law is rarely used in battery applications where different various porous materials with a varying porosities do not exhibit similar microstructures. Exceptions are very porous materials such as glass fiber separators which can be easily compressed without changing the basic features of the microstructure as done, e.g., in Nyman et al. [115]. Another exception may be the compression of self-made electrodes.

The effective conductivity as well as the associated empirical laws are based on a macroscopic perspective of the porous medium. In contrast, it is also possible to use a microscopic perspective for the description of the porous microstructure. In this case, the tortuosity is introduced as a measure for the elongation of the transport path due to the porous structure with respect to a straight line. In the publication 'Tortuosity: a guide through the maze' by Clennell [45], it is pointed out that the "*tortuosity has no simple or universal definition: different measures of tortuosity are employed by geologist, engineers and chemists to describe the resistive and retarding effects of the pore structure on a range of conduction, advection and diffusion processes*" (Clennell [45, p. 299]). For example, the path length tortuosity

$$\tau_{\text{path}} = \frac{l_{\text{path}}}{l}$$

is defined for a single channel with a constant cross sectional area as depicted in Fig. 3.2. As shown in section 3.2, this tortuosity definition can be related to the geometry coefficient T^*_{ji} and

therefore provides a geometrical interpretation of the geometry coefficient. The tortuosity can also be defined with respect to a physically motivated length definition. For instance, the path length of the electric tortuosity $\tau_{\text{el}} = \frac{l_{\text{el}}}{l}$ is based on the gradient of the electrostatic potential Φ. A similar concept is used for the hydraulic tortuosity τ_{hyd} where streamlines are used as path length. Finally, the geometrical tortuosity

$$\tau_{\text{geo}} = \frac{l_{\text{geo}}}{l} \tag{4.3}$$

is defined as the length of the shortest connection path between two points $\boldsymbol{x}_1$ and $\boldsymbol{y}_1$ through the void volume of a porous medium with respect to the length of the straight connection line between these points. As depicted in Fig. 4.1(a), the geometrical tortuosity τ_{geo} and the physically motivated tortuosity τ_{el}.

Until a few years ago, all tortuosity values derived from the microscopic perspective were usually based on simplified geometries such as channel networks or regular porous structures consisting, e.g., of agglomerated spheres (see, e.g., Wyllie and Rose [154], Cornell and Katz [47] or Zalc et al. [159]). The availability of realistic, three-dimensional representations of porous structures provided by improved imaging technologies gives completely new opportunities for the characterization of the microstructure. In this context, the geometrical tortuosity τ_{geo} is usually replaced by the mean geometrical tortuosity $\overline{\tau}_{\text{geo}}$ as explained, e.g., in Wiedenmann et al. [150]. The mean geometrical tortuosity is based on an averaged value of the length $l_{\text{geo}}(i,j)$ between two points $\boldsymbol{x}_i$ and $\boldsymbol{y}_j$ and is usually determined by numerical algorithms utilizing, e.g., the random walk theory as in Tariq et al. [138] or the graph theory as in Wiedenmann et al. [150]. It should be noted that these numerical algorithms do not include any physically motivated simulations. All these tortuosity definitions consider only the elongation of the transport path, but do not include additional factors such as non-constant cross sectional areas or the structure of the surface. Therefore, the constriction factor β is sometimes introduced to account for a non-constant cross sectional area. The concept of the constriction factor and its theoretical motivation is explained, e.g., in Holzer et al. [82]. The final goal of this approach is an educated geometrical description of the porous structure which fulfills, e.g., the relation

$$\sigma_{\text{R}} \equiv \frac{\varepsilon\beta}{\overline{\tau}_{\text{geo}}}.$$

The big advantage of this approach is that it is based on a pure geometrical description of the microstructure, especially in combination with the imaging technologies used nowadays. Additionally, a basic understanding of porous structures is generated which can be used for the design of future porous materials. Although the geometrical tortuosity is independent of physically motivated transport schemes and experimental factors, it is of course influenced by the exact definition of the mean geometrical tortuosity $\overline{\tau}_{\text{geo}}$ and the numerical algorithms employed to determine it. More importantly, the limited size of the reconstructed sample has to be considered as a potential uncertainty. The sample has to be large enough to be representative as it was observed, e.g., by Cooper et al. [46].

By now, a macroscopic and a microscopic perspective for the determination of geometrical parameters are introduced. Theoretically, it is also possible to apply the microscopic concept

of tortuosity to the macroscopic description of a porous medium. The basic equation for this approach is

$$\sigma_{\mathrm{R}} = \frac{\varepsilon}{\tau}, \tag{4.4}$$

where the tortuosity τ is determined via experiments. In this case, the tortuosity τ does not only describe the elongation of the transport path, but also includes all other effects such as variable cross sectional areas, specific surface structures and so on. The incorporation of all geometrically effects into the tortuosity τ is the main advantage of this approach. However, this is also the main disadvantage since the tortuosity may not include only geometrical information, but also experimental artifacts. As emphasized, e.g., in Holzer et al. [82], it is important to distinguish strictly between the tortuosity τ and the geometrical tortuosity τ_{geo} since they are based on different definitions. The limited sample size is usually not a problem since the complete porous medium is used for the experimental determination of the tortuosity τ. At this point, it is important to mention that the tortuosity τ in Equ. (4.4) appears sometimes as τ^2 which is the result of different assumptions as discussed, e.g., in Clennell [45] or Djian et al. [50]. Based on the principle given in Equ. (4.4), the tortuosity of a three-dimensional sample reconstructed from imaging techniques is often determined by physically motivated numerical simulations as shown, e.g., in Ender et al. [60], Joos et al. [88], Cooper et al. [46] or in Roth et al. [127].

The last important definition which is frequently used in battery applications results from the combination of Equ. (4.2) and Equ. (4.4):

$$\tau = \varepsilon^{1-\alpha}.$$

A mathematical derivation of the well-known Bruggemann relation with $\alpha = 1.5$ can be found in Bruggeman [33]. In this case, the tortuosity τ becomes

$$\tau = \frac{1}{\sqrt{\varepsilon}}.$$

The validity of this relation is investigated experimentally and numerically in, e.g., Chung et al. [42], Patel et al. [119] and Thorat et al. [140].

As a result of the huge variety of available definitions of the tortuosity, it is important to consider not only the value of the tortuosity, but also the underlying definition and experimental procedure.

4.2 An experimentally motivated approach for the definition of geometrical parameters

As already indicated in section 4.1, there are many different approaches involving different geometrical parameters to describe the influence of a porous microstructure on the macroscopic conservation laws. In this manuscript, the most popular approach based on Equ. (4.4) is introduced and embedded in the theoretical volume averaging framework derived in section 3.

In Equ. (3.34) – Equ. (3.36), the influence of the microstructure on the macroscopic conservation laws is described by the porosity ε and the theoretically motivated geometry coefficient T_{ji}^* defined in Equ. (3.18). Although a geometrical interpretation of the geometry coefficient is possible under certain assumptions (see section 3.2), it is not very practical to describe the behavior of realistic porous geometries with varying cross sectional areas and complex surface structures by the geometry coefficient T_{ji}^*. Therefore, the geometry coefficient is replaced by an experimentally motivated, isotropic interpretation, the so-called tortuosity τ:

$$T_{ji}^* := \begin{cases} 1/\tau & \text{for } i = j, \\ 0 & \text{for } i \neq j. \end{cases} \tag{4.5}$$

As a result of this definition, the effective transport parameters, namely the effective conductivity κ_{eff} and the effective diffusion coefficient $D_{\pm,\text{eff}}$ as defined in section 3.3 are given as

$$\kappa_{\text{eff}} = \frac{\varepsilon}{\tau}\kappa, \tag{4.6}$$

$$D_{\pm,\text{eff}} = \frac{\varepsilon}{\tau}D_{\pm}, \tag{4.7}$$

where Equ. (4.6) is equivalent to Equ. (4.4) with Equ. (4.1). As a result of these definitions, the conservation laws given in Equ. (3.34) – Equ. (3.36) can be written as

$$\varepsilon\frac{\partial \overline{c}^{\,\text{e}}}{\partial t} + \nabla \cdot \Big[-\frac{\varepsilon}{\tau}D_{\pm}(c)\,\nabla\overline{c}^{\,\text{e}} + \frac{t_+(c)}{\nu_+ z_+ F}\,\overline{\boldsymbol{i}}\Big] = 0, \tag{4.8}$$

$$\overline{\boldsymbol{i}} = -\frac{\varepsilon}{\tau}\kappa(c)\nabla\overline{\Phi}^{\,\text{e}} + \frac{\nu}{z_+\nu_+}\,\frac{RT}{F}\,\frac{\varepsilon}{\tau}\kappa(c)\left[1 + \frac{\mathrm{d}\ln f_{\pm}(c)}{\mathrm{d}\ln c}\right](1 - t_+(c))\,\frac{1}{\overline{c}^{\,\text{e}}}\nabla\overline{c}^{\,\text{e}}, \tag{4.9}$$

$$\nabla \cdot \overline{\boldsymbol{i}} = 0. \tag{4.10}$$

At this point, the term 'experimentally motivated' becomes clearer since the tortuosity τ can be interpreted as the ratio of the electrolyte conductivity κ to the effective conductivity κ_{eff} or the diffusion coefficient $D_{\pm}$ to the effective diffusion coefficient $D_{\pm,\text{eff}}$ scaled by the porosity ε. This enables a direct experimental determination of the tortuosity τ with all advantages and disadvantages mentioned in section 4.1. Because of this, the tortuosity τ is more precisely called experimental tortuosity. Its experimental determination is based on the representation of the porous medium by a single ohmic resistance R_{el} between two parallel electrodes as depicted in Fig. 4.2:

$$R_{\text{el}} = \frac{1}{\kappa_{\text{eff}}}\,\frac{l}{A} = \frac{1}{\kappa}\,\frac{\tau}{\varepsilon}\,\frac{l}{A}. \tag{4.11}$$

Herein, l denotes the distance between the two electrodes and A the surface area of each electrode. It is important to emphasize that this zero-dimensional projection of the original three-dimensional domain is only valid for an ideal geometrical setup consisting of two parallel and aligned electrodes enclosed by isolators as shown in Fig. 4.2.

Although the basic idea is quite simple, its experimental realization turns out to be tricky since parasitic effects as a non-ideal geometrical configuration have a large influence on the

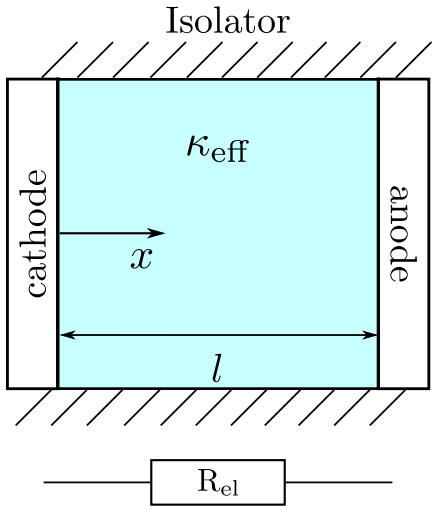

Figure 4.2: Idealized geometry and the corresponding equivalent serial circuit used for the determination of the tortuosity.

quality of the determined tortuosity τ. The most critical aspects are the evaporation of the solvent resulting in a non-constant conductivity κ and edge effects at the electrodes distorting the assumption of an ideal geometrical setup. Experimentally, the resistance R_{el} is determined by impedance spectroscopy which is described in detail, e.g., by Bard and Faulkner [14, chap. 10]. An in-depth explanation of the experimental setup and the employed methods can be found in Landesfeind et al. [97]. The tortuosity τ, the porosity ε and the thickness l of the commercial battery separator CG 2500 are summarized in Tab. 4.1.

For separators, this experimental method is without a real alternative since with current imaging technologies it is hardly possible to obtain high-quality images of porous separators made of non-conducting materials and exhibiting very fine pores. For electrodes, the experimental determination of the tortuosity τ is more challenging since the conducting matrix makes it difficult to determine an isolated resistance R_{el} of the electrolyte phase. In Landesfeind et al. [97], an alternative experimental method is presented to circumvent this problem.

Table 4.1: Geometrical parameters of the commercial battery separator CG 2500

	CG 2500
Thickness l [mm]	0.025
Porosity ε [-]	0.55
Tortuosity τ [-]	2.46 ± 0.16 [97]

5 Theoretical background for the experimental determination of ion-transport parameters

The mathematical model for binary electrolyte solutions presented in section 2 requires four different concentration dependent transport parameters, namely the conductivity $\kappa(c)$, the binary diffusion coefficient $D_{\pm}(c)$, the transference number $t_{+}(c)$ and the thermodynamic factor or the mean molar activity coefficient $f_{\pm}(c)$, respectively. The conductivity $\kappa(c)$ can be measured in a commercial conductivity cell. The determination of the remaining parameters is more elaborate. In the following, various experimental techniques for the determination of transport parameters in aprotic lithium based electrolytes are presented.

In literature, many different experimental methods are available to determine diffusion coefficients of electrolyte solutions and its components. The most popular methods are introduced in the following. In Castiglione et al. [38] or Capiglia et al. [36], pulsed-field gradient Nuclear Magnetic Resonance (NMR) is used to determine the self-diffusion coefficients of ions in an electrolyte solution. In Castiglione et al. [38], the diffusion coefficients of all ions in the ionic liquid LiTFSI:PYR_{14}TFSI (0.1:0.9, molar ratio) are determined whereas Capiglia et al. [36] investigates $LiPF_6$, $LiBF_4$ and $LiN(C_2F_5SO_2)_2$ in EC:EMC (2:8, vol. %). According to McNaught and Wilkinson [106], the self-diffusion coefficient describes the mobility of ionic species in the absence of an electrochemical potential gradient. A theoretical discussion of the experimental method is given in Price [123]. Another method is the Moir pattern technique which is used in Nishikawa et al. [114] to determine the binary diffusion coefficient $D_{\pm}$ of $LiClO_4$ in PC. This technique is based on the optical observation of the time-dependent relaxation of the concentration profile after two electrolyte solutions with different concentrations are connected. In Nishida et al. [113] the same technique is used for $LiPF_6$, LITFSI and $LiBF_4$ in PC.

The most popular method for the determination of concentration dependent binary diffusion coefficient $D_{\pm}$ is the restricted diffusion method introduced by Harned and French [79]. This method is based on the observation of the long-term relaxation behavior of an initial concentration profile. The applicability of the method for concentrated electrolyte solutions is demonstrated by Newman and Chapman [110] using the example of potassium chloride in water. The relaxation process can be observed by different methods. In Stewart and Newman [136], an optical device is used to record the relaxation of the concentration profile in $LiPF_6$ in EC:DEC (1:1, by weight) electrolyte solution. Alternatively, the relaxation of the concentration profile can be observed indirectly by the measured potential which is used, e.g., in Valøen and Reimers [142], Hiller et al. [81], Nyman et al. [115] or Thorat et al. [140]. In Hiller et al. [81], the concentration and temperature dependent diffusion coefficients of LiTFSI and LiBOB in polyethylene oxide based polymer electrolytes are determined by the long-term relaxation behavior of a re-

stricted diffusion experiment. In addition, the diffusion coefficients are also calculated based on the short-term relaxation behavior of steady-state concentration profiles. The diffusion coefficients determined by the two methods vary significantly. The restricted diffusion method is also used in Ma et al. [103], Doeff et al. [51] and Ferry et al. [62] for different polymer electrolytes. Based on different relaxation experiments, the diffusion coefficient of $LiClO_4$ polyethylene carbonate electrolyte solution soaked into a glass wool filter is determined by a numerical optimization method in Georén and Lindbergh [67]. The optimization is based on the physical model including solvent effects as introduced in Georén and Lindbergh [66] and Doyle et al. [55]. As usual convective effects are neglected. The tortuosity of the glass wool filter is determined by the Bruggeman relation. A similar approach including a more elaborate optimization framework is used in Nyman et al. [115] and Lundgren et al. [102] for $LiPF_6$ in EC:EMC (3:7, by weight) and in EC:DEC (1:1, by weight), respectively. In both publications, solvent effects and convective transport due to the motion of ions are included in the physical model used for the numerical optimization. The Bruggeman coefficient α of the used glass microfiber filters is determined experimentally. Note that the last six publications did not only determine the diffusion coefficients but the complete set of transport parameters. Recently, the influence of solvent effects on the determination of transport parameters is investigated numerically by Liu and Monroe [101]. In Xu and Farrington [155] the steady-state ion-transport-limited current at micro disc electrode in spherical diffusion geometry is used to determine the binary diffusion coefficient for 0.1 M $LiClO_4$ in PC. However, concentration dependent diffusion coefficients cannot be determined by this method since the limiting current is required. As a result, the concentration difference between micro electrode and bulk is equal to the initial concentration resulting in an averaged diffusion coefficient.

The direct determination of the activity coefficient is often based on measuring the osmotic pressure. For example, in Barthel et al. [16], the osmotic coefficient is determined based on the vapor pressure of lithium perchlorate $LiClO_4$ in various alcohols. The data for the osmotic coefficients are well represented by the Pitzer equation with seven parameters. Two of the parameters are based on experience, whereas the remaining parameters have to be determined by a regression model. The mean molal activity coefficient $\gamma_\pm$ is calculated from the osmotic coefficient by integration. In Barthel et al. [17], the same approach is used for aprotic electrolyte solutions such as $LiClO_4$ dissolved in dimethylcarbonate (DMC). In Stewart and Newman [135], the osmotic coefficient for lithium hexaflurophosphate $LiPF_6$ in Ethylene Carbonate (EC) is determined by melting point depression. However, this method may not be applicable to all solvent mixtures and the complete concentrations range since, according to the authors, it is limited by the eutectic point of the solvent mixture. Alternatively, the mean molar activity coefficient of $LiPF_6$ in EC:EMC (1:1, wt%) is determined based on experiments in a concentration cell assuming a constant transference number. In Valøen and Reimers [142], this approach is also used for $LiPF_6$ in PC:EC:EMC (10:27:63, vol%). In addition, the temperature dependence of the mean molar activity coefficient is determined in the range from 263 K – 333 K. The validity of a constant transference number is verified by experiments using the Hitdorf method and data available in literature. However, a theoretical explanation for the assumption of a constant transference number is missing in both contributions. In Nyman et al. [115], the diffusion coefficient, transference number and thermodynamic factor are determined for $LiPF_6$ in EC:EMC (3:7, wt%) by a numerical optimization approach, based on relaxation experiments in a polarization cell with a porous

separator in combination with data from a concentration cell. The numerical optimization algorithm is based on concentrated solution theory incorporating the solvent velocity into the mass balance. Recently, the temperature dependence of $LiPF_6$ dissolved in EC:DEC (1:1, wt%) was investigated by the same method by Lundgren et al. [102]. Binary diffusion coefficient, transference number and thermodynamic factor can also be determined in a set of three experimental setups. In this approach, the diffusion coefficient is measured by a galvanostatic relaxation experiment as presented, e.g., by Harned and French [79]. The concentration cell and a galvanostatic polarization experiment are then used to calculate the remaining two parameters Ma et al. [103].

The transference number $t_+(c)$ can be determined directly by the Hittorf method which is discussed for polymer electrolyte solutions, e.g., in Bruce et al. [32]. In Valøen and Reimers [142], the Hittorf method is also used for $LiPF_6$ in PC:EC:DMC (0.1:0.27:0.63, vol. %). However, in this publication, it is not anymore a direct method since it also depends on data from a concentration cell. For dilute electrolyte solution, the potentiostatic polarization method introduced in Bruce and Vincent [31] can be used for the direct determination of the transference number. In the original publication and in Hiller et al. [81], the method is used for polymer electrolytes. In Mauro et al. [105] and Zugmann et al. [163], the same method is applied for liquid electrolyte solutions such as $LiClO_4$ dissolved in PC and $LiPF_6$ in various electrolyte solutions. In Zugmann et al. [163], three additional methods, namely the electromotive force method, NMR method and the galvanostatic polarization method are discussed. The electromotive method is based on data from a concentration cell without transference. In such an experimental setup, the transference number can be determined either in the dilute limit (see, e.g., [142]) where the thermodynamic factor can be assumed to be unity or the concentration dependent behavior of the thermodynamic factor has to be known. It would also be possible to use a concentration cell with transference (see [163]) but it is difficult to find appropriate salt bridges for aprotic lithium based electrolytes fulfilling the condition $t_+ = t_- = 0.5$. Secondly, the transference number can also be determined by measuring the ionic self-diffusion coefficients as demonstrated, e.g., in Castiglione et al. [38] or Capiglia et al. [36]. In Zhao et al. [160], the method introduced by Bruce and Vincent [31] is compared to the NMR method resulting in completely different values for the transference number, even for the smallest concentration. The galvanostatic polarization method is the most popular method to determine the transference number. It is used for polymer electrolytes in Ma et al. [103], Ferry et al. [62] or Doeff et al. [51]. The diffusion coefficient, the transference number and the thermodynamic factor can also be determined by a numerical optimization approach as shown in the aforementioned publications by Georén and Lindbergh [67], Nyman et al. [115] and Lundgren et al. [102].

In section section 5.1, the basic principle of the conductivity cell used for the determination of the conductivity is explained. A novel method for the direct electrochemical determination of the mean binary activity coefficient in aprotic electrolyte solutions is introduced in section 5.2. The general principle of the parameter determination by means of polarization experiments is explained in section 5.3. Two different electrochemical methods for the determination of the binary diffusion coefficient in a two-electrode cell with a porous separator are derived in section 5.4. In section 5.5, various well-known and new methods for the determination of the transference number in two-electrode cell with a porous separator are discussed critically. In section 5.6 the transference number is calculated from data obtained in concentration cell and a known thermodynamic factor. Although both methods introduced in this section are based on a very popular

experimental procedure, the modified versions have not be used so far to determine the transference number in aprotic electrolyte solutions. In section 5.7, a very popular method for the determination of the transference number is described. The result presented in this section are also published in Landesfeind et al. [96], Ehrl et al. [57] and Ehrl et al. [56].

5.1 Conductivity

The determination of the conductivity κ of an electrolyte solution is based on the same physical principle as used for the determination of the tortuosity τ in section 4.2. The conductivity κ is calculated from the resistance R measured in an experimental setup consisting of two electrodes immersed in an electrolyte solution:

$$\kappa = \frac{C}{R}.$$

The cell constant C describes the geometrical configuration of the two electrode cell and is usually determined in an electrolyte solution of known conductivity κ. As a result of this calibration, all geometrical uncertainties such as unaligned electrodes are automatically included in the cell constant C. However, even for perfectly manufactured electrodes, it is only possible for a very small ratio l/A to replace the cell constant C by the distance between the electrodes l and the electrode surface A

$$C = \frac{l}{A}$$

which is the result of the inhomogeneous electric field around the electrodes. The relevance of this effect decreases with an increasing electrode area and a decreasing distance l.

5.2 Electrochemical determination of the thermodynamic factor

The basic idea of the method is the electrochemical determination of the mean molar activity coefficient for aprotic binary electrolyte solutions within a single experimental setup. For that, cyclic voltammetry in electrolyte solutions containing small amounts of ferrocene are measured versus a lithium reference electrode, since peak positions of the ferrocene redox couple can be related to the mean molar activity coefficient of the lithium salt. The use of the ferrocene redox couple as a quasi-reference is discussed in detail in the original contribution by Gritzner and Kuta [74]. In this context, the lithium salt is referred to as supporting electrolyte since the ferrocene concentration is mostly an order of magnitude smaller.

In the following, a general correlation between the cell potential U and the mean molar activity coefficient $f_{\pm}(c)$ of a binary salt is derived for cyclic voltammetry experiments whereas the derivation is based on the Stefan-Maxwell approach introduced in section 2.4.1. The used experimental setup is shown in Fig. 8.3. The cell potential U is the difference between the electrostatic potential Φ_{WE} of the Working Electrode (WE) and the electrostatic potential Φ_{RE} of the lithium

Reference Electrode (RE). The concentration dependence of the mean molar activity coefficient is expressed in terms of the concentration of a binary salt, which is defined as $c = \frac{c_+}{\nu_+} = \frac{c_-}{\nu_-}$. In general, the mean binary activity coefficient of any salt is defined as

$$f_\pm^\nu \equiv f_+^{\nu_+} f_-^{\nu_-}. \tag{5.1}$$

Subsequently, the subscripts '+' and '-', indicating the positive and negative ionic species, are replaced by the names of their corresponding ions, e.g., by lithium Li^+ and perchlorate ClO_4^-. The lithium perchlorate salt can also be thought of as a supporting electrolyte, whereas ferrocenium is the minor ionic species in the electrolyte solution.

Theoretical derivation The redox reaction at the Reference Electrode (RE) is defined as

$$\mathrm{Li} \rightleftarrows \mathrm{Li}^+ + \mathrm{e}^-$$

and at the Working Electrode (WE) as

$$\mathrm{Fc} \rightleftarrows \mathrm{Fc}^+ + \mathrm{e}^-$$

where Fc denotes the ferrocene and Fc^+ the ferrocenium ion. The reaction Gibbs energy $\Delta_R G$ for the lithium reaction at the RE is given by

$$\Delta_R G\big|_{\mathrm{RE}} = 0 = \mu_{\mathrm{Li}} - \tilde{\mu}_{\mathrm{Li}^+} - \tilde{\mu}_{\mathrm{e}^-}$$

and for the ferrocene reaction at the WE by

$$\Delta_R G\big|_{\mathrm{WE}} = \mu_{\mathrm{Fc}} - \tilde{\mu}_{\mathrm{Fc}^+} - \tilde{\mu}_{\mathrm{e}^-}.$$

Here, μ denotes the chemical potential of an uncharged component and $\tilde{\mu}$ the electrochemical potential of an ionic species. The reaction Gibbs energy of the RE is zero since the reference electrode is always in an equilibrium state due to negligible current flow across the interface. As a result, the cell potential U expressed in terms of electrochemical potentials of the electrons e^- in WE and RE

$$FU = F\left(\Phi_{\mathrm{WE}} - \Phi_{\mathrm{RE}}\right) = \tilde{\mu}_{\mathrm{e}^-}\big|_{\mathrm{RE}} - \tilde{\mu}_{\mathrm{e}^-}\big|_{\mathrm{WE}}$$

can be written as

$$FU = \left(\mu_{\mathrm{Li}} - \tilde{\mu}_{\mathrm{Li}^+}\right)\big|_{RE} - \left(\mu_{\mathrm{Fc}} - \tilde{\mu}_{\mathrm{Fc}^+} - \Delta_R G\right)\big|_{\mathrm{WE}} \tag{5.2}$$

where the cell potential is determined by the reactions at the interfaces of WE and RE. The electrochemical potential of an arbitrary ionic species k for any electrolyte solution can be defined, according to Newman and Thomas-Alyea [109], as

$$\tilde{\mu}_k = z_k F \Phi^n + RT \ln c_k + RT\left(\ln f_k - \frac{z_k}{z_n}\ln f_n\right) + RT\left(\ln a_k - \frac{z_k}{z_n}\ln a_n\right), \tag{5.3}$$

where the electrostatic potential Φ^n in the electrolyte solution is defined with respect to an arbitrary negative ionic species n present in the electrolyte solution as explained in section 2.4.2. The physical motivation of Equ. (5.3) is introduced in the same section. In the following, the superscript n is dropped for simplicity. Furthermore, the charge number of the ionic species k is denoted by z_k, the activity coefficient of the ionic species k by f_k, the Faraday constant by F, the gas constant by R, the temperature by T and proportionality constant of the ionic species k by a_k. In addition, the following definition for the electrochemical potential of the reference species n defined in section 2.4.2 is used

$$\tilde{\mu}_n = z_n F\Phi + RT \ln c_n. \tag{5.4}$$

In this framework, the anion of the supporting electrolyte is chosen as the reference species n since it does not contribute to any surface reaction. By combination of Equ. (5.1) and Equ. (5.3), the electrochemical potentials of lithium and ferrocenium ions can be written as

$$\tilde{\mu}_{\mathrm{Li^+}} = z_{\mathrm{Li^+}} F\Phi + RT \ln c_{\mathrm{Li^+}} + RT \ln f^2_{\mathrm{LiClO_4}} + \mu^{\theta}_{\mathrm{LiClO_4}}, \tag{5.5}$$

$$\tilde{\mu}_{\mathrm{Fc^+}} = z_{\mathrm{Fc^+}} F\Phi + RT \ln c_{\mathrm{Fc^+}} + RT \ln f^2_{\mathrm{FcClO_4}} + \mu^{\theta}_{\mathrm{FcClO_4}}. \tag{5.6}$$

The standard chemical potentials of lithium perchlorate

$$\mu^{\theta}_{\mathrm{LiClO_4}} = RT \ln \left(a_{\mathrm{Li^+}} a_{\mathrm{ClO_4^-}} \right)$$

and ferrocene perchlorate

$$\mu^{\theta}_{\mathrm{FcClO_4}} = RT \ln \left(a_{\mathrm{Fc^+}} a_{\mathrm{ClO_4^-}} \right)$$

defined according to Newman and Thomas-Alyea [109, chap. 2.3] are independent of the electrolyte composition but are a function of additional state variables such as temperature and pressure. The mean binary activity coefficients of lithium perchlorate and ferrocene perchlorate are given by $f^2_{\mathrm{LiClO_4}}$ and $f^2_{\mathrm{FcClO_4}}$ as defined in Equ. (5.1). Therefore, using Equ. (5.5) and Equ. (5.6), Equ. (5.2) can be expressed as,

$$\begin{aligned} FU = &+ RT \ln \left(c_{\mathrm{Fc^+}} f^2_{\mathrm{FcClO_4}} \right) \big|_{\mathrm{WE}} + \Delta_{\mathrm{R}} G \big|_{\mathrm{WE}} - \mu_{\mathrm{Fc}} \big|_{\mathrm{WE}} \\ &- RT \ln \left(c_{\mathrm{Li^+}} f^2_{\mathrm{LiClO_4}} \right) \big|_{\mathrm{RE}} + F \left(\Phi \big|_{\mathrm{WE}} - \Phi \big|_{\mathrm{RE}} \right) + \mu_{\mathrm{Cell}}. \end{aligned}$$

Here, the standard chemical cell potential μ_{Cell} includes the chemical potential of lithium μ_{Li} as well as the standard chemical potentials of lithium perchlorate $\mu^{\Theta}_{\mathrm{LiClO_4}}$ and ferrocenium perchlorate $\mu^{\Theta}_{\mathrm{FcClO_4}}$

$$\mu_{\mathrm{Cell}} = \left(\mu_{\mathrm{Li}} \big|_{\mathrm{RE}} - \mu^{\Theta}_{\mathrm{LiClO_4}} \big|_{\mathrm{RE}} + \mu^{\Theta}_{\mathrm{FcClO_4}} \big|_{\mathrm{WE}} \right). \tag{5.7}$$

The potential drop in the electrolyte is described by the term $\Phi|_{\mathrm{WE}} - \Phi|_{\mathrm{RE}}$. The cell potential U can also be written as

$$U = U_{\mathrm{Ref}} - \frac{RT}{F} \ln \left(c_{\mathrm{Li^+}} f^2_{\mathrm{LiClO_4}} \right) \tag{5.8}$$

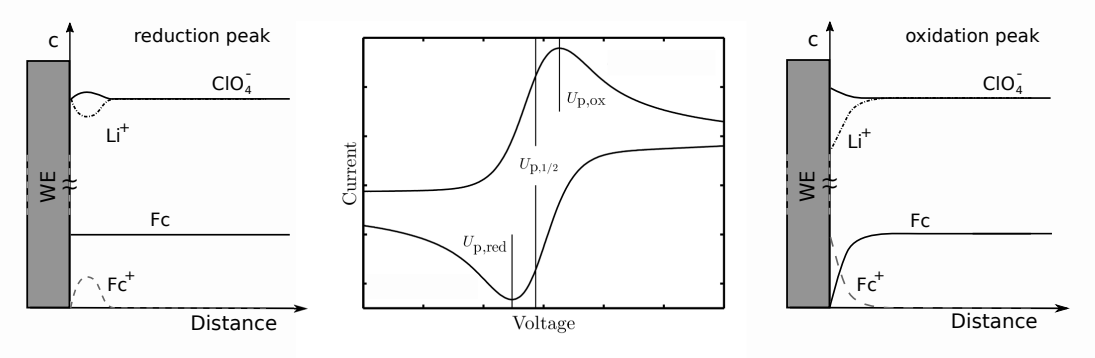

Figure 5.1: Concentration profiles in the vicinity of the Working Electrode (WE) for the components dissolved in the electrolyte solution at the oxidation peak and at the reduction peak.

where the reference potential U_{Ref} includes all remaining terms:

$$U_{\text{Ref}} = \left[\frac{RT}{F}\ln\left(\frac{c_{\text{Fc}^+}}{c_{\text{Fc}}}\right) + \Delta_{\text{R}}G + \frac{RT}{F}\ln\left(f^2_{\text{FcClO}_4}\right) - \frac{RT}{F}\ln f_{\text{Fc}}\right]_{\text{WE}} + \mu_{\text{Cell}} + \Delta\Phi. \tag{5.9}$$

The reference potential U_{Ref} is independent of the $LiClO_4$ concentration if the ferrocene concentration is kept constant.

In summery, the relation given in Equ. (5.8) is the basis for the determination of the mean molar activity coefficient by cyclic voltammetry experiments which requires a constant ferrocene concentration throughout a measurement series while the $LiClO_4$ concentration is varied. As the obtained cell potential U is given by a constant U_{Ref} and an expression containing the activity coefficient of $LiClO_4$, latter quantity can be determined mathematically.

Position of oxidation and reduction peaks Subsequently, possible influences on the peak positions of a cyclic voltammogram are analyzed. In general, the positions of oxidation and reduction peaks are defined by the ratio of ferrrocenium to ferrocene at the WE. Idealized concentration profiles at both peaks are shown in Fig. 5.1. At the oxidation peak, ferrocene is depleted at the WE while at the reduction peak the ferrocenium ion concentration approaches zero at the WE. In addition, this ratio is also the basic boundary condition for the boundary value problem as described, e.g., in Bard and Faulkner [14]. This becomes clearer, if Equ. (5.8) and Equ. (5.9) are reformulated to

$$\frac{c_{\text{Fc}^+}}{c_{\text{Fc}}} = \exp\left\{\frac{F}{RT}\left[(U - \Delta\Phi) - U_0'\right]\right\}.$$

with the formal potential U_0' of the WE with respect to the RE

$$U_0' \equiv \mu_{\text{Cell}} - \frac{RT}{F}\ln\left(\frac{f^2_{\text{FcClO}_4}}{f_{\text{Fc}}}\right) - \frac{RT}{F}\ln\left(c_{\text{Li}^+} f^2_{\text{LiClO}_4}\right).$$

Here, in a first approximation, it is assumed that the electrochemical reaction at the WE is always in an equilibrium state. In a cyclic voltammetry experiment with a RE, the potential between WE

Table 5.1: Peak separation for reversible redox reactions.

$\lvert U_{\text{p,ox}} - U_{\text{reverse}} \rvert$ [mV]	171,5	271,5	8
$U_{\text{p,ox}} - U_{\text{p,red}}$ [mV]	58,3	57,8	57,0

and RE is reduced by the potential drop $\Delta\Phi$ within the electrolyte solution. The cell potential U is time dependent and can be expressed as $U = U_{\text{init}} - s \cdot t$ where s denotes a constant scan rate, U_{init} the initial cell potential and t the time. Based on this boundary condition, the following theoretical relations can be derived for the oxidation peak in the first cycle as demonstrated in Bard and Faulkner [14]. The theoretical peak position $U_{\text{p,ox}}$ is given by

$$U_{\text{p,ox}} = U_0' + \frac{RT}{F} \ln \left(\frac{D_{\text{Fc}}}{D_{\text{Fc}^+}} \right)^{1/2} - 1.109 \frac{RT}{F} \tag{5.10}$$

and the peak current by

$$I_{\text{p,ox}} = 2.69 \cdot 10^5 A (D_{\text{Fc}})^{1/2} c_{\text{Fc}}^0 s^{1/2}, \tag{5.11}$$

for a perfectly reversible Nernstian couple. The diffusion coefficient of ferrocene is denoted by D_{Fc} and the diffusion coefficient of the ferrocenium ion by D_{Fc^+}. The ferrocene concentration in the bulk of the electrolyte solution is indicated by $c_{\text{Fc},0}$. Since ferrocenium ions are the minor species in the supporting electrolyte solution, they can be approximated by the pure diffusion problem with the ionic diffusion coefficient D_{Fc^+} as explained in Newman and Thomas-Alyea [109]. The connection of the mean molar activity coefficient with the oxidation peak position for a single forward scan becomes clear in Equ. (5.10). If the measured potential U in Equ. (5.8) is only a function of the term $\ln\left(c_{\text{Li}^+} f_{\text{LiClO}_4}^2\right)$ and all other terms are constant, it is possible to determine the mean activity coefficient from the peak position.

For a cyclic voltammogram of a reversible redox couple, it is also possible to derive a theoretical value for the peak separation defined by the potential difference between the oxidation $U_{\text{p,ox}}$ and reduction peak $U_{\text{p,red}}$. In general, the theoretical peak separation depends on the potential difference between the oxidation peak potential $U_{\text{p,ox}}$ and the upper vertex potential at which the scan rate is reversed U_{reverse}. The theoretical values for a reversible Nernstian couple are shown in Tab. 5.1. Therefore, a peak separation of about 57 mV would be expected of the difference between vertex and the peak potential is > 300 mV. This theoretical value for the peak separation can be used to evaluate the quality of the experimental data.

Reference potential To be able to use cyclic voltammetry in combination with the shown experimental setup for the determination of mean molar activity coefficients $f_{\text{LiClO}_4}(c)$, it is necessary that the reference potential U_{Ref} is independent of the supporting electrolyte salt concentration c. Therefore, it is important to get a detailed understanding of the characteristics of the individual terms contributing to the reference potential U_{Ref}.

As discussed before, the logarithmic ratio of ferrrocenium to ferrocene at the WE, the first of the terms in Equ. (5.9), defines the theoretical positions of oxidation and reduction peaks. For the derivation of the theoretical peak positions and the peak separation, it is assumed that the system is only limited by mass transport, which means that infinitely fast kinetics are assumed. However, in reality, kinetic effects have to be considered, as they also influence the peak separation and, therefore, peak positions. If the second term in Equ. (5.9), the reaction Gibbs energy $\Delta_R G$, is not negligibly small, it can be approximated by the kinetic overpotential η, which describes the deviation from the equilibrium potential at the specific condition as described in Newman and Thomas-Alyea [109]. In this case, the peak separation is linked to the parameter Ψ defined and tabulated in Bard and Faulkner [14]:

$$\Psi = \left(\frac{D_{\mathrm{Fc^+}}}{D_{\mathrm{Fc}}}\right)^{a/2} k_0 \left(\pi D_{\mathrm{Fc^+}} \frac{F}{RT} s\right)^{-1/2}. \tag{5.12}$$

Here, a denotes the transfer coefficient in the Butler-Volmer equation and k_0 the standard rate constant of the electrochemical reaction. According to Equ. (5.10), the peak separation depends on the diffusion coefficient ratio and the standard rate constant, whereas both quantities may be a function of the supporting electrolyte concentration. A decreasing parameter Ψ, e.g. slow kinetics, results in an increase in the peak separation, which is distributed symmetrically between oxidation and reduction peaks as shown, e.g., by Table 6.5.2 in Bard and Faulkner [14]. To decrease the influence of the non-ideal conditions in cyclic voltammetry experiments, the half wave potential $U_{\mathrm{p},1/2} = 1/2\,(U_{\mathrm{p,ox}} + U_{\mathrm{p,red}})$ can be used as a reference point instead of oxidation or reduction peak positions (see section 5.1). For the half wave potential, the symmetric potential shifts of oxidation and reduction peaks cancel out due to their symmetry.

The next term in Equ. (5.9), the mean molar activity coefficient of ferrocenium perchlorate $\ln\left(f_{\mathrm{FcClO_4}}\right)\big|_{\mathrm{WE}}$ is assumed to be constant in this work. Latter assumption can be endorsed with the original publication by Gritzner and Kuta [74]. In their publication the authors argue that the activity of the ferrocene – ferrocenium is independent of the surrounding solution. An even stronger argument for the constancy of the term $\ln\left(f_{\mathrm{FcClO_4}}\right)\big|_{\mathrm{WE}}$ is its influence on oxidation and reduction peak positions. As ferrocenium ions only exist at the oxidation peak, a possible contribution by this term can only occur for this peak. Thus, if the $LiClO_4$ concentration is varied between experiments, a varying contribution to oxidation peaks should be observable compared to the reduction peak. Experimental results shown in section 8.3 prove that oxidation and reduction peaks behave completely identical.

The chemical potential of the cell μ_{Cell}, as defined in Equ. (5.7), depends on the used electrode materials and the electrolyte solution and is generally constant for isothermal and isobaric conditions. So far, all discussed terms deal with the electrolyte composition in the vicinity of the electrodes. In contrast to those, the potential drop $\Delta\Phi$ describes the potential difference in the electrolyte between working and reference electrode. The potential field in such an electrolyte

solution is described by

$$\Phi = + \frac{RT}{F} \nabla \ln c_{\mathrm{ClO_4^-}} - \frac{\boldsymbol{i}}{\kappa} - \frac{RT}{F} \underbrace{\left[t_{\mathrm{Li^+}} \nabla \ln \left(c_{\mathrm{Li^+}} c_{\mathrm{ClO_4^-}} f^2_{\mathrm{LiClO_4}} \right) + t_{\mathrm{Fc^+}} \nabla \ln \left(c_{\mathrm{Fc^+}} c_{\mathrm{ClO_4^-}} f^2_{\mathrm{FcClO_4}} \right) \right]}_{\zeta}, \tag{5.13}$$

which is derived from

$$F \frac{\boldsymbol{i}}{\kappa} = - \left(\sum_{k=1}^{n} \frac{t_k}{z_k} \nabla \tilde{\mu}_k \right)$$

using Equ. (5.4) – Equ. (5.6) as described in Newman and Thomas-Alyea [109]. The latter equation is a more general form of Equ. (2.37). Here, the current density is denoted by i, the conductivity of the electrolyte solution by κ and the transference numbers of lithium and ferrocenium ions by $t_{\mathrm{Li^+}}$ and $t_{\mathrm{Fc^+}}$, respectively. A similar system is also discussed for example in Newman and Thomas-Alyea [109]. Using a one-dimensional approximation of the given setup and performing an integration along a path between RE and WE, it is possible to get an approximation for the potential drop between RE and WE

$$\Delta\Phi = \frac{RT}{F} \ln \left(\frac{c_{\mathrm{ClO_4^-}}\big|_{\mathrm{WE}}}{c_{\mathrm{ClO_4^-}}\big|_{\mathrm{RE}}} \right) - R_{\mathrm{el}} I - \frac{RT}{F} \int_{\mathrm{RE}}^{\mathrm{WE}} \zeta \, \mathrm{d}\, x. \tag{5.14}$$

The ohmic resistance of the electrolyte solution is denoted by R_{el} and the current by I. In this formulation, the third term of Equ. (5.13) is not integrated, yet. The first term on the right hand side is zero since the perchlorate ion concentration is approximately constant in the entire electrolyte solution for oxidation as well as reduction peaks as indicated in Fig. 5.1.

The second term $R_{\mathrm{el}} I$ describes the potential drop within the electrolyte solution as a result of the current. Although the current between WE and RE is negligibly small, an ohmic potential is included in the cell potential U as a result of the current flowing between WE and CE. The so-called effect of uncompensated resistance between RE and WE also leads to an increased peak separation as described by Bard and Faulkner [14]. This effect is particularly pronounced for small supporting electrolyte concentrations since the resistance of the electrolyte solution is increased drastically. The increase in peak separation is not completely symmetric, since the peak currents at oxidation and reduction peak are usually not equal in a cyclic voltammogram. In order to reduce the effect of uncompensated resistance, the current between WE and CE electrode has to be minimized. Experimental parameters influencing the current are the scan rate and the ferrocene concentration, as indicated in Equ. (5.11).

Furthermore, the potential drop $\Delta\Phi$ in the electrolyte is also influenced by the third term in Equ. (5.14), which describes the concentration overpotential resulting from concentration gradients within the electrolyte. In general, concentration gradients have to be considered only in the vicinity of the WE. The RE compartment is separated from the WE, thereby guaranteeing uniform lithium and perchlorate ion concentration profiles. Additionally, the polarization times are short enough, so that developing concentration gradients at the WE do not penetrate far into

the bulk region of the electrolyte solution. As a result of small concentration variations within the electrolyte solution, it is valid to assume constant transference numbers for the integration of the third term Equ. (5.14)

$$\frac{RT}{F}\int_{\mathrm{RE}}^{\mathrm{WE}} \zeta \,\mathrm{d}\,x = \frac{RT}{F}\left[t_{\mathrm{Li^+}} \ln\left\{\frac{\left(c_{\mathrm{Li^+}} f_{\mathrm{LiClO_4}}^2\right)_{\mathrm{WE}}}{\left(c_{\mathrm{Li^+}} f_{\mathrm{LiClO_4}}^2\right)_{\mathrm{RE}}}\right\} + t_{\mathrm{Fc^+}} \ln\left\{\frac{\left(c_{\mathrm{Fc^+}} f_{\mathrm{FcClO_4}}^2\right)_{\mathrm{WE}}}{\left(c_{\mathrm{Fc^+}} f_{\mathrm{FcClO_4}}^2\right)_{\mathrm{RE}}}\right\}\right]. \tag{5.15}$$

Contributions of the perchlorate ions in the integral cancel out due to its uniform concentration profile. The last term depending on the transference number of the ferrocenium ion can also be neglected since the transference number of the minor species in a supporting electrolyte solution is approximately zero for a high ratio of supporting electrolyte to minor component. Such a high ratio also has a positive effect on the first term of the Equ. (5.15) since the concentration difference of lithium ions between WE and RE is also minimized resulting in a small influence of the first term in Equ. (5.15). Concluding, a minimal ratio of ferrocenium ions, respective ferrocene, to supporting electrolyte is also advantageous to avoid concentration overpotentials. This is of course most critical for small concentrations of supporting electrolyte. It is emphasized that the concentration overpotential does not influence both peaks symmetrically. At the oxidation peak, the concentration difference for lithium as well as ferrocenium ions are maximal resulting in a maximum concentration overpotential. On the contrary, the concentration differences of supporting electrolyte ions between RE and WE are negligibly small at the reduction peak. As a result, concentration overpotentials influence oxidation but not reduction peaks. As for all non-symmetric terms, this has to be considered if the half wave potential is used for the determination of the mean activity coefficient, particularly for small supporting electrolyte concentrations.

Theoretical behavior of the mean molar activity coefficient of binary salts If all aforementioned theoretical assumptions and experimental requirements are fulfilled, the mean molar activity coefficient $f_{\mathrm{LiClO_4}}$ can be obtained by means of Equ. (5.8). For the validation of the experimental results, the theoretical behavior of the mean molar activity coefficient described by the Debye-Hückel law can be used which is discussed for example in Bard and Faulkner [14] or Hamann and Vielstich [78]. In general, the Debye-Hückel law is written as

$$\ln f_{\mathrm{LiClO_4}} = -\left|z_{\mathrm{Li^+}} z_{\mathrm{ClO_4^-}}\right| \frac{A\sqrt{I}}{\left(1 + B\dot{a}\sqrt{I}\right)}, \tag{5.16}$$

where the ionic strength I of the electrolyte solution is defined as

$$I = \frac{1}{2}\sum_{k=1}^{m} z_k^2 c_k \tag{5.17}$$

for $m = 3$ dissolved ionic species in the electrolyte and the parameters A and B as

$$B = \frac{\left(2e^2 N_{\mathrm{A}}\right)^{1/2}}{\left(\varepsilon_0 \varepsilon_{\mathrm{R}} kT\right)^{1/2}} = \varepsilon_{\mathrm{R}}^{-1/2} \cdot 2.914 \cdot 10^9\,\mathrm{dm^{\frac{1}{2}}\,mol^{-\frac{1}{2}}}, \tag{5.18}$$

and

$$A = \frac{e^2}{(8\pi\varepsilon_0\varepsilon_\mathrm{R}kT)}B = \varepsilon_\mathrm{R}^{-3/2} \cdot 817.1\,\mathrm{dm}^{\frac{3}{2}}\mathrm{mol}^{-\frac{1}{2}}, \tag{5.19}$$

respectively. The number of dissolved ionic species in the electrolyte solution is denoted by $m = 3$, the minimal distance between two ionic species by $\dot{a}$, the relative permittivity by ε_R, the permittivity of vacuum by $\varepsilon_0 = 8.854 \cdot 10^{-12}\,\mathrm{Fm}^{-1}$, the electronic charge by $e = 1.602 \cdot 10^{-19}\,\mathrm{C}$, the Avogadro constant by $N_\mathrm{A} = 6.022 \cdot 10^{23}\,\mathrm{mol}^{-1}$ and the gas constant by $R = 8.314\,\mathrm{J\,mol}^{-1}\,\mathrm{K}^{-1}$. As explained in Wright [153], Equ. (5.16) can also be approximated by the Debye-Hückel limiting law

$$\ln f_{\mathrm{LiClO_4}} = -\left|z_{\mathrm{Li^+}} z_{\mathrm{ClO_4^-}}\right| A\sqrt{I} \tag{5.20}$$

for low ionic strengths. For electrolyte solutions with higher ionic strengths, the Debye-Hückel theory can be extended by a linear term

$$\ln f_{\mathrm{LiClO_4}} = -\left|z_{\mathrm{Li^+}} z_{\mathrm{ClO_4^-}}\right| \frac{A\sqrt{I}}{\left(1 + B\dot{a}\sqrt{I}\right)} + x_1 I \tag{5.21}$$

as introduced, e.g., in Wright [153]. This is an empirical extension accounting for effects as for example short range interactions between ions and the solvent, dispersion forces between ions or ion association. A detailed discussion of this topic can be found, e.g., in Wright [153]. An $\mathrm{n^{th}}$-order polynomial with respect to the concentration instead of ionic strength is used to account for effects which are not included in Debye-Hückel's theory by Newman and Thomas-Alyea [109]

$$\ln f_{\mathrm{LiClO_4}} = -\left|z_{\mathrm{Li^+}} z_{\mathrm{ClO_4^-}}\right| \frac{A\sqrt{I}}{\left(1 + B\dot{a}\sqrt{I}\right)} + x_1 c + x_2 c^{3/2} + x_2 c^2 + \ldots. \tag{5.22}$$

In this work, the extended form of the Debye-Hückel law given in Equ. (5.21) is used as the suggested polynomial form given in Equ. (5.22) overinterprets the experimental results.

5.3 General principle of polarization experiments

For the determination of the diffusion coefficient and the transference number, two different experimental setups are considered. The first experimental setup, the so-called two-electrode cell, consists of two electrodes at distance l. The space between the two electrodes can be filled with an liquid electrolyte solution or, alternatively, with an electrically isolating porous medium such as a separator soaked with a electrolyte solution. Initially, the two-electrode cell without porous medium was applied, e.g., by Stewart and Newman [136] to determine the diffusion coefficient and in Valøen and Reimers [142] to determine the complete set of transport parameters. The two-electrode cell with porous medium is used in combination with a numerical optimization approach, e.g., by Georén and Lindbergh [66] or Nyman et al. [115]. The advantages and disadvantages of a cell with and without separator are discussed in the following. The second ex-

perimental setup is a concentration cell consisting of two electrodes connected by an electrolyte solution. Both experimental setups are described in detail in section 8.5.1.

In a two-electrode cell with separator, all experimental methods for the determination of ion-transport parameters are based on different analytical solutions of the volume averaged mass component-based mass conservation. The advantage of this geometrical setup is that convective effects can be neglected as discussed in section 8.5.1. Additionally, the area to distance ratio is typically larger than in a two-electrode cell without separator minimizing the influence of the edge effect and, thereby, improving the requirement of one-dimensional concentration and potential gradients. The disadvantage of the cell with separator is that only a small amount of electrolyte is used for the experiments. As a result, the experimental procedure is quite sensitive to evaporation of single electrolyte components or similar effects changing the electrolyte composition. In the following, the volume averaged ion-transport equation based on the Stefan-Maxwell approach given in Equ. (4.8) is used to determine the transport parameters. Volumetric effects are neglected in this approach as explained in section 2.4.1. In addition to these reasons, the method for the determination of the thermodynamic factor presented in section 5.2 is also based on the Stefan-Maxwell approach neglecting volumetric effects. The combination of two different physical models for the determination of transport parameter is not recommended. For the same reason, the alternative thermodynamically-consistent approach introduced in section 2.6 cannot be used either. It has to be emphasized that the experimentally determined transport parameters are influenced by potential volumetric effects although they are not considered directly in the present ion-transport model.

The mass conservation law given in Equ. (4.8) can also be written as

$$\varepsilon \frac{\partial \overline{c}^{\,\mathrm{e}}}{\partial t} - \nabla \cdot \left(\frac{\varepsilon}{\tau} D_{\pm}(c) \nabla \overline{c}^{\,\mathrm{e}} \right) + \frac{\nabla t_+(c)}{z_+ \nu_+ F} \cdot \overline{\boldsymbol{i}} + \frac{t_+(c)}{z_+ \nu_+ F} \nabla \cdot \overline{\boldsymbol{i}} = 0, \tag{5.23}$$

where the product rule is applied to the divergence of the conduction term. Potential boundary conditions for the electrodes are Dirichlet, Neuman or electrode BC whereas Neuman and electrode BC are very similar for one-dimensional domains since the overpotential η is a constant for each of the electrodes. In the context of transport parameter determination, Dirichlet BC are seldom used since the concentrations $\overline{c}^{\,\mathrm{e}}$ at both electrodes are usually unknown. A potential exception is the determination of transport parameters based on the limiting current where the concentration at the cathode can be approximated by $\overline{c}^{\,\mathrm{e}} = 0$ and at the anode by $\overline{c}^{\,\mathrm{e}} = 2\overline{c}_0^{\,\mathrm{e}}$. However, this method is limited to electrolyte solutions which are hardly influenced by concentration dependent transport parameters. In general, the flux and current density at the electrode surface is given as

$$\overline{\boldsymbol{N}} = -\frac{\varepsilon}{\tau} D_{\pm}(c) \nabla \overline{c}^{\,\mathrm{e}} + \frac{t_+(c)}{z_+ \nu_+ F} \overline{\boldsymbol{i}}, \tag{5.24}$$

and

$$\overline{\boldsymbol{i}} = z_+ \nu_+ F \overline{\boldsymbol{N}}, \tag{5.25}$$

respectively. Equ. (5.25) is based on a binary electrolyte solution with the cation as reacting species. As result, the flux density at the electrode surface can also be expressed as

$$\overline{\boldsymbol{N}} = -\frac{D_{\pm,\text{eff}}(c)}{1 - t_+(c)} \nabla \overline{c}^{\,\text{e}},$$

where Equ. (5.24) and (5.25) and the definition for the effective diffusion coefficient $D_{\pm,\text{eff}}(c) = \frac{\varepsilon}{\tau} D_{\pm}(c)$ given in Equ. (4.7) are used. Compared to the transport of uncharged components, an additional scaling factor $1/(1 - t_+(c))$ has to be considered for the calculation of the flux density which includes the effect of ion-transport due to the potential field. In case of one-dimensional ion-transport, the flux density reads

$$\overline{N} = -\frac{D_{\pm,\text{eff}}(c)}{1 - t_+(c)} \frac{\partial \overline{c}^{\,\text{e}}}{\partial x}, \tag{5.26}$$

where $\overline{N}$ denotes the volume averaged intrinsic phase average of the flux density in an one-dimensional model. The corresponding boundary condition reads

$$-\overline{N}\, n = j = \frac{1}{z_+ \nu_+ F} \frac{I}{A} \tag{5.27}$$

where I denotes the applied or measured current. The electrode surface A and the normal component n are definitions which are based on the three-dimensional domain shown in Fig. 4.2. At this point, only one-electrode reactions with $n_r = 1$ and $s_r = -1$ are considered such as the oxidation of lithium and the reduction of lithium ions. In terms of the current density, Equ. (5.27) reads

$$-\bar{i}\, n = \frac{I}{A} \tag{5.28}$$

For polarization experiments, the x-axis of the coordinate system points always from the cathode towards the anode as it is depicted in Fig. 4.2. In addition, all analytical expressions are derived with respect to the anode resulting in $n = 1$. According to the definition given in section 2.1, the current I at the anode is positive since the current flow is directed into the domain. At the cathode, the current I is negative since it exits the domain. Note that the current density $\bar{i}$ is defined with respect to the positive charges as it can be seen in Equ. (2.13). As result of this definition, the concentration difference $\Delta \overline{c}^{\,\text{e}}$ between the Anode (A) and the Cathode (C)

$$\Delta \overline{c}^{\,\text{e}} = \overline{c}^{\,\text{e}}_{\text{A}} - \overline{c}^{\,\text{e}}_{\text{C}}$$

as well as the concentration gradient $\frac{\partial \overline{c}^{\,\text{e}}}{\partial x}$ are always positive.

Using the charge conservation given in Equ. (4.10), Equ. (5.23) can be simplified to an one-dimensional scalar transport equation

$$\varepsilon \frac{\partial \overline{c}^{\,\text{e}}}{\partial t} - \frac{\varepsilon}{\tau} D_{\pm}(c_0) \frac{\partial^2 \overline{c}^{\,\text{e}}}{\partial x^2} = 0 \tag{5.29}$$

if the following assumptions are valid:

1. The experimental setup resembles an ideal geometrical configuration consisting of two parallel and aligned flat electrodes separated by an electrolyte solution and enclosed by insulators as depicted in Fig. 4.2. In such a geometrical setup, concentration and potential gradients are exclusively orientated in x-direction. As a result, ion-transport in the electrolyte solution can be described by the one-dimensional partial differential equation. In reality, this ideal configuration can be approximated by two electrode cell with a large area to distance ratio.
2. The concentration dependent diffusion coefficient $D_{\pm}(c)$ and the transference number $t_+(c)$ are assumed to be constant for small concentration variations around an initial concentration $\overline{c}_0^{\,\mathrm{e}}$. This assumption is equivalent to a zero order approximation of concentration dependent diffusion coefficient $D(c) = D_{\pm}(c_0)$ and transference number $t_+(c) = t_+(c_0)$. The same condition is required for the remaining ion-transport parameters. Typical concentration dependent transport parameters of various binary electrolyte solutions usually fulfilled this assumption as demonstrated in section 7.5.
3. The porosity ε and the tortuosity τ are constant with respect to time and space. For battery applications this condition is usually fulfilled as it is already discussed in section 3.1.2.

The partial differential equation given in Equ. (5.29) can be solved analytically for different types of BCs. As a result, an expression for the concentration difference $\Delta\overline{c}^{\,\mathrm{e}}$ between the Cathode (C) and the Anode (A) is obtained

$$\Delta\overline{c}^{\,\mathrm{e}} = \mathrm{f}(D_{\pm}(c_0), t_+(c_0), \varepsilon, \tau, \overline{c}_0^{\,\mathrm{e}}, \mathrm{BC}). \tag{5.30}$$

If the concentration difference $\Delta\overline{c}^{\,\mathrm{e}}$ is known, it is possible to calculate the effective binary diffusion coefficient $D_{\pm}$ and the transference number t_+ based on the analytical expression given in Equ. (5.30). The local concentration $\overline{c}^{\,\mathrm{e}}$ in the vicinity of the anode and cathode can be determined experimentally, e.g., by optical methods as described, e.g., in Newman and Chapman [110]. Limiting factors of this method are the spatial resolution of the optical device and the complexity of the required analysis equipment.

In this contribution, the concentration difference $\Delta\overline{c}^{\,\mathrm{e}}$ is determined indirectly utilizing a correlation with the measured cell potential U. Based on section 2.4.3 and section 5.2, the cell potential U between two lithium electrodes can be written as

$$U = \eta_{\mathrm{C}} + \Delta\overline{\Phi}^{\,\mathrm{e}} + \eta_{\mathrm{A}},$$

where η_{C} denotes the surface overpotential at the cathode, η_{A} the surface overpotential at the anode and $\Delta\overline{\Phi}^{\,\mathrm{e}}$ the potential difference between the lithium electrodes

$$\Delta\overline{\Phi}^{\,\mathrm{e}} = \overline{\Phi}_{\mathrm{A}}^{\,\mathrm{e}} - \overline{\Phi}_{\mathrm{C}}^{\,\mathrm{e}}.$$

Here, the potential is defined with respect to a lithium reference electrode as introduced in section 2.4.3. For an ideal geometrical setup, the potential difference $\Delta\overline{\Phi}^{\,\mathrm{e}}$ can be calculated by the

integrated, one-dimensional form of the current equation given in Equ. (4.9)

$$\begin{aligned}\Delta\overline{\Phi}^{\mathrm{e}} &= \int_{\mathrm{C}}^{A} \frac{\partial\overline{\Phi}^{\mathrm{e}}}{\partial x}\,\mathrm{d}\,x \\ &= \int_{\mathrm{C}}^{A} \left[-\frac{1}{\kappa_{\mathrm{eff}}(c_0)}\bar{i} + \frac{\nu}{z_+\nu_+}\frac{RT}{F}\left(1+\frac{\partial \ln f_{\pm}(c_0)}{\partial \ln c}\right)(1-t_+(c_0))\frac{\partial \ln \overline{c}^{\mathrm{e}}}{\partial x}\right]\mathrm{d}\,x, \end{aligned} \tag{5.31}$$

where the definition for the effective conductivity $\kappa_{\mathrm{eff}} = \frac{\varepsilon}{\tau}\kappa$ as given in Equ. (4.7) is used. In theory, the correlation between the measured cell potential U and the concentration $\overline{c}^{\mathrm{e}}$ at the surface of the electrode can be used for all kinds of BCs but it is most accurate for the relaxation process after the polarization. During polarization, the cell potential U is influenced additionally, e.g., by electrode reactions or modifications of the electrode surface indicated by a non-constant surface resistance R_{I}. This means that an accurate functional description of all physical phenomena is more elaborate than during the relaxation process. For the relaxation process, the integrated formulation of Equ. (5.31) can be written as

$$\Delta\overline{\Phi}^{\mathrm{e}} = \frac{\nu}{z_+\nu_+}\frac{RT}{F}\left(1+\frac{\partial \ln f_{\pm}(c_0)}{\partial \ln c}\right)(1-t_+(c_0))\ln\frac{\overline{c}^{\mathrm{e}}_{\mathrm{A}}}{\overline{c}^{\mathrm{e}}_{\mathrm{C}}}, \tag{5.32}$$

where the TDF is assumed to be constant with respect to c_0 as it is done already for the diffusion coefficient and the transference number. For small concentration variations, the natural logarithm can be approximated by

$$\ln\frac{\overline{c}^{\mathrm{e}}_{A}}{\overline{c}^{\mathrm{e}}_{C}} \approx \frac{\Delta\overline{c}^{\mathrm{e}}}{\overline{c}^{\mathrm{e}}_{0}}, \tag{5.33}$$

as it is shown, e.g. in Bruce and Vincent [31]. The error of this linear relation is shown in Fig. 5.2. As a result of this approximation, the integrated form of Equ. (5.32) reads

$$U = \Delta\overline{\Phi}^{\mathrm{e}} = \frac{\nu}{z_+\nu_+}\frac{RT}{F}\left(1+\frac{\partial \ln f_{\pm}(c_0)}{\partial \ln c}\right)(1-t_+(c_0))\frac{\Delta\overline{c}^{\mathrm{e}}}{\overline{c}^{\mathrm{e}}_{0}}. \tag{5.34}$$

In theory, the cell potential U is equivalent to the potential difference $\Delta\overline{\Phi}^{\mathrm{e}}$ between the electrodes during the relaxation process since the current flowing across the electrodes is zero. Therefore, the concentration difference $\Delta\overline{c}^{\mathrm{e}}$ is directly proportional to cell potential $U \propto \Delta\overline{c}^{\mathrm{e}}$ for the used approximations which is a central point for electrochemical determination of transport parameters. The same method is also applied, e.g., in Ma et al. [103], Zugmann et al. [163] or Valøen and Reimers [142].

5.4 Binary diffusion coefficient

The two-electrode cell as described in the beginning of section 5.3 is used for the determination of the binary diffusion coefficient $D_{\pm}$. The first geometrical setup is used, e.g., in Stewart and Newman [136] or Valøen and Reimers [142]. The second geometrical setup has not been used

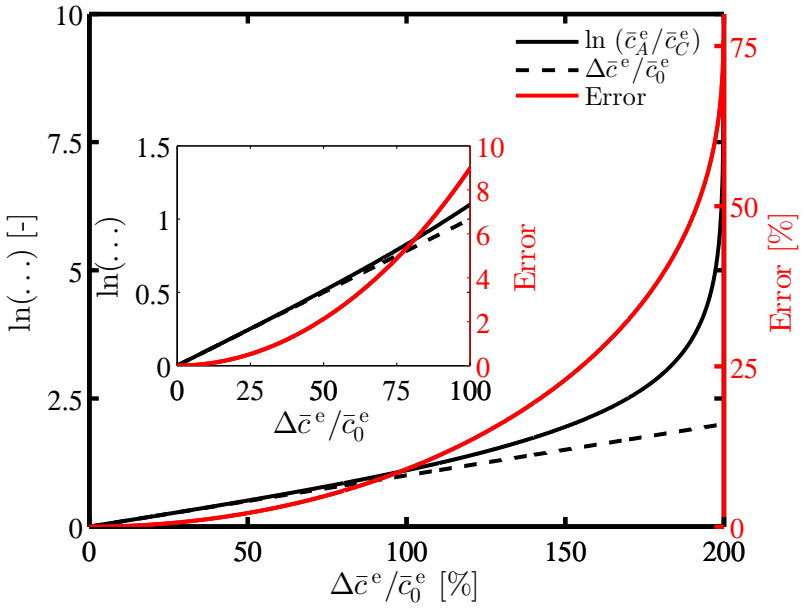

Figure 5.2: Error introduced by the linearization of $\ln(\bar{c}_A^e/\bar{c}_C^e) \approx \Delta\bar{c}^e/\bar{c}_0^e$.

so far to determine the binary diffusion coefficient $D_\pm$ experimentally by observing the time-dependent relaxation behavior after a polarization phase. In general, the presented methods for the determination of the diffusion coefficient can be used for both versions of the two-electrode cell.

5.4.1 Long-term relaxation from an non-uniform concentration profile

For the investigation of the long-term relaxation behavior, the two-electrode cell is polarized galvanostatically or potentiostatically resulting in a non-uniform concentration profile at current interruption time T_I. For this method, the concentration profile $\bar{c}^e(T_\mathrm{I})$ at the interruption time $t = T_\mathrm{I}$ is considered as the initial concentration profile $\bar{c}_0^e$. Subsequently, the relaxation of the cell potential $U(t)$ is observed for $t \to \infty$. Originally, the method was developed for dilute electrolyte solution by Harned and French [79]. The theoretical verification for concentrated solutions is given in Newman and Chapman [110]. In both publications, only electrolyte solutions without separator are considered. The analytical expression for the volume averaged and time dependent concentration difference $\Delta\bar{c}^e(t)$ is derived in this contribution assuming a constant diffusion coefficient $D_\pm(c_0)$.

The partial differential equation given in Equ. (5.23) can be reformulated to

$$\frac{\partial\bar{c}}{\partial t} - D^*_{\pm,\mathrm{eff}}(c_0)\nabla^2\bar{c} = 0, \qquad \text{in } (0,l)\times(T_\mathrm{I},T_\mathrm{end}). \tag{5.35}$$

where the relation $\varepsilon\overline{c}^{\,\mathrm{e}} = \overline{c}$ and the partial binary diffusion coefficient

$$D^*_{\pm,\mathrm{eff}}(c_0) = \frac{1}{\tau} D_{\pm}(D_0) \tag{5.36}$$

is used. The BCs for the relaxation process read

$$\frac{\partial \overline{c}^{\,\mathrm{e}}_{\mathrm{C}}}{\partial x} = \frac{\partial \overline{c}_{\mathrm{C}}}{\partial x} = 0 \qquad \text{and} \qquad \frac{\partial \overline{c}^{\,\mathrm{e}}_{\mathrm{A}}}{\partial x} = \frac{\partial \overline{c}_{\mathrm{A}}}{\partial x} = 0. \tag{5.37}$$

The concentration profile $\overline{c}^{\,\mathrm{e}}(T_{\mathrm{I}})$ at current interruption time has to be point-symmetric to $x = \frac{1}{2}l$. For ionic liquids the influence of the concentration profile $\overline{c}^{\,\mathrm{e}}(T_{\mathrm{I}})$ at current interruption is investigated theoretically and experimentally in Thompson and Newman [139]. This boundary value problem can be solved by separation of variables:

$$\begin{aligned}\Delta\overline{c}^{\,\mathrm{e}}(t) =& 2C_1 \exp\left(-\frac{\pi^2 D^*_{\pm,\mathrm{eff}}(c_0)}{l^2} t\right) + \\ & 2C_3 \exp\left(-\frac{9\pi^2 D^*_{\pm,\mathrm{eff}}}{l^2} t\right) + 2\sum_{n=3}^{\infty} C_{(2n-1)} \exp\left(-\frac{(2n-1)^2\pi^2 D^*_{\pm,\mathrm{eff}}(c_0)}{l^2} t\right).\end{aligned} \tag{5.38}$$

A short outline of the derivation is given in section C.1. Compared to the solution presented in Harned and French [79], the exponential prefactor in the second term is smaller which results in slower decay. This difference can be explained by different reference points. In the original publication, additional electrodes were placed at $x = 1/6\,l$ and $x = 5/6\,l$ whereas the concentration difference between anode $x = l$ and cathode $x = 0$ is used in this contribution. In the derivation of Newman and Chapman [110] a variable diffusion coefficient and solvent effects are considered resulting in a similar relationship with an additional term

$$B \exp\left(-3\frac{\pi^2 D^*_{\pm,\mathrm{eff}}(c_0)}{l^2} t\right) \tag{5.39}$$

where B is a function of the initial conditions and concentration derivatives of the physical properties. The potential influence of this term will be discussed in section 7.5. For large times $t \to \infty$, the first term of the analytical solution is dominating which gives a linear relationship between $\ln \Delta\overline{c}^{\,\mathrm{e}}(t)$ and the time t:

$$\ln U(t) \propto \ln \Delta\overline{c}^{\,\mathrm{e}}(t) = \ln(2|C_1|) - \underbrace{\frac{\pi^2 D^*_{\pm,\mathrm{eff}}(c_0)}{l^2}}_{m_{\ln}} t. \tag{5.40}$$

Since concentration difference $\Delta\overline{c}^{\,\mathrm{e}}$ and the measured cell potential U are directly proportional as shown by Equ. (5.34), the linear behavior can also be observed for the cell potential $U(t)$. Here, $m_{\ln}$ denotes the slope of cell potential $\ln U(t)$ plotted over the time t for $t \to \infty$. As a result, the

diffusion coefficient can be calculated from the linear slope $m_{\ln}$

$$D^*_{\pm,\text{eff}}(c_0) = \frac{l^2}{\pi^2} m_{\ln}. \tag{5.41}$$

The advantage of this method is that the concentration difference decreases with increasing time which supports the requirement of small concentration variations. The tortuosity τ of the separator is required to determine the binary diffusion coefficient $D_\pm$.

5.4.2 Short-term relaxation from a steady state concentration profile

For this method, a steady-state concentration profile $\overline{c}^{\,\text{e}}(T_\text{I})$ is considered as a concentration profile $\overline{c}^{\,\text{e}}(T_\text{I})$ at current interruption time T_I which can be approximated by a linear function for small concentration variations. Whether the steady-state concentration profile is obtained by a galvanostatic or a potentiostatic polarization phase is irrelevant for this method. After current interruption, the short-term relaxation behavior of the potential is observed.

Apart from the steady-state concentration profile, the same boundary value problem as in section 5.4.1 is considered. In this case, the boundary value problem is solved by two Laplace transformations as outlined in section C.2. For the short-term relaxation process from a steady-state concentration profile, the time dependent concentration difference $\Delta\overline{c}^{\,\text{e}}(t)$ is given by the relation

$$\Delta\overline{c}^{\,\text{e}}(t) = \Delta\overline{c}^{\,\text{e}}(T_\text{I}) \left(1 - \sqrt{\frac{16 D^*_{\pm,\text{eff}}(c_0)}{\pi l^2}\, t} \right). \tag{5.42}$$

The short-term relaxation process is linear with respect to $\sqrt{t}$. A similar equation is presented for polymer electrolytes in Hiller et al. [81]. Since the cell potential $U \propto \Delta\overline{c}^{\,\text{e}}$ for small concentration variations, Equ. (5.42) can also be expressed in terms of the cell potential

$$U(t) = U(T_\text{I}) - \underbrace{U(T_\text{I}) \frac{\sqrt{16 D^*_{\pm,\text{eff}}(c_0)}}{l\sqrt{\pi}}}_{m_\text{sqrt}} \sqrt{t},$$

where m_sqrt denotes the slope the cell potential U with respect to $\sqrt{t}$. As a result, the diffusion coefficient $D^*_{\pm,\text{eff}}$ can be determined by

$$D^*_{\pm,\text{eff}}(c_0) = \frac{\pi l^2}{16} \left(\frac{m_\text{sqrt}}{U(T_\text{I})} \right)^2. \tag{5.43}$$

As for the method based on the long term relaxation behavior, the tortuosity τ of the separator is required to determine the binary diffusion coefficient $D_\pm$.

Alternatively, it is also possible to determine the slope of $U(t)/U(T_\text{I})$ with respect to the time $\sqrt{t}$. However, this alternative method is not used in this contribution since the cell potential $U(T_\text{I})$ is influenced directly after current interruption by additional phenomena such as the dis-

charge of the double layer or lithium corrosion as presented, e.g., in Osaka et al. [118]. Therefore, a linear fit of $U(t)$ with respect to $\sqrt{t}$ would be already necessary to determine the cell potential $U(T_\mathrm{I})$ at interruption time T_I.

5.5 Transference number based on data from a polarization cell

The conductivity $\kappa(c)$, the binary diffusion coefficient $D_\pm(c)$, respectively, the partial effective binary diffusion coefficient $D^*_{\pm,\mathrm{eff}}(c)$ and the binary activity coefficient $f_\pm(c)$, respectively, the thermodynamic factor can be determined directly by independent experimental setups. In contrast, at least two different experimental setups are necessary for the determination of the transference number $t_+(c)$ as indicated already in the literature survey. A direct determination of the transference number is only possible for dilute electrolyte solutions.

In this section, the transference number is determined based on three different experiments. The TDF is determined by the experimental method described in Landesfeind et al. [96] and in section 5.2. The two-electrode cell is used for the determination of the partial effective diffusion coefficient $D^*_{\pm,\mathrm{eff}}$ as well as for a third experiment determining additional coefficients of the form

$$f(f_\pm, t_+, D^*_{\pm,\mathrm{eff}}) = \left(1 + \frac{\partial \ln f_\pm(c_0)}{\partial \ln c}\right) \frac{(1 - t_+(c_0))^2}{D^*_{\pm,\mathrm{eff}}(c_0)} \tag{5.44}$$

or, alternatively,

$$f(f_\pm, t_+, \sqrt{D^*_{\pm,\mathrm{eff}}}) = \left(1 + \frac{\partial \ln f_\pm(c_0)}{\partial \ln c}\right) \frac{(1 - t_+(c_0))^2}{\sqrt{D^*_{\pm,\mathrm{eff}}(c_0)}}. \tag{5.45}$$

Based on a known partial effective binary diffusion coefficient $D^*_{\pm,\mathrm{eff}}(c_0)$, a known TDF$(c_0)$ and one of the coefficients given in Equ. (5.44) and Equ. (5.45), it is possible to calculate transference number $t_+(c_0)$ at the concentration $\overline{c}_0$. The methods introduced in section 5.5.2, section 5.5.3 and section 5.5.4 have not been applied so far to determine the transference number experimentally.

For the determination of the transference number $t_+(c)$ the tortuosity τ of the porous medium is not required. The tortuosity τ of the porous medium is only necessary to get the binary diffusion coefficient $D_\pm(c)$ from the partial effective binary diffusion coefficient $D^*_{\pm,\mathrm{eff}}(c)$ measured by the methods introduced in section 5.4.

5.5.1 Steady-state potentiostatic polarization

The direct determination of the transference number t_+ for dilute electrolyte solutions is based on the application of a potentiostatic cell potential U_p until the steady-state current is reached. Theoretically, it is possible to calculate the transference number t_+ from the ratio between the initial current I_0 and the steady-state current I_S. However, a correction term for variable electrode

kinetics as a result of, e.g., the SEI formation or the growth of mossy Lithium has to be considered for most realistic experimental setups. In the original form introduced by Blonsky et al. [25], the method was restricted to dilute electrolyte solutions. Bruce and Vincent [31] extended it for non-ideal electrolyte solutions assuming variable ionic diffusion coefficients. In this extension, the thermodynamic factor has to be close to unity. However, this method can also be embedded into a more general framework which is also valid for concentrated electrolyte solutions.

The potential difference $\Delta\overline{\Phi}^{\mathrm{e}}$ between the anode and the cathode for an one-dimensional approximation is given by Equ. (5.31). Integration of Equ. (5.31) results in

$$\Delta\overline{\Phi}^{\mathrm{e}} = \int_{\mathrm{C}}^{\mathrm{A}} \left(\frac{1}{\kappa(c_0)} \frac{l}{A} \frac{\tau}{\varepsilon} \right) \mathrm{d}\, x\, I + \frac{\nu}{\nu_+ z_+} \frac{RT}{F} \left(1 + \frac{\partial \ln f_{\pm}(c_0)}{\partial \ln c} \right) (1 - t_+(c_0)) \frac{\Delta\overline{c}^{\mathrm{e}}(t)}{\overline{c}_0^{\mathrm{e}}}, \quad (5.46)$$

where Equ. (5.28) is used to replace the current density. In contrast to Equ. (5.34), an additional ohmic contribution has to be considered for the potential difference. The integral in Equ. (5.46) is equivalent to the ohmic resistance R_{el} of the electrolyte solution

$$R_{\mathrm{el},0} = \int_{\mathrm{C}}^{\mathrm{A}} \left(\frac{1}{\kappa(c_0)} \frac{l}{A} \frac{\tau}{\varepsilon} \right) \mathrm{d}\, x.$$

Note that this relation would also be valid for arbitrary concentration variations and not only for small concentration variations. The initial potential difference $\Delta\overline{\Phi}_0^{\mathrm{e}}$ reads

$$\Delta\overline{\Phi}_0^{\mathrm{e}} = R_{\mathrm{el},0}\, I_0 \quad (5.47)$$

since the concentration difference is very small directly after the application of the cell potential U_{p}. The initial electrolyte resistance is denoted by $R_{\mathrm{el},0}$. At the steady-state, the potential difference $\Delta\overline{\Phi}_{\mathrm{S}}^{\mathrm{e}}$ is given by

$$\Delta\overline{\Phi}_{\mathrm{S}}^{\mathrm{e}} = R_{\mathrm{el,S}}\, I_{\mathrm{S}} + \frac{\nu}{\nu_+ z_+} \frac{RT}{F} \left(1 + \frac{\partial \ln f_{\pm}(c_0)}{\partial \ln c} \right) (1 - t_+(c_0)) \frac{\Delta\overline{c}_{\mathrm{S}}^{\mathrm{e}}}{\overline{c}_0^{\mathrm{e}}}. \quad (5.48)$$

The initial and the steady-state electrolyte resistance measured by impedance spectroscopy can be assumed to be identical

$$R_{\mathrm{el},0} = R_{\mathrm{el,S}} = R_{\mathrm{el}}, \quad (5.49)$$

since the variation of the conductivity is negligibly for small concentration variations. The second term is the so-called concentration overpotential. For a steady-state concentration profile, the concentration difference $\Delta\overline{c}_{\mathrm{S}}^{\mathrm{e}}$ can be replaced by

$$\Delta\overline{c}_{\mathrm{S}}^{\mathrm{e}} = \frac{1}{z_+ \nu_+ F} \frac{1 - t_+(c_0)}{D_{\pm,\mathrm{eff}}(c_0)} \frac{l}{A}\, I_{\mathrm{S}}, \quad (5.50)$$

where Equ. (5.26) and Equ. (5.27) are used with

$$\frac{\partial c}{\partial x} = \frac{c_\mathrm{A} - c_\mathrm{C}}{l}.$$

The current I is replaced by the steady-state current I_S to emphasize that this equation is based on a linear steady-state concentration profile. As a result, Equ. (5.48) reads

$$\Delta\overline{\Phi}_\mathrm{S}^{\,\mathrm{e}} = R_\mathrm{el}\, I_\mathrm{S} + \frac{\nu}{\nu_+^2 z_+^2}\,\frac{RT}{F^2}\left(1 + \frac{\partial \ln f_\pm(c_0)}{\partial \ln c}\right)\frac{(1-t_+(c_0))^2}{D_{\pm,\mathrm{eff}}(c_0)}\,\frac{l}{A}\,\frac{I_\mathrm{S}}{\overline{c}_0^{\,\mathrm{e}}}, \tag{5.51}$$

As a result of Equ. (5.49), Equ. (5.47) and (5.51) can be combined to

$$\frac{\Delta\overline{\Phi}_0^{\,\mathrm{e}}}{I_0} = \frac{\Delta\overline{\Phi}_\mathrm{S}^{\,\mathrm{e}}}{I_\mathrm{S}} - \frac{\nu}{\nu_+^2 z_+^2}\,\frac{RT}{F^2}\left(1 + \frac{\partial \ln f_\pm(c_0)}{\partial \ln c}\right)\frac{(1-t_+(c_0))^2}{D_{\pm,\mathrm{eff}}(c_0)}\,\frac{l}{A}\,\frac{1}{\overline{c}_0^{\,\mathrm{e}}}. \tag{5.52}$$

Note that the ratio $\frac{\Delta\Phi_\mathrm{S}}{I_\mathrm{S}} \neq R_\mathrm{el,S}$ is not only the ohmic resistance but also includes a contribution of the concentration overpotential as it can be concluded from Equ. (5.51). Multiplication of Equ. (5.52) with $I_0/\Delta\overline{\Phi}_0^{\,\mathrm{e}}$ and a rearrangement results in

$$\frac{I_0\,\Delta\overline{\Phi}_\mathrm{S}^{\,\mathrm{e}}}{I_\mathrm{S}\,\Delta\overline{\Phi}_0^{\,\mathrm{e}}} = 1 + \frac{\nu}{\nu_+^2 z_+^2}\,\frac{RT}{F^2}\left(1 + \frac{\partial \ln f_\pm(c_0)}{\partial \ln c}\right)\frac{(1-t_+(c_0))^2}{D_{\pm,\mathrm{eff}}(c_0)}\,\frac{l}{A}\,\frac{1}{\overline{c}_0^{\,\mathrm{e}}}\,\frac{1}{R_\mathrm{el}}, \tag{5.53}$$

where $I_0/\Delta\overline{\Phi}_0^{\,\mathrm{e}} = 1/R_\mathrm{el}$ is used in the last term on the rhs. In Doyle [53, chap. 4.9] an equivalent formulation is given

$$\frac{I_0\,\Delta\overline{\Phi}_\mathrm{S}^{\,\mathrm{e}}}{I_\mathrm{S}\,\Delta\overline{\Phi}_0^{\,\mathrm{e}}} = 1 + \frac{\nu}{\nu_+^2 z_+^2}\,\frac{RT}{F^2}\left(1 + \frac{\partial \ln f_\pm(c_0)}{\partial \ln c}\right)\frac{(1-t_+(c_0))^2}{D_{\pm,\mathrm{eff}}(c_0)}\,\frac{1}{\overline{c}_0^{\,\mathrm{e}}}\,\kappa_\mathrm{eff}, \tag{5.54}$$

where Equ. (4.11) is used to replace the resistance of the electrolyte R_el by the effective conductivity κ_eff. This formulation is of particular interest since it is the link to the equation used for dilute electrolyte solutions:

$$t_+ = \frac{I_\mathrm{S}\,\Delta\overline{\Phi}_0^{\,\mathrm{e}}}{I_0\,\Delta\overline{\Phi}_\mathrm{S}^{\,\mathrm{e}}}. \tag{5.55}$$

Equ. (5.54) can be reformulated to Equ. (5.55) if the approximations

$$\left(1 + \frac{\partial \ln f_\pm}{\partial \ln c}\right) \approx 1, \quad \kappa_- \approx \frac{F^2}{RT} z_-^2 \nu_- D_- \overline{c}_0^{\,\mathrm{e}},$$

and definitions

$$(1 - t_+) = t_-, \quad \frac{\kappa_\mathrm{eff}}{D_{\pm,\mathrm{eff}}} = \frac{\kappa}{D_\pm}, \quad t_- = \frac{\kappa_-}{\kappa}, \quad D_\pm = \mathbb{D}_\pm = \frac{(z_+ - z_-) D_+ D_-}{D_+ + D_-},$$

according to the dilute solution theory are used. In this context, the dilute solution theory is formulated with respect to lithium reference electrodes whereas the dilute solution theory discussed in section 2.5 is based on a potential definition with respect to the negative ionic species. The comparison of Equ. (5.54) and Equ. (5.55) also gives a mathematical condition for the validity of the dilute solution theory:

$$t_+ \left(1 + \frac{\nu}{\nu_+^2 z_+^2} \frac{RT}{F^2} \left(1 + \frac{\partial \ln f_\pm}{\partial \ln c} \right) \frac{(1 - t_+(c_0))^2}{D_\pm(c_0)} \frac{\kappa}{\overline{c}_0^{\,\mathrm{e}}} \right) = 1. \tag{5.56}$$

Based on Equ. (5.53), the coefficient $f(f_\pm, t_+, D^*_{\pm,\mathrm{eff}})$ can be calculated as

$$f(f_\pm, t_+, D^*_{\pm,\mathrm{eff}}) = \left[\frac{I_0 \left(U_\mathrm{p} - (R_{\mathrm{LF,S}} - R_\mathrm{el}) I_\mathrm{S} \right)}{I_\mathrm{S} \left(U_\mathrm{p} - (R_{\mathrm{LF},0} - R_\mathrm{el}) I_0 \right)} - 1 \right] \frac{\nu_+^2 z_+^2}{\nu} \frac{F^2}{RT} \frac{A}{l} \varepsilon \, \overline{c}_0^{\,\mathrm{e}} \, R_\mathrm{el} \tag{5.57}$$

where the following relation between the potential difference $\Delta\overline{\Phi}^{\mathrm{e}}$ and the polarization potential U_p is used:

$$\Delta\overline{\Phi}^{\mathrm{e}} = U_\mathrm{p} - (R_\mathrm{LF} - R_\mathrm{el}) I. \tag{5.58}$$

Here, R_LF denotes the Low Frequency (LF) resistance determined by impedance spectroscopy. Equ. (5.58) is based on a serial equivalent circuit consisting of an electrolyte resistance R_el and additional resistances such as kinetic resistance or contact resistances. Additionally, the relation $D_{\pm,\mathrm{eff}} = \varepsilon D^*_{\pm,\mathrm{eff}}$ is applied.

An alternative formulation for Equ. (5.57) is

$$f(f_\pm, t_+, D^*_{\pm,\mathrm{eff}}) = \left[\frac{\Delta\overline{\Phi}_\mathrm{S}^{\mathrm{e}}}{I_\mathrm{S}} - R_\mathrm{el} \right] \frac{\nu_+^2 z_+^2}{\nu} \frac{F^2}{RT} \frac{A}{l} \varepsilon \, \overline{c}_0^{\,\mathrm{e}}.$$

which can further be reformulated using Equ. (5.58)

$$f(f_\pm, t_+, D^*_{\pm,\mathrm{eff}}) = \left[\frac{U_\mathrm{p}}{I_\mathrm{S}} - R_{\mathrm{LF,S}} \right] \frac{\nu_+^2 z_+^2}{\nu} \frac{F^2}{RT} \frac{A}{l} \varepsilon \, \overline{c}_0^{\,\mathrm{e}}. \tag{5.59}$$

The advantage of this formulation is that the number of parameters which has to be determined is reduced compared to Equ. (5.57). In addition, the steady-state current I_S is much easier to determine than the initial current I_0 due to additional effects such as double layer charging. The same reformulations can be applied to Equ. (5.55):

$$t_+(c_0) = \frac{I_\mathrm{S} R_\mathrm{el}}{U_\mathrm{p} - (R_{\mathrm{LF,S}} - R_\mathrm{el}) I_\mathrm{S}}. \tag{5.60}$$

This equation was introduced by Hiller et al. [81].

5.5.2 Initial time behavior of the potentiostatic polarization

The coefficient $f(f_\pm, t_+, \sqrt{D^*_{\pm,\mathrm{eff}}})$ can also be determined from the short-term relaxation behavior of the current $I(t)$ in a SSPP experiment. The theoretical time behavior of the current $I(t)$ in such an experiment can be derived from the partial differential equation of the form

$$\frac{\partial \overline{c}}{\partial t} - D^*_{\pm,\mathrm{eff}}(c_0)\nabla^2\overline{c} = 0, \qquad \text{in } (0,l)\times(0,T_\mathrm{I}) \tag{5.61}$$

with the current condition given in Equ. (5.27) as BC at anode and cathode. The semi-infinite limit

$$\lim_{x\to\infty} \overline{c} = \overline{c}_0 \tag{5.62}$$

is used as an additional condition. The semi-infinite limit can be interpreted as $\overline{c} = \overline{c}_0$ for $x \to l/2$ which introduces a limitation for the time range in which the analytical solution is valid. A uniform concentration profile is assumed as an initial condition $\overline{c}_0$. This boundary value problem can be solved by Laplace transformation as shown in appendix C.3. A similar boundary value problem is solved, e.g., in Bard and Faulkner [14].

According to Equ. (C.24), the current $I(t)$ at the anode and the cathode can be expressed as

$$I(t) = \frac{U_\mathrm{p}}{R_{\mathrm{LF},0}} \exp(H^2 t)\mathrm{erfc}(Ht^{1/2}), \tag{5.63}$$

where $\mathrm{erfc}(H\sqrt{t})$ is the complementary error function defined as $1 - \mathrm{erf}(H\sqrt{t})$. The constant H is defined as

$$H = \frac{2\nu}{z_+^2\nu_+^2}\,\frac{RT}{F^2}\,\frac{1}{A\,\varepsilon\,\overline{c}_0^{\,\mathrm{e}}\,R_{\mathrm{LF},0}}\left(1 + \frac{\partial \ln f_\pm(c_0)}{\partial \ln c}\right)\frac{(1-t_+(c_0))^2}{\sqrt{D^*_{\pm,\mathrm{eff}}(c_0)}}.$$

According to Bard and Faulkner [14, chap. 5.5.1], the factor $\exp(H^2t)\mathrm{erfc}(Ht^{1/2})$ can be linearized for small values of $H\sqrt{t}$:

$$\exp(H^2t)\mathrm{erfc}(Ht^{1/2}) \simeq 1 - \frac{2H}{\sqrt{\pi}}\sqrt{t}. \tag{5.64}$$

In this case, Equ. (5.63) can be written as

$$I(t) = \underbrace{\frac{U_\mathrm{p}}{R_{\mathrm{LF},0}}}_{I_0}\left(1 - \frac{2H}{\sqrt{\pi}}\sqrt{t}\right) = I_0 - \underbrace{I_0\frac{2H}{\sqrt{\pi}}}_{m_\mathrm{SSPP}}\sqrt{t}. \tag{5.65}$$

where m_{SSPP} denotes the slope of the current $I(t)$ with respect to $\sqrt{t}$. As a result, the coefficient $f(f_{\pm}, t_{+}, \sqrt{D^{*}_{\pm,\mathrm{eff}}})$ can be calculated by

$$f(f_{\pm}, t_{+}, \sqrt{D^{*}_{\pm,\mathrm{eff}}}) = \frac{z_{+}^{2}\nu_{+}^{2}}{4\nu}\sqrt{\pi}\,\frac{F^{2}}{RT}\,A\,\varepsilon\,\bar{c}_{0}^{\,\mathrm{e}}\,R_{\mathrm{LF},0}\,\frac{m_{\mathrm{SSPP}}}{I_{0}}. \tag{5.66}$$

If the requirements for the linearization in Equ. (5.64) are not fulfilled, the additional information provided by Equ. (5.63) is limited since the unknown factor H cannot be separated from the time t. The theoretical time behavior predicted by Equ. (5.65) can also be used to determine the initial current I_0 although it is not stringently required for the method presented in section 5.5.1. Last but not least the knowledge about the expected time behavior is a good control mechanism showing immediately the quality of experimental results.

5.5.3 Short-term relaxation from a steady-state concentration profile

This method is based on the short-term relaxation behavior from a steady-state concentration profile as it is used in section 5.4.2 for the determination of the diffusion coefficient. The starting point is Equ. (5.42) which can be inserted in Equ. (5.34) utilizing Equ. (5.50):

$$U(t) = \underbrace{\frac{\nu}{z_{+}^{2}\nu_{+}^{2}}\,\frac{RT}{F^{2}}\,\frac{l}{A}\,\frac{1}{\bar{c}_{0}^{\,\mathrm{e}}}\,I_{\mathrm{S}}\,f(f_{\pm}, t_{+}, D^{*}_{\pm,\mathrm{eff}})}_{U(T_{\mathrm{I}})}\left(1 - \underbrace{\sqrt{\frac{16D^{*}_{\pm,\mathrm{eff}}(c_0)}{\pi l^{2}}}}_{m_{\mathrm{sqrt}}}\sqrt{t}\right). \tag{5.67}$$

This equation describes the linear relaxation of the cell potential $U(t)$ with respect to $\sqrt{t}$ from the initial value $U(T_{\mathrm{I}})$ at the current interruption time T_{I}. Based on the initial value $U(T_{\mathrm{I}})$, the coefficient $f(f_{\pm}, t_{+}, D^{*}_{\pm,\mathrm{eff}})$ can be calculated by

$$f(f_{\pm}, t_{+}, D^{*}_{\pm,\mathrm{eff}}) = \frac{z_{+}^{2}\nu_{+}^{2}}{\nu}\,\frac{F^{2}}{RT}\,\frac{A}{l}\,\varepsilon\,\bar{c}_{0}^{\,\mathrm{e}}\,\frac{U(T_{\mathrm{I}})}{I_{\mathrm{S}}}. \tag{5.68}$$

Here, the cell potential $U(T_{\mathrm{I}})$ is the potential measured directly after current interruption. The idea behind this is that the cell potential U reduces immediately to $U = \Delta\overline{\Phi}^{\,\mathrm{e}}$ after polarization whereas the concentration difference $\Delta\bar{c}^{\,\mathrm{e}}$ has not changed significantly since diffusion is based on a different time scale. Therefore, it is valid to use Equ. (5.34) to get a measure for the steady-state concentration profile at current interruption time T_{I}. However, it is also difficult to determine the correct potential directly after current interruption since parasitic contributions as described in section 5.4.2 interfere with the signal due to the concentration difference $\Delta\bar{c}^{\,\mathrm{e}}$ between anode and cathode. To overcome this problem, the linear relation of the cell potential $U(t)$ with respect to $\sqrt{t}$ can be used to determine the cell potential $U(T_{\mathrm{I}})$ exactly at the current interruption time T_{I} by means of extrapolation. In addition, the observation of the time behavior gives a good indication for the quality of experimental data.

The slope m_{sqrt} is used in section 5.4.2 to determine the diffusion coefficient. Alternatively, the slope can also be used to determine the coefficient $f(f_{\pm}, t_{+}, \sqrt{D^{*}_{\pm,\mathrm{eff}}})$. Therefore, Equ. (5.67)

is reformulated to

$$U(t) = U(T_\mathrm{I}) - \underbrace{\frac{4\nu}{z_+^2\nu_+^2}\,\frac{1}{\sqrt{\pi}}\,\frac{RT}{F^2}\,\frac{1}{A}\,\frac{1}{\varepsilon}\,\frac{1}{\bar{c}_0^{\,\mathrm{e}}}\,I_\mathrm{S}\,f(f_\pm, t_+, \sqrt{D^*_{\pm,\mathrm{eff}}})}_{m_\mathrm{sqrt}}\,\sqrt{t}.$$

As a result, the coefficient $f(f_\pm, t_+, \sqrt{D^*_{\pm,\mathrm{eff}}})$ can be calculated by

$$f(f_\pm, t_+, \sqrt{D^*_{\pm,\mathrm{eff}}}) = \frac{z_+^2\nu_+^2}{4\nu}\,\sqrt{\pi}\,\frac{F^2}{RT}\,A\,\varepsilon\,\bar{c}_0^{\,\mathrm{e}}\,\frac{m_\mathrm{sqrt}}{I_\mathrm{S}}.$$

This formula is not considered anymore in the following since the slope m_sqrt is already used to determination of the binary diffusion coefficient $D_\pm$.

5.5.4 Long-term relaxation from a steady-state concentration profile

As for the determination of the diffusion coefficient described in section 5.4.1, the long-term relaxation behavior from the concentration profile at current interruption time T_I provides information for the determination of the coefficient $f(f_\pm, t_+, D^*_{\pm,\mathrm{eff}})$. In contrast to section 5.4.1, a mathematical description for the prefactor C_1 is necessary. To be able to determine the prefactors C_{2n-1}, a steady-state concentration profile is required as initial condition whereas it is arbitrary how the steady-state concentration profile is obtained. The derivation is presented in appendix C.1. As a result, the concentration difference $\Delta\bar{c}^{\,\mathrm{e}}(t)$ can be expressed as

$$\Delta\bar{c}^{\,\mathrm{e}}(t) = 8\frac{\Delta\bar{c}^{\,\mathrm{e}}(T_\mathrm{I})}{\pi^2}\exp\left(-\frac{\pi^2 D^*_{\pm,\mathrm{eff}}(c_0)}{l^2}t\right). \tag{5.69}$$

Higher order terms are already neglected in Equ. (5.69). As usual, the expression for the concentration difference $\Delta\bar{c}^{\,\mathrm{e}}(t)$ given in Equ. (5.69) can be inserted in Equ. (5.34) giving

$$\ln U(t) = \underbrace{\ln\!\left(\frac{8\nu}{z_+^2\nu_+^2}\,\frac{RT}{F}\left(1 + \frac{\partial \ln f_\pm(c_0)}{\partial \ln c}\right)(1 - t_+(c_0))\,\frac{1}{\pi^2}\,\frac{\Delta\bar{c}^{\,\mathrm{e}}(T_\mathrm{I})}{\bar{c}_0^{\,\mathrm{e}}}\right)}_{O(T_\mathrm{I})} - \underbrace{\frac{\pi^2 D^*_{\pm,\mathrm{eff}}(c_0)}{l^2}}_{m_\ln} t. \tag{5.70}$$

The long-term relaxation of the cell potential $\ln U(t)$ is proportional to the time t whereas O stands for the constant factor in the linear relationship. Based on the constant factor O and Equ. (5.50), it is possible to write

$$f(f_\pm, t_+, D^*_{\pm,\mathrm{eff}}) = \frac{z_+^2\nu_+^2}{8\nu}\,\pi^2\,\frac{F^2}{RT}\,\frac{A}{l}\,\varepsilon\,\bar{c}_0^{\,\mathrm{e}}\,\frac{\exp\,(O(T_\mathrm{I}))}{I_\mathrm{S}}. \tag{5.71}$$

5.5.5 Pulsed galvanostatic polarization

The most famous method for the determination of the coefficient $f(f_\pm, t_+, \sqrt{D^*_{\pm,\mathrm{eff}}})$ is based on the Pulsed Galvanostatic Polarization (PGP) of a two-electrode cell. In this method the concentration difference $\Delta\bar{c}^{\,\mathrm{e}}(T_\mathrm{I})$ between anode and cathode at the current interruption time T_I is used

to determine the coefficient $f(f_\pm, t_+, \sqrt{D^*_{\pm,\mathrm{eff}}})$. The analytical solution of such an procedure is based on the partial differential equation

$$\frac{\partial \overline{c}}{\partial t} - D^*_{\pm,\mathrm{eff}}(c_0)\nabla^2\overline{c} = 0, \qquad \text{in } (0, l/2) \times (0, T_\mathrm{I}),$$

for the half cell with the boundary conditions

$$-\left(-\frac{D^*_{\pm,\mathrm{eff}}(c_0)}{(1-t_+(c_0))}\,\frac{\partial \overline{c}_\mathrm{C}}{\partial x}\right) = \frac{1}{z_+\nu_+F}\,\frac{I}{A}, \tag{5.72}$$

at the cathode and

$$\overline{c}(x) = \overline{c}_0 \qquad \text{for } x \to \infty.$$

The second BC can also be interpreted as $\overline{c}(x) = \overline{c}_0$ for $x \to l/2$ which introduces a limitation for the polarization time. The BC given in Equ. (5.72) is equivalent to Equ. (5.27). In addition, a constant initial concentration profile $\overline{c}^{\,\mathrm{e}}_0$ is assumed at time $t = 0$. This boundary value problem can be solved by Laplace transformation as demonstrated for $\varepsilon = 1$, $\tau = 1$ and $t_+ = 0$ in Bard and Faulkner [14, chap. 8.2.1]. As a result, the concentration difference $\Delta\overline{c}^{\,\mathrm{e}}/2$ between the cathode and $x = l/2$ is given as

$$\frac{\Delta\overline{c}^{\,\mathrm{e}}(t)}{2} = 2\frac{1}{\sqrt{\pi}FA}\,\frac{1}{\varepsilon}\,\frac{(1-t_+(c_0))}{\sqrt{D^*_{\pm,\mathrm{eff}}(c_0)}}\,I_\mathrm{p}\sqrt{t}. \tag{5.73}$$

This relation is also known as the Sand equation. Since a one-dimensional representation of a half cell with constant transport parameters is always symmetric with respect to $x = \frac{l}{2}$ and $\overline{c}^{\,\mathrm{e}} = \overline{c}^{\,\mathrm{e}}_0$, Equ. (5.73) can be multiplied by two to obtain the concentration difference $\Delta\overline{c}^{\,\mathrm{e}}(t)$ between anode and cathode. The insertion of Equ. (5.73) into Equ. (5.34) gives an expression for the coefficient $f(f_\pm, t_+, \sqrt{D^*_{\pm,\mathrm{eff}}})$

$$f(f_\pm, t_+, \sqrt{D^*_{\pm,\mathrm{eff}}}) = \frac{z_+^2\nu_+^2}{4\nu}\,\sqrt{\pi}\,\frac{F^2}{RT}\,A\,\varepsilon\,\bar{c}^{\,\mathrm{e}}_0\,\frac{U(T_\mathrm{I})}{I_\mathrm{p}\sqrt{t}}. \tag{5.74}$$

As in section 5.5.3, $U(T_\mathrm{I})$ is the cell potential measured directly after current interruption. Therefore, the quality of the method can be improved further if the theoretical short-term relaxation behavior after the PGP is used to evaluate the cell potential $U(T_\mathrm{I})$ exactly at current interruption time T_I. According to Hafezi and Newman [77], the cell potential $U(t)$ is proportional to the artificial time τ^*

$$\tau^* = \frac{\sqrt{T_\mathrm{I}}}{\sqrt{t} + \sqrt{t - T_\mathrm{I}}}. \tag{5.75}$$

This formulation is used mainly for polymer electrolytes as, e.g., in Ma et al. [103], Ferry et al. [62] and Doeff et al. [51]. In Zugmann et al. [163], this method is applied to a liquid electrolyte solution.

5.6 Transference number based on data from a concentration cell

Compared to section 5.5, the transference number can also be determined by only two different experimental setups. Based on the known TDF, it is possible to calculate the concentration dependent transference number from experimental data obtained in a concentration cell with a liquid junction, i.e., concentration overpotentials are included. In a concentration cell, two different electrolyte solutions with defined concentrations are brought in contact. In the absence of kinetic reactions at the electrodes, the measured cell potential U is defined as

$$U = \frac{\nu}{z_+\nu_+}\frac{RT}{F}\int_{\mathrm{C}}^{\mathrm{A}}\left[\left(1+\frac{\partial \ln f_\pm(c)}{\partial \ln c}\right)(1-t_+(c))\right]\mathrm{d}\left(\ln \overline{c}^{\,\mathrm{e}}\right), \tag{5.76}$$

which can be derived from Equ. (5.31) with $I = 0$. In accordance with the concentration profile in a polarization cell, A denotes the electrode which is in contact with the higher electrolyte concentration c_{high} and C the electrode which is in contact with the lower electrolyte concentration c_{low}. The measured cell potential U is independent from the porosity ε and the tortuosity τ of the interconnecting porous medium. No restrictions regarding the concentration dependence of the transport parameters are introduced so far.

For a known functional description of the concentration dependent transference number $t_+(c)$ and for many experiments with different combinations of c_{A} and c_{C} covering the concentration range of interest, it is possible to determine the necessary functional parameters of the predefined function by numerical fitting. However, the functional description of the concentration dependent transference number $t_+(c)$ is usually not known a priori. Alternatively, a constant transference number $t_+(c_0)$ within the concentration range $c_0 = 0.5(c_{\mathrm{A}} + c_{\mathrm{C}})$ can be assumed if the concentration difference is small. In this case, the transference number $t_+(c_0)$ can be calculated by

$$t_+(c_0) = 1 - \frac{z_+\nu_+}{\nu}\frac{F}{RT}U\left[\int_{\mathrm{C}}^{\mathrm{A}}\left[\left(1+\frac{\partial \ln f_\pm(c)}{\partial \ln c}\right)\right]\mathrm{d}\left(\ln \overline{c}^{\,\mathrm{e}}\right)\right]^{-1}. \tag{5.77}$$

Compared to all other introduced methods for the determination of the concentration dependent transference number $t_+(c)$, this approach requires the least assumptions, which is a constant transference number within a small concentration range.

5.7 Transference number based on data from a concentration and a polarization cell

In literature, a popular experimental approach for the determination of the transference number is the combination a concentration cell experiments with two-electrode cell experiments. In the two-electrode cell, the diffusion coefficient $D_\pm$ and the coefficients $f(f_\pm, t_+, D^*_{\pm,\mathrm{eff}})$ or $f(f_\pm, t_+, \sqrt{D^*_{\pm,\mathrm{eff}}})$ are determined. In the concentration cell, it is possible to determine a coeffi-

cient of the form $f(f_\pm, t_+)$:

$$U = \frac{\nu}{z_+\nu_+}\frac{RT}{F}\int_{\mathrm{C}}^{\mathrm{A}} \underbrace{\left[\left(1+\frac{\partial \ln f_\pm(c)}{\partial \ln c}\right)(1-t_+(c))\right]}_{f(f_\pm,t_+)} \mathrm{d}\left(\ln \overline{c}^{\,\mathrm{e}}\right),$$

which can be determined by numerical fitting based on many concentration cell experiments with different combinations of c_A and c_C. However, as before, the functional description of the coefficient $f(f_\pm, t_+)$ has to be defined before the fitting procedure can start. This approach is used, e.g., in Ma et al. [103] or Ferry et al. [62]. The same idea is combined with a numerical optimization approach for the two-electrode cell in Nyman et al. [115] or Lundgren et al. [102].

6 Computational approach

Over the last decades, various computational approaches were proposed for the numerical simulation of electrochemical systems. For dilute electrolyte solutions, an overview is given, e.g., in Bauer et al. [19] and Bauer [18]. In contrast, the literature survey given in the following focuses on numerical schemes for concentrated electrolyte solutions as introduced in section 2 and in section 3.

In the year 2000, Botte et al. [29] reviewed different mathematical models for secondary lithium-ion batteries including an overview over used numerical solution schemes. A more recent overview is given, e.g., in Ramadesigan et al. [124]. The classical numerical solution scheme for the concentrated solution theory is the Finite Difference (FD) scheme as presented, e.g., in Newman and Thomas-Alyea [109], Fuller et al. [64], Doyle et al. [54] or Albertus et al. [3]. In these publications, the BAND algorithm introduced in Newman and Thomas-Alyea [109] is utilized for the numerical simulation of battery cells approximated by one-dimensional, volume averaged conservation equations for electrodes and separators as presented in section 3. Algorithmic improvements for the FD scheme and a decoupling of the partial differential equations are suggested in Reimers [126]. In Danilov and Notten [48], an alternative model for concentrated solutions is solved using the pre-implemented Matlab 'pdepe' solver. For such applications, the finite difference scheme is usually a sufficient numerical approach although it has its limitations regarding conservation of mass and discretization of curved domains. Therefore, alternative approaches have to be considered for the simulation of complex computational domains such as a resolved porous medium. In Popov et al. [122], a Finite Volume (FV) method is proposed as a numerical solution scheme for the thermodynamic consistent model suggested by Latz and Zausch [99]. The homogenized model developed by Ferguson and Bazant [61] is also solved using FV scheme implemented in Matlab. However, the most common solution scheme for the concentrated solution theory is the Finite Element Method (FEM) since it is implemented in many commercial software packages. A large flexibility regarding the adaptation or extension of physical models is provided by the software package Matlab. This is the main reason why it is used so frequently in the applied science community as, e.g., in Zadin et al. [158], Cai and White [35], Awarke et al. [12] or Elul et al. [59]. The software package Abaqus is used, e.g., in Awarke et al. [11], where a stress analysis for active material particles is included in the physical model. A more detailed discussion of the finite element method for concentrated solution theory is presented, e.g., in Golmon et al. [70], which includes also a multi-scale investigation with respect to the mechanical behavior.

In the following, the finite element method is presented as a numerical solution scheme for conservation equations describing concentrated binary electrolyte solutions. The numerical solution scheme is based on the computational approach presented in Bauer et al. [19] and Bauer [18]. First, different mathematical formulations for concentrated binary electrolyte solution considered in this contribution are summarized. Afterwards, the weak form of the standard

ion-transport system is given exemplarily (see section 6.2). In section 6.3 the Finite Element Method (FEM) is introduced for the spatial discretization of the weak form. The generalized time-integration scheme is introduced in section 6.4 for the time discretization of the standard Galerkin formulation. The numerical solution scheme for the nonlinear system of equations is given in section 6.5. In section 6.6 the galvanostatic constraint condition proposed in Ehrl et al. [58] is extended by two alternative predictor steps.

6.1 Ion-transport in concentrated binary electrolyte solutions

The ion-transport equations discussed in section 2 are based on a strong enforcement of the electroneutrality condition (see, e.g., Landstorfer and Jacob [98]), which means that the ENC is automatically fulfilled at each point of the computational domain. A similar approach is used for the charge-conservation Nernst-Planck formulation presented in Bauer [18]. On the contrary, the classical Nernst-Planck formulation utilizing the ENC as an closing equation is based on a weak enforcement of the ENC as used, e.g., in Bauer et al. [19]. In case of a strong enforcement of the ENC, it is mathematically sufficient to solve the ion-transport equation of the reactive ionic species. It only has to be the ion-transport equation of the reactive ionic species to be able to apply appropriate boundary conditions.

Standard formulation for ion-transport in concentrated binary electrolyte solutions So far, the ion transport system for concentrated binary electrolyte solutions given in Equ. (4.8) – Equ. (4.10) is always formulated based on three equations, being the ion-transport equation, an expression for the current density and charge conservation. It is possible to solve this system by introducing the current density as an additional primary variable. A positive effect of this approach is an improved fulfillment of the charge conservation. However, the resulting system of equations is larger, has a saddle point structure and does not fulfill the inf-sub condition (see, e.g., Brezzi and Fortin [30]) naturally. Therefore, the ion-transport system is considered in the following form where the ion-transport equation reads as

$$\varepsilon \frac{\partial \bar{c}^{\,\mathrm{e}}}{\partial t} + \nabla \cdot \overline{\boldsymbol{N}} = 0 \tag{6.1}$$

with the molar flux density defined as

$$\begin{aligned} \overline{\boldsymbol{N}} = &- \left[\frac{\varepsilon}{\tau} D_{\pm}(c)\, \nabla \bar{c}^{\,\mathrm{e}} \right] - \left[\frac{\varepsilon}{\tau} \kappa(c) \frac{t_+(c)}{\nu_+ z_+ F}\, \nabla \overline{\Phi}^{\,\mathrm{e}} \right] + \\ &\left[\frac{RT}{F^2} \frac{\varepsilon}{\tau} \kappa(c) \frac{\nu}{\nu_+^2 z_+^2} \left(1 + \frac{\partial \ln f_{\pm}(c)}{\partial \ln c} \right) \big(1 - t_+(c)\big) t_+(c) \frac{\nabla \bar{c}^{\,\mathrm{e}}}{\bar{c}^{\,\mathrm{e}}} \right] \end{aligned} \tag{6.2}$$

and the charge conservation equation as

$$\nabla \cdot \left(\frac{1}{F}\, \bar{\boldsymbol{i}} \right) = 0 \tag{6.3}$$

with current density density defined as

$$\overline{\boldsymbol{i}} = -\frac{\varepsilon}{\tau}\kappa(c)\nabla\overline{\Phi}^{\mathrm{e}} + \frac{RT}{F}\,\frac{\varepsilon}{\tau}\kappa(c)\frac{\nu}{\nu_+ z_+}\left(1 + \frac{\partial \ln f_\pm(c)}{\partial \ln c}\right)\,(1 - t_+(c))\,\frac{\nabla\bar{c}^{\mathrm{e}}}{\bar{c}^{\mathrm{e}}}. \tag{6.4}$$

Here, the charge conservation Equ. (6.3) is divided by the Faraday constant F to ensure a similar scaling compared to the ion-transport equation. The standard formulation Equ. (6.1) – Equ. (6.4) is based on Newman and Thomas-Alyea [109]. In accordance to Kontturi et al. [91], this standard formulation is named Volume-Averaged Diffusion-Conduction (VADC) formulation.

Variation 1 The thermodynamic consistent model introduced by Latz and Zausch [99] and discussed in section 2.6 is considered with the molar flux density

$$\begin{aligned}\overline{\boldsymbol{N}} = &-\left[\frac{\varepsilon}{\tau}D_{\mathrm{e}}(c)\,\nabla\bar{c}^{\mathrm{e}}\right] - \left[\frac{\varepsilon}{\tau}\kappa(c)\frac{t_+(c)}{\nu_+ z_+ F}\,\frac{\nabla\overline{\hat{\mu}}_{\mathrm{e}}^{\mathrm{R}}}{z_+ F}\right] + \\ &\left[\frac{RT}{F^2}\frac{\varepsilon}{\tau}\kappa(c)\frac{\nu}{\nu_+^2 z_+^2}\left[\frac{\nu_+}{\nu RT}\frac{\partial\mu_{\mathrm{e}}}{\partial c}\right]\big(1 - t_+(c)\big)t_+(c)\frac{\nabla\bar{c}^{\mathrm{e}}}{\bar{c}^{\mathrm{e}}}\right]\end{aligned}$$

and the current density

$$\overline{\boldsymbol{i}} = -\frac{\varepsilon}{\tau}\kappa(c)\frac{\nabla\overline{\hat{\mu}}_{\mathrm{e}}^{\mathrm{R}}}{z_+ F} + \frac{RT}{F}\,\frac{\varepsilon}{\tau}\kappa(c)\frac{\nu}{\nu_+ z_+}\left(\frac{\nu_+}{\nu RT}\frac{\partial\mu_{\mathrm{e}}}{\partial c}\right)\,(1 - t_+(c))\,\frac{\nabla\bar{c}^{\mathrm{e}}}{\bar{c}^{\mathrm{e}}}.$$

The implementation of the standard formulation can also be used in this case if the electrostatic potential $\overline{\Phi}^{\mathrm{e}}$ is interpreted as $\overline{\hat{\mu}}_{\mathrm{e}}^{\mathrm{R}}/(z_+F)$ and the thermodynamic factor $\mathcal{X}(c)$ as $\left(\frac{\nu_+}{\nu RT}\frac{\partial\mu_{\mathrm{e}}}{\partial c}\right)$.

Variation 2 The Nernst-Planck approach for dilute electrolyte solutions presented, e.g., in Bauer et al. [19], is reformulated in section 2.5 to a similar form as used for concentrated electrolyte solutions which is in accordance with the dilute limit of the concentrated solution theory. In this case, the molar flux density is given as

$$\overline{\boldsymbol{N}} = -\left[\frac{\varepsilon}{\tau}D_\pm\,\nabla\bar{c}^{\mathrm{e}}\right] - \left[\frac{\varepsilon}{\tau}\kappa(c)\frac{t_+}{\nu_+ z_+ F}\,\nabla\overline{\Phi}^{\mathrm{e}}\right] + \left[\frac{RT}{F^2}\frac{\varepsilon}{\tau}\kappa(c)\left(\frac{\nu_- - \nu t_+}{\nu_+^2 z_+^2}\right)t_+\frac{\nabla\bar{c}^{\mathrm{e}}}{\bar{c}^{\mathrm{e}}}\right]$$

and the current density as

$$\overline{\boldsymbol{i}} = -\frac{\varepsilon}{\tau}\kappa(c)\nabla\overline{\Phi}^{\mathrm{e}} + \frac{RT}{F}\,\frac{\varepsilon}{\tau}\kappa(c)\,\left(\frac{\nu_- - \nu t_+}{\nu_+ z_+}\right)\frac{\nabla\bar{c}^{\mathrm{e}}}{\bar{c}^{\mathrm{e}}}.$$

In the following, this formulation is called Volume-Averaged Dilute Diffusion-Conduction formulation (VADDC).

Variation 3 The first two formulations are based on the volume average of both ion-transport and the charge conservation equation. However, the same equations can be used when considering a computational domain consisting of a non-averaged porous medium. In this case, the

geometrical parameters have to be chosen as $\varepsilon = 1$ and $\tau = 1$. This yields for the volumetric intrinsic phase average of the concentration $\bar{c}^{\,\mathrm{e}}$ and the potential $\bar{\Phi}^{\,\mathrm{e}}$:

$$\overline{c}^{\,\mathrm{e}} = c,$$
$$\overline{\Phi}^{\,\mathrm{e}} = \Phi.$$

For simulations without the volume averaging approach introduced in section 3, the VADC formulation is named Diffusion-Conduction (DC) formulation and the VADDC formulation Dilute Diffusion-Conduction (DDC) formulation.

6.2 Weak formulation

The weak form of a boundary value problem is obtained by the multiplication with appropriate weighting functions and the subsequent integration over the computational domain Ω. The requirements regarding differentiability of the arising weighted residual formulation are decreased by a successive partial integration. The resulting weak form of the boundary value problem is the basis for the spatial discretization procedure performed in the following. The solution of the weak form are those concentration and potential functions for which the weak formulation is fulfilled for all admissible weighting functions.

The space $\mathcal{S}_c$ of trial functions with respect to the equivalent concentration c satisfying the Dirichlet boundary condition on $\Gamma_{\mathrm{D},c}$ is given as

$$\mathcal{S}_c := \left\{ c \in H^1(\Omega) \mid c = g \text{ on } \Gamma_{\mathrm{D},c} \right\}.$$

The corresponding space $\mathcal{T}_c$ of weighting functions is defined as

$$\mathcal{T}_c := \left\{ w \in H^1(\Omega) \mid w = 0 \text{ on } \Gamma_{\mathrm{D},c} \right\}.$$

In addition, the respective spaces of trial and weighting functions for the potential Φ are given as

$$\mathcal{S}_\Phi := \left\{ \Phi \in H^1(\Omega) \mid \Phi = g_\Phi \text{ on } \Gamma_{\mathrm{D},\Phi} \right\}$$

and

$$\mathcal{T}_\Phi := \left\{ \varphi \in H^1(\Omega) \mid \varphi = 0 \text{ on } \Gamma_{\mathrm{D},\Phi} \right\},$$

where the Dirichlet boundary conditions on $\Gamma_{\mathrm{D},\Phi}$ are also satisfied. The space $\mathrm{H}^1(\Omega)$ is a subset of the Hilbert space $\mathrm{L}^2(\Omega)$ and denotes the Sobolev space of $\mathrm{L}^2(\Omega)$-functions possessing a weak derivative. Note that the concentration c and the potential Φ are only defined up to constant in the absence of Dirichlet conditions or equivalent boundary conditions such as the electrode kinetic condition. This is the consequence of the coinciding spaces for trial and weighting functions. For getting a unique solution, different strategies are conceivable such as the definition of a reference value at a single point within the domain Ω or alternative solver strategies utilizing, e.g., the Krylov space projection (see, e.g., Bochev and Lehoucq [26]).

The ion-transport equation given in Equ. (6.1) and the charge conservation in Equ. (6.3) are multiplied with arbitrary weighting functions $w \in \mathcal{T}_c$ and $\varphi \in \mathcal{T}_\Phi$, respectively, and integrated over Ω. As a result, the weighted residual formulations read

$$\int_\Omega w\, \varepsilon \dot{\bar{c}}^{\,\mathrm{e}}\, \mathrm{d}\,\boldsymbol{x} + \int_\Omega w\, \nabla \cdot \overline{\boldsymbol{N}}\, \mathrm{d}\,\boldsymbol{x} = 0 \qquad \forall w \in \mathcal{T}_c, \tag{6.5}$$

$$\int_\Omega \varphi\, \nabla \cdot \left(\frac{1}{F}\, \bar{\boldsymbol{i}}(c, \Phi) \right) \mathrm{d}\,\boldsymbol{x} = 0 \qquad \forall \varphi \in \mathcal{T}_\Phi. \tag{6.6}$$

The second term of Equ. (6.5) and Equ. (6.6) are integrated by parts resulting in

$$\left(w, \varepsilon \dot{\bar{c}}^{\,\mathrm{e}}\right) - \left(\nabla w, \overline{\boldsymbol{N}}\right) + \left(w, \overline{\boldsymbol{N}} \cdot \boldsymbol{n}\right)_\Gamma = 0 \qquad \forall w \in \mathcal{T}_c, \tag{6.7}$$

$$-\left(\nabla \varphi, \frac{1}{F}\, \bar{\boldsymbol{i}}\right) + \left(\varphi, \frac{1}{F}\, \bar{\boldsymbol{i}} \cdot \boldsymbol{n}\right)_\Gamma = 0 \qquad \forall \varphi \in \mathcal{T}_\Phi. \tag{6.8}$$

Here, $(\cdot, \cdot)$ denotes the L^2-inner product in Ω and $(\cdot, \cdot)_\Gamma$ the L^2-inner product on the boundary Γ of Ω. As introduced in section 2.1, the boundary conditions Equ. (2.1) and Equ. (2.4) on the boundary partition $\Gamma = \Gamma_\mathrm{D} \cup \Gamma_\mathrm{N} \cup \Gamma_\mathrm{E}$ and $\Gamma = \Gamma_{\mathrm{D},\Phi} \cup \Gamma_{\mathrm{N},\Phi} \cup \Gamma_{\mathrm{E},\Phi}$ are inserted. In addition, the property $w = 0$ is used on Γ_D and $\varphi = 0$ on $\Gamma_{\mathrm{D},\Phi}$. As a result, the final weak formulation of the binary ion-transport system can be written as

$$\left(w, \varepsilon \dot{\bar{c}}^{\,\mathrm{e}}\right) - \left(\nabla w, \overline{\boldsymbol{N}}\right) - \left(w, \bar{j}(c, \Phi)\right)_{\Gamma_\mathrm{E}} = (w, h)_{\Gamma_\mathrm{N}} \qquad \forall w \in \mathcal{T}_c, \tag{6.9}$$

$$-\left(\nabla \varphi, \frac{1}{F}\, \bar{\boldsymbol{i}}\right) - \left(\varphi, \frac{1}{F}\, \overline{i_n}(c, \Phi)\right)_{\Gamma_{\mathrm{E},\Phi}} = \left(\varphi, \frac{1}{F}\, h_\Phi\right)_{\Gamma_{\mathrm{N},\Phi}} \qquad \forall \varphi \in \mathcal{T}_\Phi. \tag{6.10}$$

In accordance to the notation used in Equ. (6.7) and Equ. (6.8), the L^2-inner product with respect to Γ_N, Γ_E, $\Gamma_{\mathrm{N},\Phi}$ and $\Gamma_{\mathrm{E},\Phi}$ are denoted by $(\cdot, \cdot)_{\Gamma_\mathrm{N}}$, $(\cdot, \cdot)_{\Gamma_\mathrm{E}}$, $(\cdot, \cdot)_{\Gamma_{\mathrm{N},\Phi}}$ and $(\cdot, \cdot)_{\Gamma_{\mathrm{E},\Phi}}$, respectively. Using Equ. (6.2), the second term in Equ. (6.9) can be reformulated to

$$\begin{aligned} -\left(\nabla w, \overline{\boldsymbol{N}}\right) = &\left(\nabla w, \left[\frac{\varepsilon}{\tau} D_\pm(c)\, \nabla \bar{c}^{\,\mathrm{e}}\right]\right) + \left(\nabla w, \left[\frac{\varepsilon}{\tau} \kappa(c) \frac{t_+(c)}{\nu_+ z_+ F}\, \nabla \overline{\Phi}^{\,\mathrm{e}}\right]\right) - \\ &\left(\nabla w, \left[\frac{RT}{F^2} \frac{\varepsilon}{\tau} \kappa(c) \frac{\nu}{\nu_+^2 z_+^2} \left(1 + \frac{\partial \ln f_\pm(c)}{\partial \ln c}\right) \big(1 - t_+(c)\big) t_+(c) \frac{\nabla \bar{c}^{\,\mathrm{e}}}{\bar{c}^{\,\mathrm{e}}}\right]\right). \end{aligned} \tag{6.11}$$

Equivalently, the first term in Equ. (6.10) can be expressed as

$$\begin{aligned} -\left(\nabla \varphi, \frac{1}{F}\, \bar{\boldsymbol{i}}\right) = &\left(\nabla \varphi, \left[-\frac{1}{F} \frac{\varepsilon}{\tau} \kappa(c) \nabla \overline{\Phi}^{\,\mathrm{e}}\right]\right) - \\ &\left(\nabla \varphi, \left[\frac{RT}{F^2} \frac{\varepsilon}{\tau} \kappa(c) \frac{\nu}{\nu_+ z_+} \left(1 + \frac{\partial \ln f_\pm(c)}{\partial \ln c}\right) (1 - t_+(c)) \frac{\nabla \bar{c}^{\,\mathrm{e}}}{\bar{c}_+^{\,\mathrm{e}}}\right]\right), \end{aligned}$$

using Equ. (6.4). Note that the molar flux boundary conditions on $\Gamma_{\mathrm{N},c}$, $\Gamma_{\mathrm{E},c}$ and the current boundary conditions on $\Gamma_{\mathrm{N},\Phi}$, $\Gamma_{\mathrm{E},\Phi}$ are naturally fulfilled assuming sufficiently smooth solution functions. This is an inherent characteristic of the weak form as demonstrated, e.g., in Bauer et al. [19].

To sum up, the entire weak formulation of the binary ion-transport system reads as follows: find $c \in \mathcal{S}_c$ and $\Phi \in \mathcal{S}_\Phi$, such that

$$\begin{aligned}
&\left(w, \varepsilon \dot{\bar{c}}^{\,\mathrm{e}}\right) + \left(\nabla w, \left[\frac{\varepsilon}{\tau} D_\pm(c)\, \nabla \bar{c}^{\,\mathrm{e}}\right]\right) + \left(\nabla w, \left[\frac{\varepsilon}{\tau}\kappa(c) \frac{t_+(c)}{\nu_+ z_+ F}\, \nabla \overline{\Phi}^{\,\mathrm{e}}\right]\right) - \\
&\qquad \left(\nabla w, \left[\frac{RT}{F^2}\frac{\varepsilon}{\tau}\kappa(c)\frac{\nu}{\nu_+^2 z_+^2}\left(1 + \frac{\partial \ln f_\pm(c)}{\partial \ln c}\right)\big(1 - t_+(c)\big) t_+(c) \frac{\nabla \bar{c}^{\,\mathrm{e}}}{\bar{c}^{\,\mathrm{e}}}\right]\right) - \qquad (6.12)\\
&\qquad (w, j)_{\Gamma_\mathrm{E}} = (w, h)_{\Gamma_\mathrm{N}} \qquad\qquad \forall w \in \mathcal{T}_c,
\end{aligned}$$

$$\begin{aligned}
&\left(\nabla \varphi, \left[\frac{1}{F}\frac{\varepsilon}{\tau}\kappa(c) \nabla \overline{\Phi}^{\,\mathrm{e}}\right]\right) - \\
&\left(\nabla \varphi, \left[\frac{RT}{F^2}\frac{\varepsilon}{\tau}\kappa(c)\frac{\nu}{\nu_+ z_+}\left(1 + \frac{\partial \ln f_\pm(c)}{\partial \ln c}\right)\big(1 - t_+(c)\big) \frac{\nabla \bar{c}^{\,\mathrm{e}}}{\bar{c}^{\,\mathrm{e}}_+}\right]\right) - \qquad (6.13)\\
&\left(\varphi, \frac{1}{F} i_n\right)_{\Gamma_{\mathrm{E},\Phi}} = \left(\varphi, \frac{1}{F} h_\Phi\right)_{\Gamma_{\mathrm{N},\Phi}} \qquad\qquad \forall \varphi \in \mathcal{T}_\Phi.
\end{aligned}$$

In a more compact formulation, Equ. (6.12) and Equ. (6.13) can be written as

$$\mathcal{B}_\mathrm{M}(w, c, \Phi) - \mathcal{I}(w, c, \Phi) = \mathcal{F}(w) \qquad \forall w \in \mathcal{T}_c, \qquad (6.14)$$

$$\mathcal{B}_\mathrm{C}(\varphi, c, \Phi) - \mathcal{I}_\mathrm{C}(\varphi, c, \Phi) = \mathcal{F}_\mathrm{C}(\varphi) \qquad \forall \varphi \in \mathcal{T}_\Phi, \qquad (6.15)$$

where the following notation is used:

$$\begin{aligned}
\mathcal{B}_\mathrm{M}(w, c, \Phi) &:= \left(w, \varepsilon \dot{\bar{c}}^{\,\mathrm{e}}\right) + \left(\nabla w, \left[\frac{\varepsilon}{\tau} D_\pm(c)\, \nabla \bar{c}^{\,\mathrm{e}}\right]\right) + \left(\nabla w, \left[\frac{\varepsilon}{\tau}\kappa(c) \frac{t_+(c)}{\nu_+ z_+ F}\, \nabla \overline{\Phi}^{\,\mathrm{e}}\right]\right) - \\
&\qquad \left(\nabla w, \left[\frac{RT}{F^2}\frac{\varepsilon}{\tau}\kappa(c)\frac{\nu}{\nu_+^2 z_+^2}\left(1 + \frac{\partial \ln f_\pm(c)}{\partial \ln c}\right)\big(1 - t_+(c)\big) t_+(c) \frac{\nabla \bar{c}^{\,\mathrm{e}}}{\bar{c}^{\,\mathrm{e}}}\right]\right), \\
\mathcal{I}_\mathrm{M}(w, c, \Phi) &:= (w, j(c, \Phi))_{\Gamma_\mathrm{E}}, \\
\mathcal{F}_\mathrm{M}(w) &:= (w, h)_{\Gamma_\mathrm{N}}, \\
\mathcal{B}_\mathrm{C}(\varphi, c, \Phi) &:= \left(\nabla \varphi, \left[\frac{1}{F}\frac{\varepsilon}{\tau}\kappa(c) \nabla \overline{\Phi}^{\,\mathrm{e}}\right]\right) - \\
&\qquad \left(\nabla \varphi, \left[\frac{RT}{F^2}\frac{\varepsilon}{\tau}\kappa(c)\frac{\nu}{\nu_+ z_+}\left(1 + \frac{\partial \ln f_\pm(c)}{\partial \ln c}\right)\big(1 - t_+(c)\big) \frac{\nabla \bar{c}^{\,\mathrm{e}}}{\bar{c}^{\,\mathrm{e}}}\right]\right), \\
\mathcal{I}_\mathrm{C}(\varphi, c, \Phi) &:= \left(\varphi, \frac{1}{F} i_n(c, \Phi)\right)_{\Gamma_{\mathrm{E},\Phi}},
\end{aligned}$$

and

$$\mathcal{F}_\mathrm{C}(\varphi) := \left(\varphi, \frac{1}{F} h_\Phi\right)_{\Gamma_{\mathrm{N},\Phi}}. \qquad (6.16)$$

As discussed in section 2.7, the current density $\bar{\boldsymbol{i}}$ and the molar flux density $\overline{\boldsymbol{N}}$ are related to each other by Equ. (2.93). As a consequence, the boundary terms $\mathcal{I}_{\mathrm{M}}(w, c, \Phi)$ and $\mathcal{I}_{\mathrm{C}}(w, c, \Phi)$ as well as $\mathcal{F}_{\mathrm{M}}(w, c, \Phi)$ and $\mathcal{F}_{\mathrm{C}}(w, c, \Phi)$ are correlated by the following relations:

$$\mathcal{I}_{\mathrm{C}}(w, c, \Phi) = \nu_+ z_+ \mathcal{I}_{\mathrm{M}}(w, c, \Phi), \tag{6.17}$$

$$\mathcal{F}_{\mathrm{C}}(w, c, \Phi) = \nu_+ z_+ \mathcal{F}_{\mathrm{M}}(w, c, \Phi). \tag{6.18}$$

Note that the Faraday constant F is missing in both equations since the charge conservation equation given in Equ. (6.3) is already scaled with the Faraday constant. The inherent coupling of molar fluxes and current densities has to be considered for the application of boundary conditions. This is straight forward for flux conditions where the corresponding, scaled molar fluxes or current densities have to be applied on the respective boundaries. In case of Dirichlet conditions, the situation is more complex since the molar flux or current density at the Dirichlet boundaries $\Gamma_{\mathrm{D},c}$ and $\Gamma_{\mathrm{D},\Phi}$ are not known a priori. However, the weak form of the ion-transport system provides a method to calculate the molar and current flux densities at the Dirichlet boundaries. A comprehensive overview over a consistent flux calculation is provided, e.g., in Gresho et al. [73] or Bauer [18]. Based on Equ. (6.7) and Equ. (6.8), the molar flux density at $\Gamma_{\mathrm{D},c}$ and the current density at $\Gamma_{\mathrm{D},\Phi}$ are given as

$$\left(w, \overline{\boldsymbol{N}} \cdot \boldsymbol{n}\right)_{\Gamma_{\mathrm{D}}} = -\mathcal{B}_{\mathrm{M}}(w, c, \Phi) \tag{6.19}$$

and

$$\left(\varphi, \frac{1}{F}\bar{\boldsymbol{i}} \cdot \boldsymbol{n}\right)_{\Gamma_{\mathrm{D},\Phi}} = -\mathcal{B}_{\mathrm{C}}(\varphi, c, \Phi), \tag{6.20}$$

respectively. As a result, the molar flux density resulting from a Dirichlet condition on $\Gamma_{\mathrm{D},c}$ can be prescribed as a Neumann condition on $\Gamma_{\mathrm{N},\Phi}$ to ensure a consistent coupling between the molar flux and the current density. The same concept can be applied to a Dirichlet condition on $\Gamma_{\mathrm{D},\Phi}$.

6.3 Standard Galerkin formulation

In the following, the standard Galerkin finite element method is used for the spatial discretization of the weak form of the binary ion-transport system given in Equ. (6.14) and Equ. (6.15). The Galerkin approximation restricts the function spaces to finite-dimensional subspaces $\mathcal{T}^h_{\{c,\Phi\}} \subset \mathcal{T}_{\{c,\Phi\}}$ and $\mathcal{S}^h_{\{c,\Phi\}} \subset \mathcal{S}_{\{c,\Phi\}}$ resulting in a discrete version of the weak form. The standard Galerkin finite element formulation reads: find $c^h \in \mathcal{S}^h_c$ and $\Phi^h \in \mathcal{S}^h_\Phi$ such that

$$\mathcal{B}_{\mathrm{M}}(w^h, c^h, \Phi^h) - \mathcal{I}_{\mathrm{M}}(w^h, c^h, \Phi^h) = \mathcal{F}_{\mathrm{M}}(w^h) \qquad \forall w^h \in \mathcal{T}^h_c, \tag{6.21}$$

$$\mathcal{B}_{\mathrm{C}}(\varphi^h, c^h, \Phi^h) - \mathcal{I}_{\mathrm{C}}(\varphi^h, c^h, \Phi^h) = \mathcal{F}_{\mathrm{C}}(\varphi^h) \qquad \forall \varphi^h \in \mathcal{T}^h_\Phi. \tag{6.22}$$

The computational domain Ω is discretized with n_{el} non-overlapping domains Ω_e, the so-called finite elements, whereas each finite element consists of n_{node} nodal points. Based on this spatial

discretization, the finite element approximation c^h to the concentration c is given as

$$c^h = \sum_{i=1}^{n_{\text{node}}} N_i^h \tilde{c}_i,$$

where $\tilde{c}_i$ denotes the unknown concentration value at node i and N_i^h the shape function associated to node i. A similar approximation is used for the potential Φ^h

$$\Phi^h = \sum_{i=1}^{n_{\text{node}}} N_i^h \tilde{\Phi}_i,$$

where $\tilde{\Phi}_i$ is the unknown potential value at node i. Identical shape functions are used for all solution variables. A more detailed discussion of the finite element method, in general, is provided, e.g., in Zienkiewicz et al. [161]. A specific introduction for scalar transport problems with convective flow is given in Donea and Huerta [52] or Zienkiewicz et al. [162], for instance.

In this work, the stabilized finite element formulation for multi-ion transport proposed in Bauer et al. [20] is not considered since convective transport can usually be neglected as a relevant transport mechanism in typical battery applications. In addition, the so-called 'migration velocity' resulting from the migration term in the dilute solution theory does not show up in the present formulation. Even if an additional convective transport has to be considered for battery applications in the future, there is hardly any application addressing convection-dominated ion-transport in concentrated electrolyte solutions. However, there is no technical reason against the application of the residual-based variational multiscale finite element method to the present framework.

6.4 Time discretization

In this contribution, the generalized-alpha time-integration scheme for a first-order system proposed in Jansen et al. [87] is used for the discretization in time of Equ. (6.21) and (6.22). Originally, the generalized-alpha time-integration scheme was introduced for structural dynamics by Chung and Hulbert [43]. In Bauer et al. [21], the time-integration scheme was already applied successfully to the ion-transport equations in dilute electrolyte solutions. A big advantage of this time-integration scheme is the inherent incorporation of several well-known and popular time integration schemes as special cases as discussed, e.g., in Gamnitzer [65].

The basic principle of the generalized-alpha time-integration scheme is demonstrated based on the general, ordinary differential equation of the order one

$$\frac{\partial}{\partial t} y(t) = f(y(t), t) \tag{6.23}$$

in combination with the initial values for the solution $y(t_0 = 0)$. The time period of interest $[0, T_{\text{end}}]$ is divided into n time steps with the constant interval Δt. The next time value t^{n+1} is related to the previous time t^n by $t^{n+1} = t^n + \Delta t$. In the generalized-alpha time-integration

scheme, two additional intermediate time levels with the parameters α_m and α_f are introduced:

$$t^{n+\alpha_\mathrm{f}} = (1-\alpha_\mathrm{f})t^n + \alpha_\mathrm{f}\, t^{n+1},$$
$$t^{n+\alpha_\mathrm{m}} = (1-\alpha_\mathrm{m})t^n + \alpha_\mathrm{m}\, t^{n+1}.$$

As a result, Equ. (6.23) can be discretized as

$$\dot{y}^{n+\alpha_\mathrm{m}} = f(y^{n+\alpha_\mathrm{f}}, t^{n+\alpha_\mathrm{f}}), \tag{6.24}$$
$$\dot{y}^{n+\alpha_\mathrm{m}} = (1-\alpha_\mathrm{m})\dot{y}^n + \alpha_\mathrm{m}\, \dot{y}^{n+1}, \tag{6.25}$$
$$y^{n+\alpha_\mathrm{f}} = (1-\alpha_\mathrm{f})y^n + \alpha_\mathrm{f}\, y^{n+1}, \tag{6.26}$$
$$y^{n+1} = y^n + \Delta t((1-\gamma)\dot{y}^n + \gamma\, \dot{y}^{n+1}) \tag{6.27}$$

At this point, a third parameter γ is introduced. For a stable method, the relation $\alpha_\mathrm{m} \geq \alpha_\mathrm{f} \geq 0.5$ has to be fulfilled as shown in Jansen et al. [87].

The so-called ρ_∞-family introduced in Jansen et al. [87] is a second-order accurate method characterized by the single parameter ρ_∞. Hence, the parameters α_m, α_f and γ are defined based on this parameter ρ_∞:

$$\alpha_\mathrm{m} = \frac{1}{2}\left(\frac{3-\rho_\infty}{1+\rho_\infty}\right), \qquad \alpha_\mathrm{f} = \frac{1}{1+\rho_\infty} \qquad \text{and} \qquad \gamma = \frac{1}{2} + \alpha_\mathrm{m} - \alpha_\mathrm{f}.$$

The last relation is essential to satisfy second-order accuracy for the generalized-alpha time-integration scheme, in general. A typical value for the parameter $\rho_\infty \in [0;1]$ is $\rho_\infty = 0.5$ which is used throughout this contribution. As a result of this choice, the three parameters of the generalized-alpha time-integration scheme are given as $\alpha_\mathrm{m} = 5/6$, $\alpha_\mathrm{f} = 2/3$ and $\gamma = 2/3$.

The application of generalized-alpha time-integration scheme to Equ. (6.21) and Equ. (6.22) gives

$$\mathcal{B}_\mathrm{M}(w^h, c^{h,n+\alpha_\mathrm{m}}, c^{h,n+\alpha_\mathrm{f}}, \Phi^{h,n+\alpha_\mathrm{f}}) - \mathcal{I}_\mathrm{M}(w^h, c^{h,n+\alpha_\mathrm{f}}, \Phi^{h,n+\alpha_\mathrm{f}}) = \mathcal{F}_\mathrm{M}(w^h) \quad \forall w^h \in \mathcal{T}_c^h, \tag{6.28}$$
$$\mathcal{B}_\mathrm{C}(\varphi^h, c^{h,n+\alpha_\mathrm{f}}, \Phi^{h,n+\alpha_\mathrm{f}}) - \mathcal{I}_\mathrm{C}(\varphi^h, c^{h,n+\alpha_\mathrm{f}}, \Phi^{h,n+\alpha_\mathrm{f}}) = \mathcal{F}_\mathrm{C}(\varphi^h) \quad \forall \varphi^h \in \mathcal{T}_\Phi^h, \tag{6.29}$$

where the term including the time derivative of the concentration c is evaluated at the intermediate time level $n+\alpha_\mathrm{m}$. The solution variables of all remaining terms in Equ. (6.28) and Equ. (6.29) are evaluated at the intermediate time level $n+\alpha_\mathrm{f}$. The residuals $\mathcal{R}_\mathrm{M}(w^h, c^{h,n+1}, \Phi^{h,n+1})$ and $\mathcal{R}_\mathrm{C}(\varphi^h, c^{h,n+1}, \Phi^{h,n+1})$ of the fully discretized standard Galerkin formulation are defined as

$$\begin{aligned}\mathcal{R}_\mathrm{M}(w^h, c^{h,n+1}, \Phi^{h,n+1}) := {} & \mathcal{B}(w^h, c^{h,n+\alpha_\mathrm{m}}, c^{h,n+\alpha_\mathrm{f}}, \Phi^{h,n+\alpha_\mathrm{f}}) - \\ & \mathcal{I}(w^h, c^{h,n+\alpha_\mathrm{f}}, \Phi^{h,n+\alpha_\mathrm{f}}) - \mathcal{F}(w^h) = 0 \qquad \forall w^h \in \mathcal{T}_c^h, \end{aligned} \tag{6.30}$$
$$\begin{aligned}\mathcal{R}_\mathrm{C}(\varphi^h, c^{h,n+1}, \Phi^{h,n+1}) := {} & \mathcal{B}_\mathrm{C}(\varphi^h, c^{h,n+\alpha_\mathrm{f}}, \Phi^{h,n+\alpha_\mathrm{f}}) - \\ & \mathcal{I}_\mathrm{C}(\varphi^h, c^{h,n+\alpha_\mathrm{f}}, \Phi^{h,n+\alpha_\mathrm{f}}) - \mathcal{F}_\mathrm{C}(\varphi^h) = 0 \qquad \forall \varphi^h \in \mathcal{T}_\Phi^h, \end{aligned} \tag{6.31}$$

where the intermediate time levels $n+\alpha_\mathrm{m}$ and $n+\alpha_\mathrm{f}$ are summarized in the time level $n+1$.

6.5 Nonlinear solution procedure

For the following presentation of the nonlinear solution procedure, a solution vector $\boldsymbol{z} = \{\tilde{\boldsymbol{c}}, \tilde{\boldsymbol{\Phi}}\}$ containing all concentration and potential degrees of freedom is defined. A Newton-Raphson scheme is used to solve the residuals of the time discretized standard Galerkin formulation given in Equ. (6.30) and (6.31):

$$\left.\frac{\partial \boldsymbol{F}(\boldsymbol{z}_i^{n+1})}{\partial \boldsymbol{z}^{n+1}}\right|_{\boldsymbol{z}_i^{n+1}} \Delta \boldsymbol{z}_i^{n+1} = -\boldsymbol{F}(\boldsymbol{z}_i^{n+1}). \tag{6.32}$$

Here, $\boldsymbol{F}(\boldsymbol{z})$ contains the residuals of the ion-transport equation and charge conservation given in Equ. (6.30) and Equ. (6.31) in matrix notation. The increment vector $\Delta \boldsymbol{z}_i^{n+1}$ of the iteration i determined by the linear equation system given in Equ. (6.32) is used to calculate the solution vector $\boldsymbol{z}_{i+1}^{n+1}$ of the next iteration step $i+1$:

$$\boldsymbol{z}_{i+1}^{n+1} = \Delta \boldsymbol{z}_i^{n+1} + \boldsymbol{z}_i^{n+1}.$$

The binary ion-transport system at time step $n+1$ reads

$$\boldsymbol{F}(\boldsymbol{z}_i^{n+1}) = \begin{bmatrix} \boldsymbol{R}_{\mathrm{M}}\left(\mathbf{c}_i^{n+1}, \boldsymbol{\Phi}_i^{n+1}\right) \\ \boldsymbol{R}_{\mathrm{C}}\left(\boldsymbol{c}_i^{n+1}, \boldsymbol{\Phi}_i^{n+1}\right) \end{bmatrix} = \begin{bmatrix} \mathbf{0} \\ \mathbf{0} \end{bmatrix} \qquad \text{with } \boldsymbol{z}_i^{n+1} = \begin{bmatrix} \boldsymbol{c}_i^{n+1} \\ \boldsymbol{\Phi}_i^{n+1} \end{bmatrix}, \tag{6.33}$$

where $\boldsymbol{R}_{\mathrm{M}}\left(\boldsymbol{c}_i^{n+1}, \boldsymbol{\Phi}_i^{n+1}\right)$ is defined as

$$\begin{aligned} \boldsymbol{R}_{\mathrm{M}}\left(\boldsymbol{c}_i^{n+1}, \boldsymbol{\Phi}_i^{n+1}\right) = \boldsymbol{M}\dot{\boldsymbol{c}}_i^{n+\alpha_{\mathrm{m}}} + \boldsymbol{D}\left(\boldsymbol{c}_i^{n+\alpha_{\mathrm{f}}}\right) + \boldsymbol{O}_{\mathrm{M}}\left(\boldsymbol{c}_i^{n+\alpha_{\mathrm{f}}}, \boldsymbol{\Phi}_i^{n+\alpha_{\mathrm{f}}}\right) - \\ \boldsymbol{C}_{\mathrm{M}}\left(\boldsymbol{c}_i^{n+\alpha_{\mathrm{f}}}\right) - \boldsymbol{I}_{\mathrm{M}}\left(\boldsymbol{c}_i^{n+\alpha_{\mathrm{f}}}, \boldsymbol{\Phi}_i^{n+\alpha_{\mathrm{f}}}\right) - \boldsymbol{f}_{\mathrm{N}}^{n+\alpha_{\mathrm{f}}} \end{aligned} \tag{6.34}$$

and $\boldsymbol{R}_{\mathrm{C}}\left(\boldsymbol{c}_i^{n+1}, \boldsymbol{\Phi}_i^{n+1}\right)$ as

$$\begin{aligned} \boldsymbol{R}_{\mathrm{C}}\left(\boldsymbol{c}_i^{n+1}, \boldsymbol{\Phi}_i^{n+1}\right) = \boldsymbol{O}_{\mathrm{C}}\left(\boldsymbol{c}_i^{n+\alpha_{\mathrm{f}}}, \boldsymbol{\Phi}_i^{n+\alpha_{\mathrm{f}}}\right) - \boldsymbol{C}_{\mathrm{C}}\left(\boldsymbol{c}_i^{n+\alpha_{\mathrm{f}}}\right) - \\ \boldsymbol{I}_{\mathrm{C}}\left(\boldsymbol{c}_i^{n+\alpha_{\mathrm{f}}}, \boldsymbol{\Phi}_i^{n+\alpha_{\mathrm{f}}}\right) - \boldsymbol{f}_{\mathrm{N},\Phi}^{n+\alpha_{\mathrm{f}}}. \end{aligned} \tag{6.35}$$

Here, $\boldsymbol{M}$ denotes the mass matrix. The matrices $\boldsymbol{D}\left(\boldsymbol{c}_i^{n+\alpha_{\mathrm{f}}}\right)$, $\boldsymbol{O}_{\mathrm{M}}\left(\boldsymbol{c}_i^{n+\alpha_{\mathrm{f}}}, \boldsymbol{\Phi}_i^{n+\alpha_{\mathrm{f}}}\right)$ and $\boldsymbol{C}_{\mathrm{M}}\left(\boldsymbol{c}_i^{n+\alpha_{\mathrm{f}}}\right)$ result from the respective terms in Equ. (6.12). Contributions emanating from electrode kinetic conditions and Neumann conditions are denoted by $\boldsymbol{I}_{\mathrm{M}}\left(\boldsymbol{c}_i^{n+\alpha_{\mathrm{f}}}, \boldsymbol{\Phi}_i^{n+\alpha_{\mathrm{f}}}\right)$ and $\boldsymbol{f}_{\mathrm{N},\Phi}^{n+\alpha_{\mathrm{f}}}$, respectively. The matrices $\boldsymbol{O}_{\mathrm{C}}\left(\boldsymbol{c}_i^{n+\alpha_{\mathrm{f}}}, \boldsymbol{\Phi}_i^{n+\alpha_{\mathrm{f}}}\right)$ and $\boldsymbol{C}_{\mathrm{C}}\left(\boldsymbol{c}_i^{n+\alpha_{\mathrm{f}}}\right)$ arise from the first two terms of the Equ. (6.13). The matrix $\boldsymbol{I}_{\mathrm{C}}\left(\boldsymbol{c}_i^{n+\alpha_{\mathrm{f}}}, \boldsymbol{\Phi}_i^{n+\alpha_{\mathrm{f}}}\right)$ and the vector $\boldsymbol{f}_{\mathrm{N},\Phi}^{n+\alpha_{\mathrm{f}}}$ are the result of kinetic electrode conditions and Neumann conditions. Note that, as a result of the relations given in Equ. (6.17) and (6.18), the matrices $\boldsymbol{I}_{\mathrm{C}}\left(\boldsymbol{c}_i^{n+\alpha_{\mathrm{f}}}, \boldsymbol{\Phi}_i^{n+\alpha_{\mathrm{f}}}\right)$ and $\boldsymbol{I}_{\mathrm{M}}\left(\boldsymbol{c}_i^{n+\alpha_{\mathrm{f}}}, \boldsymbol{\Phi}_i^{n+\alpha_{\mathrm{f}}}\right)$ as well as the vectors $\boldsymbol{f}_{\mathrm{N},\Phi}^{n+\alpha_{\mathrm{f}}}$ and $\boldsymbol{f}_{\mathrm{N}}^{n+\alpha_{\mathrm{f}}}$ are related to each other if kinetic boundary conditions or Neumann conditions are defined at the boundary of the computational domain Ω. As explained in section 6.2, the effect of a Dirichlet condition on $\Gamma_{\mathrm{D},c}$ or $\Gamma_{\mathrm{D},\Phi}$ on the respective charge conservation or ion-transport equation is incorporated into the numerical solution scheme.

As a result, the final linear system of equations solved in each iteration step i can be written as

$$\begin{bmatrix} \boldsymbol{M} + \alpha_f \frac{\gamma\Delta t}{\alpha_\mathrm{m}} \boldsymbol{K}_{wc,i}^{n+1} & \alpha_f \frac{\gamma\Delta t}{\alpha_\mathrm{m}} \boldsymbol{K}_{w\Phi,i}^{n+1} \\ \alpha_f \frac{\gamma\Delta t}{\alpha_\mathrm{m}} \boldsymbol{K}_{\varphi c,i}^{n+1} & \alpha_f \frac{\gamma\Delta t}{\alpha_\mathrm{m}} \boldsymbol{K}_{\varphi\Phi,i}^{n+1} \end{bmatrix} \begin{bmatrix} \Delta \boldsymbol{c}_i^{n+1} \\ \Delta \boldsymbol{\Phi}_i^{n+1} \end{bmatrix} = - \begin{bmatrix} \frac{\gamma\Delta t}{\alpha_\mathrm{m}} \boldsymbol{R}_\mathrm{M}\left(\mathbf{c}_i^{n+1}, \boldsymbol{\Phi}_i^{n+1}\right) \\ \frac{\gamma\Delta t}{\alpha_\mathrm{m}} \boldsymbol{R}_\mathrm{C}\left(\boldsymbol{c}_i^{n+1}, \boldsymbol{\Phi}_i^{n+1}\right) \end{bmatrix}, \tag{6.36}$$

where the matrices are defined as

$$\begin{aligned}
\boldsymbol{K}_{wc,i}^{n+1} &= \frac{\partial}{\partial \boldsymbol{c}^{n+1}} \Big[\boldsymbol{D}\left(\boldsymbol{c}_i^{n+\alpha_\mathrm{f}}\right) + \boldsymbol{O}_\mathrm{M}\left(\boldsymbol{c}_i^{n+\alpha_\mathrm{f}}, \boldsymbol{\Phi}_i^{n+\alpha_\mathrm{f}}\right) - \boldsymbol{C}_\mathrm{M}\left(\boldsymbol{c}_i^{n+\alpha_\mathrm{f}}\right) - \boldsymbol{I}_\mathrm{M}\left(\boldsymbol{c}_i^{n+\alpha_\mathrm{f}}, \boldsymbol{\Phi}_i^{n+\alpha_\mathrm{f}}\right) \Big], \\
\boldsymbol{K}_{w\Phi,i}^{n+1} &= \frac{\partial}{\partial \boldsymbol{\Phi}^{n+1}} \Big[\boldsymbol{O}_\mathrm{M}\left(\boldsymbol{c}_i^{n+\alpha_\mathrm{f}}, \boldsymbol{\Phi}_i^{n+\alpha_\mathrm{f}}\right) - \boldsymbol{I}_\mathrm{M}\left(\boldsymbol{c}_i^{n+\alpha_\mathrm{f}}, \boldsymbol{\Phi}_i^{n+\alpha_\mathrm{f}}\right) \Big], \\
\boldsymbol{K}_{\varphi\Phi,i}^{n+1} &= \frac{\partial}{\partial \boldsymbol{c}^{n+1}} \Big[\boldsymbol{O}_\mathrm{C}\left(\boldsymbol{c}_i^{n+\alpha_\mathrm{f}}, \boldsymbol{\Phi}_i^{n+\alpha_\mathrm{f}}\right) - \boldsymbol{C}_\mathrm{C}\left(\boldsymbol{c}_i^{n+\alpha_\mathrm{f}}\right) - \boldsymbol{I}_\mathrm{C}\left(\boldsymbol{c}_i^{n+\alpha_\mathrm{f}}, \boldsymbol{\Phi}_i^{n+\alpha_\mathrm{f}}\right) \Big], \\
\boldsymbol{K}_{\varphi c,i}^{n+1} &= \frac{\partial}{\partial \boldsymbol{\Phi}^{n+1}} \Big[\boldsymbol{O}_\mathrm{C}\left(\boldsymbol{c}_i^{n+\alpha_\mathrm{f}}, \boldsymbol{\Phi}_i^{n+\alpha_\mathrm{f}}\right) - \boldsymbol{I}_\mathrm{C}\left(\boldsymbol{c}_i^{n+\alpha_\mathrm{f}}, \boldsymbol{\Phi}_i^{n+\alpha_\mathrm{f}}\right) \Big].
\end{aligned}$$

As stated, e.g., in Gravemeier and Wall [72], the time integration factors $\frac{\gamma\Delta t}{\alpha_\mathrm{m}}$ and $\alpha_f \frac{\gamma\Delta t}{\alpha_\mathrm{m}}$ of the generalized-alpha time-integration scheme result from the Newton-Raphson linearization of the intermediate time levels with respect to the time level $n+1$:

$$\frac{\partial \dot{\boldsymbol{c}}^{n+\alpha_\mathrm{m}}}{\partial \boldsymbol{c}^{n+1}} = \frac{\partial \dot{\boldsymbol{c}}^{n+\alpha_\mathrm{m}}}{\partial \dot{\boldsymbol{c}}^{n+1}} \frac{\partial \dot{\boldsymbol{c}}^{n+1}}{\partial \boldsymbol{c}^{n+1}} = \frac{\alpha_\mathrm{m}}{\gamma\Delta t}, \qquad \frac{\partial \boldsymbol{c}^{n+\alpha_\mathrm{f}}}{\partial \boldsymbol{c}^{n+1}} = \alpha_\mathrm{f} \qquad \text{and} \qquad \frac{\partial \boldsymbol{\Phi}^{n+\alpha_\mathrm{f}}}{\partial \boldsymbol{\Phi}^{n+1}} = \alpha_\mathrm{f}.$$

These relations are derived based on Equ. (6.25) – Equ. (6.27). The whole linear system of equations given in Equ. (6.36) is scaled with $\frac{\gamma\Delta t}{\alpha_\mathrm{m}}$ to ensure a mass matrix $\boldsymbol{M}$ without additional scaling factors.

The linear equation system defined by Equ. (6.36) can be solved using iterative Krylov methods (see, e.g., Saad [129]), combined with algebraic multigrid preconditoners (see, e.g., U. Trottenberg [141]). Compared to an ion-transport system closed by the mathematical electroneutrality condition resulting in a saddle-point structure of the linear equation system as discussed, e.g., in Bauer [18], no special solution strategies are required for the considered linear system of equations.

6.6 Galvanostatic constraint condition

For galvanostatic problems, the polarization current $I_\mathrm{p}(t)$ passing an electrochemical system is prescribed. In experiments, an external control device is used to continually adjust the applied cell voltage to the prescribed current curve. The continuous adjustment of the cell voltage also has to be realized numerically within the computational approach. In the following, the focus is on galvanostatic applications, for which the polarization current is kept constant over time.

As outlined in section 2.1, the boundary Γ_E can be subdivided into any number of cathodic and anodic parts representing the electrode surfaces. In the following, an exclusive decompo-

Algorithm 1 Galvanostatic constraint condition

Solve ion-transport system Equ. (6.32)

Compute $\Delta\Phi^{\mathrm{C}}_{i,j}, \Delta\Phi^{\mathrm{A}}_{i,j}$ **and** $\Delta\Phi^{\mathrm{e}}_{i,j}$**:**

$$\left.\frac{\partial \mathcal{R}^{\mathrm{C}}_{\mathrm{E}}\left(\Phi^{\mathrm{C}}_{i,j}\right)}{\partial \Phi^{\mathrm{C}}}\right|_{\Phi^{\mathrm{C}}_{i,j}} \Delta\Phi^{\mathrm{C}}_{i,j} = -\mathcal{R}^{\mathrm{C}}_{\mathrm{E}}\left(\Phi^{\mathrm{C}}_{i,j}\right) \tag{6.37}$$

$$\left.\frac{\partial \mathcal{R}^{\mathrm{A}}_{\mathrm{E}}\left(\Phi^{\mathrm{A}}_{i,j}\right)}{\partial \Phi^{\mathrm{A}}}\right|_{\Phi^{\mathrm{A}}_{i,j}} \Delta\Phi^{\mathrm{A}}_{i,j} = -\mathcal{R}^{\mathrm{A}}_{\mathrm{E}}\left(\Phi^{\mathrm{A}}_{i,j}\right) \tag{6.38}$$

$$\Delta\Phi^{\mathrm{e}}_{i,j} \approx R_{i,j}\Delta I_{n,i,j}$$

Check convergence:

$$|\Delta\Phi^{\mathrm{C}}_{i,j} + \Delta\Phi^{\mathrm{A}}_{i,j} + \Delta\Phi^{\mathrm{e}}_{i,j}| \leq \varepsilon_{\mathrm{GCC}},$$
$$|\mathcal{R}^{\mathrm{C}}_{\mathrm{E}}\left(\Phi^{\mathrm{C}}_{i,j}\right)| \leq \varepsilon_{\mathrm{R}} \text{ and } |\mathcal{R}^{\mathrm{A}}_{\mathrm{E}}\left(\Phi^{\mathrm{A}}_{i,j}\right)| \leq \varepsilon_{\mathrm{R}} \tag{6.39}$$

Update:

$$U_{i,j+1} = U_{i,j} + \Delta U_{i,j} \tag{6.40}$$

sitions based on two electrodes, a cathode $\Gamma^{\mathrm{C}}_{\mathrm{E}}$ and an anode $\Gamma^{\mathrm{A}}_{\mathrm{E}}$ is considered. However, the consideration of any number of electrode surfaces does not pose a problem for the presented computational approach. Each electrode surface represents an equipotential surface on the metal side of the corresponding metal-solution interface. The electric potential on the metal side of the cathode $\Gamma^{\mathrm{C}}_{\mathrm{E}}$ and anode $\Gamma^{\mathrm{A}}_{\mathrm{E}}$ are denoted by Φ^{C} and Φ^{A}, respectively. The overall cell voltage $U = \Phi^{\mathrm{A}} - \Phi^{\mathrm{C}}$ resulting from the Faradaic current I_{n} follows the prescribed current I_{p}. Thus, at each time t, the following equations have to be satisfied both at the cathode and anode surface, respectively:

$$\mathcal{R}^{\mathrm{C}}_{\mathrm{E}}\left(\Phi^{\mathrm{C}}\right) := I_{\mathrm{p}} - I^{\mathrm{C}}_{\mathrm{n}}\left(\Phi^{\mathrm{C}}\right) = I_{\mathrm{p}} - \int_{\Gamma^{\mathrm{C}}_{\mathrm{E}}} i^{\mathrm{C}}_{\mathrm{n}}\left(\Phi^{\mathrm{C}}\right) \mathrm{d}S = 0 \qquad \text{on } \Gamma^{\mathrm{C}}_{\mathrm{E}} \times (0, T_{\mathrm{end}}), \tag{6.41}$$

$$\mathcal{R}^{\mathrm{A}}_{\mathrm{E}}\left(\Phi^{\mathrm{A}}\right) := I_{\mathrm{p}} - I^{\mathrm{A}}_{\mathrm{n}}\left(\Phi^{\mathrm{A}}\right) = I_{\mathrm{p}} - \int_{\Gamma^{\mathrm{A}}_{\mathrm{E}}} i^{\mathrm{A}}_{\mathrm{n}}\left(\Phi^{\mathrm{A}}\right) \mathrm{d}S = 0 \qquad \text{on } \Gamma^{\mathrm{A}}_{\mathrm{E}} \times (0, T_{\mathrm{end}}), \tag{6.42}$$

where $I_{\mathrm{n}} = I^{C}_{\mathrm{n}} = I^{A}_{\mathrm{n}}$ has to hold to ensure charge conservation. The current I_{p} can also be expressed as the mean current density $i_{\mathrm{p}} = I_{\mathrm{p}}/A$ where A denotes the respective electrode surface. The superscript $n+1$ indicating the current time step is not used in this section to simplify notation. For the case of only one reactive ionic species and a single electrochemical reaction process, the Faradaic current density i_{n} normal to an electrode surface is given by any reaction model defined in section 2.7. Note that Equ. (6.41) and Equ. (6.42) are nonlinear since i_{n} depends on all governing equations of the electrochemical system given in Equ. (6.1) and Equ. (6.3), including nonlinear bulk and boundary equations. From a computational point of view it is convenient to

set $\Phi^{\mathrm{A}} = 0\,\mathrm{V}$ to define a zero level for the electric potential. Given that, $U = -\Phi^{\mathrm{C}}$ represents the only additional degree of freedom within the considered Galvanostatic Constraint Condition (GCC). Based on a Newton-Raphson scheme, increments $\Delta\Phi^{\mathrm{C}}_{i,j}$, $\Delta\Phi^{\mathrm{A}}_{i,j}$ and $\Delta\Phi^{\mathrm{e}}_{i,j}$ are computed iteratively, yielding the new overall cell potential

$$U_{i,j+1} = -\Phi^{\mathrm{C}}_{i,j+1} = \underbrace{-\Phi^{\mathrm{C}}_{i,j}}_{=U_{i,j}} + \underbrace{\Delta\Phi^{\mathrm{C}}_{i,j} + \Delta\Phi^{\mathrm{A}}_{i,j} + \Delta\Phi^{\mathrm{e}}_{i,j}}_{=:\Delta U_{i,j}},$$

until convergence is achieved, as shown in Algorithm 1.

After solving the ion-transport system Equ. (6.36), the new overall cell potential needs to be evaluated. Therefore, the potential increments $\Delta\Phi^{\mathrm{C}}_{i,j}$ and $\Delta\Phi^{\mathrm{A}}_{i,j}$ depending on the results of the ion-transport solver in GCC iteration j are determined via Equ. (6.37) and Equ. (6.38). An additional potential increment $\Delta\Phi^{\mathrm{e}}_{i,j}$ accounting for the potential drop within the electrolyte solution is also necessary to preserve a fast convergence rate of the applied overall cell potential $U_{i,j+1}$. This predictor step is particularly important for electrolyte solutions with a high potential drop within the electrolyte as it is the case for rather long distances between the electrodes or electrolyte solutions with a rather low ionic conductivity. The electrical resistance of an electrolyte solution can be approximated by Ohm's law, including a one-dimensional projection of the two-dimensional or three-dimensional domain:

$$\Delta\Phi^{\mathrm{e}}_{i,j} \approx \underbrace{\frac{\tau}{\varepsilon\kappa}\frac{L}{A}}_{R_{i,j}}\underbrace{(-I_{\mathrm{p}} + I_{\mathrm{n},i,j})}_{\Delta I_{n,i,j}}. \tag{6.43}$$

Here, κ is the specific conductivity of the bulk electrolyte solution, A the area of an electrode, and generally, L the average length of the electric field lines (for simple geometries, L is the inter-electrode distance). For this preconditioner, the electrical resistance $R_{i,j}$ is constant $R_{i,j} = R$ since the conductivity is computed once in the beginning assuming a uniform concentration level. Conductivity variations in the electrolyte solution due to concentration variations in the vicinity of the electrode are neglected in this approximation. Thus, this approach is only valid for small concentration variations across the electrolyte solutions. For significant concentration variations, the approximation given in Equ. (6.43) underestimates the potential drop which results in an increased number of GCC iterations. This becomes particularly important if the applied current density is close to the limiting current. Therefore, the constant conductivity κ used for the calculation of the resistance $R_{i,j}$ in Equ. (6.43) is replaced by the volume average of the concentration dependent conductivity $\kappa(c)$ to improve the quality of the predicted potential increment:

$$R_{i,j} = \frac{L}{A}\frac{1}{V}\int_{\Omega}\frac{\tau}{\varepsilon\kappa(c)}\,\mathrm{d}\,\boldsymbol{x}. \tag{6.44}$$

Here, a one-dimensional projection of the two-dimensional or three-dimensional domain is also used as in Equ. (6.43) which requires a basic knowledge about the average length of the electric field lines L in the beginning of the simulation. For simple domains the length L is usually known but it can only be approximated for complex geometries.

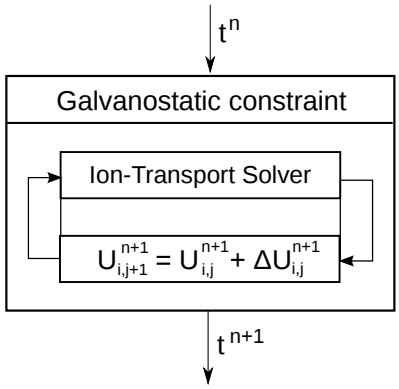

Figure 6.1: Numerical solution scheme for the galvanostatic constraint condition.

The length L is not necessary if the resistance $R_{i,j}$ is calculated according to

$$R_{i,j} = \frac{\Delta\Phi_{i,j}}{I_{\mathrm{n},i,j}}. \tag{6.45}$$

In this third variant, all effects such as geometry, ohmic potential drop and concentration overpotentials are included automatically which should result in an optimal prediction for the new cell potential $U_{i,j+1}$. Here, the current flow $I_{\mathrm{n},i,j}$ based on the previous GCC iteration is used for a consistent calculation of the resistance $R_{i,j}$.

After determining $U_{i,j+1}$ in the update step given in Equ. (6.40) and if not converged, the ion-transport system Equ. (6.36) has to be solved again to compute the new current $I_{\mathrm{n},i,j+1}$ and the resulting variations in all solution variables caused by the new overall cell voltage $U_{i,j+1}$. The GCC iteration is terminated when the absolute value of the computed voltage increment falls below a user-specified tolerance $\varepsilon_{\mathrm{GCC}}$ or the absolute L_2 error norm of the residuals $|\mathcal{R}_{\mathrm{E}}^{\mathrm{C}}\left(\Phi_{i,j}^{\mathrm{C}}\right)|$ and $|\mathcal{R}_{\mathrm{E}}^{\mathrm{A}}\left(\Phi_{i,j}^{\mathrm{C}}\right)|$ is smaller than ε_{R}, where ε_{R} denotes the tolerance for the residual norm. To proceed to the next time step, both the criteria for terminating the outer iteration loop and the GCC have to be fulfilled. The iterative scheme for a computation including the GCC is shown in Fig. 6.1.

The proposed methodology works also for simpler cases, for example, when neglecting contributions due to anode overpotential $\Delta\Phi_{i,j+1}^{\mathrm{A}}$ and ohmic drop $\Delta\Phi_{i,j}^{\mathrm{e}}$. However, as a consequence, very slow convergence can be observed for particular configurations, since the computed voltage increment is considerably underestimated if not all potential increments are considered. In the presented method, a temporal or spatial distribution of the local current density is not assumed; only the total amount of current is controlled. This galvanostatic control can be easily added to already existing electrochemical solution schemes, just introducing a GCC loop. The evaluation of I_{n} and its derivative represent the only additional evaluations in the galvanostatic solution procedure.

A potential future extension would be a simultaneous solution of the equation for U and all governing equations of the electrochemical problem. This would result in a monolithic solution approach for galvanostatic applications with U as an additional degree of freedom. In that case, no nested solution loops would be required.

7 Numerical examples

In this chapter, various numerical examples are presented to demonstrate the robustness and the accuracy of the computational method introduced in section 6. In addition, the general applicability of the computational method to miscellaneous problems such as one-dimensional volume averaged simulations of porous media or simulations of complex three-dimensional geometries is proven in this section.

This chapter is organized as follows. In the beginning, some generally valid simulation parameters are introduced which are used throughout this contribution. In section 7.2, the Dilute Diffusion-Conduction (DDC) formulation is compared with two different computational methods for dilute electrolyte solutions presented in Bauer et al. [19] using a three-dimensional example with a known analytical solution. It is shown that all three computational methods yield the same results, but the efficiency is different. In section 7.3, the optimal convergence rate of the Volume Averaged Diffusion-Conduction (VADC) scheme is demonstrated for a one-dimensional problem. In section 7.4, the VADC formulation is compared with numerical results presented in Thorat et al. [140]. In addition, the numerical efficiency of the galvanostatic constraint condition proposed in section 6.6 is investigated. The different methods for the determination of the diffusion coefficient and the transference number introduced in section 5 are evaluated in section 7.5. These examples can also be considered as numerical validation of the VADC formulation. The applicability of the Diffusion-Conduction (DC) formulations for complex three-dimensional geometries is demonstrated in section 7.6.

7.1 General simulation procedures and parameters

The following simulation procedures and parameters are used for the simulations presented in this chapter if not explicitly mentioned otherwise. The computational domain is always discretized by linear finite elements. For three-dimensional problem setups, hexahedral elements with tri-linear shape functions are used. Two-dimensional geometries are discretized by bilinearly interpolated quadrilateral elements and a one-dimensional domain is meshed with linearly interpolated line elements. For all simulations presented in this section, the second-order accurate generalized-alpha time-integration scheme presented in section 6.4 is used. The three parameters of this time-integration scheme are $\alpha_\mathrm{m} = 5/6$, $\alpha_\mathrm{f} = 2/3$ and $\gamma = 2/3$. In all simulations, the following units are used for the amount of substance, current, voltage, space and time: μmol, μA, V, mm and s.

With the exception of the numerical example presented in section 7.2, all simulations are based on lithium salts with stoichiometry $\nu_+ = \nu_- = 1$ and charge numbers $z_+ = -z_- = 1$. As a result, the concentration of the cation, the anion and the salt are equivalent, i.e., $c_+ = c_- =$

c. This simplification is quite realistic since many of the lithium-based salts as, e.g., $LiClO_4$, $LiAsF_6$, $LiBF_4$ and $LiPF_6$ fulfill this condition.

Since the initial transients in experiments are important, e.g., for the determination of transport parameters, it is crucial to model them correctly in numerical simulations. If required, a simulation is started with a kick-start, although the application of the full load at $t = 0$ is numerically more challenging than ramping it up slowly. For such a kick-start, the initial time step size Δt has to be very small. The time step is increased later in discrete steps. Additionally, it is beneficial to calculate the initial time derivative $\dot{c}$ at $t = 0$ based on the relation

$$\varepsilon \frac{\partial \overline{c}^{\mathrm{e}}}{\partial t} = -\nabla \cdot \overline{\boldsymbol{N}}(c, \Phi),$$

using all BCs, the initial concentration field $\overline{c}_0^{\mathrm{e}}$ and a consistent potential field $\overline{\Phi}_0^{\mathrm{e}}$ determined by Equ. (6.3).

An important method for the determination of transport parameters is based on relaxation experiments. In such experiments, the polarization phase induced by the application of a polarization current I_{p} or potential U_{p} is followed by a relaxation phase with no-flux boundary conditions at the cathode and the anode. The polarization phase always obeys a Butler-Volmer law of the form Equ. (2.97) describing the kinetic effects at the electrode surfaces. The transfer form polarization to relaxation at the current interruption time T_{I} is realized by a restart from the last time step during the polarization phase with the original BCs replaced by no-flux BCs. During the relaxation process, the uniqueness of the numerical solution for the potential field is guaranteed by the Krylov space projection as introduced in Bochev and Lehoucq [26]. The advantage of this method is that the reference level of the potential field after current interruption is defined by the potential field before current interruption. However, the time step size has to be very small to avoid oscillations in the potential field.

In all simulations, an iterative Krylov solver with an algebraic multigrid preconditioner is used for solving the linear system of equations

7.2 Transient three-dimensional diffusion-migration problem for dilute electrolytes

As explained in section 2, the dilute solution theory is a special case of the concentrated solution theory with a constant diffusion coefficient $D_{\pm}$, transference number t_+ and thermodynamic factor $\left(1 + \frac{\partial \ln f_{\pm}}{\partial \ln c}\right) = 1$. Additionally, the potential Φ has to be defined with respect to the negative ionic species present in the electrolyte solution. In this special case, the analytical solution for the three-dimensional transient diffusion-migration problem introduced in Bauer et al. [19] can be used to validate the basic implementation of the concentrated solution theory. Therefore, the standard Galerkin DDC formulation is compared to the standard Galerkin formulations of the Electroneutrality-Nernst-Planck (ENP) and Charge-conservation Nernst-Planck (CNP) systems introduced in Bauer et al. [19] and Bauer [18].

The transient diffusion-migration problem presented in Bauer et al. [19] can be described as a relaxation process starting from predefined initial concentration fields $c_{+,0}$ and $c_{-,0}$ with

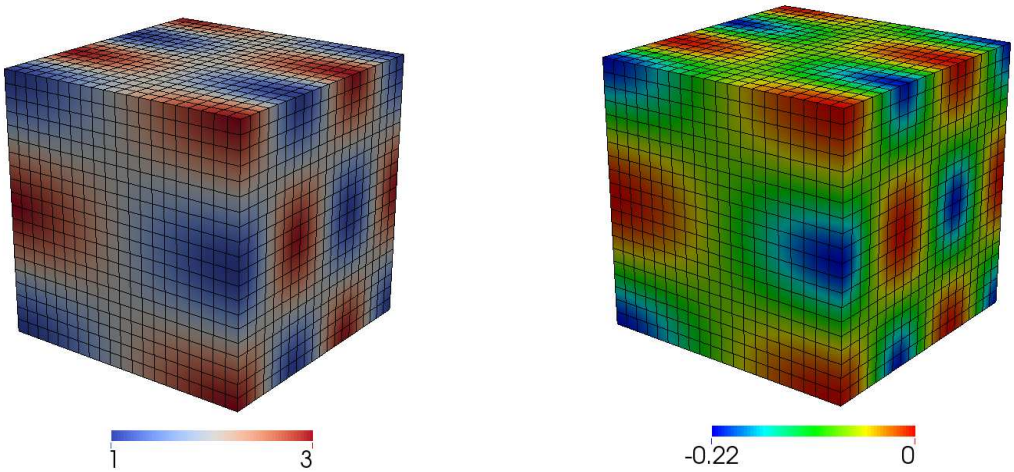

(a) Initial concentration field $c_{+,0}$.

(b) Initial potential field Φ_0.

Figure 7.1: Initial concentration field $c_{+,0}$ and potential field Φ_0 for the transient three-dimensional ion-transport problem with element length $h = 0.05$.

zero-flux conditions at all boundaries and for all ionic species. The time-dependent relaxation process of the concentration field c_+ is described by the relation

$$c_+(x, y, z, t) = 2.0 + \cos(\pi x)\cos(2\pi y)\cos(3\pi z)\exp(-14 D_\pm \pi^2 t),$$

where x, y and z denote the spatial coordinates, t the time and $D_\pm$ the binary diffusion coefficient. As a result of the ENC, the analytical solution for the concentration field c_- is

$$c_-(x, y, z, t) = -\frac{z_+}{z_-} c_+(x, y, z, t).$$

Note that the concentration c_- of the negative ionic species is only a solution variable in the ENP formulation, but not in the DDC and CNP formulations. The potential field Φ can also be calculated from the concentration field c_+ by the relation

$$\frac{F}{RT}\Phi(x, y, z, t) = \left(\frac{\nu_- - \nu t_+}{\nu_+ z_+}\right) \ln\left(\frac{c_+(x, y, z, t)}{c_+(0, 0, 0, t)}\right). \tag{7.1}$$

Compared to the formulation given in Bauer et al. [19], the analytical solution for the potential field Φ is reformulated to be consistent with the DDC formulation. As in the original publication, the factor F/RT is assumed to be 1.0. In contrast to the definition given in section 7.1, a different salt with stoichiometry $\nu_+ = 2$, $\nu_- = 1$ and charge numbers $z_+ = 1$, $z_- = -2$ is used. The initial concentration field $c_{+,0}$ is given in Tab. 7.1 and depicted in Fig. 7.1(a). The initial potential field Φ_0 shown in Fig. 7.1(b) can be calculated from Equ. (7.1). The remaining parameters such as geometrical dimensions, discretization and transport parameters are summarized in Tab. 7.1.

Spatial convergence is investigated for five uniform discretizations with characteristic element lengths $h = 0.2$, $h = 0.1$, $h = 0.05$, $h = 0.025$ and $h = 0.0125$ utilizing absolute errors $||c_+^h - c_+||_{\mathrm{L}_2(\Omega)}$ and $||\Phi^h - \Phi||_{\mathrm{L}_2(\Omega)}$ based on the L^2-norm. The results are depicted in Fig. 7.2.

Table 7.1: Dimensionless simulation parameters for the transient three-dimensional diffusion-migration problem based on the dilute solution theory.

Computation domain Ω	$(0,1)^3$
Number of elements	5^3, 10^3, 20^3, 40^3, 80^3
Element size h	0.2, 0.1, 0.05, 0.025, 0.0125
Porosity ε	1
Tortuosity τ	1
Initial concentration $c_{+,0}$	$2.0 + \cos(\pi x)\cos(2\pi y)\cos(3\pi z)$
Time step Δt	0.005
End time T_{end}	0.1
Charge numbers z_k	$z_+ = 1$, $z_- = -2$
Stoichiometry η_k	$\eta_+ = 2$, $\eta_- = 1$
Diffusion coefficient $D_\pm$	$2.4 \cdot 10^{-3}$
Transference number t_+	0.2
Thermodynamic factor $\left(1 + \frac{\partial \ln f_\pm}{\partial \ln c}\right)$	1
Conductivity κ	$\frac{F^2}{RT}\, 10.0 \cdot 10^{-3} c$

Both the concentration c_+ and the potential Φ computed with the DDC and ENP formulations exhibit a second-order convergence rate. Additionally, the absolute errors produced by the DDC and ENP formulations are equal within the chosen tolerance 10^{-12} for the linear solver and the Newton iteration. The same results are also obtained for the CNP formulation. This is expected since the DDC, ENP and CNP formulations are analytically equivalent. In this contribution, temporal convergence is not explicitly investigated since the numerical results are identical for simulations with different time step sizes Δt. This indicates that the implementations of the three formulations are absolutely equivalent.

In a next step, the computational efficiency of the three formulations is estimated and compared to each other. The numbers are based on discretizations with 20^3 and 40^3 elements. The most efficient formulation with respect to element evaluation time is the CNP formulation. The ENP formulation is about a factor 1.4 slower than the CNP formulation, and the DDC formulation is about a factor 2.05 slower. The reason for the difference between the CNP and ENP formulations is that the ENP formulation is based on three Degrees Of Freedom (DOF) per node (c_+, c_- and Φ) whereas the CNP formulation is only based on two DOF per node (c_+ and Φ). In case of the DDC formulation, the element evaluation time is increased compared to the CNP and ENP formulations since the same implementation is used as for the DC formulation involving

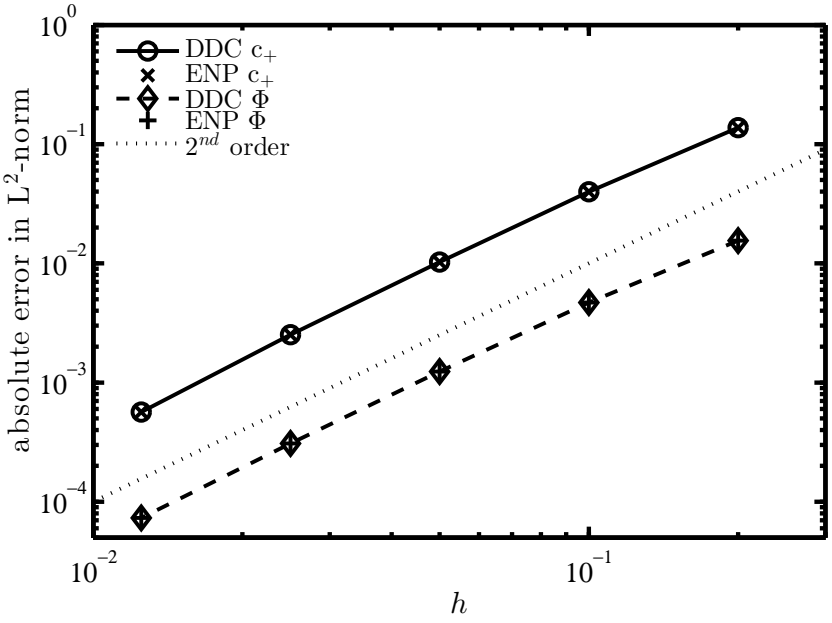

Figure 7.2: Spatial convergence of the abslute error of the concentration field c_+ and the electric potential field Φ over the element size h.

concentration dependent transport parameters as shown in Equ. (6.1) – Equ. (6.4). As a result, the computational costs for the complete linearization of all terms are much higher. This effect even dominates the decreased number of DOF as compared to the ENP formulation. The efficiency of the DDC and DC formulations could be increased by exploiting similarities between the second terms on the right-hand sides in Equ. (6.2) and (6.4) in the implementation. The averaged number of linear iterations per Newton iteration is comparable for the DDC and CNP formulation amounting to 18.55 and 18.25 linear iterations, respectively. The ENP formulation requires about 48.5 linear iterations per Newton step until the solution is converged. The ENP formulation is based on a weak enforcement of the ENC and yields a saddle point system requiring special solution strategies. By contrast, the element matrices resulting from the DDC and CNP formulations are completely filled due to the strong enforcement of the ENC allowing the usage of standard non-linear solvers. Improved solution strategies for saddle point systems may reduce the number of linear iterations required for the ENP formulation. All three formulations converge within three Newton iterations. The same qualitative behavior of the element evaluation time and number of linear iterations can also be observed in other numerical examples, although the absolute numbers may be different.

7.3 Transient one-dimensional ion-transport problem for concentrated electrolytes

In the previous section, it is demonstrated that the Dilute Diffusion-Conduction (DDC) formulation gives the same results as the dilute solution theory presented in Bauer et al. [19]. The standard Diffusion-Conduction (DC) formulation is based on the same implementation where all transport parameters are potentially concentration dependent. In this section, the convergence behavior of the Volume Averaged Diffusion-Conduction (VADC) formulation is investigated for a one-dimensional computational domain with Dirichlet boundary conditions on the concentration at both ends. The Dirichlet boundary conditions are ramped up linearly until the maximum values are reached at $T_{\text{end}} = 1$. To define a reference value for the potential field $\overline{\Phi}^{\text{e}}$, the potential is set to zero at $x = 0.1$. The domain is discretized uniformly by a varying number of elements with element lengths h as given in Tab. 7.2. Since there is no analytical solution available, a simulation with 5480 linearly-interpolated line elements is used as reference solution. The remaining parameters such as geometrical dimensions, discretization and transport parameters are summarized in Tab. 7.2.

The concentration and potential profiles of the reference solution involving 5120 elements are depicted in Fig. 7.3. In case A, the variation of the concentration is limited to ± 0.2 M whereas the mass-transport limited current is reached in case B. Both concentration profiles exhibit distinct diffusion layers at the cathode and the anode enclosing a bulk region of unchanged concentration. In this bulk region, the potential $\overline{\Phi}^{\text{e}}$ shows a linear behavior since Equ. (6.4) simplifies to

$$\overline{\boldsymbol{i}} = -\frac{\varepsilon}{\tau}\kappa(c)\nabla\overline{\Phi}^{\text{e}}$$

in the absence of concentration gradients. Hence, the gradient of the potential is determined by the overall current flow which is much higher in case B. In the bulk region, the only active transport mechanism is migration where the cations move towards the cathode $x = 0$ and the anions towards the anode $x = 0.1$. Within the diffusion layers, the potential is also influenced by concentration gradients resulting in a deviation from the linear potential profile. This is particularly pronounced in case B with the mass-transport limited current. Two effects influence the deviation from the linear behavior in the bulk region. The first effect is the non-constant conductivity $\kappa(c)$ and the second effect is the influence of the last term in Equ. (6.4), the so-called concentration overpotential.

The resulting spatial convergence in case A and case B is depicted in Fig. 7.4(a) and Fig. 7.4(b), respectively. In these figures, the relative errors

$$\varepsilon_{\overline{c}^{\text{e}}} = \frac{||\overline{c}^{\text{e},h} - \overline{c}^{\text{e}}||_{\text{L}_2(\Omega)}}{||\overline{c}^{\text{e}}||_{\text{L}_2(\Omega)}} \qquad \text{and} \qquad \varepsilon_{\overline{\Phi}^{\text{e}}} = \frac{||\overline{\Phi}^{\text{e},h} - \overline{\Phi}^{\text{e}}||_{\text{L}_2(\Omega)}}{||\overline{\Phi}^{\text{e}}||_{\text{L}_2(\Omega)}}$$

are used. In case A, both the concentration and the potential exhibit a perfect second-order convergence rate. In case B, only the concentration shows a second-order convergence rate over the entire range of the element length h. The potential approaches the second-order convergence rate

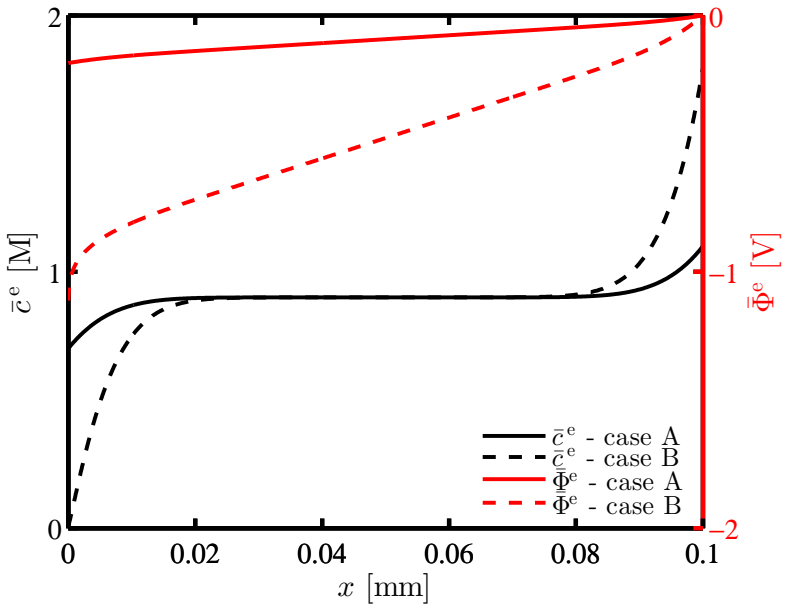

Figure 7.3: Concentration and potential profiles of the reference solution along the x-axis involving 5120 elements for case A and case B at $t = 1$ s.

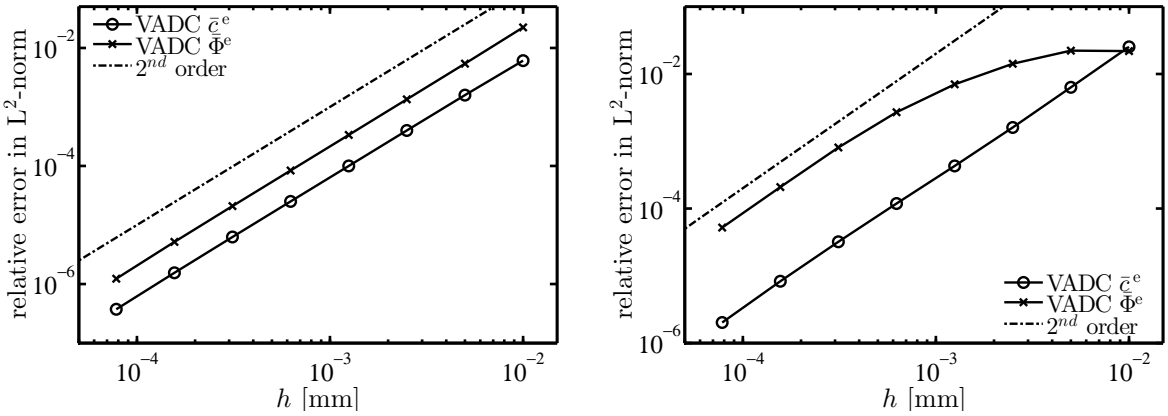

(a) case A (b) case B

Figure 7.4: Spatial convergence of the relative error of the concentration field and the potential field over the element size h with respect to the reference solution involving 5120 elements.

Table 7.2: Simulation parameters for the transient one-dimensional ion-transport problem with concentration dependent transport parameters.

Computation domain Ω [mm]	$(0, 0.1)$	
Number of elements	10, 20, 40, 80, 160, 320, 640, 1280, (5120)	
Element size h [μm]	10, 5, 2.5, 1.25, 0.625,	
	0.3125, 0.15625, 0.078125, (0.01953125)	
Porosity ε [$-$]	0.55	
Tortuosity τ [$-$]	2.899	
Initial concentration $\overline{c}_0^{\,\mathrm{e}}$ [M]	0.9	
Dirichlet BC $\overline{c}^{\,\mathrm{e}}(x = 0)$ [M]	0.7 (case A)	0.005 (case B)
Dirichlet BC $\overline{c}^{\,\mathrm{e}}(x = 0.1)$ [M]	1.1 (case A)	1.795 (case B)
Dirichlet BC $\overline{\Phi}^{\,\mathrm{e}}(x = 0.1)$ [M]	0 (case A)	0 (case B)
Time step Δt [s]	0.01	
End time T_{end} [s]	1	
Diffusion coefficient $D_{\pm}(c)$ [$\frac{\mathrm{mm}^2}{\mathrm{s}}$]	$1.48 \cdot 10^{-4}\, c^{-0.125}$	
Transference number $t_+(c)$ [$-$]	$0.4 - 0.01c$	
Thermodynamic factor $\left(1 + \frac{\partial \ln f_{\pm}}{\partial \ln c}\right)$ [$-$]	$1 - 0.5c^{1/2} + 2c$	
Conductivity $\kappa(c)$ [$\frac{\mu\mathrm{S}}{\mathrm{mm}}$]	$\dfrac{3900c - 8700c^{3/2} + 8000c^2 + 5000c^3}{1.0 + 7.0c^2 + 9.0c^4}$	

with decreasing element length h. This behavior can be explained by a steep potential gradient at the cathode for $\overline{c}^{\,\mathrm{e}} \to 0$ resulting from the natural logarithm in the concentration as given in Equ. (6.4). This is the so-called concentration overpotential. Accordingly, the error level of the potential field is clearly increased whereas the error level of the concentration field is only slightly influenced. In the following numerical examples, this effect is integrated by non-uniform discretizations with smaller elements near the electrodes.

7.4 Quasi one-dimensional simulation with a galvanostatic constraint condition

Galvanostatic experiments and associated galvanostatic simulations constitute a very important operation mode in battery research. Unfortunately, a galvanostatic load involving kinetic effects is a non-trivial phenomenon for two- and three-dimensional geometrical configurations since the current density is a function of the local concentration and electric potential and, therefore,

Table 7.3: Simulation parameters taken from Thorat et al. [140] for a quasi one-dimensional domain with a galvanostatic constraint condition on both electrodes.

Computational domain Ω [mm]	$(0, 0.075)$
Electrode area A [mm^2]	$1.0 \cdot 10^{-4}$
Number of elements	1000
Element size h [mm]	non-uniform element size (dual bias scheme)
	$h(x = 0) = h(x = 0.075) = 0.25 \cdot 10^{-4}$
Porosity ε [$-$]	0.37
Tortuosity τ [$-$]	3.15, 3.65
Initial concentration $\overline{c}_0^{\,\mathrm{e}}$ [M]	1.0
Galvanostatic current density $\overline{i}_{\mathrm{n}}$ [$\frac{\mu\mathrm{A}}{\mathrm{mm}^2}$]	12.5 , 90
Min. and max. time step size Δt [s]	0.001 / 0.5
Current interruption time T_{I} [s]	120
Diffusion coefficient $D_{\pm}$ [$\frac{\mathrm{mm}^2}{\mathrm{s}}$]	$2.582 \cdot 10^{-3} \exp(-2.856c)$
Transference number t_+ [$-$]	0.36
Thermodynamic factor $\left(1 + \frac{\partial \ln f_{\pm}}{\partial \ln c}\right)$ [$-$]	1
Conductivity κ [$\frac{\mu\mathrm{S}}{\mathrm{mm}}$]	$780 \left(\frac{1.262c}{1.0 + 0.2c^2 + 0.08c^4} + 0.014\right)$
Butler-Volmer boundary conditions	$i_0 = 4.1 \mu\mathrm{A\,mm}^{-2}$, $\gamma = 0.5$, $\alpha_{\mathrm{A}} = \alpha_{\mathrm{C}} = 0.5$

in general non-uniformly distributed at the electrode surfaces. The general numerical implementation of the galvanostatic constraint condition has been described in section 6.6. For one-dimensional or quasi one-dimensional domains, a different approach is possible since the current density $\boldsymbol{i}$ is known throughout the computational domain. As a result, the system Equ. (4.8) – Equ. (4.10) can be solved by a partitioned scheme. In a first step, the concentration profile $\overline{c}^{\,\mathrm{e}}$ is determined by Equ. (4.8) where the term $\frac{t_+(c)}{\nu_+ z_+ F}\,\overline{\boldsymbol{i}}$ is considered as a concentration dependent reaction term r. In a second step, the determined concentration profile $\overline{c}^{\,\mathrm{e}}$ is used to calculate the potential profile $\overline{\Phi}^{\,\mathrm{e}}$ based on Equ. (4.9) and, afterwards, the cell potential U incorporating the Butler-Volmer law. However, in this contribution the general approach presented in section 6.6 is also used for one-dimensional or quasi one-dimensional simulations.

Comparison with literature First, the results produced by the VADC approach including galvanostatic BCs are validated against an analytical solution which is based on the steady-state reached at the end of the polarization phase. In a second step, the results are also compared to

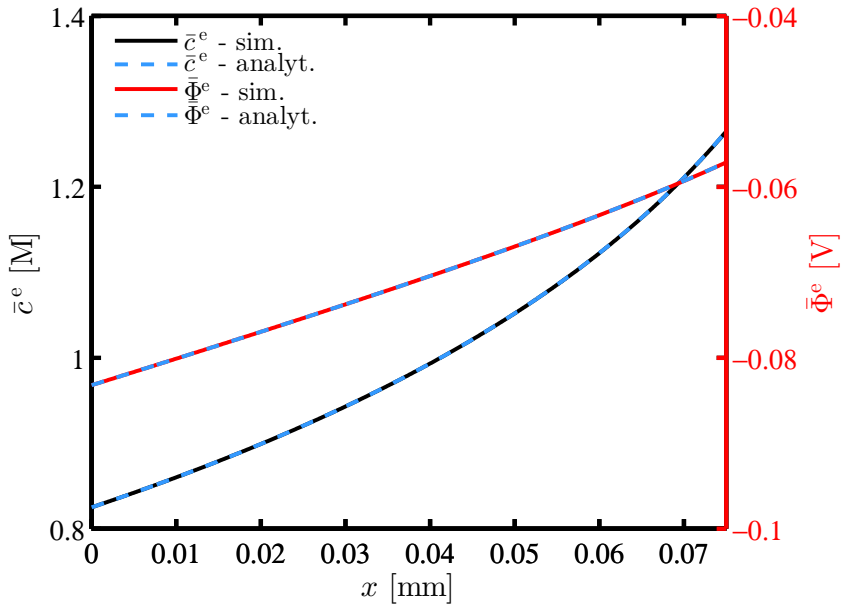

Figure 7.5: Numerical and analytical concentration and potential profiles at time $t = 120\,\mathrm{s}$.

experimental and numerical data for a relaxation experiment provided by Thorat et al. [140]. Therein, the tortuosity τ of the separator is determined by varying it in a numerical model until the data from the corresponding steady-state galvanostatic polarization experiment is best reproduced. The dimensions of the quasi one-dimensional domain as well as the transport and kinetic parameters summarized in Tab. 7.3 are taken from that publication. The basic simulation procedure for relaxation experiments can be found in section 7.1 and section 7.5.1.

Since the transference number t_+ is constant in this case, it is possible to write the standard partial differential equation for the mass conservation given in Equ. (6.1) and (6.2) as

$$\varepsilon \frac{\partial \bar{c}^{\,e}}{\partial t} - \frac{\varepsilon}{\tau} D_{\pm}(c) \frac{\partial^2 \bar{c}^{\,e}}{\partial x^2} = 0$$

with the reformulated boundary condition given in Equ. (5.26) for the anode and the cathode:

$$\frac{\partial \bar{c}^{\,e}}{\partial x} = j = \frac{1}{z_+ \nu_+ F} \frac{(1 - t_+)}{\frac{\varepsilon}{\tau} D_{\pm}(c)} \frac{\bar{i}_{\mathrm{n}}}{n_x}.$$

Herein, the current density $\bar{i}_{\mathrm{n}}$ at the electrode is given as 12.5 $\frac{\mu\mathrm{A}}{\mathrm{mm}^2}$. As an additional condition, the concentration $\bar{c}^{\,e}_{\mathrm{C}} = 0.824881\ \mu\mathrm{mol\,mm}^{-3}$ at the cathode is given to define the reference level of the steady-state concentration profile. This value is taken from the numerical simulation shown in Fig. 7.5.

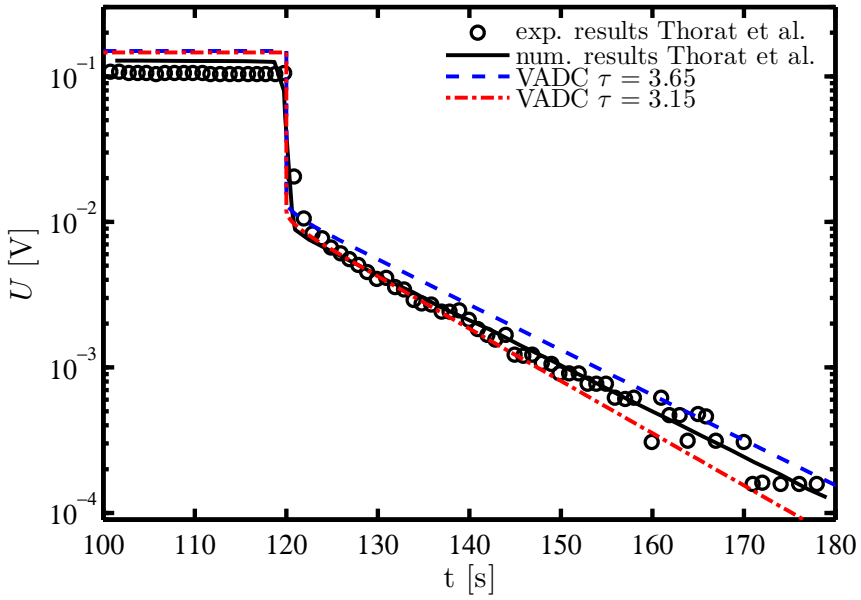

Figure 7.6: Comparison of the time dependent cell potential U resulting from a steady-state galvanostatic polarization experiment given in Thorat et al. [140] with numerical results also given in Thorat et al. [140] and numerical results obtained by the VADC approach.

The analytical solution of this boundary value problem is determined by the software Maple:

$$\overline{c}^{\,\mathrm{e}}(x) = \frac{1}{b} \ln\left(\frac{1}{b\,A(B+x)}\right).$$

The factor $b = 2.856$ is related to the concentration dependent diffusion coefficient $D_{\pm} = a\exp(-bc)$. The parameters A and B

$$A = \frac{1}{b\,B\exp\left(b\,\overline{c}^{\,\mathrm{e}}_{\mathrm{C}}\right)} \qquad \text{and} \qquad B = -\frac{1}{b\,j}$$

involve the prescribed flux density j and the Dirichlet boundary condition $\overline{c}^{\,\mathrm{e}}_{\mathrm{C}}$ at the cathode. Based on the concentration profile $\overline{c}^{\,\mathrm{e}}$, the potential profile $\overline{\Phi}^{\,\mathrm{e}}$ can be calculated from the one-dimensional form of the current equation (5.31). At steady-state after 120 s polarization time, the analytical and numerical solutions are equivalent as shown in Fig. 7.5.

In Fig. 7.6, the time dependent behavior of the cell potential U obtained by the VADC approach is compared to numerical and experimental data provided by Thorat et al. [140]. Therefore, two simulations with different tortuosities $\tau = 3.15$ and $\tau = 3.65$ are considered. At the end of the polarization time, the cell potential U resulting from the VADC algorithm is constant since steady-state has already been reached. However, it is about 21 mV larger than the numerical results and about 41 mV larger than the experimental results presented by Thorat et al. [140].

The influence of the different tortuosities on the cell potential U is minimal. After current interruption, the cell potential U drops rapidly since the ohmic overpotential has no contribution anymore. The remaining cell potential U only depends on the concentration difference $\Delta\overline{c}^{\,\mathrm{e}}$ between the anode and the cathode. During relaxation, the logarithm of the cell potential $\log_{10} U$ decreases linearly with time t. The slope $m_{\log 10}$ is defined as $m_{\log 10} = \frac{1}{\ln 10} \frac{\pi^2 D_{\pm}(c_0)}{l^2 \tau}$. Compared to Equ. (5.41), an additional factor for the transformation between the natural logarithm and the common logarithm is included. It is important to emphasize that this formula is not used for the determination of the tortuosity τ in Thorat et al. [140]. The cell potential U of the simulation using the lower tortuosity relaxes faster than the experimental and numerical results provided in Thorat et al. [140]. The simulation results using the higher tortuosity exhibit the same slope but on a higher level. Since the diffusion coefficient $D_{\pm}$ is clearly defined for both numerical simulations, the different slopes of the cell potential U during relaxation can only be explained by different values for the tortuosity τ. The two values applied to the simulations in Fig. 7.6 can be motivated by the experimental approach used in Thorat et al. [140] to determine the tortuosity. As mentioned at the beginning of this section, the tortuosity is determined by varying it in a numerical model until the experimental data are reproduced best. This procedure is not only applied to an experimental setup consisting of two lithium electrodes separated by a single separator but repeated for many different numbers of separators. The tortuosity $\tau = 3.15$ is the averaged value resulting from all experiments with a varying number of separators whereas $\tau = 3.65$ is the specific value resulting from a single experiment with three separators which corresponds to the numerical setup used in this section. The latter value for the tortuosity can be extracted from Thorat et al. [140, Fig. 7].

Unfortunately, the constant offset in Fig. 7.6 between the VADC result using the tortuosity $\tau = 3.65$ and the experimental and numerical results presented in Thorat et al. [140] cannot be explained. The concentration profile as well as the potential difference $\Delta\Phi^{\mathrm{e}}$ resulting from the VADC formulation at $t = 120\,\mathrm{s}$ are confirmed by the analytical solution depicted in Fig. 7.5. Different models for the electrode reaction can be excluded since the difference can be observed during the polarization phase and the relaxation phase. Therefore, the lower cell potential level in Thorat et al. [140] can only be explained by a lower concentration difference between the anode and the cathode at current interruption time which is in contrast to the aforementioned analytical solution. An incorrect time behavior of the VADC approach resulting in an early steady-state can also be excluded since the time dependent behavior of the simulation with the higher tortuosity and the numerical results provided in Thorat et al. [140] is equivalent during the relaxation process. In addition, the time behavior of the present implementation is validated for the DDC approach in section 7.2 and for the VADC approach in section 7.5. Other numerical examples such as an adapted Gaussian hill presented in Donea and Huerta [52] and a comparison between the VADC and the DC approaches based on a two-dimensional porous geometry consisting of spheres also confirm a correct implementation. These numerical examples are not further discussed in this contribution.

Numerical efficiency of the galvanostatic constraint condition The numerical efficiency of the galvanostatic constraint condition introduced in section 6.6 is discussed based on the same numerical example as before, but with an increased polarization current density $\overline{i}_{\mathrm{n}} = 90\,\frac{\mu\mathrm{A}}{\mathrm{mm}^2}$ to generate a more challenging numerical setup. With this polarization current density, the mass-

Table 7.4: Number of Galvano-Static Iterations (GSI) for different predictors in a galvanostatic simulation reaching the mass-transport limited current at $t = 45\,\mathrm{s}$.

Prediction step based on	num. of GSI	GSI / time step	max. GSI in one time step
1.) Initial cond. (Equ. (6.43))		not converged	
2.) Integrated cond. (Equ. (6.44))	2723	2.48	13 ($t = 45\,\mathrm{s}$)
3.) Overall resistance (Equ. (6.45))	4651	4.23	9 ($38.6 < t < 43.5\,\mathrm{s}$)

transport limited current is reached after 45 s. The remaining simulation parameters in Tab. 7.3 are left unchanged.

The numerical efficiency of the galvanostatic constraint condition is especially important for large, three-dimensional computational domains due to the additional outer loop enclosing the ion-transport solver as introduced in section 6.6. In such a partitioned scheme, the galvanostatic constraint condition is enforced iteratively which requires an educated prediction of the resistance R within the electrolyte to minimize computational costs. Afterwards, the predicted resistance R is used to calculate the potential difference $\Delta\overline{\Phi}^{\mathrm{e}}$ between the two electrodes. An accurate prediction of the surface overpotentials η_{C} and η_{A} is provided by Equ. (6.37) and Equ. (6.38), respectively. In the following, the three different predictor steps for the resistance R presented in section 6.6 are compared to each other based on a quasi one-dimensional simulation. The same numerical behavior is also observed for more complex geometries as used, e.g., in section 7.6. The results are summarized in Tab. 7.4. The outer iteration loop of the partitioned scheme fails to converge after about 9 s simulation time if the first predictor based on the initial electrolyte conductivity $\kappa(c_0)$ is used. Even before 9 s, the number of Galvano-Static Iterations (GSI) per time step is very high. The predicted resistance R corresponds to the initial electrolyte resistance $R_{\mathrm{el},0}$ which is usually too small for non-uniform concentration fields $\overline{c}^{\mathrm{e}}$. Since the electrolyte conductivity $\kappa(c)$ is concentration dependent, the resistance R is dominated by the decreased electrolyte conductivity at the cathode as a result of the inverse relation between R and $\kappa(c)$:

$$R = \frac{L}{A}\frac{1}{V}\int_{\Omega}\frac{\tau}{\varepsilon\kappa(c)}\,\mathrm{d}\boldsymbol{x}.$$

As a result of the resistance R being too small, the potential difference $\Delta\overline{\Phi}^{\mathrm{e}}$ is also underestimated which is the reason for the limited convergence of the numerical scheme.

In the second approach based on Equ. (6.44), the concentration dependence of the electrolyte conductivity $\kappa(c)$ is considered for the prediction of the resistance R which improves the performance of the galvanostatic constraint condition dramatically as can be seen in Tab. 7.4. In this case, the resistance R is always equal to the electrolyte resistance R_{el}, not only at the beginning of the simulation.

The third approach is based on the resistance R calculated from the ratio between the potential difference $\Delta\overline{\Phi}^{\mathrm{e}}$ and the current I as given in Equ. (6.45). In this case, the resistance R

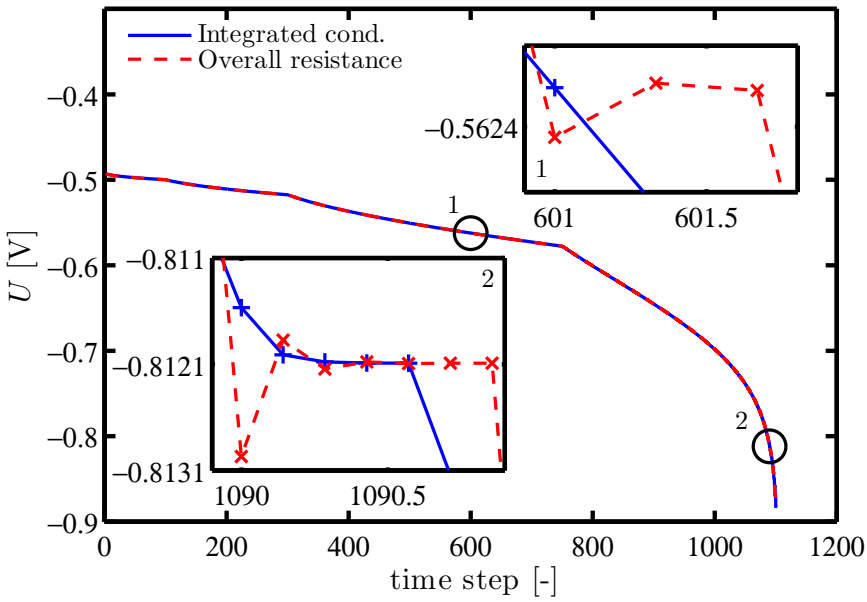

Figure 7.7: Comparision of the cell potential U resulting from the galvanostatic constraint condition for all time steps including the intermediate GSI.

includes the electrolyte resistance R_{el} as well as the resistive contribution of the concentration overpotential. Therefore, it should be the most accurate prediction of the resistance R. However, the number of GSI per time step is almost twice as large as compared to the second approach. This behavior can be explained by a numerical damping effect which is inherently introduced by the approach and often used in numerical solution schemes. However, in this case, the amount of numerical damping is physically motivated and not arbitrarily selected as in other cases. By contrast, the third approach tends to overestimate the potential difference $\Delta\overline{\Phi}^{\text{e}}$ as it can be observed in Fig. 7.7. Only in the case of for the mass-transport limited current, the third approach converges faster than the second approach since the concentration overpotential is the dominating contribution.

As a result of the preceding numerical investigation, the second approach based on the integrated electrolyte conductivity $\kappa(c)$ is chosen as the standard predictor for the galvanostatic constraint condition. In the following, this predictor is used for all galvanostatic simulations.

7.5 Numerical analysis of polarization experiments used for transport parameter determination

The analytical expressions for the determination of the diffusion coefficient $D_{\pm}$ or the transference number t_+ introduced in section 5.4 and 5.5 are analyzed in terms of their potential applicability for the experimental determination of transport parameters by means of numerical

Table 7.5: Parameters used for the numerical simulation of polarization experiments.

Computational domain Ω [mm]	$(0, 0.5)$
Electrode area A [mm^2]	$2.0 \cdot 10^{-4}$
Scaled electrode area A [mm^2]	226.98
Number of elements	1000
Element size h [mm]	dual bias scheme
	with $h(x = 0) = h(x = 0.5) = 1.0 \cdot 10^{-4}$
Porosity ε [$-$]	0.55
Tortuosity τ [$-$]	2.6
Initial concentration $\overline{c}_0^{\,e}$ [M]	0.1 / 1.0 / 2.0
Min. and max. time step size Δt [s]	0.001 / 1
Diffusion coefficient $D_\pm$ [$\frac{\text{mm}^2}{\text{s}}$]	$2.8 \cdot 10^{-4} \exp(-0.45c)$
Transference number t_+ [$-$]	$0.4 + 0.2c - 0.125c^2$
Thermodynamic factor $\left(1 + \frac{\partial \ln f_\pm}{\partial \ln c}\right)$ [$-$]	$1 - \frac{1}{2} \frac{3.95\sqrt{c}}{(1 + 63.05\sqrt{c})^2} + 0.907c$
Conductivity κ [$\frac{\mu\text{S}}{\text{mm}}$]	$\frac{3400c - 4700c^{3/2} + 2000c^2}{1.0 + 0.2c^4}$
BV conditions	$i_0 = 3\mu\text{A mm}^{-2}$, $\gamma = 0.0$, $\alpha_\text{A} = \alpha_\text{C} = 0.5$

simulations. In addition, the excellent match between theory and simulation can also be interpreted as a validation for the simulation approach. The result presented in this section are also published in Ehrl et al. [57] and Ehrl et al. [56].

7.5.1 General principle of polarization experiments

The analytical methods for the determination of transport parameter described in section 5.4 and 5.5 can be combined with the following relaxation experiments: Pulsed Galvanostatic Polarization (PGP) and Steady-State Potentiostatic Polarization (SSPP). The different experimental procedures with the associated analytical methods are explained in the following.

The numerical simulations are based on a quasi one-dimensional domain with an electrode area $A = 2.0 \cdot 10^{-4}\,\text{mm}^2$. In a postprocessing step, the results are scaled to represent the experimental setup with an electrode area $A = 226.98\,\text{mm}$ used in section 8. The basic numerical methods used for the simulation of relaxation experiments are described in section 7.1. The remaining simulation and transport parameters are summarized in Tab. 7.5 whereas the functional description of the transport parameters is guided by the experimental results for an electrolyte

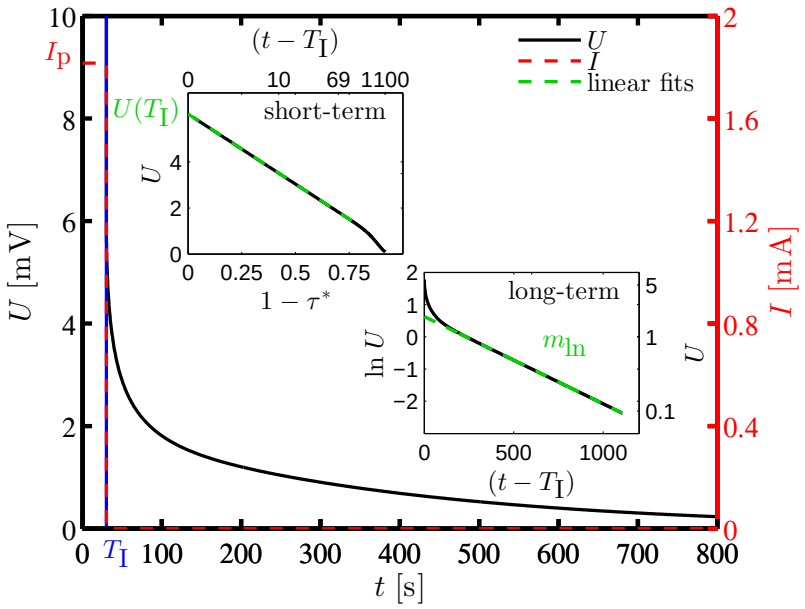

Figure 7.8: Simulation of a PGP experiment with a polarization time of 30 s, a polarization current density $\bar{i}_\mathrm{p} = 8 \cdot 10^{-3}\,\frac{\mathrm{mA}}{\mathrm{mm}^2}$ corresponding to the polarization current $I_\mathrm{p} = 1.82\,\mathrm{mA}$ and an initial electrolyte concentration $\bar{c}_0^{\,\mathrm{e}} = 1\,\mathrm{M}$.

solution consisting of lithium perchlorate ($LiClO_4$) dissolved in an Ethylene Carbonate (EC, 50 % wt.) and Diethyl Carbonate (DEC, 50 % wt.) presented in section 8.

Pulsed Galvanostatic Polarization (PGP) As shown in Fig. 7.8, a PGP experiment consists of a polarization and relaxation phase. During the polarization phase, a short galvanostatic pulse with the current I_p is applied to establish a concentration gradient within the two-electrode cell. The concentration difference $\Delta\bar{c}^{\,\mathrm{e}}(t)$ between anode and cathode develops according to Equ. (5.73). During this phase, the cell potential $U(t)$ is influenced by the concentration difference $\Delta\bar{c}^{\,\mathrm{e}}(t)$, the current flow I_p and kinetic effects at the electrode. At the time $t = T_\mathrm{I}$ the current I_p is interrupted. During the following relaxation phase, the concentration difference $\Delta\bar{c}^{\,\mathrm{e}}(t)$ as well as the corresponding cell potential $U(t)$ slowly relax with time. In contrast to the polarization phase, the cell potential $U(t)$ is only influenced by the concentration difference $\Delta\bar{c}^{\,\mathrm{e}}(t)$. As long as the applied polarization current I_p is small, a linear relationship between the cell potential $U(t)$ and the concentration difference $\Delta\bar{c}^{\,\mathrm{e}}(t)$ can be assumed as explained in section 5.3. In this case, the non-linearities introduced by the concentration dependence of the transport parameters and by the linearization of the natural logarithm are negligibly small.

The expected linear behavior of the cell potential U with respect to the artificial time τ^* for the short-term relaxation as well as the linear behavior of the cell potential $\ln U$ with respect to the time t for the long-term relaxation are clearly observable for reasonable time periods in Fig. 7.8. Since the determination of the coefficient $f(f_\pm, t_+, \sqrt{D^*_{\pm,\mathrm{eff}}})$ according to Equ. (5.74)

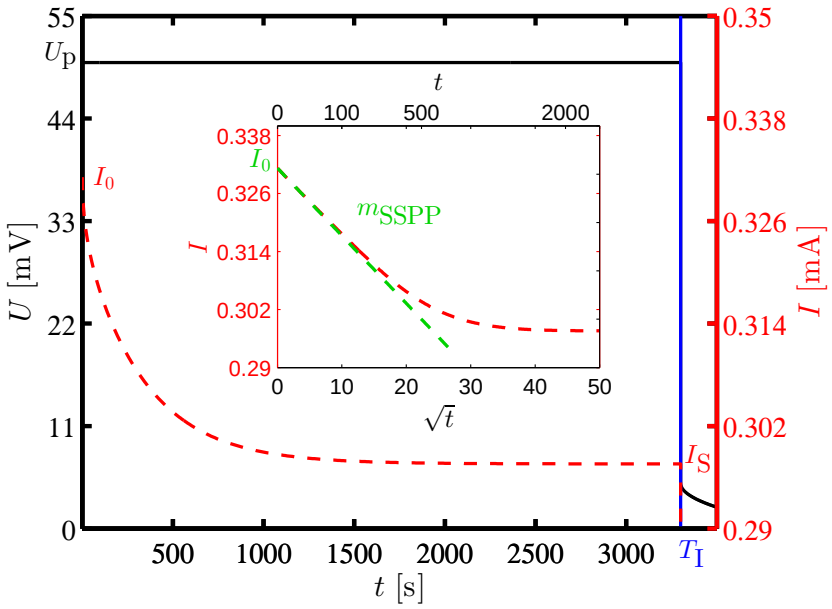

Figure 7.9: Polarization phase of a SSPP experiment with the polarization time of 3300 s, a polarization potential $U_\mathrm{p} = 50\,\mathrm{mV}$ and an initial electrolyte concentration $\bar{c}_0^\mathrm{e} = 1\,\mathrm{M}$.

is based on the cell potential $U(T_\mathrm{I})$ at the current interruption time, the linearity in τ^* can be used to determine the cell potential $U(T_\mathrm{I})$ at current interruption time T_I more accurately. This is particularly important for experiments where the cell potential $U(t)$ is influenced by additional parasitic contributions as, e.g., the discharge of the double layer. The slope m_ln obtained from the long-term relaxation behavior is proportional to the diffusion coefficient $D_\pm$ as indicated by Equ. (5.41).

Steady-State Potentiostatic Polarization (SSPP) A SSPP experiment also consists of two phases. In the first phase, the two-electrode cell is polarized with a constant cell potential U_p until the steady-state current I_S is established as shown in Fig. 7.9. The steady-state current I_S is based on a steady-state concentration profile within the cell. The electrode kinetics are modeled by a Butler-Volmer law without concentration dependency $\gamma = 0$ resulting in a constant interface resistance R_I due to the linearity of the Butler-Volmer law for small surface overpotentials η. The initial current I_0 is the maximal current value obtained during polarization since the concentration overpotential is negligible small in the beginning as explained in section 5.5.1. Due to an increasing concentration overpotential with time, the current I decreases until the steady-current I_S is reached. For concentrated electrolyte solutions, the same SSPP experiment can be used to determine the coefficient $f(f_\pm, t_+, D^*_{\pm,\mathrm{eff}})$ with Equ. (5.59). The short-term relaxation of the current $I(t)$ is linear with respect to time $\sqrt{t}$. Based on the slope m_SSPP, the coefficient $f(f_\pm, t_+, \sqrt{D^*_{\pm,\mathrm{eff}}})$ can be calculated by Equ. (5.66).

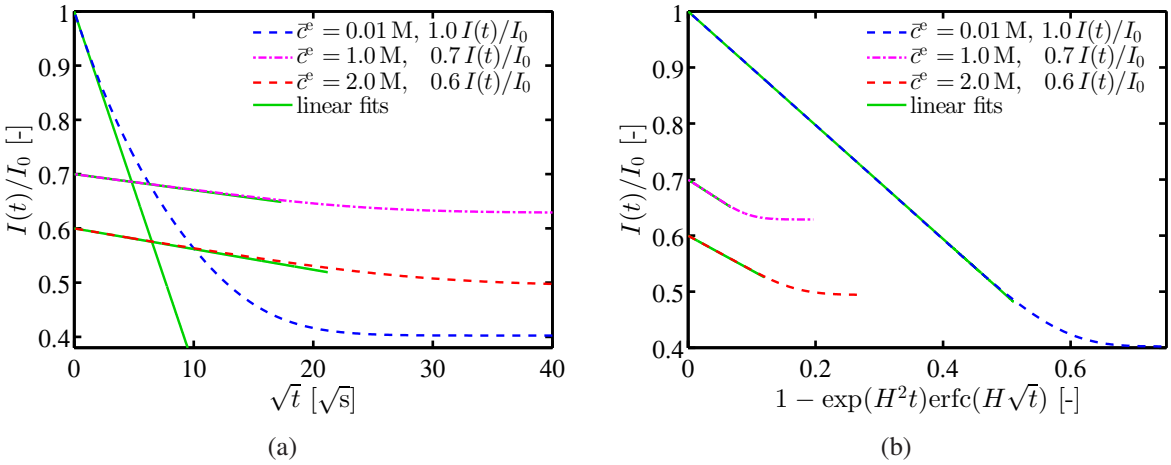

Figure 7.10: Relaxation behavior of $I(t)/I_0$ with respect to (a) the square root of time $\sqrt{t}$ and (b) a complex function of time derived in Equ. (5.64). The smallest concentration is polarized with $U_\mathrm{p} = 20\,\mathrm{mV}$ and the remaining concentrations with $U_\mathrm{p} = 50\,\mathrm{mV}$. The length of the green line corresponds to equal time ranges in (a) and (b).

The linear behavior of the current $I(t)$ with respect to the square root of time is already an approximation for the more complex function $\exp(H^2 t)\,\mathrm{erfc}(H\sqrt{t})$ which is given in Equ. (5.64). The influence of this approximation is highlighted in Fig. 7.10. The scaling of the concentrations $\bar{c}^{\,\mathrm{e}} = 1.0\,\mathrm{M}$ and $\bar{c}^{\,\mathrm{e}} = 2.0\,\mathrm{M}$ with the factors 0.7 and 0.6, respectively, is only introduced since otherwise all three curves would have been on top of each other in Fig. 7.10(b). A clear difference between Fig. 7.10(a) and Fig. 7.10(b) can only be observed for the smallest concentration $\bar{c}^{\,\mathrm{e}} = 0.01\,\mathrm{M}$. For the higher concentrations, the differences are marginal but still visible. A good indication for the difference is the green line representing equivalent time ranges of the linear fits in Fig. 7.10(a) and Fig. 7.10(b). In Fig. 7.10(a), the normalized current $I(t)/I_0$ starts to deviated already from the linear fit whereas both lines are still on top of each other in Fig. 7.10(b). This behavior can be explained by a smaller value of H for the higher concentrations. For the smallest concentration, H is given as $H = 0.0595\,\frac{1}{\sqrt{\mathrm{s}}}$ whereas $H = 0.0036\,\frac{1}{\sqrt{\mathrm{s}}}$ and $H = 0.0055\,\frac{1}{\sqrt{\mathrm{s}}}$ for $\bar{c}^{\,\mathrm{e}} = 1.0\,\mathrm{M}$ and $\bar{c}^{\,\mathrm{e}} = 2.0\,\mathrm{M}$, respectively. Consequently, the approximation given in Equ. (5.64) is fulfilled for longer time periods for $\bar{c}^{\,\mathrm{e}} = 1.0\,\mathrm{M}$ and $\bar{c}^{\,\mathrm{e}} = 2.0\,\mathrm{M}$. As a result, this method can be only used for electrolyte solutions where a clear linear trend with respect to the square root of time can be observed.

If the steady-state current I_S is reached, the polarization of the cell is interrupted and the relaxation phase of the SSPP experiment starts. During the relaxation phase, the cell potential $U(t)$ decreases continuously as shown in Fig. 7.11. The relaxation process is much longer than in a PGP experiment because of the larger changes to the salt concentration profile. The same linearity of the cell potential $\ln U$ with respect to time t for the long-term relaxation can be observed as in a PGP experiment which allows to determine the diffusion coefficient $D_\pm$ based on Equ. (5.41). In addition, the offset $O(T_\mathrm{I})$ can be used to calculate the coefficient $f(f_\pm, t_+, D^*_{\pm,\mathrm{eff}})$ by means of Equ. (5.71). The short-term relaxation behavior is different than in a PGP experiment. In a SSPP experiment, the cell potential $U(t)$ is proportional to the time $\sqrt{t}$. The slope

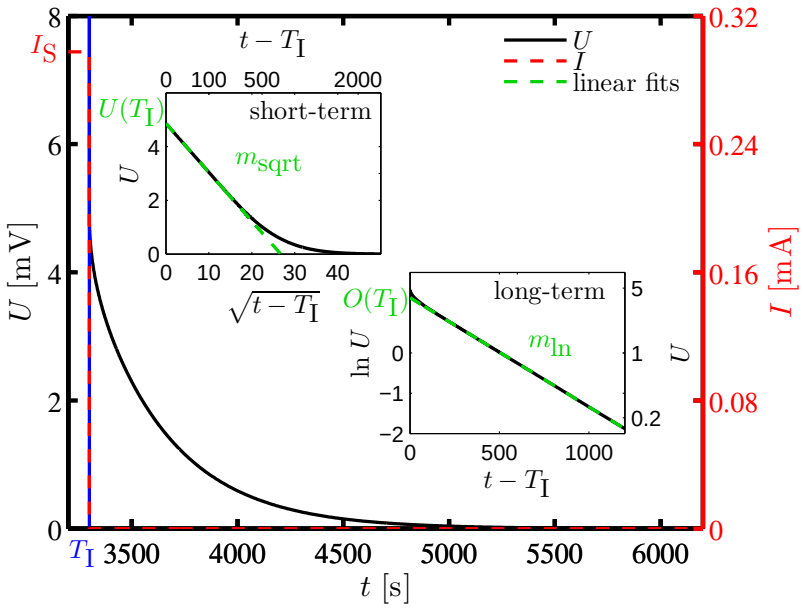

Figure 7.11: Relaxation phase of a SSPP experiment with the polarization time of 3300 s, a polarization potential $U_p = 50$ mV and an initial electrolyte concentration $\overline{c}_0^e = 1$ M.

m_{sqrt} is related to the binary diffusion coefficient $D_\pm$ by Equ. (5.43). The extrapolated cell potential $U(T_I)$ at current interruption time T_I can be used to calculate the coefficient $f(f_\pm, t_+, D^*_{\pm,eff})$ with Equ. (5.68).

7.5.2 Binary diffusion coefficient

In a two-electrode cell, the binary diffusion coefficient $D_\pm$ can be determined by three different methods which are summarized in Tab. 7.6. The diffusion coefficient $D_\pm|_{\text{PGP-ln}}$ and $D_\pm|_{\text{SSPP-ln}}$ are based on the long-term relaxation behavior of a PGP and a SSPP experiment, respectively. The diffusion coefficient $D_\pm|_{\text{SSPP-sqrt}}$ can be calculated from the short term relaxation behavior of a SSPP experiment. The basic principles for the experimental determination of diffusion coefficients $D_\pm|_{\text{PGP-ln}}$, $D_\pm|_{\text{SSPP-ln}}$ and $D_\pm|_{\text{SSPP-sqrt}}$ are explained in section 7.5.1.

The only design parameter influencing the results of the three methods is the concentration difference $\Delta\overline{c}^{\,e}(T_I)$ at current interruption time T_I. The polarization time in a PGP experiment is not a major factor since the long-term relaxation behavior is independent from the concentration profile at current interruption time T_I. However, a short polarization time in a PGP experiment results in a short relaxation period which makes it more difficult to observe the linear relaxation behavior of the cell potential $\ln U$ with respect to time t. This is of particular interest for experimental investigations since the accuracy of the measured cell potential is limited to values of a few hundred μV. In Fig. 7.12 the diffusion coefficients determined by the different determination methods are depicted with respect to the concentration difference $\Delta\overline{c}^{\,e}(T_I)$ at the current inter-

Table 7.6: Analytical methods for the determination of the binary diffusion coefficient $D_{\pm}$.

	$D_{\pm}$	
$D_{\pm}\vert_{\text{PGP-ln}}$, $D_{\pm}\vert_{\text{SSPP-ln}}$	$\frac{l^2}{\pi^2}\,\tau\, m_{\ln}$	Equ. (5.41)
$D_{\pm}\vert_{\text{SSPP-sqrt}}$	$\frac{\pi l^2}{16}\,\tau \left(\frac{m_{\text{sqrt}}}{U(T_{\text{I}})}\right)^2$	Equ. (5.43)

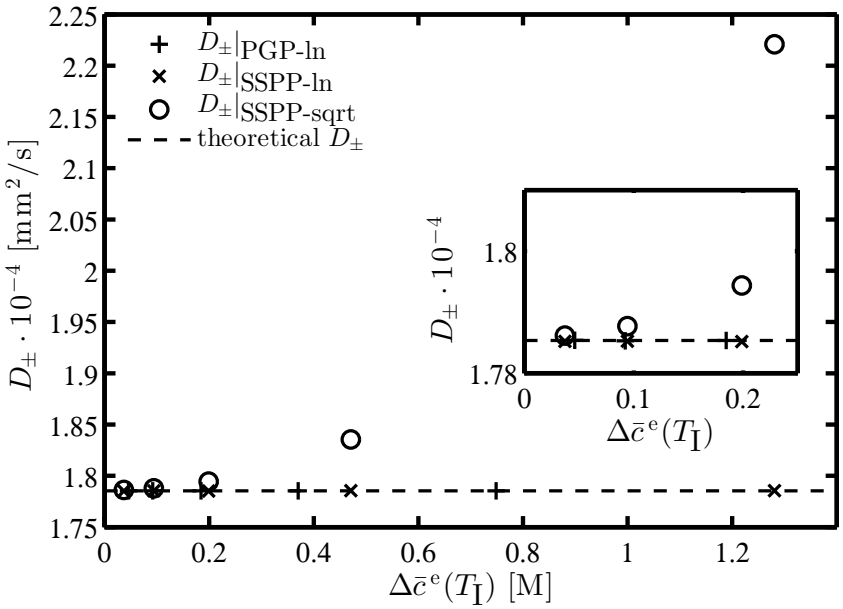

Figure 7.12: Binary diffusion coefficient $D_{\pm}$ with respect to the concentration difference $\Delta\bar{c}^{\,\text{e}}(T_{\text{I}})$ at the current interruption time for $\bar{c}_0^{\,\text{e}} = 1\,\text{M}$.

ruption time for $\bar{c}_0^{\,\text{e}} = 1\,\text{M}$. To demonstrated the independence of the initial concentration $\bar{c}_0^{\,\text{e}}$, the results of two additional initial concentrations $\bar{c}_0^{\,\text{e}} = 0.1\,\text{M}$ and $\bar{c}_0^{\,\text{e}} = 2\,\text{M}$ are listed in Tab. 7.7. The diffusion coefficient $D_{\pm}|_{\text{PGP-ln}}$ is based on the current interruption time $T_{\text{I}} = 300\,\text{s}$. The results presented in Fig. 7.12 and Tab. 7.7 confirm that all three methods are accurate enough for a moderate relative concentration difference $\Delta\bar{c}^{\,\text{e}}/\bar{c}_0^{\,\text{e}}$ at the current interruption time of up to 20 %. The concentration difference $\Delta\bar{c}^{\,\text{e}}(T_{\text{I}})$ at the current interruption time does not have any influence on the results obtained by the two methods based on the long-term relaxation behavior. At one point during the relaxation process, the concentration difference $\Delta\bar{c}^{\,\text{e}}$ is small enough to fulfill the requirement of small concentration variations. In real experiments, the maximal concentration difference $\Delta\bar{c}^{\,\text{e}}(T_{\text{I}})$ is limited by the polarization current I_{p} since high current densities during

Table 7.7: Influence of the concentration difference $\Delta\overline{c}^{\,\mathrm{e}}(T_\mathrm{I})$ at the current interruption time on the determination of the diffusion coefficient.

$\overline{c}_0$ [M]	$D_\pm(\overline{c}_0)$ [mm^2/s]		$\Delta\overline{c}/\overline{c}_0$		
	$1 \cdot 10^{-4}$		$< 5\,\%$	$10 - 20\,\%$	$> 60\,\%$
0.01	2.787	$D_\pm\vert_{\text{PGP-ln}}$	-	2.787	2.787
		$D_\pm\vert_{\text{SSPP-ln}}$	-	2.787	2.787
		$D_\pm\vert_{\text{SSPP-sqrt}}$	-	2.791	3.106 (11%)
1	1.785	$D_\pm\vert_{\text{PGP-ln}}$	1.785	1.785	1.785
		$D_\pm\vert_{\text{SSPP-ln}}$	1.785	1.785	1.785
		$D_\pm\vert_{\text{SSPP-sqrt}}$	1.786	1.794	2.167 (21%)
2	1.138	$D_\pm\vert_{\text{PGP-ln}}$	1.139	1.139	1.139
		$D_\pm\vert_{\text{SSPP-ln}}$	1.138	1.138	1.138
		$D_\pm\vert_{\text{SSPP-sqrt}}$	1.141	1.163 (2.1%)	1.973 (73%)

polarization increase the probability of an electrode surface modifications as, e.g., by the growth of lithium dendrites.

The long-term relaxation behavior of an electrolyte solution may be deteriorated by the first term on the rhs

$$U(t) \propto \Delta\overline{c}^{\,\mathrm{e}}(t) = B \exp\left(-3\frac{\pi^2 D^*_{\pm,\mathrm{eff}}}{l^2}t\right) + 2C_1 \exp\left(-\frac{\pi^2 D^*_{\pm,\mathrm{eff}}}{l^2}t\right)$$

introduced in section 5.4.1. This term is a result of the concentration dependent diffusion coefficient and variations of the solution volume as indicated in Newman and Chapman [110]. Nevertheless, the numerical results depicted in Fig. 7.8 and Fig. 7.11 exhibit a distinct linear behavior for a considerably long time period although concentration dependent transport parameter are considered. This observation can be confirmed by the following additional theoretical considerations. According to Newman and Chapman [110, p. 346], "*it is not necessary in practice to recognize the variation in solution volume*" since the second and third derivative of the density $\rho(c)$ with respect to the concentration c in the factor B can be neglected as a result of the almost linear behavior of the electrolyte density $\rho(c)$ as shown in Fig. 8.1 and Equ. (8.1). This linear behavior of the electrolyte density $\rho(c)$ is typical for many electrolyte solutions and leads to a simplification of the factor B

$$B = \frac{\sqrt{3}}{16} C_1^3 \left[\frac{1}{D_\pm}\frac{\mathrm{d}^2 D_\pm}{\mathrm{d}\,c^2} - 2\left(\frac{1}{D_\pm}\frac{\mathrm{d}\,D_\pm}{\mathrm{d}\,c}\right)^2\right].$$

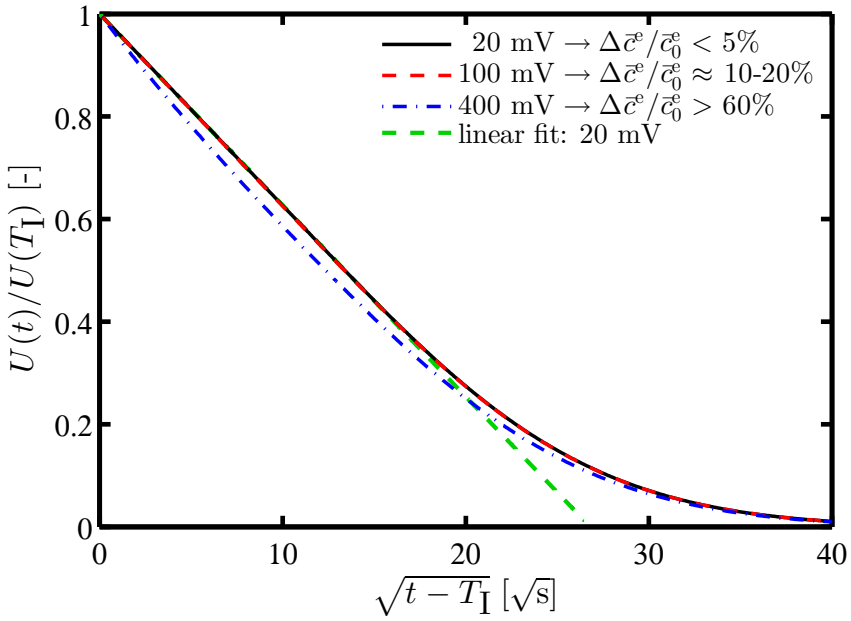

Figure 7.13: Relaxation behavior of the relative cell potential $U(t)/U(T_I)$ with respect to $\sqrt{t}$ for different polarization potentials U_0 and $\bar{c}_0^{\mathrm{e}} = 1\,\mathrm{M}$, fit range [1, 10]

only being influenced by the concentration dependent diffusion coefficient and the factor C_1. For the used concentration dependence of the diffusion coefficient $D_\pm = a\exp(-bc)$, the first and the second term in the brackets are b^2 and $-2b^2$ with $b = 0.45$. For a steady-state concentration profile, the coefficient C_1 is given by $C_1 = 8\frac{\Delta\bar{c}^{\mathrm{e}}(T_\mathrm{I})}{\pi^2}$ as given in Equ. (5.69). As a result, the factor C_1^3 is always much smaller than factor C_1 for small concentration variations $\Delta\bar{c}^{\mathrm{e}}(T_\mathrm{I})$ at current interruption time as used for the determination of transport parameter. For shorter polarization times, the coefficient C_1 cannot be determined exactly but it will not exhibit a completely different behavior. As a result of both estimations, the coefficient B is always much smaller than the coefficient C_1 which reduces the influence of the term given by Equ. (5.39). This is an additional indication for the assumption of negligible small volumetric effects, at least for small concentration variations arising during the determination of transport parameters.

Compared to the two methods which are based on the long-term relaxation behavior, the results of the short-term relaxation are clearly influenced by the concentration difference $\Delta\bar{c}^{\mathrm{e}}(T_\mathrm{I})$ at the current interruption time since high values of $\Delta\bar{c}^{\mathrm{e}}(T_\mathrm{I})$ violate the requirement of small concentration variations automatically. Additionally, the error for the determined diffusion coefficient $D_\pm|_{\text{SSPP-sqrt}}$ increases for an increasing initial concentration $\bar{c}_0^{\mathrm{e}}$ as shown in Tab. 7.7 since the absolute concentration difference $\Delta\bar{c}^{\mathrm{e}}(T_\mathrm{I})$ at current interruption is larger for a high initial concentration $\bar{c}_0^{\mathrm{e}}$. The effect of the concentration difference $\Delta\bar{c}^{\mathrm{e}}(T_\mathrm{I})$ on the linearity of the cell potential $U(t)$ with respect to the time $\sqrt{t}$ is shown in Fig. 7.13 for $\bar{c}_0^{\mathrm{e}} = 1\,\mathrm{M}$. A variation of about 20% with respect to the initial concentration $\bar{c}_0^{\mathrm{e}}$ does not influence the linearity of the cell potential $U(t)$ significantly. For a higher relative concentration difference, a notable deviation of

the linear behavior can be observed. Two different effects are the reason for this deviation. First, the concentration dependent thermodynamic factor and transference number $t_+(c)$ as well as the linearization of the natural logarithm in Equ. (5.34) violate the ideal proportionality between the concentrations difference $\Delta\bar{c}^{\,\mathrm{e}}(t)$ and the cell potential U(t). Additionally, the concentration dependent diffusion coefficient $D_\pm(c)$ violates the condition of a constant diffusion coefficient used for the derivation of the analytical solution. In case of numerical simulations, the diffusion coefficient $D_\pm|_{\text{SSPP-sqrt}}$ can also be determined directly based on the relaxing concentration difference $\Delta\bar{c}^{\,\mathrm{e}}(t)$ and not on the cell potential $U(t)$. The advantage of this approach is that non-linearities introduced by the concentration dependent thermodynamic factor and transference number as well as the linearization of the natural logarithm are not included. As a result, the error in the diffusion coefficient $D_\pm|_{\text{SSPP-sqrt}}$ reduces, e.g., from 21% to 7% for a 1 M electrolyte solution and for the highest polarization. These values are a good indication for the errors resulting from the indirect observation of the concentration difference $\Delta c(t)$ by the cell potential $U(t)$.

7.5.3 Transference number

In this section, the transference number t_+ is calculated from the coefficients $f(f_\pm, t_+, D^*_{\pm,\text{eff}})$ and $f(f_\pm, t_+, \sqrt{D^*_{\pm,\text{eff}}})$ determined by the five methods introduced in section 5.5 and summarized in Tab. 7.8, the diffusion coefficient $D_\pm$ determined in section 7.5.2 and the thermodynamic factor TDF(c) which is assumed to be known. In case of an experimental determination of the transference number t_+, the TDF is measured by the method introduced in section 5.2. The basic principle of the determination of the coefficients $f(f_\pm, t_+, D^*_{\pm,\text{eff}})$ and $f(f_\pm, t_+, \sqrt{D^*_{\pm,\text{eff}}})$ is explained in section 7.5.1.

As for the diffusion coefficient, the influence of the concentration difference $\Delta\bar{c}^{\,\mathrm{e}}(T_\mathrm{I})$ between the two electrodes at current interruption time T_I is investigated numerically. For a SSPP experiment, the concentration difference $\Delta\bar{c}^{\,\mathrm{e}}(T_\mathrm{I})$ defined by the polarization cell potential U_p is

Table 7.8: Analytical methods for the determination of the transference number t_+ by the coefficients $f(TDF, t_+, \sqrt{D_\pm})$ or $f(TDF, t_+, D_\pm)$, the binary diffusion coefficient and the TDF.

$f(f_\pm, t_+, \sqrt{D^*_{\pm,\text{eff}}})\|_{\text{PGP}}$	$\frac{z_+\nu_+}{8}\sqrt{\pi}\,\frac{F^2}{RT}\,A\,\frac{\varepsilon}{\sqrt{\tau}}\,\bar{c}_0^{\,\mathrm{e}}\,\frac{U(T_\mathrm{I})}{I_\mathrm{p}\sqrt{t}}$	Equ. (5.74)
$f(f_\pm, t_+, \sqrt{D^*_{\pm,\text{eff}}})\|_{\text{SSPP-pol-sqrt}}$	$\frac{1}{8}\sqrt{\pi}\,\frac{F^2}{RT}\,A\frac{\varepsilon}{\sqrt{\tau}}\,\bar{c}_0^{\,\mathrm{e}}\,R_{\text{LF,0}}\,\frac{m_{\text{SSPP}}}{I_0}$	Equ. (5.66)
$f(f_\pm, t_+, D^*_{\pm,\text{eff}})\|_{\text{SSPP-ss}}$	$\frac{z_+\nu_+}{2}\,\frac{F^2}{RT}\,\frac{A}{l}\,\frac{\varepsilon}{\tau}\,\bar{c}_0^{\,\mathrm{e}}\,\frac{U(T_\mathrm{I})}{I_\mathrm{S}}$	Equ. (5.68)
$f(f_\pm, t_+, D^*_{\pm,\text{eff}})\|_{\text{SSPP-ln}}$	$\frac{z_+\nu_+}{16}\,\pi^2\,\frac{F^2}{RT}\,\frac{A}{l}\,\frac{\varepsilon}{\tau}\,\bar{c}_0^{\,\mathrm{e}}\,\frac{\exp\,(O(T_\mathrm{I}))}{I_\mathrm{S}}$	Equ. (5.71)
$f(f_\pm, t_+, D^*_{\pm,\text{eff}})\|_{\text{SSPP-pol}}$	$\left[\frac{U_\mathrm{p}}{I_\mathrm{S}} - R_{\text{LF,S}}\right]\,\frac{\nu_+ z_+}{2}\,\frac{F^2}{RT}\,\frac{A}{l}\,\frac{\varepsilon}{\tau}\,\bar{c}_0^{\,\mathrm{e}}$	Equ. (5.59)

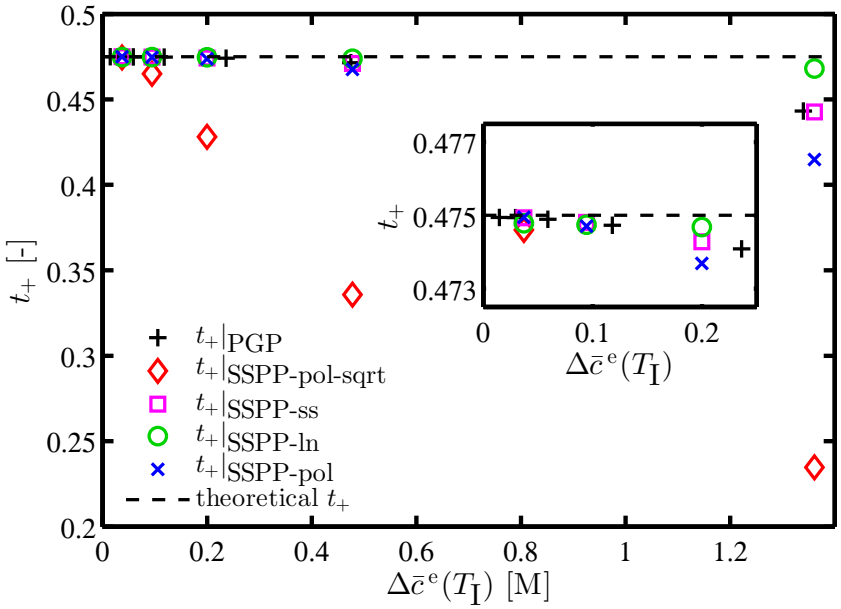

Figure 7.14: Influence of the concentration difference $\Delta\bar{c}^{\,\mathrm{e}}(T_\mathrm{I})$ at the current interruption time on the determination of the transference number t_+ for a $\bar{c}_0^{\,\mathrm{e}} = 1\,\mathrm{M}$ electrolyte solution.

the only design parameter influencing the quality of the determined transference number. The results are shown for the 1 M electrolyte solution in Fig. 7.14 and for the 0.1 M and 2 M electrolyte solutions in Tab. 7.9. All methods summarized in Tab. 7.8 are capable to determine the exact transference number t_+ for a small concentration difference $\Delta\bar{c}^{\,\mathrm{e}}(T_\mathrm{I})$. For higher concentration differences $\Delta\bar{c}^{\,\mathrm{e}}(T_\mathrm{I})$, it is not possible to determine the transference accurately by the method SSPP-pol-sqrt which is based on the initial time behavior of the current $I(t)$ during the polarization phase in a SSPP experiments. In this case, the initial time behavior is not just influenced by concentration dependent transport parameters and the linearization of the natural logarithm but also by the basic characteristic of the electrode kinetics. For an increasing concentration differences $\Delta\bar{c}^{\,\mathrm{e}}$, the Butler-Volmer law cannot be assumed anymore to be linear which violates the linear boundary condition used for the derivation of Equ. (5.65). As a result, the linear behavior of the current $I(t)$ can only be observed clearly for the lowest polarization potential U_p. For this method, as mentioned already in section 7.5.1, the linearity of the time dependent current is a very good indication for the reliability of experimentally measured data. Therefore, this method is only considered for the determination of the transference number if a clear linear trend is observable. All remaining methods are accurate up to relative concentration differences $\Delta\bar{c}^{\,\mathrm{e}}(T_\mathrm{I})/\bar{c}_0^{\,\mathrm{e}}$ of about 20 %. The method SSPP-ln is also very accurate for higher polarization potentials since it is based on the long-term relaxation behavior. Therefore, a small concentration difference between the electrodes is fulfilled automatically with increasing time.

As explained in section 5.5.1, the transference number t_+ can also be calculated directly from Equ. (5.60) for dilute electrolyte solutions. The method is based on the steady-state current

Table 7.9: Influence of the concentration difference $\Delta\overline{c}^{\,\mathrm{e}}(T_\mathrm{I})$ at the current interruption time on the determination of the transference number t_+.

$\overline{c}_0$ [M]	$t_+(\overline{c}_0)$		$\Delta\overline{c}/\overline{c}_0$		
			$\sim 5\,\%$	$\sim 20\,\%$	$> 60\,\%$
0.01	0.402	$t_+\vert_{\mathrm{PGP}}$	-	0.402	0.391 (3%)
		$t_+\vert_{\mathrm{SSPP\text{-}pol\text{-}sqrt}}$	-	-	-
		$t_+\vert_{\mathrm{SSPP\text{-}ss}}$	-	0.402	0.383 (5%)
		$t_+\vert_{\mathrm{SSPP\text{-}ln}}$	-	0.402	0.401
		$t_+\vert_{\mathrm{SSPP\text{-}pol}}$	-	0.402	0.37 (8%)
2	0.3	$t_+\vert_{\mathrm{PGP}}$	0.3	0.296	0.213 (29%)
		$t_+\vert_{\mathrm{SSPP\text{-}pol\text{-}sqrt}}$	0.305	0.251 (16%)	0.027 (91%)
		$t_+\vert_{\mathrm{SSPP\text{-}ss}}$	0.3	0.297	0.206 (31%)
		$t_+\vert_{\mathrm{SSPP\text{-}ln}}$	0.3	0.3	0.286 (5%)
		$t_+\vert_{\mathrm{SSPP\text{-}pol}}$	0.3	0.297	0.187 (38%)

I_S, the steady-state low frequency resistance R_LF, the electrolyte resistance R_el and the polarization potential U_p. For the smallest polarization potential U_p, the transference numbers t_+ are 0.32, 0.525 and 0.465 for the concentrations 0.01 M, 1 M and 2 M, respectively. Even for smaller concentrations $\overline{c}_0^{\,\mathrm{e}}$, the expected transference number t_+ cannot be determined correctly since the mathematical condition given in Equ. (5.56) is not fulfilled for the given parameters set and for $\overline{c}_0^{\,\mathrm{e}} \to 0$. However, it is possible to calculate the transference number correctly for the initial concentration $\overline{c}_0^{\,\mathrm{e}} = 0.5\,\mathrm{M}$ since the mathematical condition is fulfilled in this case. As a result, Equ. (5.60) can be used as an additional condition for the determination of the parameter set for dilute electrolyte solutions $\overline{c}_0^{\,\mathrm{e}} \to 0$.

Influence of a non steady-state concentration profile on the determination of the transference number Although the concentration difference $\Delta\overline{c}^{\,\mathrm{e}}(T_\mathrm{I})$ at the current interruption time is the only design parameter in a SSPP experiment which can be influenced actively, it is possible that a non steady-state concentration profile at the current interruption time deteriorates the results of the determined transference number. A non steady-state concentration profile originates from too short polarization times or from the continuous variation of the interface resistance R_I during a SSPP experiment. The influence of a non steady-state concentration profile as a result of too short polarization times on the determined transference number is depicted in Fig. 7.15 for all methods which rely on a steady-state concentration profile at current interruption time. The relaxation of the current $I(t)$ during the polarization with selected interruption times indicated by vertically dashed black lines is depicted in Fig. 7.16(a) and the relaxation behavior of the relative cell potential $U(t)/U(T_\mathrm{I})$ with respect to the time $\sqrt{t}$ is shown in Fig. 7.16(b).

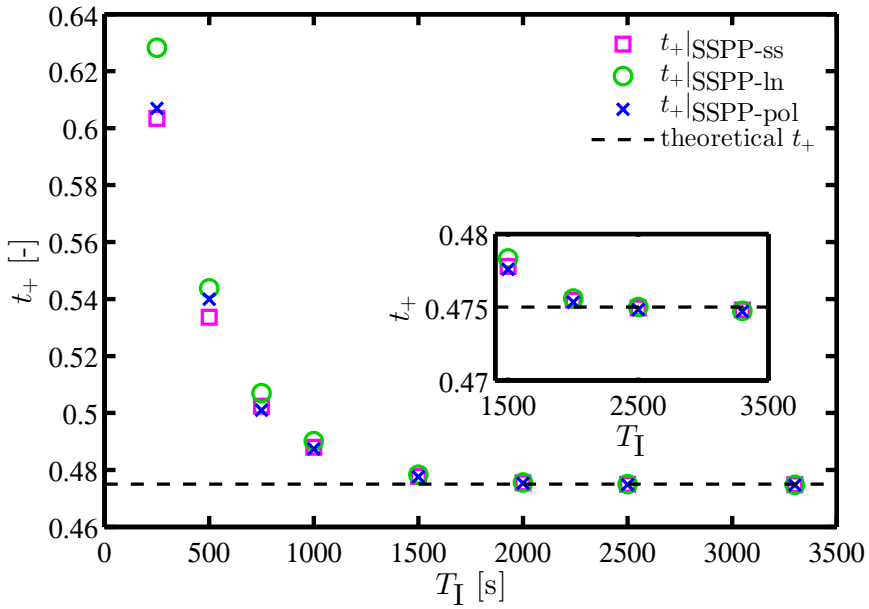

Figure 7.15: Influence of the polarization time T_I on the determined transference number t_+ for a polarization potential $U_\mathrm{p} = 50\,\mathrm{mV}$ and an initial concentration $\overline{c}_0^{\,\mathrm{e}} = 1\,\mathrm{M}$.

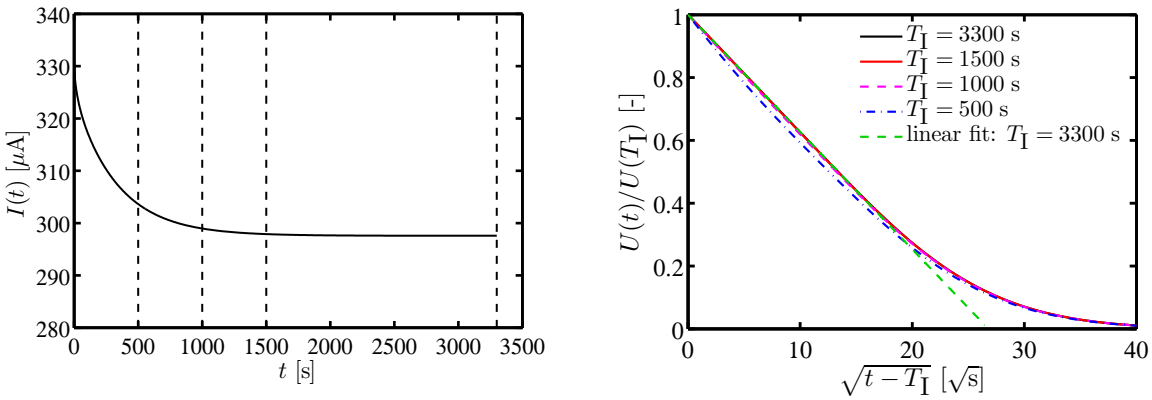

(a) (b)

Figure 7.16: Polarization and relaxation phase of a SSPP experiment with the polarization potential $U_\mathrm{p} = 50\,\mathrm{mV}$ and the initial concentration $\overline{c}_0^{\,\mathrm{e}} = 1\,\mathrm{M}$: (a) current I over time t during polarization phase with selected current interruption times T_I and (b) relative cell potential $U(t)/U(T_\mathrm{I})$ over time $\sqrt{t}$ during the relaxation phase.

The presented numerical data are the result of a 1 M electrolyte solution polarized with a cell potential $U_\mathrm{p} = 50\,\mathrm{mV}$ which corresponds to a 10% relative concentration difference. The error for the transference number t_+ based on a polarization time of $t = 1000 - 1500\,\mathrm{s}$ is below 5%. For short polarization times $t > 1500\,\mathrm{s}$, the determined transference number t_+ does not exhibit a distinct deterioration at all. For polarization times $t < 1000\,\mathrm{s}$, the error in the transference number t_+ increases rapidly because the steady-state concentration profile is not reached yet. After a polarization time of $t = 1000 - 1500\,\mathrm{s}$, the current $I(t)$ approaches a horizontal line as shown in Fig. 7.16(a) and the relative cell potential $U(t)/U(T_\mathrm{I})$ exhibits a clear linear behavior with respect to time $\sqrt{t}$ as depicted in Fig. 7.16(b). For shorter polarization times, it is clearly visible from the current $I(t)$ relaxation behavior shown in Fig. 7.16(a) that the steady-state is not reached yet. In contrast, the corresponding non-linearity of the relative cell potential during subsequent relaxation is not so significant as depicted in Fig. 7.16(b). Therefore, it is important for a SSPP experiment to observe the relaxation behavior of the current $I(t)$ during polarization as well as the relaxation behavior of the cell potential $U(t)$ after current interruption. Numerical simulations indicate that a similar behavior can be expected for non steady-state concentration profile as a result of a continuously varying interface resistance R_I.

Influence of polarization time for the determination transference number by a PGP experiment In a PGP experiment, the polarization current I_p and the polarization time defined by current interruption time T_I influence the concentration difference $\Delta\bar{c}^{\,\mathrm{e}}(T_\mathrm{I})$ according to Equ. (5.73).

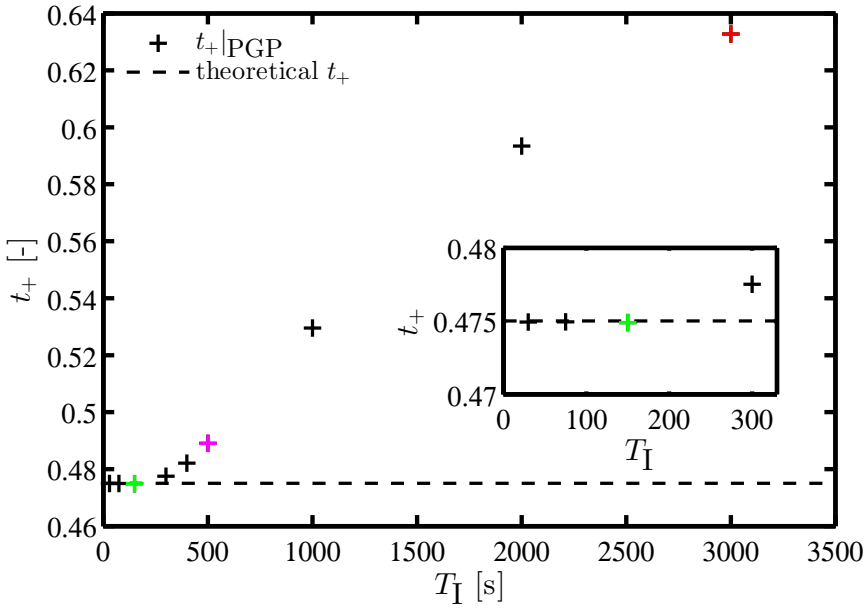

Figure 7.17: Influence of polarization time T_I in a PGP experiment with the polarization current $I_\mathrm{p} = 0.454\,\mathrm{mA}$ and the initial concentration $\bar{c}_0^{\,\mathrm{e}} = 1\,\mathrm{M}$ on the quality of the determined transference number t_+.

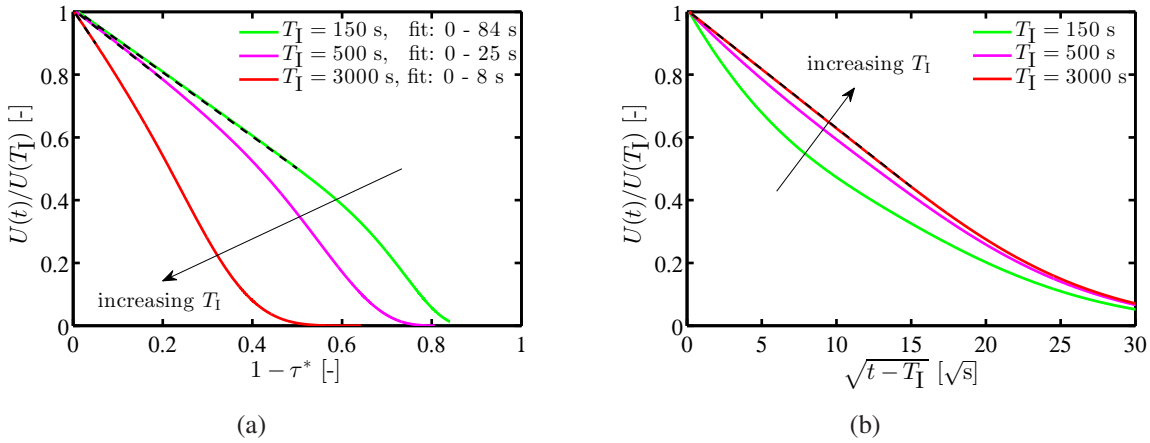

(a) (b)

Figure 7.18: Relaxation behavior of the relative cell potential $U(t)/U(T_\mathrm{I})$ after the PGP pulse with respect to (a) the artificial time $1-\tau^*$ and (b) the time $\sqrt{t-T_\mathrm{I}}$ with the cell potential $U(T_\mathrm{I})$ at current interruption time: $U(150\,\mathrm{s}) = 3.36\,\mathrm{mV}$, $U(500\,\mathrm{s}) = 5.83\,\mathrm{mV}$ and $U(3000\,\mathrm{s}) = 7.38\,\mathrm{mV}$

Both design parameters have to be chosen so that the relative concentration difference $\Delta\overline{c}^{\,\mathrm{e}}(T_\mathrm{I})/\overline{c}_0^{\,\mathrm{e}}$ does not exceed 20 %. Additionally, the current interruption time T_I has to be short enough to ensure that the semi-infinite limit used for the derivation of Equ. (5.73) is not violated. For longer polarization times, the concentration profile will slowly approach the steady-state case which is desired for a SSPP experiment. In Fig. 7.17, the calculated transference number t_+ with respect to the polarization time for a 1 M electrolyte solution polarized with a current density $I_\mathrm{p} = 0.454\,\mathrm{mA}$ is depicted. For polarization times of about 500 s, the deviation of the determined transference number is below 5%. The corresponding relaxation behavior of the relative cell potential $U(t)/U(T_\mathrm{I})$ with respect to the artificial time $1-\tau^*$ and the time $\sqrt{t-T_\mathrm{I}}$ are shown in Fig. 7.18(a) and Fig. 7.18(b), respectively. Additionally, simulations with a shorter and longer polarization time are shown to discuss the differences. As expected, the relative cell potential is linear with respect to the time $\sqrt{t-T_\mathrm{I}}$ for long polarization times. A distinct non-linearity can be observed for short polarization times. With respect to the artificial time $1-\tau^*$, the cell potential U exhibits a linear behavior over long time period for short polarization time whereas the length of time period in tau^* is decreased for an increasing polarization time.

7.6 Galvanostatic simulation of a realistic porous medium

In this section, it is demonstrated that the proposed DC approach can also be applied to complex porous geometries such as resolved electrodes or separators. For this purpose, a galvanostatic polarization step with a polarization current I_p approaching the mass-transport limited current followed by a relaxation phase is selected since it is the most challenging load case for the numerical solution scheme as it is demonstrated in section 7.3 and section 7.4. This procedure corresponds to a PGP experiment with a high polarization current. Unfortunately, the reconstruction of a three-dimensional porous battery separator could not be achieved within this project since

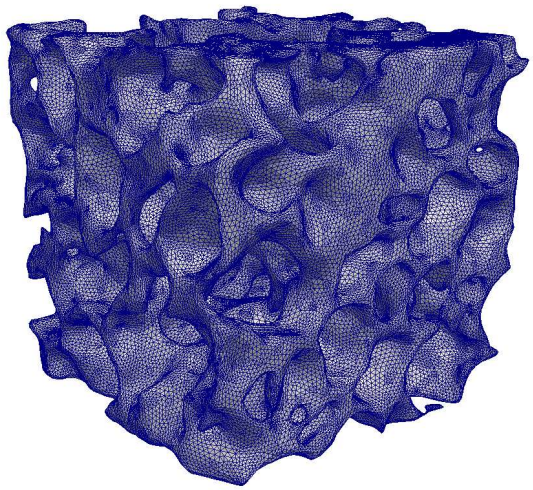

Figure 7.19: Reconstructed cubical-shaped volume meshes of synchrotron-based X-ray tomography scans of a sample of lung tissue.

the Scanning Electron Microscope (SEM) used for the imaging process is not suitable for non-conducting samples such as separators. Electrones induced by the SEM cannot be conducted away resulting in a blurred image. Hence, a sample of lung tissue is used to demonstrate the suitability of the computational approach for complex geometries. For the proof of concept, this does not make any difference since the porous structure of the lung tissue exhibits some similarities with porous media used in battery applications.

The computational domain of the porous lung tissue is depicted in Fig. 7.19. The imaging procedure, the reconstruction process and the mesh generation resulting in the computational domain are explained in Roth et al. [127]. Compared to all other numerical examples presented in this chapter, the domain is discretized by linearly-interpolated tetrahedral elements to account for the complexity of the porous structure. The sample is characterized by a porosity of $\varepsilon = 0.319$ and a tortuosity of $\tau = 1.71$. In Roth et al. [127], the tortuosity of the porous sample is determined based on Equ. (4.11) and physically-motivated numerical simulations as discussed in section 4.2. The electrolyte resistance R_{el} of the porous sample defined as the ratio $\frac{\Delta\Phi}{I}$ is calculated from numerical simulations based on the charge conservation law given in Equ. (2.15) with $\boldsymbol{i} = -\kappa\nabla\Phi$, the so-called Laplace equation. The term describing the concentration overpotential is not considered since only the ohmic resistance R_{el} of the electrolyte is required for the determination of the tortuosity. In this case, the current flow I is the result of the potential difference $\Delta\Phi$ applied as Dirichlet condition between opposite surfaces. A detailed description of the method is given in Roth et al. [127]. The same method is used for porous electrodes, e.g., in Ender et al. [60], Joos et al. [88] or Cooper et al. [46]. In general, the simulation is based on the same procedure as used for the quasi one-dimensional PGP simulations performed in section 7.5.1. Further details on the computational domain and simulation parameters are given in Tab. 7.11 (Table is located at the end of section 7.6).

In Fig. 7.20 the concentration field c and the potential field Φ are depicted for selected cross-sections of the computational domain at current interruption time T_{I}. The current flow is directed from the anode on the left hand side to the cathode on the right hand side resulting

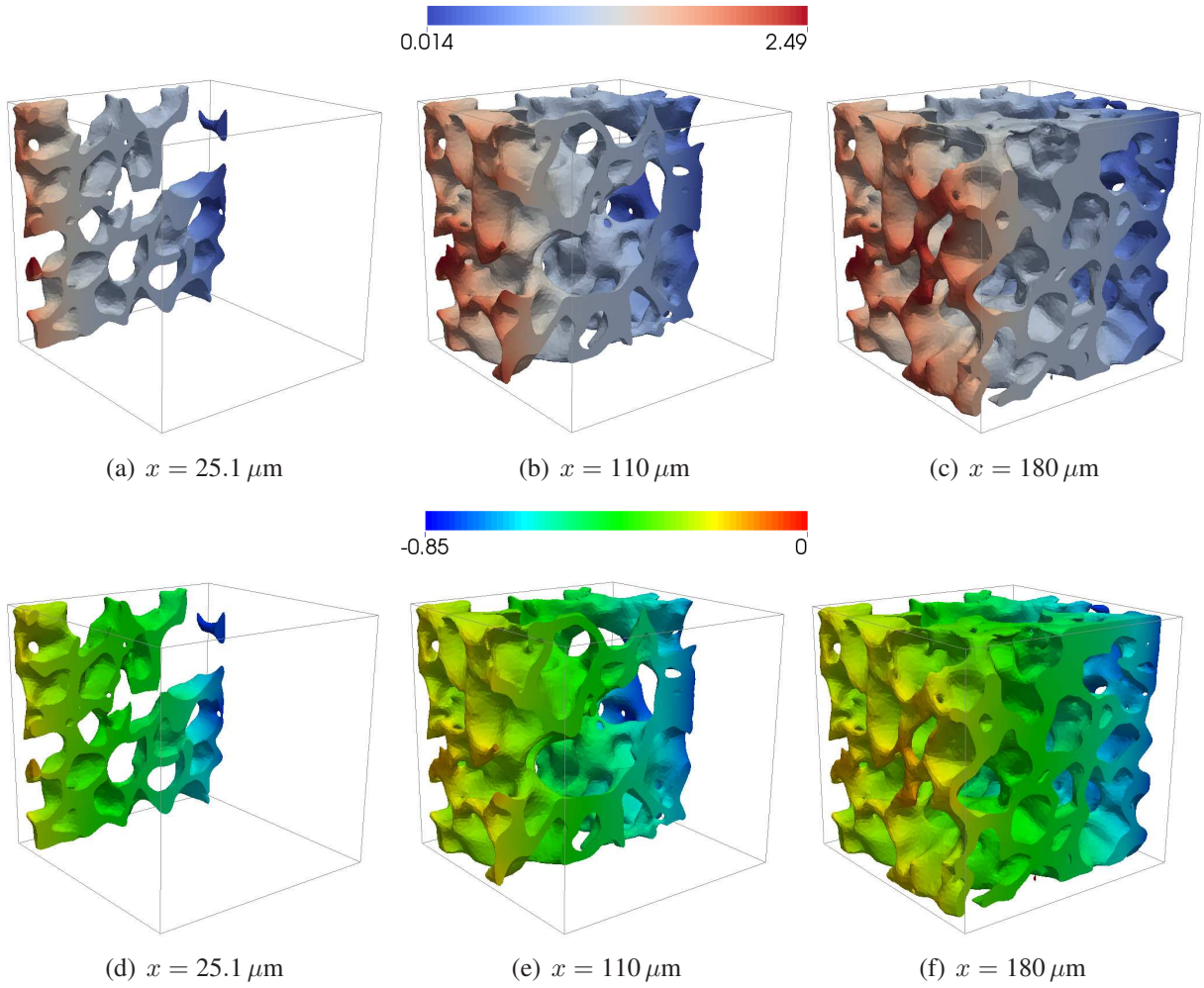

(a) $x = 25.1\,\mu\text{m}$ (b) $x = 110\,\mu\text{m}$ (c) $x = 180\,\mu\text{m}$

(d) $x = 25.1\,\mu\text{m}$ (e) $x = 110\,\mu\text{m}$ (f) $x = 180\,\mu\text{m}$

Figure 7.20: Selected cross-section of the computational domain at current interruption time $T_\text{I} = 10\,\text{s}$: a) – c) concentration field c in [M] and e) – f) potential field Φ in [V].

in an increased concentration level on the left hand side and in a decreased concentration level on the right hand side. The local reaction rate which is directly related to the current density i at the electrode surface is non-constant as a result of the galvanostatic boundary condition in combination with the Butler-Volmer law given in Equ. (2.97). In this case, the reaction rate depends on the local concentration c and potential Φ next to the electrode as well as on the adjustable cell potential U. The concentration profiles c at anode and cathode are inhomogeneous with a maximum concentration at the anode of $c = 2.49\,\text{M}$ and a minimum concentration at the cathode of $c = 0.014\,\text{M}$. The areal intrinsic phase average of the concentration at the anode is $\overline{c}^{\,\text{e}}_\text{A} = 2.16\,\text{M}$ and at the cathode $\overline{c}^{\,\text{e}}_\text{C} = 0.063\,\text{M}$. These numbers confirm the visual impression that the inhomogenity of the concentration profile at the anode is higher than at the cathode which is a result of the mass-transport limitation. The same inhomogenity can be also observed for the electric potential in the electrolyte solution next to anode and cathode.

The current $I(t)$ and the cell potential $U(t)$ during the polarization phase and the relaxation phase are depicted in Fig. 7.21. As for the PGP experiment shown in Fig. 7.8, the current is con-

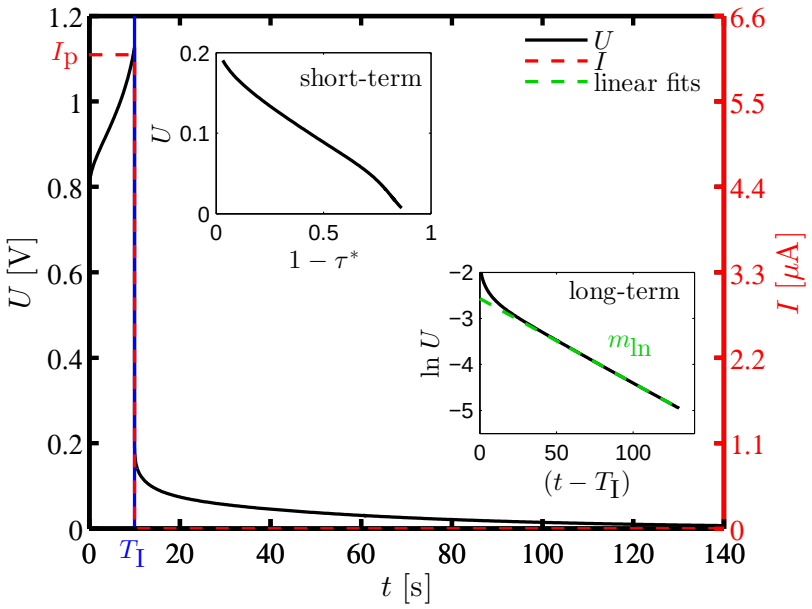

Figure 7.21: Time-dependent cell potential $U(t)$ for polarization and relaxation phase as a result of the a polarization current $I_\mathrm{p} = 6.1\,\mu\mathrm{A}$.

stant during the polarization and zero after current interruption. As a result of the concentration dependent conductivity and the increasing concentration and surface overpotentials, the cell potential raises continuously from about 0.8 V to about 1.15 V during the polarization phase. After current interuption, the cell potential is slowly decreased as a result of the relaxing concentration profile. Compared to simulations presented in section 7.5, the cell potential $U(T_\mathrm{I})$ is much higher since limiting current and, therefore, the maximum possible concentration difference for a 1 M electrolyte solution is reached at current interuption time. As a result, the linearity of the cell potential $U(t)$ with respect to the artificial time τ^* cannot be observed anymore. In contrast, the long-term relaxation behavior of the cell potential $U(t)$ exhibits the same characteristic as for smaller polarization currents. However, the tortuosity $\tau_{m_\mathrm{ln}} = 2.1$ calculated based on the slope m_ln and the known diffusion coefficient $D(c_0 = 1\ \mathrm{M})$ differs significantly from the tortuosity calculated from electrolyte resistance. This can be explained by the mass limiting current resulting in a non-symmetric concentration difference as indicated in the previous paragraph. For PGP and SSPP experiments with smaller applied currents, the tortuosity based on electrolyte resistance R_el is confirmed.

In section 7.2 and section 7.4, the computational efficiency was shown for simple three-dimensional and quasi one-dimensional computational domains, respectively. The efficiency and stability of the proposed computational approach for a complex domain discretized with a large number of elements is demonstrated by this numerical example. The simulation was performed with 64 processors resulting in about 25 000 DOF's per processor. A tolerance of $1 \cdot 10^{-8}$ is required for the linear solver and a tolerance of $1 \cdot 10^{-6}$ for the Newton-Raphson iteration and

the galvanostatic constraint condition. The mean element evaluation time was 3.4 s. This number could be decreased further if the similarity between two terms were used as discussed in section 7.2. The number of GMRES iteration per Newton iteration is given in Tab. 7.10. During the polarization phase, the number of GMRES iterations is higher than during the relaxation phase. Both numbers are slightly larger than the number of GMRES iterations resulting from the three-dimensional test case discretized with hexahedral elements presented in section 7.2. During the polarization and relaxation phase, two Newton iteration per galvanostatic iteration (GSI) are necessary to get a converged solution. As indicated by the low number of GSI per time step, the galvanostatic constraint condition using the integrated conductivity as predictor step also performs very well in complex three-dimensional domains with non-uniform electrode areas. During the relaxation phase, the number of GSI corresponds to the number of time steps since the no-flux condition is fulfilled automatically.

Table 7.10: Numerical efficiency of the proposed numerical solution scheme for a realistic domain.

	linear GMRES iterations per Newton iteration	Newton iterations per GSI	num. GSI	GSI per time step
Polarization phase	30.01	2.02	2581	2.15
Relaxation phase	23.83	2.0	13300	1

Table 7.11: Simulation parameter for the galvanostatic simulation of lung tissue.

Edge length of computational domain [mm]	0.2
Volume of computational domain V^{e} [mm^3]	$2.7 \cdot 10^{-3}$
Number of elements / degrees of freedom	2,272,169 / 1,428,708
Element size h [mm]	$2.25 \cdot 10^{-3}$
Initial concentration $\overline{c}_0^{\mathrm{e}}$ [M]	1.0
Polarization current I_{p} [μA]	6.1
Min. and max. time step size Δt [s]	0.001 / 0.1
Current interruption time T_{I} [s]	10
Diffusion coefficient $D_{\pm}$ [$\frac{\mathrm{mm}^2}{\mathrm{s}}$]	$1.48 \cdot 10^{-4}\, c^{-0.125}$
Transference number t_+ [$-$]	$0.4 - 0.01c$
Thermodynamic factor $\left(1 + \frac{\partial \ln f_{\pm}}{\partial \ln c}\right)$ [$-$]	$1 - 0.5c^{1/2} + 2c$
Conductivity κ [$\frac{\mu\mathrm{S}}{\mathrm{mm}}$]	$\frac{3900c - 8700c^{3/2} + 8000c^2 + 5000c^3}{1.0 + 7.0c^2 + 9.0c^4}$
BV conditions	$i_0 = 10\mu\mathrm{A\,mm}^{-2}$, $\gamma = 1.0$, $\alpha_{\mathrm{A}} = \alpha_{\mathrm{C}} = 0.5$

8 Determination of a complete set of transport parameters

In this work, transport parameters are determined exemplarily for an electrolyte solution consisting of Lithiumperchlorate ($LiClO_4$) dissolved in a mixture of Ethylene Carbonate (EC, 50 % wt.) and Diethyl Carbonate (DEC, 50 % wt.) which is abbreviated by x M $LiClO_4$ in EC:DEC (1:1 w %). Generally, the mixture of a polar (EC) and an nonpolar (DEC) solvent is favorable to guarantee good wettability of the nonpolar polypropylene separator as well as good solubility of the polar salt. A detailed review on nonaqueous liquid electrolytes for lithium-ion-based batteries is given, e.g., by Xu [156] and on porous separators, e.g., by Arora and Zhang [8]. It is important to emphasize that all presented methods can also be applied to any lithium-ion-based binary electrolyte solutions.

In section 8.1, various physical properties of individual components and of the electrolyte solution such as molar mass M and density ρ are summarized. The results of the conductivity cell introduced in section 5.1 are discussed shortly in section 8.2. In section 8.3, the novel experimental procedure for the determination of the mean molar activity coefficient $f_\pm$ or, respectively, the thermodynamic factor proposed in section 5.2 is analyzed. In section 8.4, the transference number is determined based on concentration cell data as described in section 5.6. The different methods for the determination of the diffusion coefficient and the transference number based on polarization experiments introduced in section 5.4 and section 5.5 are discussed critically in section 8.5. The results presented in this section are also published in Landesfeind et al. [96] and Ehrl et al. [56].

8.1 Physical properties of the electrolyte solution

In Tab. 8.1, the density ρ, the molar mass M and the relative permittivity ε_R of all electrolyte components and of the solvent mixture EC:DEC (1:1 w%) are given. The molar mass $M_\mathrm{EC:DEC}$ is calculated based on the formula

$$M_\mathrm{EC:DEC} = \frac{M_\mathrm{EC} M_\mathrm{DEC}}{(w_\mathrm{EC} M_\mathrm{DEC} + w_\mathrm{DEC} M_\mathrm{EC})}.$$

The density ρ of the solvent EC:DEC (1:1 w%) can be approximated by the mass of EC and DEC contained in 1 L solvent

$$\rho = \frac{m_\mathrm{EC} + m_\mathrm{EC}}{1\,\mathrm{L}} = 2\frac{\rho_\mathrm{EC}\,\rho_\mathrm{DEC}}{\rho_\mathrm{EC} + \rho_\mathrm{DEC}}.$$

Table 8.1: Physical properties of all electrolyte components and the solvent mixture EC:DEC (1:1 w %) at $T = 25°C$.

		$LiClO_4$ (solid)	EC	DEC	EC:DEC(1:1 w %) calc.	EC:DEC(1:1 w %) meas.
Density ρ	$\left[\frac{g}{cm^3}\right]$	2.42[1]	1.321[156]	0.969[156]	1.118	1.124
Molar mass M	$\left[\frac{g}{mol}\right]$	106.4[1]	88[156]	118[156]	100.8	-
Relative permittivity ε_R	$[-]$	-	89.78[156]	2.805[156]	-	35 ± 3[96]

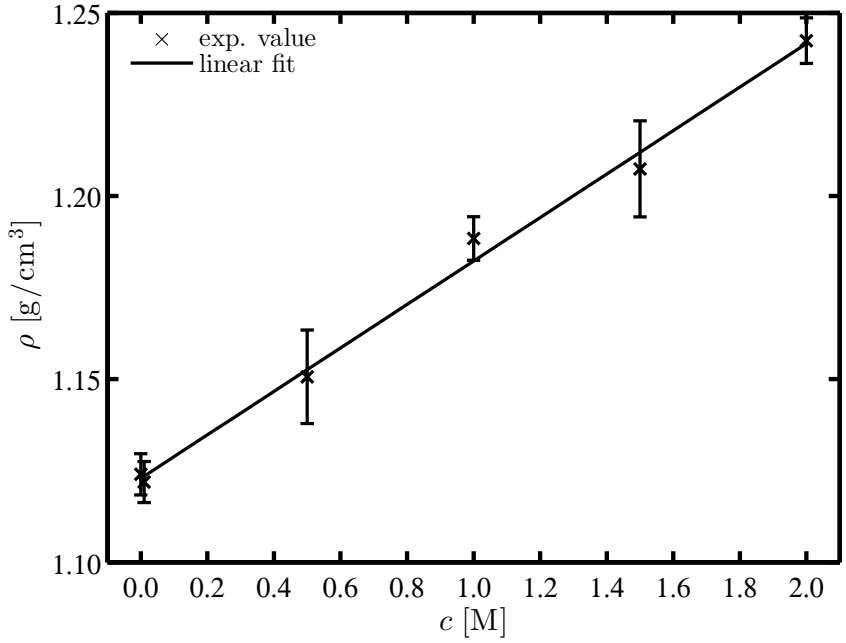

Figure 8.1: Density ρ of $LiClO_4$ in EC:DEC (1:1 w %).

The calculated density ρ of the solvent is confirmed experimentally as indicated in Tab. 8.1. The same density measurements were repeated for the electrolyte solution with a varying $LiClO_4$ concentration. The results are depicted in Fig. 8.1 showing almost a linear behavior for an increasing $LiClO_4$ concentration. Such a behavior is typical for many electrolyte solutions as shown, e.g., in Barthel et al. [17]. The experimental data are represented well by the linear function

$$\rho(c) = 1.124 + 0.06c. \tag{8.1}$$

As a result, the total concentration $c_T = c_0 + c$ and the solvent concentration c_0 can be calculated based on the ratio of components, the salt concentration c and the density ρ. These quantities are only important for the model suggested by Latz and Zausch [99] and for the refor-

mulation of the binary diffusion coefficient in terms of the molecular diffusion coefficients $\mathcal{D}_{kl}$ as explained in section 2.4.1. The total concentration c_T is related to the total amount of n_T

$$n_\mathrm{T} = n_\mathrm{EC} + n_\mathrm{DEC} + n_{\mathrm{LiClO_4}} = \left(\frac{1}{M_\mathrm{EC}} + \frac{1}{M_\mathrm{DEC}}\right) m_\mathrm{EC/DEC} + n_{\mathrm{LiClO_4}}, \tag{8.2}$$

where n_EC denotes the amount of EC, n_DEC the amount of DEC, $n_{\mathrm{LiClO_4}}$ the amount of the salt and $m_\mathrm{EC/DEC}$ the mass of the single solvent components. For the used solvent, the mass of single components is given by $m_\mathrm{EC/DEC} = m_\mathrm{EC} = m_\mathrm{DEC}$. Based on the definition of the electrolyte density $\rho = (2m_\mathrm{EC/DEC} + m_{\mathrm{LiClO_4}})/V$, the mass $m_\mathrm{EC/DEC}$ can be also written as

$$m_\mathrm{EC/DEC} = \frac{1}{2}\left(\rho V - M_{\mathrm{LiClO_4}} n_{\mathrm{LiClO_4}}\right). \tag{8.3}$$

In terms of the total concentration $c_\mathrm{T} = n_\mathrm{T}/V$, Equ. (8.2) and Equ. (8.3) can be combined to

$$c_\mathrm{T} = \left(\frac{1}{M_\mathrm{EC}} + \frac{1}{M_\mathrm{DEC}}\right)\frac{1}{2}\left(\rho - M_{\mathrm{LiClO_4}} c\right) + c,$$

where $c = n_{\mathrm{LiClO_4}}/V$. The solvent concentration c_0 is given by $c_\mathrm{T} - c$.

8.2 Conductivity

As presented in section 5.1, the concentration dependent conductivity $\kappa(c)$ of the electrolyte solution is measured with a conductivity cell. The resulting experimental data depicted in Fig. 8.2 are fitted by the function

$$\kappa(c) = \kappa_\mathrm{max}\left(\frac{c}{c_\mathrm{max}}\right)^{x_3} \exp\left(x_4\left(c - c_\mathrm{max}\right)^2 - \frac{x_3}{c_\mathrm{max}}\left(c - c_\mathrm{max}\right)\right) \tag{8.4}$$

proposed by Casteel and Amis [37] or, alternatively, by the function

$$\kappa(c) = \frac{x_1 c - x_2 c^{3/2} + x_3 c^2 + x_4 c^3}{1.0 + x_5 c^2 + x_6 c^4}. \tag{8.5}$$

In Kreysa et al. [92], Equ. (8.4) is introduced as a fitting function representing best the conductivity of moderate and high concentrated electrolyte solutions. Equ. (8.5) is defined in order to

Table 8.2: Fitting parameters for Equ. (8.4) and Equ. (8.5) describing the conductivity $\kappa(c)$.

	x_1	x_2	x_3	x_4	x_5	x_6
Equ. (8.4)	$0.83(c_\mathrm{max})$	5.94 (κ_max)	0.81	-0.06	-	-
Equ. (8.5)	39.0	75.13	67.60	-10.38	2.30	0.30

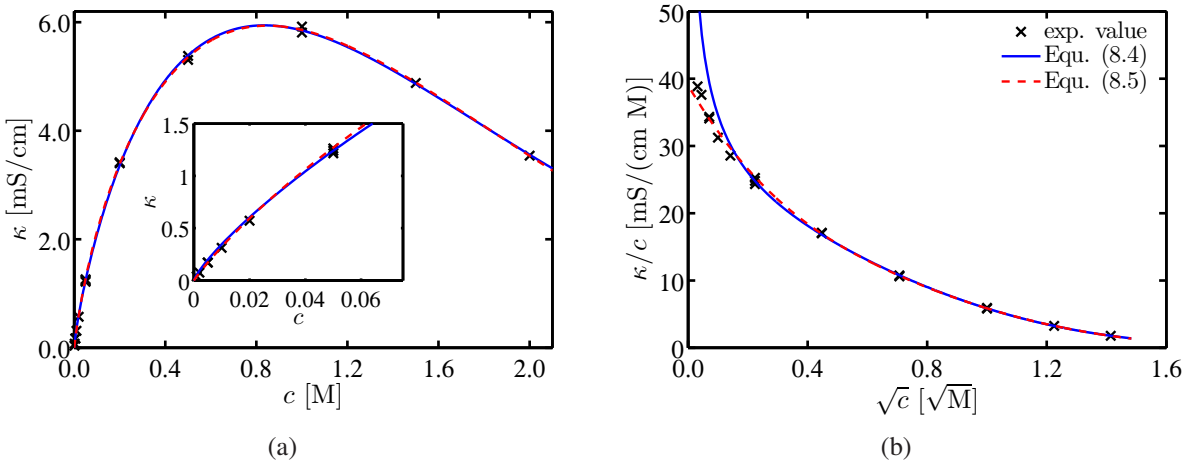

Figure 8.2: Conductivity κ and molar conductivity κ/c for $LiClO_4$ in EC:DEC (1:1 w %).

fulfill additionally the Kohlrausch square law $\lambda_m(c) = \frac{\kappa(c)}{c} = \lambda_m^0 - k\sqrt{c}$ for dilute solutions as discussed, e.g., in Hamann and Vielstich [78]. Similar functions are used, e.g., in Nyman et al. [115] or Thorat et al. [140]. The corresponding fitting parameters for both functions are given in Tab. 8.2. For Equ. (8.4), the parameters x_1 and x_2 are equal to c_{max} and κ_{max}, respectively. For Equ. (8.5), the parameter x_1 can be interpreted as the molar conductivity λ_m^0 at infinite dilution and the parameter x_2 as parameter k of Kohlrausch square law. For the conductivity shown in Fig. 8.2(a), the differences between the two fits are negligibly small. In case of the molar conductivity, differences are observable for dilute solutions. Therefore, Equ. (8.5) is used as functional description for the conductivity in this contribution. However, for the investigated electrolyte solution, the differences between Equ. (8.4) and Equ. (8.5) are so small that the numerical results would not be influenced significantly if Equ. (8.5) was used instead of Equ. (8.4).

8.3 Thermodynamic factor

In the following section, the experimental setup and procedure for the determination of the transference number introduced in section 5.2 is described in detail. Afterwards, the experimental results are presented.

8.3.1 Experimental procedure

Measurements and electrolyte preparations were performed in an argon filled and temperature controlled glove box (MBraun, 25 °C ± 1°C, water content <0.1 ppm, Ar 5.0, Westfalen, 99.999 % Vol). A custom made three electrode glass setup as shown in Fig. 8.3 was used with a platinum (Advent, 99.99+ %) counter electrode (CE), gold (Alfa Aesar, 99.999 %) working electrode (WE) and a lithium (Rockwood Lithium, 0.45 mm, high purity) reference electrode (RE). Individual cell compartments were separated by porous glass frits. The distance between the

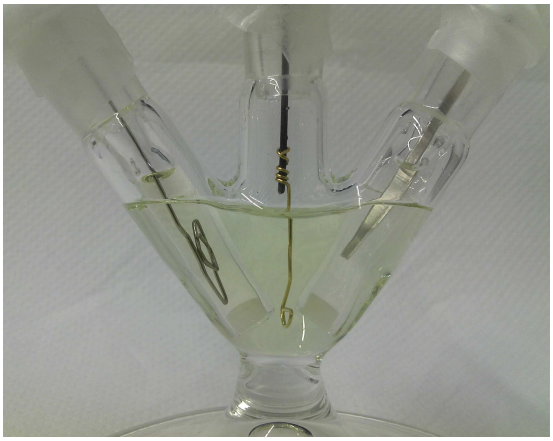

Figure 8.3: Three electrode glass setup: platinum counter electrode and gold working electrode in EC:DEC (1:1, wt%) electrolyte containing $LiClO_4$ concentrations from 0.1 x 10^{-3} to 2 M and 50 μM ferrocene and lithium reference electrode in same electrolyte without ferrocene.

electrodes was kept small ($\sim$ 1 cm) to minimize ohmic drops in the electrolyte phase. To prevent electrolyte evaporation the cell is sealed with polytetrafluorethylen sealing rings (Glindemann) at all grounded glass joints and the electrodes are electronically connected with the potentiostat via fused-in tungsten wires. All glass cell parts were cleaned by boiling them in a mixture of ethanol and water (Millipore, Elix, 15 MΩ), thoroughly rinsed with water and then dried at 70 °C in a heating oven before bringing them into the glove box. Relative solvent permittivities were measured in a custom made coaxial stainless steel setup using impedance spectroscopy. A mixture of ethylene carbonate (EC, 50 %, by weight, Sigma Aldrich, anhydrous, 99 %) and diethyl carbonate (DEC, 50 %, by weight, Sigma Aldrich, anhydrous, >99 %) was used as solvent for the investigated electrolytes, containing $LiClO_4$ (Sigma Aldrich, 99.99%) concentrations from 0.1 x 10^{-3} to 2 M. Ferrocene (Fc, Merck, > 98 %) was added to the electrolyte in CE and WE compartment at concentrations of 50 μM or 100 μM. Due to the small association constant of comparable electrolytes, 48 dm^3/mol for $LiClO_4$ in PC/EMC as discussed, e.g., by Besenhard [24], ion pair formation is neglected in this work. In consecutive measurement series with multiple $LiClO_4$ concentrations, smallest concentrations were measured first to avoid contamination by salt remains of previous experiments.

A Biologic VMP3 potentiostat/galvanostat was connected to the cell inside the glove box using actively shielded cables. The cell impedance was measured and the high frequency resistance between WE and RE was extracted by linear extrapolation of the high frequency part in a Nyquist plot. Recorded cyclic voltammograms between 2.5 V and 4 V versus Li/Li^+ were online IR corrected for different percentages of the determined WE-RE resistance. Always five consecutive scans were performed per analyzed scan rate (10 mV/s or 20 mV/s).

8.3.2 Results and discussion

Selection of experimental procedure As the parameters of the CV measurements influence the validity of theoretical assumptions, it is necessary to identify a proper set of measurement conditions to fulfill the requirements described in the theoretical part of this work, mostly the

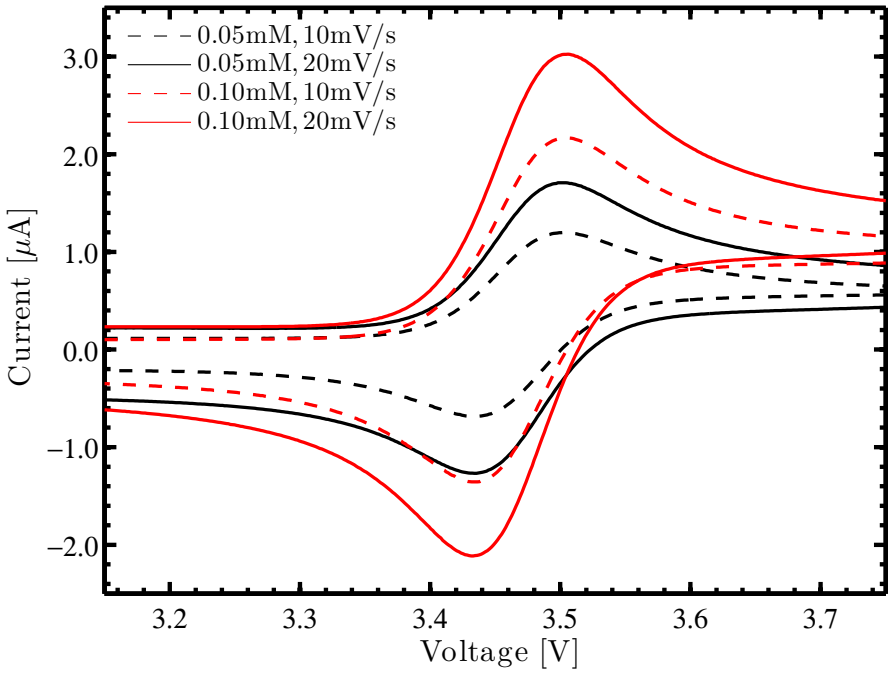

Figure 8.4: Cyclic voltammetry using two different scan rates (10 mV/s, dashed line and 20 mV/s, solid line) of two different ferrocene concentrations ($c_{\mathrm{Fc}} = 50\,\mu$M, black and $c_{\mathrm{FC}} = 100\,\mu$M, red) in a 2 mM $LiClO_4$ electrolyte solution, 85 % online IR correction.

small ferrocene concentration in comparison with the $LiClO_4$ salt. Fig. 8.4 shows the second CVs with 50 μM and 100 μM concentrations of ferrocene in 2 mM $LiClO_4$ at scan rates of 10 mV/s and 20 mV/s. Of five consecutive voltammograms only scans 2 – 4 are used in the following analysis. The first scan is always omitted. All curves show reversible oxidation and reductions peaks of the ferrocene couple at $\sim$ 3.51 V and $\sim$ 3.43 V respectively. Following the argumentation in the theoretical part of this work, the smaller ferrocene concentration of 50 μM was used for the following experiments in order to satisfy the requirement of a small c_{Fc^+} to $c_{\mathrm{LiClO_4}}$ ratio to avoid parasitic effects such as diffusion overpotentials. Additionally, small ferrocene concentrations result in small currents and, thus, small ohmic drops in the electrolyte phase. It also guarantees that the ionic strength can be approximated by the concentration of supporting electrolyte. Extraction of oxidation and reduction peak potentials was done by calculation of maximum and minimum of a fifth order polynomials which were fitted through the data points $\pm \sim 50$ mV around the measured extrema. Due to the sensitivity of this procedure on the peak sharpness, the larger scan rates of 20 mV/s, showing higher oxidation and reduction currents, are used subsequently. For the same reason the ferrocene concentration is not reduced further. All following experiments have been conducted using the just determined set of measurement conditions, a scan rate of 20 $\frac{\mathrm{mV}}{\mathrm{s}}$ and a ferrocene concentration of 50 μM.

Ohmic drop compensation and correction The effect of uncompensated resistance is discussed in the following using the aforementioned set of measurement conditions, a scan rate of

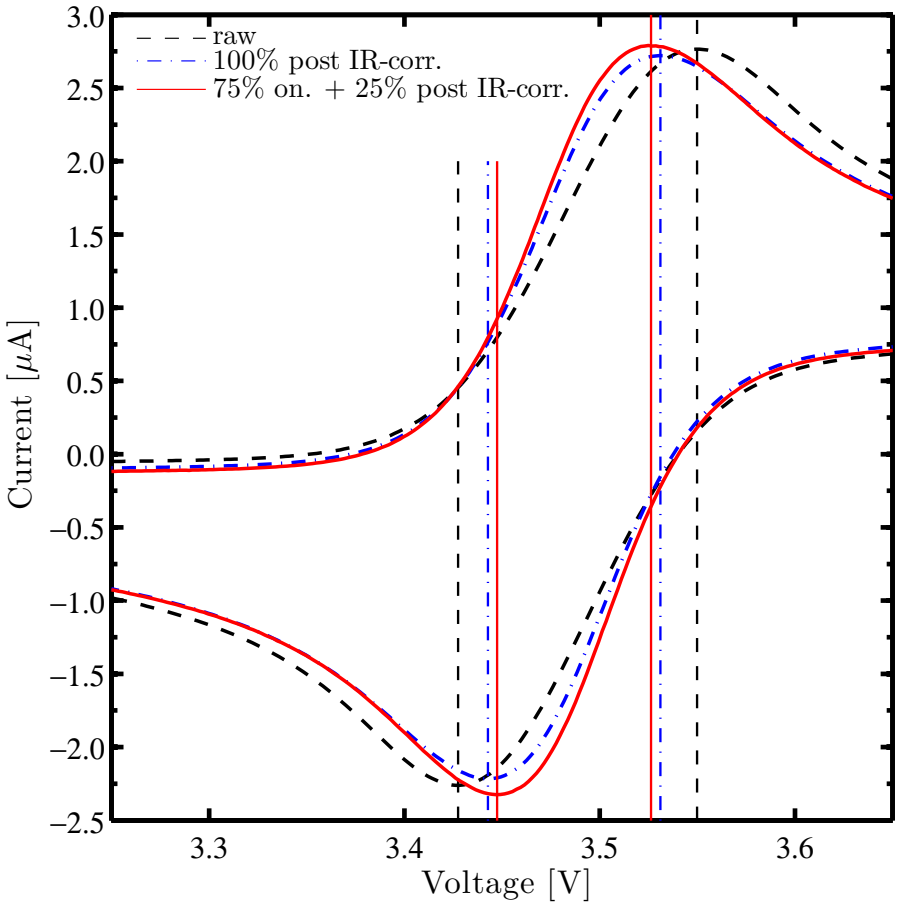

Figure 8.5: CVs showing the influence of IR correction on oxidation and reduction peak positions of 50 μM ferrocene, scan rate of 20 mV/s, 1 mM $LiClO_4$ supporting electrolyte solution. Different methods for the IR-correction: raw data (dashed line), 100 % post IR-correction (dash-dotted line) and 75 % online + 25 % post IR-correction (solid line).

20 mV/s and a ferrocene concentration of 50 μM. Fig. 8.5 shows an example for the influence of different types of IR correction on the peak positions. Without IR correction, oxidation and reduction peak potentials in a 1 mM $LiClO_4$ electrolyte are 3.550 V and 3.428 V respectively. Ferrocene oxidation and reduction peak potentials of 3.531 V and 3.443 V are obtained if raw data are IR corrected after the measurement according to

$$U_{i,\text{corr}} = U_{i,\text{meas}} - I_{i,\text{meas}} \cdot R_{\text{RE-WE}}$$

In the following, this method is called post IR correction, according to its execution after the measurement. The resistance $R_{\text{RE-WE}}$ was determined from impedance measurements prior to the cyclic voltammetry scans. As oxidation and reduction currents are different (2.8 μA and 2.3 μA respectively), the IR correction has different impacts on oxidation and reduction peak potentials resulting in a non-symmetric behavior which can be observed in Fig. 8.5. Note that oxidation and reduction currents also include a current flow which is used for the build-up of the

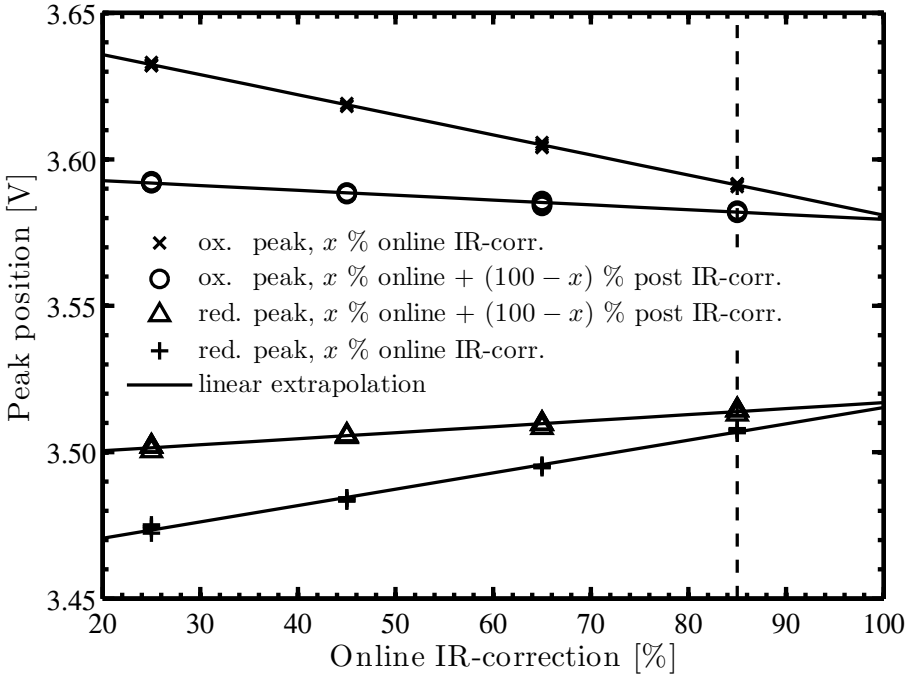

Figure 8.6: Oxidation (cross, circle) and reduction (triangle and plus) peak potentials for different percentages of online IR-corrections (cross, plus) and same potentials for x % online + $(100 - x)$ % post IR correction (circle, triangle).

double layer and, therefore, do not impose an ohmic drop in the electrolyte phase. Double layer currents were estimated from the capacity obtained by impedance measurements as well as the scan rate. Although this correction was done for all post IR corrected potentials reported below, its magnitude is negligible as the double layer currents are 10 to 40 times smaller than the CV's peak currents.

For electrolyte solutions with RE-WE resistances in the kΩ range, the effective potential in the cyclic voltammogram is not truly linear with time anymore. This behavior can be circumvented by an online, i.e. live, IR correction for a certain percentage of the uncompensated resistance as explained theoretically, e.g., in Bard and Faulkner [14]. Essentially, the scan rate is adjusted continuously during the scan resulting in a linear effective potential time behavior although the applied potential is non-linear as discussed by Bond et al. [27]. As oscillations are observed for online IR corrections close to 100 % of the total uncompensated resistance which are due to the measurement hardware, it is only possible to correct for 85 % of the ohmic drop. As a result, a combined IR correction consisting of an online IR correction and a subsequent post IR correction is introduced in the following. Fig. 8.5 shows the effect of such a combined IR correction, based on 75 % online + 25 % post IR correction, giving a peak potential of 3.526 V for oxidation and 3.447 V for reduction peak potentials, respectively. Although both cases, 100 % post IR correction and a combined 75 % on. + 25 % post. IR correction, theoretically account for the same total ohmic drop, a difference in peak positions of $\sim$ 5 mV is observed between both

methods. This shows the importance of online over post IR correction and raises the question of remaining uncertainties within the combined IR correction.

As a 100 % online IR correction cannot be realized, CVs with four different percentages of online IR correction were measured in a 0.1 mM $LiClO_4$ electrolyte as shown in Fig. 8.6 to validate the following analysis procedure. This smallest $LiClO_4$ concentration is chosen on purpose to visualize the methodology best. Cross and plus symbols in Fig. 8.6 correspond to oxidation and reduction peak potentials which are only improved by an x % online IR correction. Further $(100 - x)$ % post IR correction of these potentials by the remaining resistance results in oxidation and reduction potentials indicated by circles and triangles, respectively. Both peak potentials resulting from an x % online IR correction and an x % online + $(100 - x)$ % post IR corrections are extrapolated to 100 % based on the peak potential values for 25 %, 45 %, 65 % and 85 % online correction. The data are well represented by linear extrapolation lines as shown in Fig. 8.6 with an interception point close to 100 % IR correction. It is concluded that the peak potentials obtained by 85 % online + 15 % post IR correction still shows a small deviation of about 3 mV from the extrapolated value for 100 % online IR correction. Therefore, measurements for two ratios of x % online + $(100 - x)$ % post IR correction were performed and extrapolated to 100 % online IR correction. For concentrations above 5 mM $LiClO_4$ this procedure leads to negligibly small corrections compared to the value obtained from a 85 % online + 15 % post IR correction and cannot be distinguished from non-extrapolated values in the following figures.

Data selection A quality measure for obtained oxidation and reduction potentials is the peak separation. For reversible processes with fast electrode kinetics, the theoretical peak separation as given in Tab. 5.1 should be 58 ± 1 mV since the potential difference between the oxidation peak and the vertex potential is larger than 300 mV.

For all measured $LiClO_4$ concentrations, the potential differences between oxidation and reduction peaks are plotted in Fig. 8.7. To show reproducibility, the peak separation data are shown for three independent measurement series. In the measurement series three, extrapolated values exist only for concentrations between 0.5 mM and 20 mM. Other measurements in this series were only done using 85 % online + 15 % post IR correction. In the following analysis data points for measurement series three for concentrations above 20 mM are the values from the combined IR correction directly, without extrapolation. Fig. 8.7 depicts a constant peak separation for concentrations above 5 mM. For concentrations below 5 mM $LiClO_4$, the peak potential increases to 90 – 100 mV for the extrapolated values of a 0.1 mM $LiClO_4$ concentration. From the constant peak separation of all measurement series for concentrations above 5 mM it is concluded, that all aforementioned parasitic effects influencing the peak potentials are negligible for these measurements. The first measurement series shows a shift of all measured peak separations by about 5mV compared to measurement two and three. This was identified as an experimental artifact caused by not flame annealing, and thereby removing thin oxide layers on the working electrode for this set of measurements. As explained in Besenhard [24], a thin oxide film on the gold WE reduces the rate constant k_0 of the outer electron transfer of the ferrocene / ferrocenium couple, which depends on the electron tunneling length, i.e., the thickness of the oxide layer on the gold surface. A smaller rate constant k_0 results in an increased peak separation according to Equ. (5.12). Nevertheless, a deviation from the expected peak separation according to Tab. 5.1

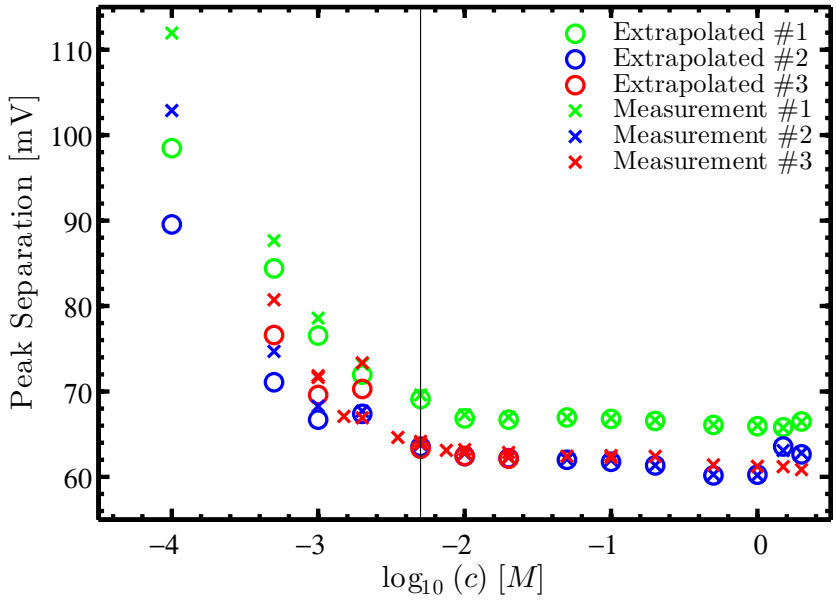

Figure 8.7: Peak separation of three independent measurement series with extrapolated values. The solid line indicates a concentration of 5 mM.

remains which can also be explained by non-ideal kinetic effects resulting in a decreased rate constant k_0 as indicated in Bard and Faulkner [14].

However, for the methodology presented in the theoretical part as well as below, a constant peak separation is sufficient for further analysis. For concentrations below 5 mM, the observed increase in peak separation can be ascribed to the following effects. The kinetic rate constant k_0, the ratio of diffusion coefficients of ferrocene and ferrocenium as well as the activity coefficient of $FcClO_4$ may depend on the concentration of supporting electrolyte as explained in the theoretical part of this work. In addition, the ratio of ferrocene to supporting electrolyte may introduce a diffusion overpotential, which affects oxidation and reduction peak potentials asymmetrically (compare Equ. (5.15)). The concentration overpotential can be estimated by Equ. (5.15), only partly explaining the increase in peak separation. For example, a decrease in peak separation of about 2 mV is expected for a 1 mM $LiClO_4$ concentration if the concentration overpotential is subtracted from the oxidation peak potential. This low value is a result of the chosen experimental setup with a minimal ferrocene to supporting electrolyte concentration ratio. An obvious trend is only visible for the smallest $LiClO_4$ concentration where the half peak potential is clearly shifted towards the oxidation peak as a result of the non-symmetric behavior of the concentration overpotential as explained in the theory section.

In addition, the ratio between ferrocenium and ferrocene diffusion coefficients as shown in Equ. (5.12), which may depend on the supporting electrolyte concentration as indicated, e.g., in Wang et al. [148] or Ruff et al. [128], also influences the peak separation. A quantitative estimation is not possible as no literature values exist for the considered system. The reaction

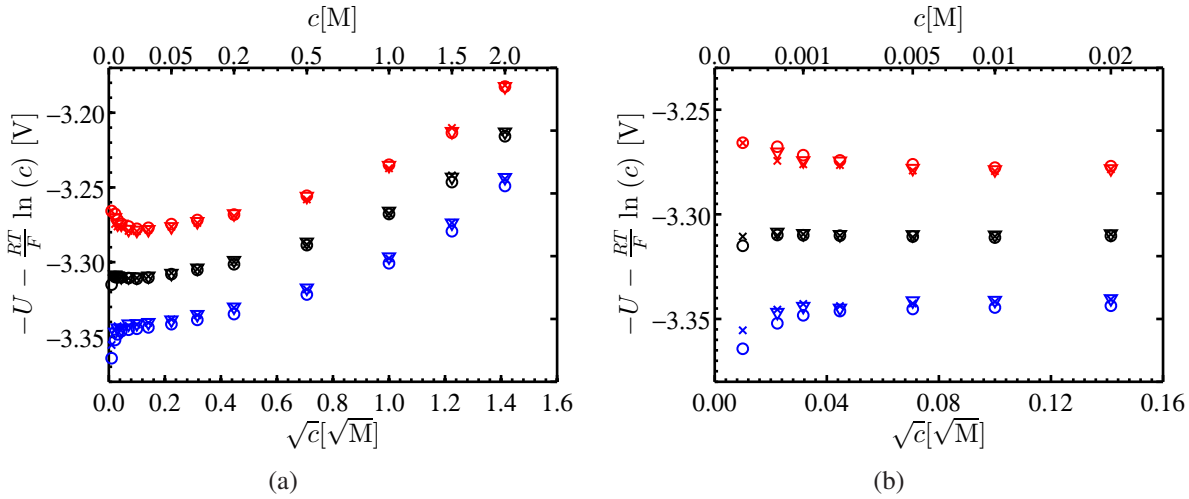

Figure 8.8: a) Potentials, extrapolated to 100 % online IR correction, of reduction peaks (red), half wave positions (black) and oxidation peaks (blue) for measurement series one (circles), two (crosses) and three (triangles), for different salt concentrations, b) zoom to small concentration region.

rate constant k_0 may also depend on the concentration of the supporting electrolyte as was shown, e.g., by Peter et al. [120]. In the same publication, the effect of ion pairing is also mentioned as an explanation for the non-ideal behavior of a cyclic voltammogram. A similar concept is discussed in Redepenning et al. [125]. The best explanation for the increase in peak separation is, in our opinion, a supporting electrolyte concentration dependence of the rate constant k_0. Nonetheless, for concentrations below 5 mM, a combination of all of the described effects has to be assumed. The result of the data selection is that only concentrations above 5 mM $LiClO_4$ are used for evaluating the activity coefficient from measured data points while smaller concentrations are still plotted for comparison.

Parameter extraction In Fig. 8.8, oxidation, reduction and half wave potentials of all measured concentrations are subtracted by $RT/F \ln c$ and their negative values are plotted over the square root of concentration to visualize the theoretically expected linear behavior for lowest concentrations as shown in Equ. (5.8) and Equ. (5.21):

$$y_{\mathrm{Axis}} = -U_{\mathrm{meas}} - \frac{RT}{F} \ln(c_{\mathrm{Li^+}}) = -U_{\mathrm{Ref}} + 2\frac{RT}{F} \ln(f_{\mathrm{LiClO_4}})$$

In Fig. 8.8, the previously mentioned constant peak separation as well as its increase for concentrations below 5 mM can be observed. It can also be seen that above 5 mM the curves look identical, only shifted along the y-axis. Data fitting with Equ. (5.21) can therefore be done for oxidation, half wave or reduction peak potential for concentrations above 5 mM, as the only necessity is a constant reference potential. For lowest concentrations, Equ. (5.21) simplifies to the Debye-Hückel limiting law given by Equ. (5.20) which predicts a linear slope of the logarithmic mean molar activity coefficient over the square root of concentration. As the concentration is equivalent to the ionic strength for small ferrocene concentrations, the slope of the tangent at

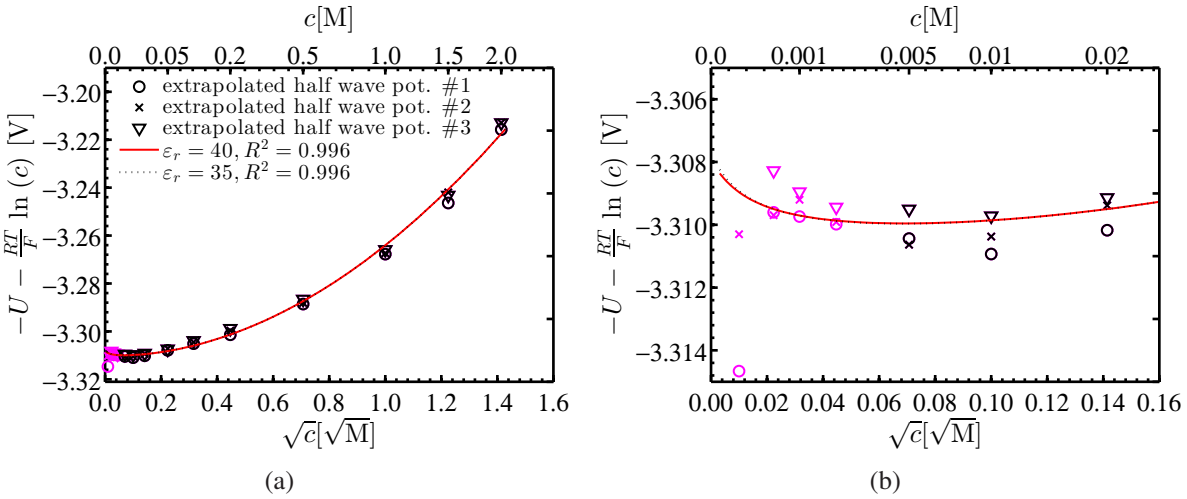

Figure 8.9: a) Fit of reformulated, extrapolated to 100 % online IR correction, half wave potentials for measurement series one (circles), two (crosses) and three (triangles) in concentration range from 5 mM to 2 M with Debye-Hückel behavior of activity coefficient. Concentrations below 5 mM are neglected for the fit (magenta), b) zoom to small concentration region.

concentration zero corresponds to the Debye-Hückel parameter A. The concentration range, in which this linear relationship is still visible, can be estimated by comparing Equ. (5.21) with its simplified form, Equ. (5.20). As long as $B\dot{a}\sqrt{I}$ in the denominator of Equ. (5.21) is small, a linear behavior is expected. Parameter $\dot{a}$ is proportional to a distance of closest approach and parameter B depends on the relative permittivity of the solvent as discussed, e.g., in Hamann and Vielstich [78]. The relative permittivity was measured in a coaxial cell setup using impedance spectroscopy resulting in a value of$\varepsilon_\mathrm{R} \approx 35 \pm 3$. This value is further confirmed for a similar system of $LiClO_4$ in PC:DEC, 1:1 by weight by Ding [49]. A reasonable assumption for the distance of closest approach of lithium and perchlorate ions in the used aprotic solvent is 1 nm as given in Hamann and Vielstich [78]. Based on the aforementioned parameters, the concentration range showing the linear relationship is up to $LiClO_4$ concentrations of 0.1 mM, which is way below the range of previously selected good quality measurement points. In comparison, a linear trend should be observable up to concentrations of about 2.5 mM for aqueous systems ($\varepsilon_\mathrm{R} \approx 80$, distance of closest approach 0.3 nm) as given in Hamann and Vielstich [78]. For the investigated non-aqueous electrolyte solution a linear behavior is thus not expected in the measured concentration range. Hence, data points were fitted using a calculated slope A based on the measured relative permittivity of the solvent.

Resulting fits of the reformulated half wave potentials are depicted in Fig. 8.9 with fixed relative permittivities ε_R of the solvent of 35 or 40. A second relative permittivity is shown to analyze the sensitivity of the fit towards the relative permittivity. Although half wave potentials are used in further analysis, essentially identical results can be obtained for a fit utilizing the oxidation or reduction peak potentials as long as only concentrations above 5 mM are considered. Extracted fitting parameters, the distance of closest approach $\dot{a}$, the reference potential as well as the slope x_1 of the linear term of the extended Debye-Hückel equation, are collected in Tab. 8.3.

Table 8.3: Extracted fitting parameters for fixed relative permittivities of 35 and 40.

$\varepsilon_r[-]$	U_{Ref}[V]	$\dot{a}$[nm]	$x_1[-]$	R^2 $[-]$
35	3.3079 ± 0.0042	12.8 ± 23.4	0.907 ± 0.016	0.996
40	3.3077 ± 0.0047	13.7 ± 25.6	0.907 ± 0.016	0.996

For both relative permittivities, Tab. 8.3 and Fig. 8.9 show the same good correlation, indicated by the good fit parameter R^2. Within the given errors, the same constant reference potentials, distances of closest approach as well as linear slopes x_1 are determined. While for the first and the last of those parameters, the error is negligibly small, this is not true for the distance of closest approach, where a standard deviation of nearly 200 % indicates the invariance of the fit with respect to $\dot{a}$. In aqueous electrolyte theory the parameter $\dot{a}$ commonly ranges from 0.3 nm to 0.6 nm as given, e.g., in Wright [153]. A large size of the ferrocene molecule, a shielding by solvent molecules as well as a changed relative permittivity compared to water based systems can only explain a tendency towards larger distances of closest approach. Bottom line, given the quality and number of data points, especially at the low concentration region, $\dot{a}$ cannot be determined from the fit of measured half wave potentials of $LiClO_4$ concentrations of 5 mM to 2 M in EC:DEC. Interestingly concentrations below 5 mM, which are not taken into account in the fitting procedure, are in good accordance with the result of the fit. This means that oxidation and reduction peak potentials are affected more or less symmetrically by additional effects altering the peak separation, as discussed in detail above. It has to be added that an extension of the Debye-Hückel equation to higher orders, compare Equ. (5.22), do not improve the quality of the fit significantly.

Discussion of determined activity coefficient The mean molar activity coefficient of $LiClO_4$ in a mixture of EC:DEC(1:1, by weight) was determined by fitting measured potentials of a lithium reference electrode versus half wave potentials of the ferrocene / ferrocenium redox system. The natural logarithm of the resulting activity coefficient is shown in Fig. 8.10(a), based on parameters obtained by fixing the relative permittivity to 35. Apart for a rescaled y-axis, this graph is, identical with Fig. 8.9(a). In the equations of the concentrated electrolyte theory the binary activity coefficient often appears in the form of a so-called thermodynamic factor (TDF):

$$\mathrm{TDF} = \left(1 + \frac{\partial \ln f_\pm}{\partial \ln c}\right) \approx 1 + 0.907\, c$$

Fig. 8.10(a) shows the TDF for the investigated electrolyte in a concentration range from 0 M to 2 M. As only linear terms in the extended Debye-Hückel equation were considered, also the TDF can be considered linear from 5 mM to 2 M. Only at lowest concentrations a deviation from the linear slope can be seen in the inset of Fig. 8.10(b). This is the result of the assumed Debye-Hückel behavior at lowest concentrations which should be understood as a reliable result given the fit's insensitivity towards the distance of closest approach. Concluding, for determination of

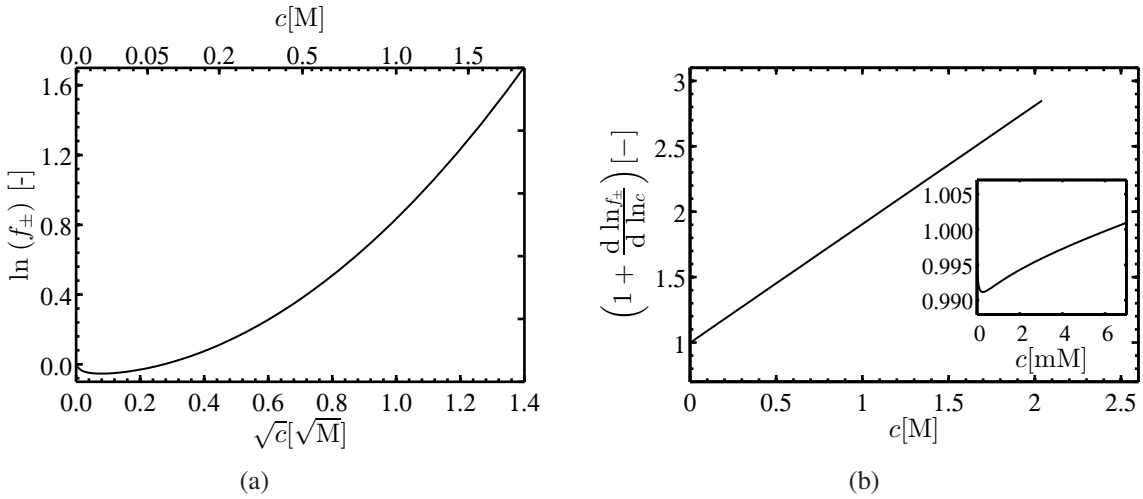

Figure 8.10: a) Concentration dependent mean molar activity coefficient of $LiClO_4$ in EC:DEC (1:1, w:w), b) corresponding thermodynamic factor.

the TDF, it is sufficient to determine the mean molar activity coefficient in a concentration range from 5 mM to 2 M.

Comparison with literature A comparison with similar electrolytes investigated in literature is shown in Fig. 8.11. Direct comparison is difficult though, as all were performed with $LiPF_6$ salts. In all publications the TDFs show a mostly linear concentration dependence for concentrations above 0.5 M. Different slopes in this region may result from different solvents, being used by the individual groups. The behavior at low concentrations in these publications are either neglected as, e.g., in Nyman et al. [115] and Lundgren et al. [102], or fixed with a theoretically assumed Debye-Hückel behavior as discussed, e.g., in Stewart and Newman [135] and Valøen and Reimers [142]. A distinct non-linear behavior can be observed in the determined TDF of Valøen and Reimers [142]. In this case the natural logarithm of the mean molar activity coefficient is only assumed to be a series expansion of $\sqrt{c}$ terms. This formulation does not allow for a fast deviation from the linear Debye-Hückel behavior and thus leads to a pronounced negative bump in the TDF. Only in the publication by Stewart and Newman [135], a Debye-Hückel behavior as described by Equ. (5.21) is assumed for small concentrations. In this case, the Debye-Hückel behavior also does not affect the curvature of the resulting TDF, but only imposes a small correction at lowest concentrations.

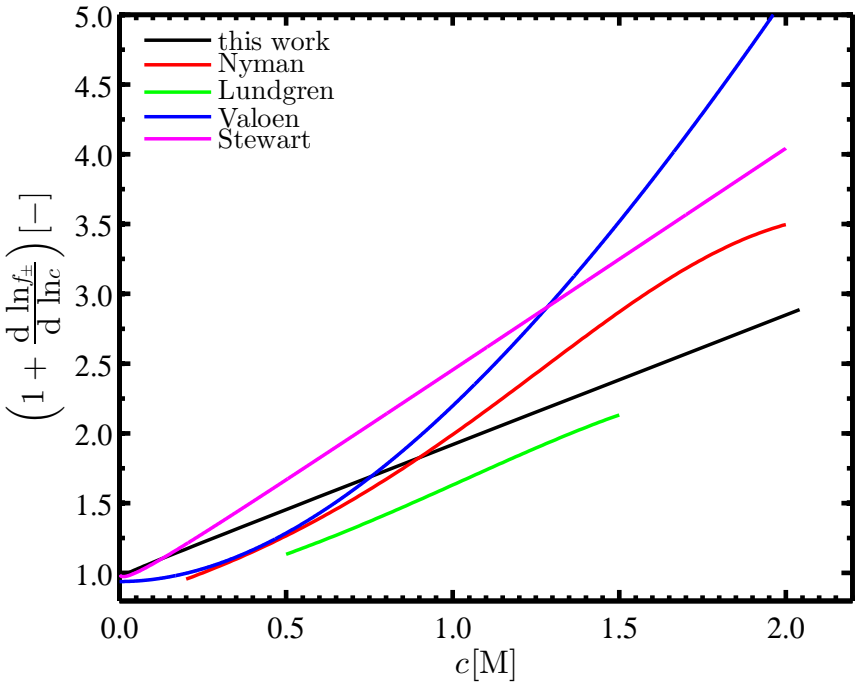

Figure 8.11: Comparison of determined thermodynamic factor for $LiClO_4$ in EC:DEC, 1:1 w/w, with similar electrolytes in literature, Nyman et al. [115]: $LiPF_6$ in EC:EMC, 3:7 w/w, Lundgren et al. [102]: $LiPF_6$ in EC:DEC, 1/1 w/w, Valøen and Reimers [142]: $LiPF_6$ in PC:EC:DMC, 10:27:63, v/v/v, Stewart and Newman [135]: $LiPF_6$ in EC:EMC, 1:1 w/w.

8.4 Transference number based on data from a concentration cell

In this section, the concentration dependent transference number $t_+(c)$ is determined from experiments in a concentration cell in combination with the thermodynamic factor determined in section 8.3. For this purpose, two different experimental procedures are proposed which are explained theoretically in section 5.6.

8.4.1 Experimental procedure

The electrolyte solution, consisting of a mixture of ethylene carbonate (EC, 50 %, by weight, Sigma Aldrich, anhydrous, 99 %), diethyl carbonate (DEC, 50 %, by weight, Sigma Aldrich, anhydrous, >99 %) and lithium perchlorate $LiClO_4$ (Sigma Aldrich, 99.99%), was prepared in an argon filled and temperature controlled glove box (MBraun, 25 °C ± 1 °C, water content <0.1 ppm, Ar 5.0, Westfalen, 99.999 % Vol). The concentrations of $LiClO_4$ ranged from $c = 0.1 \cdot 10^{-3}$ M to $c = 2$ M. Metallic lithium (Rockwood Lithium, 0.45 mm, high purity) was used as counter electrode (CE) and working electrode (WE). The concentration cell consisted of two parallel lithium stripes which were in contact with a stripe of glass fiber separator soaked with an electrolyte solution of two salt concentrations. To minimize electrolyte evaporation, separator

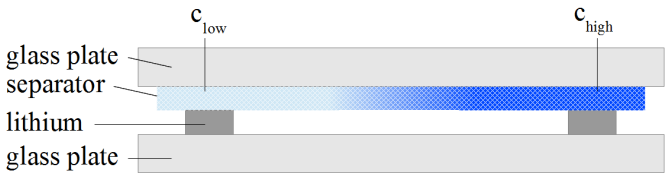

Figure 8.12: Concentration cell setup between two glass plates.

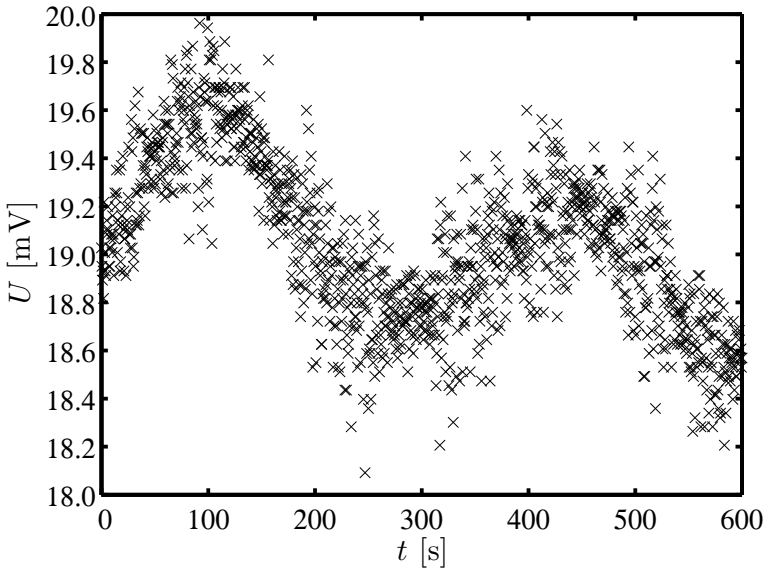

Figure 8.13: Transient of cell potential U of a concentration cell measurement inside the temperature controlled glovebox (temperature hysteresis of 25.6°C $\pm$ 1.1 K) for 0.8 M versus 1.2 M $LiClO_4$ in EC:DEC (1:1, wt.%).

and electrodes were sandwiched between two glass plates as depicted in Fig. 8.12 in a side view. Concentration cell potentials were measured over a time interval of four minutes using either a handheld voltmeter (Voltcraft VC830) inside the glovebox or a Biologic VMP3.

8.4.2 Results and discussion

In the following, the transference number of lithium ions will be determined based on concentration cell data and a known thermodynamic factor determined in section 8.3. For a precise determination of transport parameters, a controlled temperature environment is required since the transport parameters show a distinct temperature dependence as shown, e.g., in Valøen and Reimers [142] or Lundgren et al. [102]. The temperature influence on the cell potential can be observed in Fig. 8.13. Although the temperature was regulated by the climate control system inside the glovebox, a pronounced temperature hysteresis can be monitored leading to a non-negligible variation in the measured cell potential. The concentration cell setup described in section 8.5.1 is particularly sensitive for such temperature variations since the amount of elec-

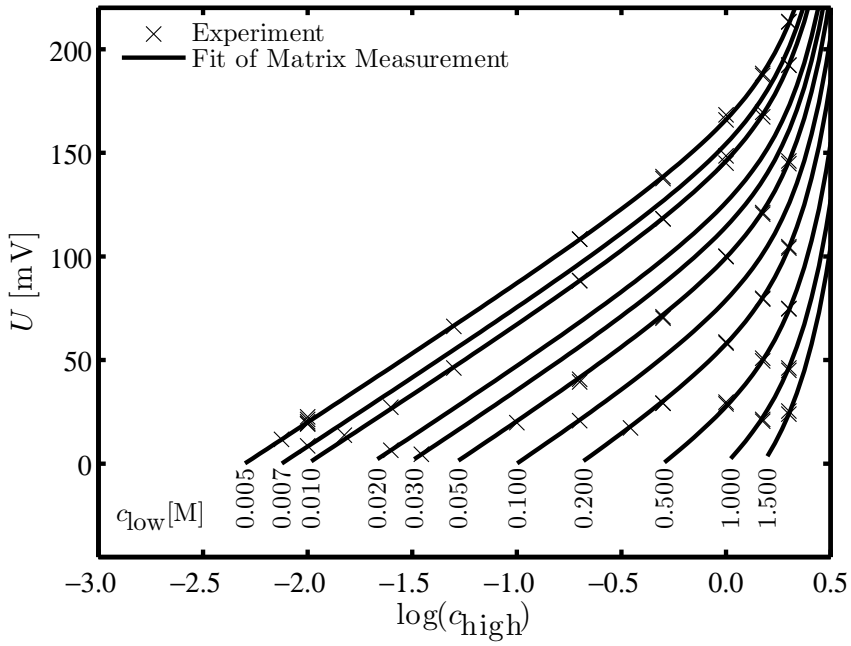

Figure 8.14: Concentration overpotentials resulting from a set of permutations of low and high salt concentrations measured in the concentration cell setup: lower concentrations are indicated below the fit lines, higher concentrations are plotted as the common logarithm ($\log_{10}$) on the x-axis.

trolyte is very small. The temperature was observed manually and correlates with the measured potential fluctuations. In the depicted case the temperature varied between 24.5 °C and 26.8 °C. Based on these temperature extremes the concentration overpotential at 25 °C is interpolated between the potential maxima. Due to the large influence of the temperature, subsequently an error of ± 0.3 mV is assumed for the measured cell potential.

First, a set of concentration overpotentials are measured with the experimental setup described in Fig. 8.12. Because all permutations of low and high concentrated electrolytes are measured in a matrix style, the method is refereed as matrix measurement or matrix method. Over 70 concentrations cell were measured, of which most combinations are conducted at least twice. In Fig. 8.14, the cell potentials are plotted versus the higher salt concentration. Each line corresponds to a fixed lower salt concentration. The solid lines represent the numerical fit of the measured concentration cell potentials using Equ. (5.76). As a result of the integral in Equ. (5.76), a functional description has to be assumed for the transference number dependence on the salt concentration. As a constant or a linear functional result in poor representation of measured data and third and higher order polynomials only improve the fit quality mathematically, a quadratic description for the transference number is used for the fits in Fig. 8.14.

In addition to the matrix method, an alternative approach also described in section 5.6 is applied to determine the transference number. In this case, the concentration overpotentials between two electrolytes of concentrations $c - \Delta c$ and $c + \Delta c$ are measured. In the following, this

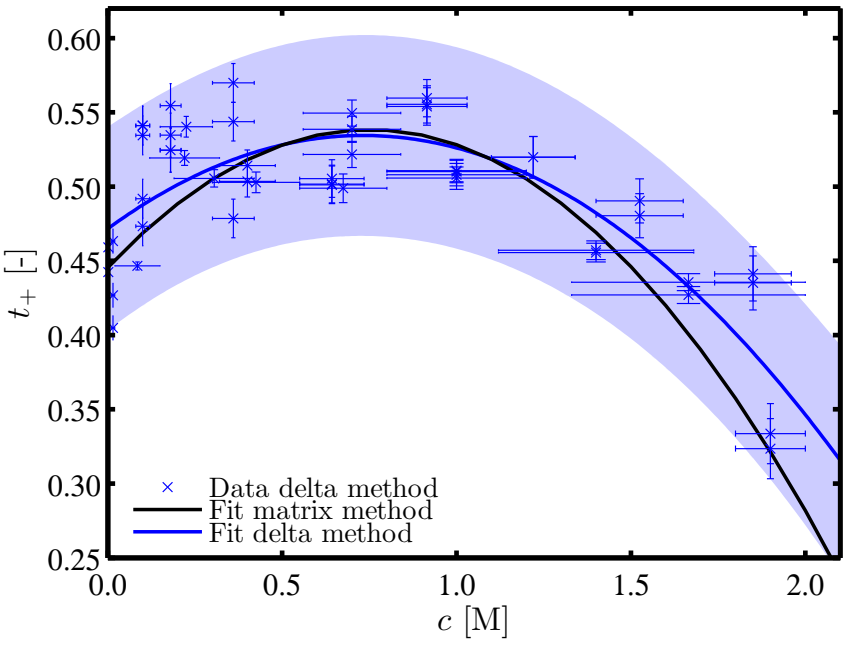

Figure 8.15: Transference numbers $t_+(c)$ determined from concentration cell data using the delta and the matrix method.

approach is called the delta method. The advantage of the latter approach is that no functional description for the transference number has to be assumed and a pointwise calculation is possible within the concentration $c \pm \Delta c$. In this case, the transference number is approximated by a constant value within the considered concentration range $c \pm \Delta c$. The transference number resulting from this approach is depicted in Fig. 8.15. The concentration ranges used for the determination of the concentration potentials are indicated by the widths of the x-error bars. Error bars in y-direction are the result of $\pm$ 0.3 mV uncertainty due to the temperature hysteresis. Exemplarily, the temperature induced potential variation shown in Fig. 8.13 yields a variation of the calculated transference number between 0.50 and 0.52 for 19.5 $\pm$ 0.3 mV. A quadratic fit based on data from the delta method with its confidence interval as well as the quadratic functional for the transference number resulting from the matrix method are also depicted in Fig. 8.15. The corresponding functional descriptions are given by

$$t_{+,\text{delta}}(c) = -0.117c^2 + 0.171c + 0.472, \tag{8.6}$$

$$t_{+,\text{matrix}}(c) = -0.165c^2 + 0.247c + 0.446. \tag{8.7}$$

As a result, the quadratic functional assumed for the matrix methods can be confirmed by the delta method. The two different experimental approaches represent the experimental data shown in Fig. 8.14 and Fig. 8.15 very well. In both cases, the transference number shows a peak around 0.8 M of $t_+ \approx 0.53$. It is striking that the peak coincides with the peak of conductivity as shown in Fig. 8.2(a). For $c \to 0$, a value of $t_+ \approx 0.45$ is found. For $c = 2$ M salt concentration, the transference number drops to about $t_+ \approx 0.35$.

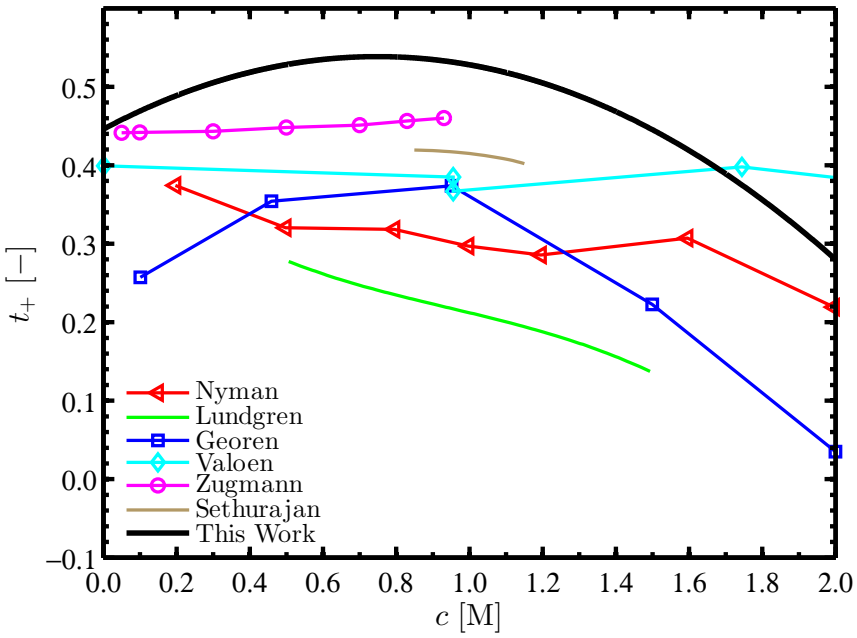

Figure 8.16: Overview over transference numbers available in literature: Nyman et al. [115] ($LiPF_6$ in EC:EMC, 3:7, wt.%, 25 ± 1 °C), Lundgren et al. [102] ($LiPF_6$ in EC:DEC, 1:1, wt.%, 25 ± 1 °C), Georén and Lindbergh [67] ($LiClO_4$ in PC, RT), Valøen and Reimers [142] ($LiPF_6$ in PC:EC:DMC, 10:27:63, vol.%, 21 °C), Zugmann et al. [163] (LiD-BOB in EC:DEC, 3:7, wt.%, 24 °C), Sethurajan et al. [132] (LiTFSI in PC, RT).

For comparison with literature shown in Fig. 8.16, the concentration dependent transference number determined with the matrix method is used. In literature, a wide variety of transference numbers of liquid non-aqueous electrolytes is reported. Rather constant transference numbers of about 0.412 or about 0.4528 are reported by Zugmann et al. [163] for $LiPF_6$ in a mixture of PC, DC and DMC (10:27:63, vol.) and by Valøen and Reimers [142] for LiDFOB in EC:DEC (3:7, wt.), respectively. Monotonically decreasing values for the lithium transference number are reported by Nyman et al. [115] for $LiPF_6$ in EC:EMC (3:7, wt.) and Lundgren et al. [102] for $LiPF_6$ in EC:DEC (1:1, wt.). Georén and Lindbergh [67] also use a second order polynomial to describe the concentration dependence of the transference number resulting in a similar behavior as in the present results, only shifted to smaller values. The latter publication is also based on the salt $LiClO_4$ but uses PC as a solvent. To the authors best knowledge, no literature sources exist, investigating exactly the same electrolyte solution EC:DEC (1:1, wt.%) with $LiClO_4$ salt as used in this work. A similar behavior for the transference number of lithium bis(trifluoromethanesulfonyl)imide lithium salt (LiTFSI) is obtained by Sethurajan et al. [132]. In this publication, the decreasing transference number with an increasing salt concentration is explained by the formation of ion-pairs. A similar effect was previously reported by Vatamanu et al. [143]. Another explanation why the mobility of the highly solvated lithium ions are affected more than the perchlorate ions at high concentrations might be the interaction with the solvent

molecules rather than with each other. At low concentrations the lithium ions are likely to be surrounded by a solvation shell of multiple EC molecules while the perchlorate ions exist more or less freely in the solvent. Due to the larger volume of the latter ion, over which the charge is smeared out, it only scarcely interacts with the solvent. In a dilute electrolyte solution, a balance of concentrations may be given as follows. The electrolyte consists roughly of 5 M of DEC, 5 M of EC as indicated in section 8.1 and, e.g., 0.1 M of $LiClO_4$. The fully dissociated lithium ions may be solvated by 2 to 4 EC molecules leaving 4.7 M of EC in the non-solvated electrolyte. In contrast, a large fraction of the EC molecules are solvated to the lithium ion at higher concentrations such as 2 M electrolyte solution to maintain the same solvation shell around itself. As a result, lithium ions have to drag along half of the solvent at high concentrations while the perchlorate ions remain rather unperturbed by the changing quantity of non-solvated EC molecules. An explanation for the increase of the lithium ion transference number at concentrations below 0.5 M could be ion-ion interactions. While at infinite dilution the ion-ion distance is large, their movement may couple at medium concentrations before at high concentrations the lithium solvation effect becomes predominant.

The advantage of the delta method is that almost no assumptions are necessary for the determination of the concentration dependent transference number $t_+(c)$. In particular, no functional description is required for the fitting procedure. However, the measured cell potentials U are small compared to the arising cell potentials in the matrix method resulting in higher relative errors and, therefore, an increased influence of experimental uncertainties. Consequently, the combination of both methods would provide the best result.

8.5 Binary diffusion coefficient and transference number based on polarization experiments

The diffusion coefficient can be determined directly by experiments in a polarization cell as introduced in section 5.4. For the determination of the transference number, the partial effective diffusion coefficient $D^*_{\pm,\text{eff}}(c)$, the thermodynamic factor and experiments in a polarization cell are required as outlined in section 5. The tortuosity τ of the separator is not needed for the determination of the transference number $t_+(c)$, but for the calculation of the binary diffusion coefficient $D_\pm(c)$ from the partial effective diffusion coefficient $D^*_{\pm,\text{eff}}(c)$.

8.5.1 Experimental procedure

The electrolyte solutions for these experiments were prepared as described in section 8.4.1. Polarization experiments were executed in a two electrode cell schematically shown in Fig. 8.17. Twenty circular layers of Celgard 2500 separator (porosity 55%, thickness 25 μm) with a diameter of 20 mm were placed between two lithium electrodes with a diameter of 17 mm. A larger separator size ensured that no stray currents could flow around the porous medium. The electrode distance is determined by the thickness of these separators, which are incompressible in the pressure range induced by the mechanical spring. Due to the chosen setup, the geometrical distance between the electrodes can be adjusted accurately to small values such as $l = 20\,\text{x}\,25\,\mu\text{m} = 0.5\,\text{mm}$. As a result, a large area to distance ratio was obtained, minimizing

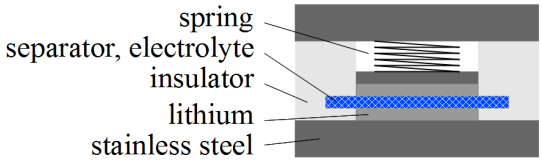

Figure 8.17: Schematic of a two electrode cell.

Table 8.4: Experimental procedure for potentiostatic and galvanostatic experiments.

Salt Concentration	PGP	SSPP
0.01 M	2 min, $\pm 50\ \mu$A 4 min, $\pm 50\ \mu$A 3 min, $\pm 75\ \mu$A	20 mV, $\sim$ 60 min
0.5 M 1.0 M 1.5 M 2.0 M	6 min, $\pm 500\ \mu$A 16 min, $\pm 500\ \mu$A 12 min, $\pm 750\ \mu$A	50 mV, $\sim$ 15 min

the influence of the edge effects of the electric field and thereby fulfilling the requirement of a one-dimensional concentration and potential gradients. It is emphasized that convective effects are also suppressed using this setup. After positive and negative polarization of the two electrode cell, with electrodes aligned perpendicularly to the gravitational field, equivalent potential relaxation transients were observed. Convective electrolyte transference can thus be neglected. After the cells were sealed with PTFE gaskets, measurements were conducted in a climate chamber outside the glovebox. All experiments were repeated at least twice if not stated otherwise. All cell parts were cleaned by boiling them in a mixture of ethanol and water (Millipore, Elix, 15 MΩ), thoroughly rinsed with water and then dried at 70 °C in a heating oven overnight before bringing them into the glove box. A Biologic VMP3 potentiostat/galvanostat was used to measure polarization experiments. Cell impedances were measured in a frequency range from 200 kHz to 1 Hz.

Steady state potentiostatic and pulsed galavanostatic polarization experiments (SSPP, PGP) were conducted in this two electrode cell. In each cell a 6 h OCV phase was followed by several PGP experiments with various polarization currents I_p and times T_I whereas a pulse with a positive current flow was always followed by an identical pulse with a reversed current flow. After each individual polarization, an OCV phase of at least 3 h ensured a complete relaxation of remaining concentration profile. Following the set of PGP experiments, a SSPP experiment was conducted. In these experiments, the polarization phase was terminated individually for each cell when the current $I(t)$ has remained stable for at least 2 minutes. The high frequency resistance R_HF of cells were measured before and at the end of the polarization step. Applied potentiostatic

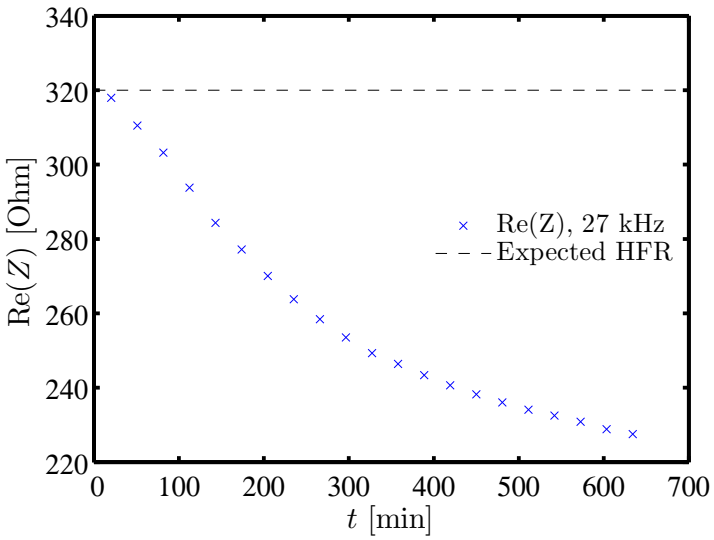

Figure 8.18: High frequency resistance (200 kHz) of cell with 0.01 M $LiClO_4$ in EC:DEC (1:1, wt.%) over time at OCV.

and galvanostatic pulses are summarized in Tab. 8.4. The polarization times for the SSPP experiments are only approximated since they varied also within cells of identical concentrations. The constant polarization currents and potentials were selected to ensure a current density below 0.3 mA/cm^2. For such conditions, metallic lithium electrodes were reported to be comparably stable as discussed in Aurbach et al. [10].

8.5.2 Results and discussion

Experiments with dilute electrolyte solutions in the two electrode cell setup Polarization experiments conducted with the lowest salt concentration of $c_0 = 0.01$ M exhibit a non-constant electrolyte resistance R_{el} as shown in Fig. 8.18. Within the first 10 h of OCV, the electrolyte resistance R_{el} decreases from the expected resistance of 320 Ω to about 220 Ω. This change in electrolyte resistance R_{el} could result e.g. from a 50 % up to a 100 % increase in ion concentration. As no final assignment of latter effect was possible, polarization cell data with 0.01 M salt concentrations could only be used for the determination of the diffusion coefficient since the potential error of +0.01 M is almost not visible in this case. For the determination of the coefficients $f(f_\pm,\ t_+,\ \sqrt{D^*_{\pm,\text{eff}}})$ or $f(f_\pm, t_+, D^*_{\pm,\text{eff}})$ and, therefore, for the determination of the transference number, this error is not marginal since the concentration is used directly for the calculation of the coefficients as it can be seen in Tab. 7.8. As a result, a large error for both coefficients and, therefore, for the transference number has to be considered. This also means that the widely applied transference number estimation at low concentrations given in Equ. (5.60) cannot be applied in this experimental setup as a result of the non-constant electrolyte resistance. The used two electrode cell setup described in section 8.5.1 is particularly sensitive for such parasitic effects since the amount of electrolyte in the cell is very small.

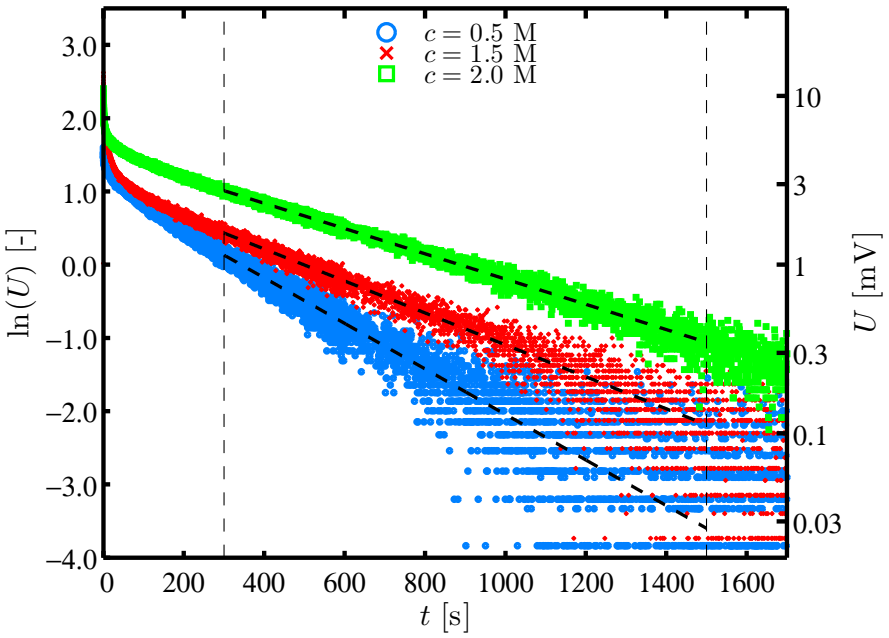

Figure 8.19: Long-term relaxation of the cell potential $\ln U(t)$ for 0.5 M, 1.5 M and 2.0 M $LiClO_4$ electrolyte solution after a SSPP experiment with a polarization potential $U_p = 50\,mV$ and the corresponding linear fits.

Diffusion coefficient from polarization experiments First, the partial effective diffusion coefficient $D^*_{\pm,\text{eff}}(c)$ as well as the binary diffusion coefficient $D_\pm(c)$ are determined directly based on PGP and SSPP experiments as outlined in section 5.4. The tortuosity τ, which is necessary for the calculation of the binary diffusion coefficient $D_\pm(c)$, is given in section 4.2.

In general, the diffusion coefficient can be determined based on the long-term relaxation of the cell potential $U(t)$ after a PGP experiment and based on the short and long-term relaxation of the cell potential $U(t)$ after a SSPP experiment. In Fig. 8.19, the relaxation of the potential $\ln U(t)$ with respect to time t for a 0.5 M, 1.5 M and 2.0 M $LiClO_4$ electrolyte solution after a SSPP experiment is shown. The cell potential $U(t)$ never relaxes exactly to zero which means that a stable open circuit potential between $-0.5\,mV$ and $+0.5\,mV$ remains even for long times. Therefore, all relaxation curves are fitted with an offset potential since the linear relaxation behavior can only be observed if the open circuit potential $U(t)$ approaches zero for long times. As a result of this approach, the linear behavior is observable over a time range from 5 to 25 minutes which allows the quantification of the partial effective diffusion coefficient $D^*_{\pm,\text{eff}}|_{\text{SSPP-ln}}$ according to Equ. (5.41). The apparent increase in noise for long times is due to the logarithmic scale which also leads to the visibility of the digital accuracy of the potentiostat. By the application of the same method, the diffusion coefficient $D_\pm|_{\text{PGP-ln}}$ can be obtained from the long-term relaxation of the cell potential $U(t)$ after a PGP experiment which is not shown explicitly in this work.

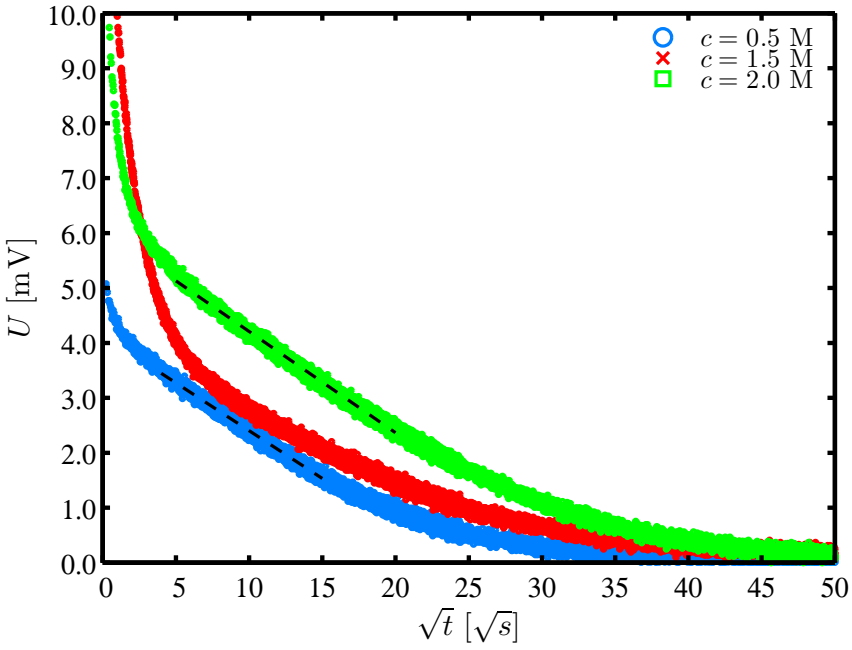

Figure 8.20: Short-term relaxation of the potential $U(t)$ for 0.5 M, 1.5 M and 2.0 M $LiClO_4$ electrolyte solution after a SSPP experiment with a polarization potential $U_p = 50$ mV and the corresponding linear fits.

The short-term relaxation of the cell potential $U(t)$ with respect to the time $\sqrt{t}$ after a SSPP experiment is the basis for the determination of the diffusion coefficient according to Equ. (5.43). In this case, the binary diffusion coefficient $D_\pm$ does not only depend on the slope of the relaxing cell potential but also on the cell potential $U(T_I)$ at the current interruption time. In Fig. 8.20, representative relaxation curves are plotted for 0.5 M, 1.5 M and 2 M electrolyte solutions. The experimental cells with $c_0 = 0.5$ M and $c_0 = 2$ M show a linear correlation of the relaxing cell potential $U(t)$ with the square root of time $\sqrt{t}$. The indicated fitting ranges correspond to real times between 25 s and 300 s and 25 s and 400 s for $c_0 = 0.5$ M and $c_0 = 2$ M, respectively. The cell filled with $c_0 = 1.5$ M electrolyte solution shows only a poor linearity which possibly results from the relaxation from a non-steady state concentration profile as discussed later on and shown in Fig. 8.24. As outlined in section 7.5.3, the diffusion coefficients $D_\pm|_{\text{SSPP-sqrt}}$ can only be determined from the short-term relaxation behavior after a SSPP experiment with a confirmed steady-state current flow $I(t)$. Therefore, the summary of determined diffusion coefficients given in Fig. 8.21 does not include any values for $D_\pm|_{\text{SSPP-sqrt}}$ at $c_0 = 1.5$ M. An explanation for the pronounced drop in the cell potential $U(t)$ within a time range of a view seconds after current interruption may be the reformation of the SEI. Similar transients have been recorded by Odziemkowski and Irish [116] when metallic lithium was cut while being in contact with an electrolyte solution. However, this relaxation behavior is a good example for necessity of the extrapolation technique as introduced in section 5.5.3.

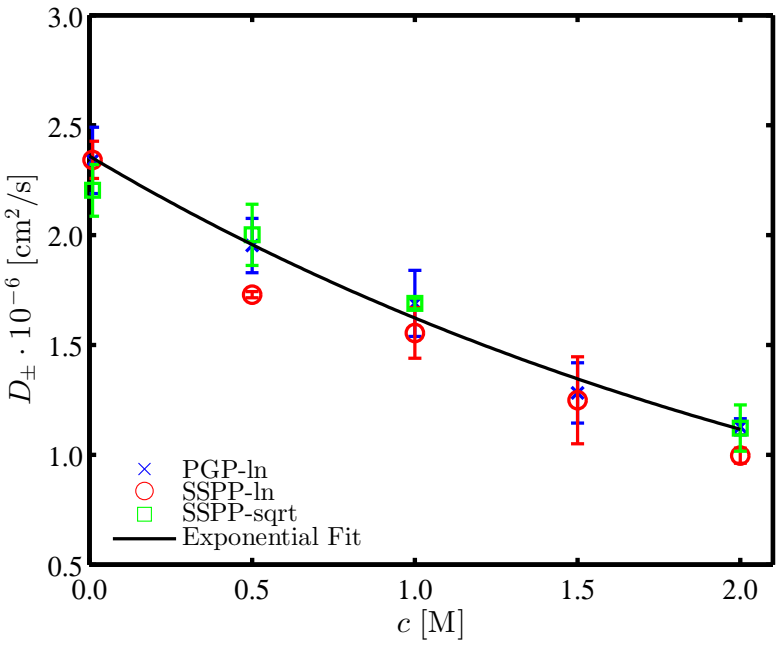

Figure 8.21: Concentration dependent binary diffusion coefficient $D_\pm$ of $LiClO_4$ in EC:DEC (1:1, wt.%) with the standard deviation resulting from multiple cells and experiments and the nonlinear fit based on $D_\pm|_{\text{PGP-ln}}$.

In summery, the binary diffusion coefficients depicted in Fig. 8.21 show a good correlation between the three methods within the common standard deviation of individual pulses and cells. Highest confidence is presumed for the diffusion coefficient determined from the long term relaxation after PGP experiments. In this case, the measured potentials during relaxation are larger compared to the relaxation after SSPP experiments which results in a better signal to noise ratio and a longer time range in which the expected behavior can be observed. Due to the long polarization times in a SSPP experiment, large polarization potentials U_p have to be avoided in order to prevent pronounced lithium dendrite formation. Consequently, further analysis of the diffusion coefficient $D_\pm$ and the transference number t_+ is based on values obtained from the long-term relaxation behavior after PGP experiments. Fig. 8.21 also includes an exponential fit for the diffusion coefficient of the $D_\pm|_{\text{PGP-ln}}$ values giving

$$D_\pm(c) = 2.36 \cdot 10^{-6} \exp\left(-0.375c\right) \quad \left[\frac{\text{cm}^2}{\text{s}}\right].$$

A decrease in the binary diffusion coefficient $D_\pm(c)$ as observed in Fig. 8.21 is expected theoretically since an increasing salt concentration results in an increased electrolyte viscosity and, thereby, a reduced the ionic mobility. In addition, the binary diffusion coefficient $D_\pm$ determined by the described experimental method also includes additional factors such as the ratio between the total concentration and solvent concentration, the thermodynamic factor and potential volumetric effects as discussed, e.g., by Nyman et al. [115] or Georén and Lindbergh [67] and derived

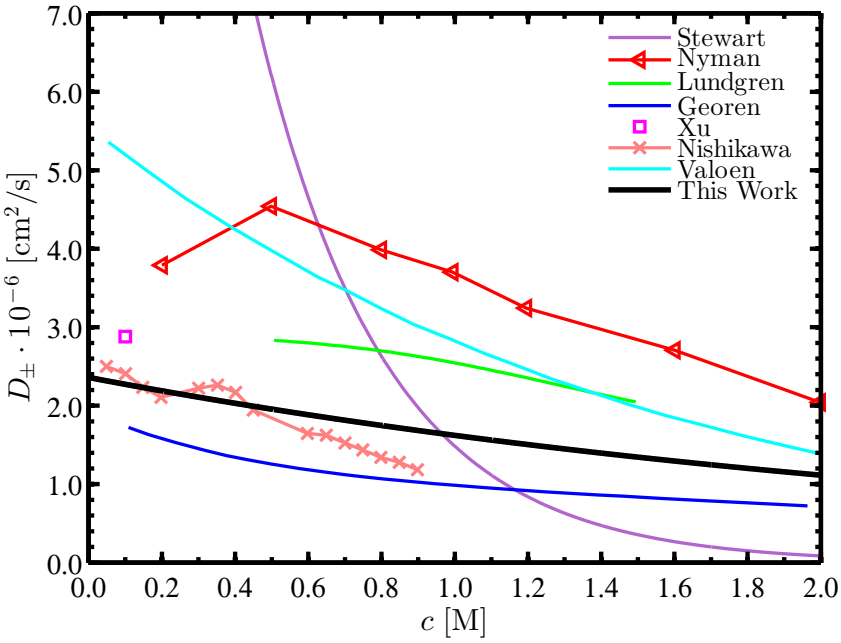

Figure 8.22: Overview over binary diffusion coefficients available in literature: Stewart and Newman [136] ($LiPF_6$ in EC:DEC, 1:1, wt.%, RT), Nyman et al. [115] ($LiPF_6$ in EC:EMC, 3:7, wt.%, 25 ± 1 °C), Lundgren et al. [102] ($LiPF_6$ in EC:DEC, 1:1, wt.%, 25 ± 1 °C), Georén and Lindbergh [67] ($LiClO_4$ in PC, RT), Xu [156] ($LiClO_4$ in PC, 25 °C), Nishikawa et al. [114] ($LiClO_4$ in PC, 25 °C), Valøen and Reimers [142] ($LiPF_6$ in PC:EC:DMC, 10:27:63, vol.%, 21 °C).

in section 2.4. However, it is not necessary to separate these different effects from each other in order to use the determined diffusion coefficient, e.g., in numerical simulations with a consistent physical model.

In literature, binary diffusion coefficients are determined by various techniques such as rotating disc measurements, numerical fitting procedures, relaxations experiments with optical observation of the concentration gradient and the Moiré pattern as indicated in the introduction of section 5. As depicted in Fig. 8.22, a similar trend is described by all publications showing a decrease of the binary diffusion coefficient which is in accordance with theory. Lundgren et al. [102], Nyman et al. [115] and Valøen and Reimers [142] get a very similar strong concentration dependence for $LiPF_6$ dissolved in different electrolyte solutions ranging from $5.5 \cdot 10^{-6}$cm^2/s at infinite dilution to $1.5 \cdot 10^{-6}$cm^2/s for a 2 M electrolyte solution. The differences may be explained by different solvents viscosities. An unproportionally strong concentration dependence for a $LiPF_6$ electrolyte solution is reported by Stewart and Newman [136]. In this publication, the diffusion coefficient is determined based on concentration gradient measurements with an optical sensor. Georén and Lindbergh [67], Xu [156] and Nishikawa et al. [114] determine the binary diffusion coefficient of $LiClO_4$ in PC. Their results compare well with the binary diffusion coefficient of $LiClO_4$ in EC:DEC (1:1 w %) presented in this work.

Transference number from polarization experiments In the following, the procedure for the determination of the concentration dependent transference number $t_+(c)$ based on polarization experiments as outlined in section 5.5 is investigated and compared to the methodology based on concentration cell experiments. As described in section 5.5, the alternative method is based on three experiments in two different experimental setups. The determination of the thermodynamic factor is described in section 8.3 and the diffusion coefficient $D_\pm(c)$ is obtained from polarization experiments as discussed in the previous paragraph. In addition, either the coefficient $f(f_\pm,\ t_+,\ \sqrt{D^*_{\pm,\mathrm{eff}}})$ or the coefficient $f(f_\pm, t_+, D^*_{\pm,\mathrm{eff}})$ is required to calculate the transference number. In this contribution, the diffusion coefficient and the coefficients $f(f_\pm,\ t_+,\ \sqrt{D^*_{\pm,\mathrm{eff}}})$ and $f(f_\pm,\ t_+, D^*_{\pm,\mathrm{eff}})$ are determined at discrete concentrations whereas the thermodynamic factor is given as a continuous functional description. As presented in section 7.5.3, five different analytical expressions based on PGP and SSPP experiments are considered finally for the determination of $f(f_\pm,\ t_+,\ \sqrt{D^*_{\pm,\mathrm{eff}}})$ and $f(f_\pm,\ t_+, D^*_{\pm,\mathrm{eff}})$. The analytical expressions are summarized in Tab. 7.8 and their accuracy was demonstrated by means of numerical simulations.

First of all, the coefficient $f(f_\pm,\ t_+,\ \sqrt{D^*_{\pm,\mathrm{eff}}})|_{\mathrm{PGP}}$ can be determined from PGP experiments based on Equ. (5.74), which requires only the cell potential $U(T_\mathrm{I})$ at current interruption time. The accuracy of the method is improved by the observation of the short term relaxation after current interruption which exhibits a linear relationship with respect to the artificial time τ^* defined in Equ. (5.75). In Fig. 8.23, four normalized potential transients are depicted over the artificial time $1-\tau^*$. The relaxation curves resulting from the short polarization time exhibit the theoretically expected s-shape which can also be observed in Fig. 7.18(a). The linear fits

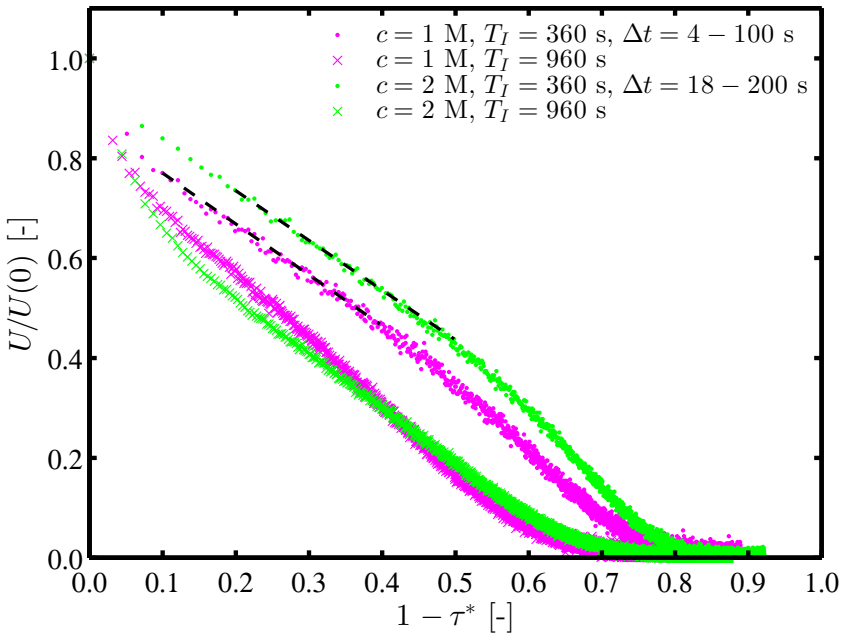

Figure 8.23: Relaxation of the normalized cell potential $U(t)$ after a PGP experiment with $I_\mathrm{p} = 0.5\,\mathrm{mA}$ for 360 s or 960 s in a 1.0 M and 2.0 M electrolyte solution.

indicated by the dashed black lines correspond to real times between about 10 s and about 150 s. The extrapolation of these fits to $(1 - \tau^*) = 0$ gives the desired cell potential $U(T_\mathrm{I})$ at current interruption time. A linear relaxation behavior can also be observed for longer polarization times but, the typical s-shape as depicted in Fig. 7.18(a) is missing. This is an indication for a violation of the semi-infinite limit as a result of too long polarization times as discussed in section 7.5.3. However, the polarization time of 960 s is not long enough to reach the steady-state which is indicated by the nonlinear relaxation behavior of the cell potential $U(t)$ with respect to $\sqrt{t}$. A further reduction of the polarization time beyond 360 s decreases the signal to noise ratio and is thus unsuitable for the precise determination of the cell potential at the polarization interruption time. Higher polarization currents I_p should not be used since the stability of metallic lithium electrodes cannot be guaranteed anymore as indicated by Aurbach et al. [10]. As a result, only the coefficients $f(f_\pm,\ t_+,\ \sqrt{D^*_{\pm,\mathrm{eff}}})|_{\mathrm{PGP}}$ based on 360 s – 0.5 mA PGPs are used in the following analysis. It is emphasized that the experiments with the longer polarization time are used for the determination of the diffusion coefficient since the long-term relaxation time is increased in this case.

All other methods for the determination of the coefficients $f(f_\pm,\ t_+,\ \sqrt{D^*_{\pm,\mathrm{eff}}})$ and $f(f_\pm,\ t_+,\ D^*_{\pm,\mathrm{eff}})$ are based on SSPP experiments. At first, the transient behavior of the current $I(t)$ during the potentiostatic polarization with U_p is analyzed. Exemplary current transients for a 0.5 M, 1.5 M and a 2 M electrolyte solutions are depicted in Fig. 8.24. While a linear current relaxation with respect to time $\sqrt{t}$ can be observed for concentrations larger than $c_0 = 0.5\,\mathrm{M}$, this linearity is not apparent for $c_0 = 0.5\,\mathrm{M}$. This cannot be explained by the approximation of the term $\exp(H^2 t)(1 - \mathrm{erf}(H\sqrt{t}))$ with the square root of time $\sqrt{t}$ as outlined in section 7.5.1 since the values for $H \approx 0.003\,(\sqrt{\mathrm{s}})^{-1}$ are of the same order for all depicted concentrations. Since the theoretical relation between the current $I(t)$ and the square root of time $\sqrt{t}$ is derived based on the linearized Butler-Volmer law and, therefore, on a constant interface resistance, the observed curvature may result from parasitic effects such as the reduction of the total charge transfer resistance which can be measured during the polarization time. The distinct drop of the current in the beginning of the polarization time may also be related to this effect. For larger concentrations, this effect may be restricted to a short time period in the beginning of the polarization whereas it is distributed over a longer time period for the concentration $c_0 = 0.5\,\mathrm{M}$, thereby interfering with the expected $\sqrt{t}$ relaxation. As a result of Fig. 8.24, the coefficient $f(f_\pm,\ t_+,\ \sqrt{D^*_{\pm,\mathrm{eff}}})|_{\text{SSPP-pol-sqrt}}$ is determined only for concentrations $c_0 \geq 1\,\mathrm{M}$ by means of Equ. (5.66). In this case, the ratio m_{SSPP}/I_0 is determined based on the linear fits indicated by the back dashed lines. Additionally, the required low frequency resistance $R_{\mathrm{LF},0}$ is measured by impedance spectroscopy before each SSPP experiment. For this method, it is not important that the steady-state is reached at the end of the polarization.

For the remaining three coefficients $f(f_\pm,\ t_+, D^*_{\pm,\mathrm{eff}})|_{\text{SSPP-pol}}$, $f(f_\pm,\ t_+, D^*_{\pm,\mathrm{eff}})|_{\text{SSPP-ss}}$ and $f(f_\pm,\ t_+, D^*_{\pm,\mathrm{eff}})|_{\text{SSPP-ln}}$, a linear, steady-state concentration profile is strictly required at the end of the polarization time as discussed in section 7.5.3. In a SSPP experiment, the steady state is indicated by a distinct current plateau at the end of polarization time as it is depicted in Fig. 8.24 for $c_0 = 0.5\,\mathrm{M}$ and $c_0 = 2\,\mathrm{M}$. The pronounced time dependence of the current at the end of the polarization phase for $c_0 = 1.5\,\mathrm{M}$ excludes this experiment from analysis of latter factors because a linear concentration profile may not be given at the end of the polarization. The increase in the current may be explained by a decreasing interface resistance as a result of a modification

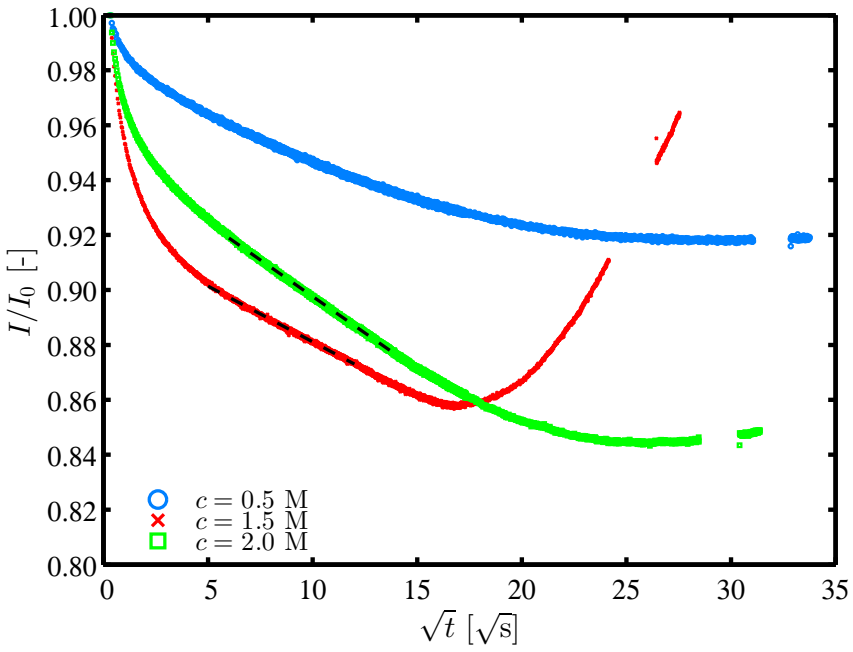

Figure 8.24: Time dependent current $I(t)$ of SSPP experiments with a constant polarization potential $U_\text{p} = 50\,\text{mV}$ for a 0.5 M, 1.5 M and 2.0 M electrolyte solution. The gaps at the end of the polarization are due to an impedance measurement.

of the lithium electrode – electrolyte interface. It is emphasized that the electrolyte resistance remains almost unchanged over the time of polarization.

The first coefficient $f(f_\pm,\ t_+, D^*_{\pm,\text{eff}})|_{\text{SSPP-pol}}$ defined by Equ. (5.59) is based on the steady state current I_S and the low frequency resistance $R_{\text{LF,S}}$ at steady state which is determined by impedance spectroscopy in the end of the polarization time. The second coefficient $f(f_\pm,\ t_+,\ D^*_{\pm,\text{eff}})|_{\text{SSPP-ss}}$ depends on the analytical solution for a steady state concentration profile at the end of the polarization. In this case, the cell potential $U(T_\text{I})$ at current interruption and the steady state current I_S are used to calculate the coefficient by means Equ. (5.68). As for the coefficient $f(f_\pm,\ t_+, \sqrt{D^*_{\pm,\text{eff}}})|_{\text{PGP}}$, the short-term relaxation behavior of the cell potential can be used to determine the cell potential $U(T_\text{I})$ at current interruption. The usage of the measured cell potential $U(T_\text{I})$ at current interruption, being much higher than the extrapolated cell potential $U(T_\text{I})$ as shown in Fig. 8.20, results in an unrealistic transference number. The expected linear relation with respect to time $\sqrt{t}$ can only be observed for $c_0 = 0.5\,\text{M}$ and $c_0 = 2\,\text{M}$. A non-linear behavior with respect to time $\sqrt{t}$ is a sign for an instationary concentration profile at the end of the polarization or, alternatively, for experimental data with dominating parasitic effects. As a result, such experimental data are not used for the determination of the coefficient $f(f_\pm,\ t_+, D^*_{\pm,\text{eff}})|_{\text{SSPP-ss}}$ in the following. In a SSPP experiment, the coefficient $f(f_\pm,\ t_+, D^*_{\pm,\text{eff}})|_{\text{SSPP-ln}}$ can also be determined from the long-term relaxation behavior by means of Equ. (5.71). In this context, a linear fit of $\ln U(t)$ with respect to the time t is required as it is shown in Fig. 8.19. The offset of such an linear fit is the basis for the determination of the coefficient $f(f_\pm,\ t_+, D^*_{\pm,\text{eff}})|_{\text{SSPP-ln}}$.

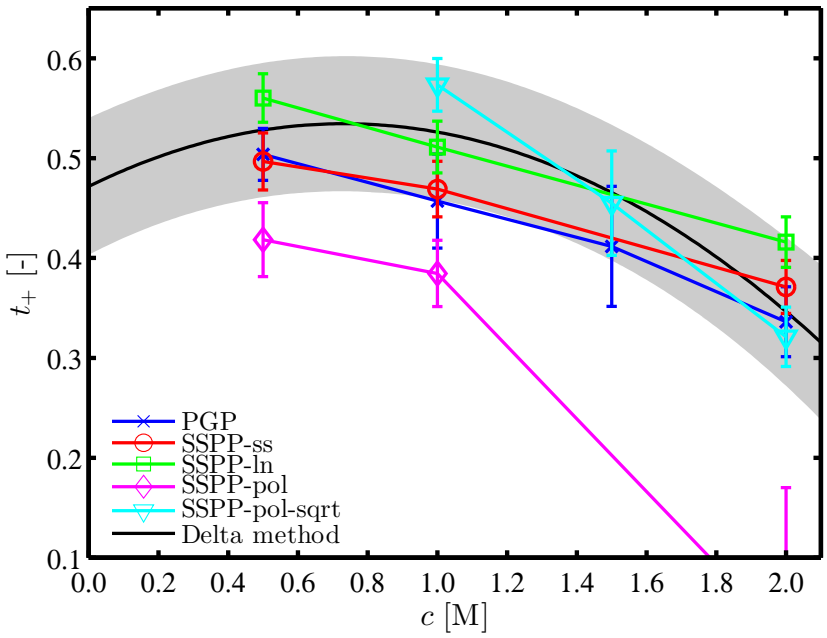

Figure 8.25: Overview over transference numbers determined from polarization experiments by the coefficients summarized in Tab. 7.8 and comparison with transference number obtained from the delta method given in Equ. (8.6).

In Fig. 8.25, the concentration dependent transference numbers calculated from polarization experiments in a two electrode cell are collected. Additionally, the transference number based on the delta method discussed in section 8.4 is inserted into the same figure. In general, a qualitative agreement can be found between both experimental approaches. The only outlier is the transference number calculated from the coefficient $f(f_{\pm},\ t_+, D^*_{\pm,\mathrm{eff}})|_{\text{SSPP-pol}}$ which is based on the polarization phase of a SSPP experiment. The qualitative behavior is in accordance with the other methods but the absolute value is significantly smaller. Unfortunately, there is no obvious reason for this shift. Although the qualitative results of the transference number determined by polarization experiments are comparable to the transference number determined by the matrix and the delta method in a concentration cell, the method based on data from a concentration cell is clearly superior since it is much easier to perform experiments in the concentration cell than in the two electrode cell. Another advantage of the concentration cell is that only the concentration overpotential resulting from two different concentrated electrolyte solutions is measured. Therefore, additional physical phenomena such as mass and current transport does not influence the result. In addition, the number of required experiments is reduced resulting in a decreased number of potential error sources.

A similar result as shown in Fig. 8.25 is obtained if the half-cell potential measurements versus the ferrocene redox potential for the determination of the thermodynamic factor are replaced by measurements in a concentration cell as introduced theoretically in section 5.7.

9 Conclusions and outlook

In this work, a combined approach consisting of a computational method for ion-transport in concentrated binary electrolyte solutions and the experimental determination of all corresponding model parameters is developed. The presented computational method is based on the ion-transport model for concentrated electrolyte solution derived from the Stefan-Maxwell approach and is related to an alternative ion-transport model based on non-equilibrium thermodynamics. For isothermal and isobaric conditions, the only difference between both models is the definition of the chemical potential being the driving force for the ion-transport. In the Stefan-Maxwell approach, the chemical potential of the salt is derived from the chemical potentials of the positive and the negative ionic species whereas in the approach based on non-equilibrium thermodynamics the chemical potential of the electrolyte includes the chemcial potentials of the positive and the negative ionic species and the solvent. The second model is also incorporated into the presented computational approach. To ensure a consistent modeling approach for dilute and concentrated electrolyte solutions, the dilute solution theory derived from the Nernst-Planck approach is related to the concentrated solution theory which is only applicable if a consistent definition for the reference potential is employed. The correlation between dilute and concentrated solution theory is of particular interest for the evaluation and validation of the experimental methods used for the determination of concentration dependent transport parameters.

The presented computational approach enables both the simulation of resolved porous media as well as the simulation of porous media homogenized with the volume averaging approach. To account for the geometrical complexity of resolved porous media, the finite element method is used for the discretization of the computational domain. The employed standard finite element approach also includes a consistent computational model for galvanostatic boundary conditions including non-constant electrode kinetics which is of particular interest in three-dimensional models. Additionally, it is shown mathematically that the volume averaging approach used for the homogenization of porous media is not influenced by concentration dependent transport parameters. The robustness, the accuracy and the efficiency of the computational approach is verified by several numerical examples including one and three-dimensional simulations. Among others, the simulation of a realistic porous structure with galvanostatic boundary conditions and a polarization current approaching the mass-limited current is considered as most challenging test case.

Although appropriate physical models and computational methods are important for numerical simulations of ion-transport in concentrated electrolyte solutions, the quality of the numerical results strongly depends on the accuracy of the used transport and geometrical parameters. Therefore, the main focus of this work is on the determination of all required transport parameters. The transport parameters of interest are the conductivity of the electrolyte solution, the binary diffusion coefficient and the transference number of the reacting ionic species. In addition, the thermodynamic factor is required as a thermodynamic quantity. This specific parameter

set results from the Stefan-Maxwell approach which is used for the derivation of experimental methods. Modifications may be necessary if the experimental procedures are applied to the ion-transport model derived from non-equilibrium thermodynamics. The presented methods are partly validated and analyzed by the developed computational approach. To demonstrate the accuracy and the simplicity of the proposed experimental methods, the transport parameters are determined exemplarily for an electrolyte solution consisting of lithium perchlorate dissolved in a mixture of Ethylene Carbonate (EC, 50 % wt.) and Diethyl Carbonate (DEC, 50 % wt.). In addition to the aforementioned transport parameters, geometrical parameters describing the effect of the microstructure on the macroscopic behavior in a homogenization approach are necessary for numerical simulations and the determination of transport parameters. In this work, only the porosity and the tortuosity of the porous media are considered as geometrical parameters since the used experimental procedure for the determination of the tortuosity does not only include the elongation of the diffusion path but also other effects such as varying cross sectional areas.

The conductivity of the electrolyte solution is measured with a standard conductivity cell and the resulting experimental data are fitted with two different functionals. For the thermodynamic factor, a novel experimental procedure is proposed which allows for a direct determination by measurements conducted in a standard three electrode glass cell using cyclic voltammetry. Therefore, the relation between peak position and mean molar activity coefficient is derived in detail which is necessary to understand underlying principles as well as parasitic effects such as non-ideal kinetics or diffusion overpotentials. To evaluate the influence of these parasitic effects, the peak separation between ferrocene oxidation and reduction peak potentials is used as a quality measure for experimental data. Application of this quality measure to exemplary measurements allowed to select a data set for determination of the mean molar activity coefficient. The selected half wave potentials are successfully correlated with an extended Debye Hückel law finally allowing for an extraction of the mean molar activity coefficient. The quantity of interest for simulations, the thermodynamic factor, can further be calculated from the activity coefficient. Compared to the available literature for mean molar activity coefficients in similar electrolyte systems, the same qualitative trend is observed.

In this work, the effective diffusion coefficient is determined from the short-term and long-term relaxation behavior after a galvanostatic or a potentiostatic polarization pulse. In contrast to other experimental procedures available in literature, the distance between the lithium electrode is minimized to ensure a large area to distance ratio for the electrodes and, therefore, to reduce the influence of a non-homogenous electrical field. The small distance between the electrodes is realized by several layers of separators. Potential convective effects are also suppressed by this setup. As a result of the used experimental setup, it was necessary to extend analytical methods available in literature to include the effect of the porous medium. The resulting concentration dependent binary diffusion coefficient obtained by the presented experimental methods is in good agreement with binary diffusion coefficients available in literature.

As a result of the direct determination of the thermodynamic factor, the transference number can be calculated from experimental data measured in a concentration cell. For this purpose, two different experimental procedures are proposed resulting in comparable concentration dependent transference numbers. The first procedure is based on measurements over the entire concentration range including large concentration differences and a numerical fitting procedure with an assumed concentration dependence for the transference number. The second procedure based on

small concentration variations does not require a functional description for the concentration dependence. In addition to the determination via the concentration cell, the transference number is also determined by a different experimental approach based on a known thermodynamic factor, a known binary diffusion coefficient and data from a polarization cell. In literature, a comparable approach consisting of a known binary diffusion coefficient and measurements in a concentration and a polarization cell is popular. In this work, five different experimental methods for the determination of the transference number based on polarization cell experiments are discussed whereas three of the five methods have not yet been used in literature for the determination of the transference number. The new methods are based on the initial relaxation behavior of the current in a potentiostatic polarization experiment and on the short-term and the long-term relaxation behavior of the cell potential after a potentiostatic polarization experiment. The resulting transference numbers also confirm the concentration dependent transference number determined by the first approach. However, experimental efforts and uncertainties are much higher in the second approach based on polarization cell experiments since it is required to combine results of three different experimental procedures.

In summary, the presented work is an important contribution for the development of a predictive simulation tool for battery applications. The combined approach including the development of a computational approach and the determination of the corresponding transport parameters by simple experimental procedures enables new opportunities in the field of computational electrochemistry.

The proposed computational approach provides for example the opportunity to investigate the influence of the microstructure of the porous medium on the macroscopic behavior of an elementary cell. Therefore, three-dimensional simulations of resolved porous media could be analyzed and compared to simulations using a homogenization approach. By this comparison, it would be possible to establish a general understanding of ion-transport in porous media. In addition, this approach would support the definition and the determination of improved geometrical parameters. In a final step, geometrical parameters determined by numerical simulations could be validated with experimentally determined geometrical parameters.

A theoretical and experimental framework for the determination of ion-transport parameters is developed in this work. In a next step, additional electrolyte solution used in lithium ion batteries have to be investigated whereas the temperature dependence of the transport parameters also has to be taken into account. In general, the same experimental methods could be used for the determination of the temperature dependence of the transport parameters. However, modifications of the experimental setups are necessary to guarantee constant isothermal conditions within an experiment because transport parameters are sensitive to temperature fluctuations as indicated in this work. In addition, the determined ion-transport parameters are not sufficient for the numerical simulation of complete charge and discharge cycles in an elementary cell. Therefore, it is necessary to determine further physically-motivated parameters describing, e.g., the electrode kinetics of common electrode materials or the lithiation and delithiation process of the active materials in anode and cathode.

A A brief introduction into non-equilibrium thermodynamics

As stated in Atkins and de Paula [9], thermodynamics is "*the study of the transformation of energy*' and allows the prediction of energy release in various systems. Therefore, thermodynamics is a central point in the modeling of electrochemical systems such as batteries. In this section, a short review of the basic thermodynamic principles is given. A detailed derivation can be found, e.g., in Atkins and de Paula [9, chap. 2 - 5], Newman and Thomas-Alyea [109], Kontturi et al. [91, chap. 1] or Kjelstrup and Bedeaux [90, chap. 3]. The following derivation is inspired by Kjelstrup and Bedeaux [90].

A.1 Heterogeneous system in a global equilibrium

In the following, a heterogeneous system consisting of two homogeneous phases separated by an interface is considered. The different phases are assumed to be in equilibrium with each other. This setup can also be interpreted as an electrode immersed in an electrolyte solution. The total internal energy U of the system is the sum of the internal energies of the different phases

$$U = U_{\text{el}} + U_{\text{I}} + U_{\text{so}},$$

where the subscripts el, I and so stand for the electrolyte phase, the interface and the solid phase, respectively. However, to explain the basic principle of a thermodynamic system, the thermodynamic relations are only shown for the homogeneous phase el. The same principles are also valid for the other phases, although different physical phenomena have to be considered possibly. In the following, the subscript el is dropped for notational simplicity. For a homogeneous system, the total differential of the internal energy can be written as the total differential of the extensive variables S, N_k and V:

$$\mathrm{d}\,U = T\,\mathrm{d}\,S - p\,\mathrm{d}\,V + \sum_{k=0}^{m} \mu_k\,\mathrm{d}\,N_k. \tag{A.1}$$

Here, T denotes the temperature, S the entropy, p the pressure, V the volume, μ_k the chemical potential of the component k and N_k the particle number of the component k. This equation is also called the Gibbs equations. The formulation is in accordance with the formulation given in Atkins and de Paula [9, chap. 5.1c]. In Kjelstrup and Bedeaux [90] or Henjes and Liu [80], this equation is extended with additional terms accounting for systems being polarizable in an electrical field such as an electrolyte solution. The solvent with index $k = 0$ is not always included in the term $\sum_{k=0}^{m} \mu_k\,\mathrm{d}\,N_k$, as, e.g., Kontturi et al. [91, chap. 1.1.3] or Newman and Thomas-Alyea

[109]. In this case, it is assumed that the number of solvent particles is constant in the considered volume. Integration of Equ. (A.1) for constant temperature, pressure and composition fields within the considered phase gives

$$U = TS - pV + \sum_{k=0}^{m} \mu_k N_k. \tag{A.2}$$

The Gibbs-Duhem equation is obtained by differentiating Equ. (A.2) and subtracting Equ. (A.1):

$$0 = S\,\mathrm{d}\,T - V\,\mathrm{d}\,p + \sum_{k=0}^{m} N_k\,\mathrm{d}\,\mu_k. \tag{A.3}$$

A.2 Local description of the global equilibrium

In section A.1, a system in a global equilibrium is considered where the state variables are constant throughout the phase. To transfer the global formulation of the thermodynamic relations to a local formulation, the internal energy density $u = \frac{U}{V}$, the entropy density $s = \frac{S}{V}$ and the concentration $c_k = \frac{N_k}{V}$ are introduced. By dividing Equ. (A.2) by the volume V, the internal energy density u is obtained

$$u = Ts - p + \sum_{k=0}^{m} \mu_k c_k. \tag{A.4}$$

To get the differential of the internal energy density, the definitions of the extensive variables per volume are inserted into Equ. (A.1):

$$V\,\mathrm{d}\,u + u\,\mathrm{d}\,V = TV\,\mathrm{d}\,s + Ts\,\mathrm{d}\,V - p\,\mathrm{d}\,V + \sum_{k=0}^{m} \left(\mu_k V\,\mathrm{d}\,c_k + \mu_k c_k\,\mathrm{d}\,V\right).$$

Inserting Equ. (A.4) into the term $(u\,\mathrm{d}\,V)$ and dividing this formulation by the volume V gives the differential of the internal energy density

$$\mathrm{d}\,u = T\,\mathrm{d}\,s + \sum_{k=0}^{m} \mu_k\,\mathrm{d}\,c_k. \tag{A.5}$$

Compared to the formulation in Equ. (A.1), the term including the pressure is missing, since a constant volume V was assumed for the derivation. The Gibbs-Duhem equation given in Equ. (A.3) becomes

$$0 = s\,\mathrm{d}\,T - \mathrm{d}\,p + \sum_{k=0}^{m} c_k\,\mathrm{d}\,\mu_k. \tag{A.6}$$

An equivalent approach is presented in Kontturi et al. [91, chap. 1.1.2]. In this approach, Equ. (A.5) can be directly deduced from Equ. (A.1) after division by the volume element $\mathrm{d}\,V$.

The volume element $\mathrm{d}\,V$ has to be sufficiently small such it can be considered as a homogeneous subsystem.

A.3 Definition of local equilibrium

Equ. (A.4) – Equ. (A.6) are the local thermodynamic relations for a system which is in global equilibrium. As stated in Kjelstrup and Bedeaux [90, chap. 3.5], "*a local equilibrium can be assumed for an arbitrary volume element V within the considered homogeneous phase fulfilling the equations*" (A.4) – (A.6). The size of the volume element V has to be chosen carefully since it includes an averaging of the quantities over the chosen volume element. As stated in Kjelstrup and Bedeaux [90, chap. 3.5], the volume element has to be "*large compared to microscopic distances, and small compared to distances over which the averaged quantity varies*". From this point on, all local variables are functions of time and space, as $u(\boldsymbol{x}, t)$ and $T(\boldsymbol{x}, t)$. Since the local formulation of the thermodynamic relations does not refer to a closed system anymore, the thermodynamic quantities are also conserved according to the rules used for balance equations. A detailed discussion is given in Kontturi et al. [91, chap. 1.2].

The temperature dependent ion-transport model introduced by Latz and Zausch [99] and discussed in section 2.6 is derived from the principles of non-linear thermodynamics utilizing the aforementioned local equilibrium. In contrast, the Stefan-Maxwell approach is based on particle dynamics which is combined with some thermodynamic principles.

A.4 Concept of electrochemical potential

In many textbooks, the concept of electrochemical potential is used to incorporate the effect of an electrostatic potential Φ into the thermodynamic relations. The most basic approach is the introduction of an electrical work $\mathrm{d}\,w_{\mathrm{el}} = \Phi\,\mathrm{d}\,Q$ contributing to the inner energy U of the system. Using the definition of the charge density $\rho_{\mathrm{e}} = \frac{Q}{V}$, the differential of the internal energy density reads

$$\mathrm{d}\,u = T\,\mathrm{d}\,s + \sum_{k=0}^{m} \mu_k\,\mathrm{d}\,c_k + \Phi\,\mathrm{d}\,\rho_{\mathrm{e}}, \tag{A.7}$$

as suggested in Atkins and de Paula [9, chap. 2.3]. Mathematically, Equ. (A.7) is equivalent to Equ. (A.5) as long as only electrical neutral electrolyte solutions $\rho_{\mathrm{e}} = 0$ are considered.

Equ. (A.7) can be reformulated to define the electrochemical potential $\hat{\mu}_k$ of ionic species k:

$$\begin{aligned} \mathrm{d}\,u &= T\,\mathrm{d}\,s + \sum_{k=0}^{m} \mu_k\,\mathrm{d}\,c_k + \Phi \sum_{k=0}^{m} (z_k F\,\mathrm{d}\,c_k) \\ &= T\,\mathrm{d}\,s + \sum_{k=0}^{m} \Big[(\mu_k + z_k F\Phi)\ \mathrm{d}\,c_k \Big] \\ &= T\,\mathrm{d}\,s + \sum_{k=0}^{m} \hat{\mu}_k\,\mathrm{d}\,c_k. \end{aligned} \tag{A.8}$$

Therefore, the chemical potential μ_k can be replaced by the electrochemical potential $\hat{\mu}_k$ without changing in the internal energy density u in electrical neutral electrolyte solutions. Based on this derivation, the electrochemical potential of the ionic species k is defined as

$$\hat{\mu}_k \equiv \mu_k + z_k F\Phi. \tag{A.9}$$

The same result can be derived based on the differential of the Gibbs energy density $\mathrm{d}\,g$, as shown, e.g., in Kharton [89, chap. 3.3.2]. In Kontturi et al. [91], the same result is obtained although the electrical work w_{el} does not contribute to the internal energy U. In this case, the electrical field is considered to be external to the system. In Kjelstrup and Bedeaux [90], Henjes and Liu [80] or Latz and Zausch [99], the electrochemical potential is not used for the derivation of the ion-transport equations since terms due to polarization are already included in the internal energy density.

A.5 Chemical potential of a salt

Another important implication of Equ. (A.5) and (A.7) is that chemical potentials of charged components can be expressed as neutral combinations without changing the internal energy. Therefore, the chemical potential $\mu_\pm$ of a salt can be written as

$$\mu_\pm\,\mathrm{d}\,c = (\nu_+\mu_+ + \nu_-\mu_-)\ \mathrm{d}\,c = (\nu_+\hat{\mu}_+ + \nu_-\hat{\mu}_-)\ \mathrm{d}\,c, \tag{A.10}$$

where the equivalent concentration c is defined as

$$c = \frac{c_+}{\nu_+} = \frac{c_-}{\nu_-}. \tag{A.11}$$

The positive ionic species of a binary electrolyte solution is denoted by '$+$' and the negative ionic species by '$-$'. The approach to replace the chemical potentials of the single ionic species by an equivalent chemical potential $\mu_\pm$ of the salt is not just valid for binary systems, but also for multi-ion systems as emphasized in Kontturi et al. [91, chap. 1.1.3].

As discussed, e.g., in Newman and Thomas-Alyea [109, chap. 2.3], the chemical potential μ_k of the charged or uncharged component k is defined as

$$\mu_k \equiv RT \ln \lambda_k = RT \ln(c_k f_k a_k), \tag{A.12}$$

where λ_k denotes the absolute activity of the component k, f_k the molar activity coefficient of component k and a_k a proportionality constant which is independent of composition and electrical state, but dependent on temperature and pressure. Based on Equ. (A.12), Equ. (A.10) can be reformulated to

$$\begin{aligned} \mu_\pm &= RT \ln \left(c_+^{\nu_+} c_-^{\nu_-} \, f_\pm^{\nu} \, a_+^{\nu_+} a_-^{\nu_-} \right) \\ &= \nu RT \ln \left(c \, f_\pm \right) + RT \ln \left(\nu_+^{\nu_+} \nu_-^{\nu_-} \right) + RT \ln \left(a_+^{\nu_+} a_-^{\nu_-} \right), \end{aligned} \tag{A.13}$$

where Equ. (A.11), $\nu = \nu_+ + \nu_-$ and the definition of the mean activity coefficient of a binary electrolyte,

$$f_\pm^{\nu} \equiv f_+^{\nu_+} f_-^{\nu_-},$$

are used. In literature, an alternative definition of the binary activity coefficient, $\mu_\mathrm{A} = RT \ln \left(c f_\mathrm{A} a_\mathrm{A} \right)$, is also popular. The two definitions are connected to each other via

$$f_\mathrm{A} = \left(\nu_+^{\nu_+} \nu_-^{\nu_-} \right) c^{\nu - 1} f_\pm^{\nu}.$$

If constant temperature and pressure fields can be assumed, the terms $\nu_+^{\nu_+} \nu_-^{\nu_-}$ and $a_+^{\nu_+} a_-^{\nu_-}$ are independent of the position and the gradient of the chemical potential $\mu_\pm$ can be written as

$$\nabla \mu_\pm = \nu RT \, \nabla \Big[\ln \left(c \, f_\pm \right) \Big] = \nu RT \, \Big[\nabla \ln c + \nabla \ln f_\pm \Big].$$

Alternatively, this equation can be expressed using the thermodynamic factor $\mathcal{X}$:

$$\nabla \mu_\pm = \nu RT \underbrace{\left(1 + \frac{\partial \ln f_\pm}{\partial \ln c} \right)}_{\mathcal{X}} \nabla \ln c = \nu RT \left(1 + \frac{\partial \ln f_\pm}{\partial \ln c} \right) \frac{1}{c_+} \nabla c_+. \tag{A.14}$$

A.6 Application of thermodynamic principles to surface reactions

The thermodynamic principles of chemical reactions are explained in detail, e.g., in Atkins and de Paula [9, chap. 6]. Here, only a short review is given. As given already in Equ. (2.3), an electrochemical half cell reaction can be formulated as

$$\sum_k s_{r,k} \mathrm{A}_k^{z_k} \rightleftarrows n_r e^- \tag{A.15}$$

where charge balance is fulfilled according to $\sum_i s_{r,k} z_k = -n_r$. In the following, the subscript r is dropped since only a single reaction is considered. The change in the reaction Gibbs energy $\Delta_\mathrm{R} G$ can be written as

$$\Delta_\mathrm{R} G = -n\hat{\mu}_{e^-} + \sum_i s_i \hat{\mu}_i, \tag{A.16}$$

as shown, e.g., in Newman and Thomas-Alyea [109, chap. 8]. Alternatively, the reaction Gibbs energy can also be formulated based on chemical potentials as discussed, e.g., in Atkins and de Paula [9, chap. 6.1]. Macroscopically, both formulations should be equivalent since charge is conserved in every electrochemical reaction. For $\Delta_\mathrm{R} G < 0$, the forward reaction is spontaneous, for $\Delta_\mathrm{R} G > 0$, the backward reaction is spontaneous and for $\Delta_\mathrm{R} G = 0$, the reaction is in chemical equilibrium, i.e., that the forward reaction rate is as fast as the backward reaction rate resulting in a net reaction rate of zero. As a consequence, the current density i_n normal to the interface is zero. The Gibbs energy can also be related to the overpotential η of a reaction, which describes the deviation from the equilibrium state. As defined in Newman and Thomas-Alyea [109], the overpotential can be written as

$$\eta \equiv \frac{\Delta_\mathrm{R} G}{nF} = -\frac{\hat{\mu}_{e^-}}{F} + \sum_i \frac{s_i}{nF} \hat{\mu}_i. \tag{A.17}$$

For chemical equilibrium with $\Delta_\mathrm{R} G = \eta = 0$, Equ. (A.16) reduces to

$$n\hat{\mu}_{e^-} = \sum_i s_i \hat{\mu}_i.$$

B Variable transport parameters on micro- and macroscale

In this section, it is demonstrated that it is also possible to consider a multi-field problem with variable transport parameters within the REV instead of the simplified Equ. (3.14) where constant transport parameter are assumed within the REV.

In a first step, Green's vector theorem given, e.g., in Bear and Bachmat [23, chap. 2.1.10 is applied to

$$\begin{aligned}\int_{\Gamma^{\mathrm{e,e}}} a(c)c\frac{\partial \hat{x}_j}{\partial x_i}n_i \,\mathrm{d}\,A &= \int_{\Omega^{\mathrm{e}}} \frac{\partial}{\partial x_i}\left(a(c)c\frac{\partial \hat{x}_j}{\partial x_i}\right)\,\mathrm{d}\,V \\ &= \int_{\Omega^{\mathrm{e}}} \frac{\partial}{\partial x_i}\Big(a(c)c\Big)\frac{\partial \hat{x}_j}{\partial x_i}\,\mathrm{d}\,V + \int_{\Omega^{\mathrm{e}}} \Big(a(c)c\Big)\frac{\partial^2 \hat{x}_j}{\partial x_i^2}\,\mathrm{d}\,V \end{aligned} \tag{B.1}$$

and

$$\begin{aligned}\int_{\Gamma^{\mathrm{e,e}}} a(c)\frac{\partial c}{\partial x_i}\hat{x}_j n_i \,\mathrm{d}\,A &= \int_{\Omega^{\mathrm{e}}} \frac{\partial}{\partial x_i}\left(a(c)\frac{\partial c}{\partial x_i}\hat{x}_j\right)\,\mathrm{d}\,V \\ &= \int_{\Omega^{\mathrm{e}}} \frac{\partial}{\partial x_i}\left(a(c)\frac{\partial c}{\partial x_i}\right)\hat{x}_j\,\mathrm{d}\,V + \int_{\Omega^{\mathrm{e}}} \left(a(c)\frac{\partial c}{\partial x_i}\right)\frac{\partial \hat{x}_j}{\partial x_i}\,\mathrm{d}\,V, \end{aligned} \tag{B.2}$$

where $\hat{x}_j$ denotes the vector between an arbitrary point within REV and the volumetric center of the REV $\hat{x}_j = (x'_j - x_{j,0})$. By subtracting Equ. (B.2) from Equ. (B.1) and reformulation of the first term on rhs of Equ. (B.1), an alternative formulation of the Green's vector theorem is obtained

$$\begin{aligned}&\int_{\Gamma^{\mathrm{e,e}}} \left(a(c)c\frac{\partial \hat{x}_j}{\partial x_i} - a(c)\frac{\partial c}{\partial x_i}\hat{x}_j\right)n_i \,\mathrm{d}\,A = \\ &= \int_{\Omega^{\mathrm{e}}} \frac{\partial a(c)}{\partial x_i}c\frac{\partial \hat{x}_j}{\partial x_i}\,\mathrm{d}\,V + \int_{\Omega^{\mathrm{e}}} \Big(a(c)c\Big)\frac{\partial^2 \hat{x}_j}{\partial x_i^2}\,\mathrm{d}\,V - \int_{\Omega^{\mathrm{e}}} \frac{\partial}{\partial x_i}\left(a(c)\frac{\partial c}{\partial x_i}\right)\hat{x}_j\,\mathrm{d}\,V. \end{aligned} \tag{B.3}$$

The alternative Green's vector theorem can be also formulated with respect to the potential field Φ and the conductivity $\kappa(c)$ giving

$$\begin{aligned}&\int_{\Gamma^{\mathrm{e,e}}} \left(-\kappa(c)\Phi\frac{\partial \hat{x}_j}{\partial x_i} + \kappa(c)\frac{\partial \Phi}{\partial x_i}\hat{x}_j\right)n_i \,\mathrm{d}\,A = \\ &= \int_{\Omega^{\mathrm{e}}} -\frac{\partial \kappa(c)}{\partial x_i}\Phi\frac{\partial \hat{x}_j}{\partial x_i}\,\mathrm{d}\,V + \int_{\Omega^{\mathrm{e}}} \Big(-\kappa(c)\Phi\Big)\frac{\partial^2 \hat{x}_j}{\partial x_i^2}\,\mathrm{d}\,V - \int_{\Omega^{\mathrm{e}}} \frac{\partial}{\partial x_i}\left(-\kappa(c)\frac{\partial \Phi}{\partial x_i}\right)\hat{x}_j\,\mathrm{d}\,V. \end{aligned} \tag{B.4}$$

Summation of Equ. (B.3) and Equ. (B.4) leads to

$$\begin{aligned}
&\int_{\Gamma^{\mathrm{e,e}}} \left(a(c)c - \kappa(c)\Phi\right)\frac{\partial \hat{x}_j}{\partial x_i} n_i \,\mathrm{d}\,A + \int_{\Gamma^{\mathrm{e,e}}} \left(-a(c)\frac{\partial c}{\partial x_i} + \kappa(c)\frac{\partial \Phi}{\partial x_i}\right)\hat{x}_j n_i \,\mathrm{d}\,A \\
&= \int_{\Omega^{\mathrm{e}}} \left(\frac{\partial a(c)}{\partial x_i}c - \frac{\partial \kappa(c)}{\partial x_i}\Phi\right)\frac{\partial \hat{x}_j}{\partial x_i}\,\mathrm{d}\,V + \\
&\int_{\Omega^{\mathrm{e}}} \left(a(c)c - \kappa(c)\Phi\right)\frac{\partial^2 \hat{x}_j}{\partial x_i^2}\,\mathrm{d}\,V - \int_{\Omega^{\mathrm{e}}} \frac{\partial}{\partial x_i}\left(-\kappa(c)\frac{\partial \Phi}{\partial x_i} + a(c)\frac{\partial c}{\partial x_i}\right)\hat{x}_j \,\mathrm{d}\,V, \qquad \text{(B.5)}
\end{aligned}$$

where similar terms are grouped together. It is possible to replace some of the terms in Equ. (B.5) by

$$\frac{\partial \hat{x}_j}{\partial x_i} = \frac{\partial (x_j' - x_{j,0})}{\partial x_i} = \delta_{ji}, \qquad \text{(B.6)}$$

$$\frac{\partial^2 \hat{x}_j}{\partial x_i^2} = \frac{\partial \delta_{ji}}{\partial x_i^2} = 0, \qquad \text{(B.7)}$$

$$\delta_{ji} n_i = n_j. \qquad \text{(B.8)}$$

These relation are only defined within the REV. Additionally, the last term of Equ. (B.5) can be replaced by

$$\frac{\partial}{\partial x_i}\left(-\kappa(c)\frac{\partial \Phi}{\partial x_i} + a(c)\frac{\partial c}{\partial x_i}\right) = 0, \qquad \text{(B.9)}$$

which is the same as Equ. (3.11) with Equ. (3.13). This equation is equivalent to Equ. (3.14) in the original derivation. However, compared to the original derivation, concentration depending transport parameters and the multi-field problem are included. In case of time-dependent problem types such as Equ. (3.12) with Equ. (3.13), it is additionally necessary that the problem can be approximated by its quasi-stationary formulation within the REV. As a result of Equ. (B.6) – Equ. (B.9), Equ. (B.5) can be also written as

$$\begin{aligned}
\int_{\Gamma^{\mathrm{e,e}}} \left(a(c)c - \kappa(c)\Phi\right) n_j \,\mathrm{d}\,A = &\int_{\Gamma^{\mathrm{e,e}}} \left(a(c)\frac{\partial c}{\partial x_i} - \kappa(c)\frac{\partial \Phi}{\partial x_i}\right)\hat{x}_j n_i \,\mathrm{d}\,A + \\
&\int_{\Omega^{\mathrm{e}}} \left(\frac{\partial a(c)}{\partial x_i}c - \frac{\partial \kappa(c)}{\partial x_i}\Phi\right)\delta_{ji}\,\mathrm{d}\,V. \qquad \text{(B.10)}
\end{aligned}$$

In addition, it is possible to reformulate the first term by the Gauss theorem

$$\begin{aligned}
\int_{\Gamma^{\mathrm{e,e}}} \left(a(c)c - \kappa(c)\Phi\right) n_j \,\mathrm{d}\,A &= \int_{\Omega^{\mathrm{e}}} \frac{\partial}{\partial x_j}\left(a(c)c - \kappa(c)\Phi\right)\mathrm{d}\,V \\
&= \int_{\Omega^{\mathrm{e}}} \left(a(c)\frac{\partial c}{\partial x_j} - \kappa(c)\frac{\partial \Phi}{\partial x_j}\right)\mathrm{d}\,V + \\
&\int_{\Omega^{\mathrm{e}}} \left(\frac{\partial a(c)}{\partial x_j}c - \frac{\partial \kappa(c)}{\partial x_j}\Phi\right)\mathrm{d}\,V. \qquad \text{(B.11)}
\end{aligned}$$

Using Equ. (B.11), Equ. (B.10) can be simplified to

$$\int_{\Omega^{\mathrm{e}}} \left(a(c)\frac{\partial c}{\partial x_j} - \kappa(c)\frac{\partial \Phi}{\partial x_j} \right) \mathrm{d}\, V = \int_{\Gamma^{\mathrm{e,e}}} \left(a(c)\frac{\partial c}{\partial x_i} - \kappa(c)\frac{\partial \Phi}{\partial x_i} \right) \hat{x}_j n_i \,\mathrm{d}\, A,$$

where the last integral of Equ. (B.10) and Equ. (B.11) cancel out. In a next step, the surface area enclosing the electrolyte phase can be split into the outer boundary of the electrolyte phase $\Gamma^{\mathrm{e,e}}$ and into the interface between electrolyte and solid phase $\Gamma^{\mathrm{e,s}}$

$$V^{\mathrm{e}} \left(\overline{a(c)\frac{\partial c}{\partial x_j}}^{\mathrm{e}} - \overline{\kappa(c)\frac{\partial \Phi}{\partial x_j}}^{\mathrm{e}} \right) = \int_{\Gamma^{\mathrm{e,s}}} \hat{x}_j \left(a(c)\frac{\partial c}{\partial x_i} - \kappa(c)\frac{\partial \Phi}{\partial x_i} \right) n_i \,\mathrm{d}\, A + \int_{\Gamma^{\mathrm{e,e}}} \left(a(c)\frac{\partial c}{\partial x_i} \right) \hat{x}_j n_i \,\mathrm{d}\, A + \int_{\Gamma^{\mathrm{e,e}}} \left(-\kappa(c)\frac{\partial \Phi}{\partial x_i} \right) \hat{x}_j n_i \,\mathrm{d}\, A.$$

The application of the approximation given in Equ. (3.15) 'allows' to split the surface integral of $\Gamma^{\mathrm{e,e}}$ into two parts

$$V^{\mathrm{e}} \left(\overline{a(c)\frac{\partial c}{\partial x_j}}^{\mathrm{e}} - \overline{\kappa(c)\frac{\partial \Phi}{\partial x_j}}^{\mathrm{e}} \right) = \int_{\Gamma^{\mathrm{e,s}}} \hat{x}_j \left(a(c)\frac{\partial c}{\partial x_i} - \kappa(c)\frac{\partial \Phi}{\partial x_i} \right) n_i \,\mathrm{d}\, A + \underbrace{\frac{1}{A^{\mathrm{e,e}}} \int_{\Gamma^{\mathrm{e,e}}} \left(a(c)\frac{\partial c}{\partial x_i} \right) \mathrm{d}\, A}_{\widetilde{\left(a(c)\frac{\partial c}{\partial x_i} \right)}^{\mathrm{e,e}}} \int_{\Gamma^{\mathrm{e,e}}} \hat{x}_j n_i \,\mathrm{d}\, A + \frac{1}{A^{\mathrm{e,e}}} \int_{\Gamma^{\mathrm{e,e}}} \left(-\kappa(c)\frac{\partial \Phi}{\partial x_i} \right) \mathrm{d}\, A \int_{\Gamma^{\mathrm{e,e}}} \hat{x}_j n_i \,\mathrm{d}\, A,$$

where the integral $\widetilde{\left(a(c)\frac{\partial c}{\partial x_i} \right)}^{\mathrm{e,e}}$ is the areal intrinsic phase average over the area of the boundary $\Gamma^{\mathrm{e,e}}$. The information about the orientation of the surface is included in the second surface integral. This equation can be further reformulated using the definition for the coefficient T^*_{ji} given in Equ. (3.18)

$$\overline{a(c)\frac{\partial c}{\partial x_j}}^{\mathrm{e}} - \overline{\kappa(c)\frac{\partial \Phi}{\partial x_j}}^{\mathrm{e}} = \frac{1}{V^{\mathrm{e}}} \int_{\Gamma^{\mathrm{e,s}}} \hat{x}_j \left(a(c)\frac{\partial c}{\partial x_i} - \kappa(c)\frac{\partial \Phi}{\partial x_i} \right) n_i \,\mathrm{d}\, A + T^*_{ji} \left(\frac{1}{A^{\mathrm{e,e}}} \int_{\Gamma^{\mathrm{e,e}}} \left(a(c)\frac{\partial c}{\partial x_i} \right) \mathrm{d}\, A + \frac{1}{A^{\mathrm{e,e}}} \int_{\Gamma^{\mathrm{e,e}}} \left(-\kappa(c)\frac{\partial \Phi}{\partial x_i} \right) \mathrm{d}\, A \right). \tag{B.12}$$

This equation is equivalent to Equ. (3.27).

C Analytical solutions for the one-dimensional diffusion equation

C.1 Long-term relaxation from an non-uniform concentration profile

The differential Equ. (5.35) with the boundary conditions given in Equ. (5.37) describes the relaxation behavior from a non-uniform concentration profile with respect to time t. The partial differential equation can also be expressed with respect to the following dimensionless variables

$$\theta = \frac{\overline{c}^{\,\mathrm{e}}}{\overline{c}_0^{\,\mathrm{e}}}, \quad \xi = \frac{x}{l}, \quad \text{and} \quad \mathrm{Fo} = \frac{D^*_{\pm,\mathrm{eff}}\, t}{l^2},$$

which gives the dimensionless partial differential equation

$$\frac{\partial \theta(\xi, \mathrm{Fo})}{\partial \mathrm{Fo}} = \frac{\partial^2 \theta(\xi, \mathrm{Fo})}{\partial \xi^2},$$

and for the boundary conditions

$$\frac{\partial \theta_{\mathrm{C}}(0, \mathrm{Fo})}{\partial x} = 0, \qquad \text{and} \qquad \frac{\partial \theta_{\mathrm{A}}(1, , \mathrm{Fo})}{\partial x} = 0. \tag{C.1}$$

In the appendix, the zero order approximation $D^*_{\pm,\mathrm{eff}}(c_0)$ of the concentration dependent diffusion coefficient $D^*_{\pm,\mathrm{eff}}(c)$ is abbreviated by $D^*_{\pm,\mathrm{eff}}$ to simplify the notation. For the long-term relaxation behavior, the boundary value problem is solved based on the separation of variables

$$\theta(\xi, \mathrm{Fo}) = \psi(\xi)\varphi(\mathrm{Fo}) \tag{C.2}$$

with the general solutions

$$\begin{aligned} \varphi(\mathrm{Fo}) &= A_1 \exp(\pm\delta^2 \mathrm{Fo}), \\ \psi(\xi) &= A_2 \sin(\delta\xi) + A_3 \cos(\delta\xi), \end{aligned}$$

as shown, e.g., in Polifke and Kopitz [121, chap. 14]. As a result of the relaxation process, the negative sign in the exponential term has to be considered for the following expression:

$$\theta(\xi, \mathrm{Fo}) = [A_2 \sin(\delta\xi) + A_3 \cos(\delta\xi)] \ \exp(-\delta^2 \mathrm{Fo}).$$

Based on the boundary condition at $\xi = 0$ given in Equ. (C.1)

$$\frac{\partial\theta(\xi,\mathrm{Fo})}{\partial\xi} = [\delta A_2\cos(0) - \delta A_3\sin(0)] = 0$$

it follows that $A_2 = 0$. On the other hand, based on the boundary condition at $\xi = 1$

$$\begin{aligned}\frac{\partial\theta(\xi,\mathrm{Fo})}{\partial\xi} &= [\delta A_2\cos(\delta) - \delta A_3\sin(\delta)] = 0\\ 0 &= A_3\sin(\delta),\end{aligned}$$

it follows that $\delta_n = i\pi$, where $i \in [0, 1, ..]$. Each eigenvalue δ_n corresponds to an eigenfunction θ_n, which gives, with Equ. (C.2)

$$\theta_n(\xi,\mathrm{Fo}) = A_3\cos(\delta_n\xi)\,\exp(-\delta_n^2\mathrm{Fo}).$$

Therefore, the general solution can also be expressed as a Fourier series

$$\theta(\xi,\mathrm{Fo}) = 1 + \sum_{n=1}^{\infty}\overline{C}_n\theta_n = 1 + \sum_{n=1}^{\infty}\overline{C}_nA_3\cos(\delta_n\xi)\,\exp(-\delta_n^2\mathrm{Fo}), \tag{C.3}$$

where the factor $\overline{C}_nA_3$ can be combined to $C_n = \overline{C}_nA_3$. The coefficients C_n are weighting factors for the single eigenfunctions θ_n in order to fulfill the initial concentration field. Finally, Equ. (C.3) can be transformed to dimensional values

$$\overline{c}^{\,\mathrm{e}}(x,t) = \overline{c}_0^{\,\mathrm{e}} + \overline{c}_0^{\,\mathrm{e}}\sum_{n=1}^{\infty}C_n\cos\left(\frac{n\pi}{l}x\right)\,\exp\left(-\frac{n^2\pi^2D^*_{\pm,\mathrm{eff}}}{l^2}t\right).$$

The concentration difference between the two electrodes $\Delta\overline{c}^{\,\mathrm{e}}(t) = \overline{c}^{\,\mathrm{e}}_{\mathrm{A}}(l,t) - \overline{c}^{\,\mathrm{e}}_{\mathrm{C}}(0,t)$ is given by

$$\Delta\overline{c}^{\,\mathrm{e}}(t) = \overline{c}_0^{\,\mathrm{e}}\sum_{n=1}^{\infty}C_n\,(\cos(n\pi) - 1)\exp\left(-\frac{n^2\pi^2D^*_{\pm,\mathrm{eff}}}{l^2}t\right), \tag{C.4}$$

with

$$\begin{aligned}(\cos(n\pi) - 1) &= -2 \quad &&\text{for} \quad &&\{2n-1 : n \in \mathrm{Z}^+\},\\ (\cos(n\pi) - 1) &= 0 \quad &&\text{for} \quad &&\{2n : n \in \mathrm{Z}^+\}.\end{aligned} \tag{C.5}$$

As a result, Equ. (C.4) reads as

$$\Delta\overline{c}^{\,\mathrm{e}}(t) = -2\overline{c}_0^{\,\mathrm{e}}\sum_{n=1}^{\infty}C_{(2n-1)}\exp\left(-\frac{(2n-1)^2\pi^2D^*_{\pm,\mathrm{eff}}}{l^2}t\right), \tag{C.6}$$

where the coefficients $C_{(2n-1)}$ have to be negative to give a physically meaningful concentration difference. The sign of the concentration difference $\Delta\overline{c}^{\,\mathrm{e}}(t)$ is closely related to its definition and

the orientation of the initial field in the one-dimensional domain. The same result is presented in Harned and French [79] without the specification of the coefficients $C_{(2n-1)}$.

For a known concentration profile such as a steady-state concentration profile at current interruption time T_I, it is possible to determine the coefficients C_n in Equ. (C.4) based on the dimensionless form

$$C_n = \frac{\int_0^1 \theta_0(\xi,0)\cos(\delta_n\xi)\mathrm{d}\xi}{\int_0^1 \cos^2(\delta_n\xi)\mathrm{d}\xi}, \tag{C.7}$$

given in Polifke and Kopitz [121, chap. 14.1]. The concentration profile at current interruption time is defined as

$$\overline{c}^{\,\mathrm{e}}(x,T_\mathrm{I}) = \left(\frac{x}{l}-\frac{1}{2}\right)\Delta\overline{c}^{\,\mathrm{e}}(T_\mathrm{I}) + \overline{c}_0^{\,\mathrm{e}}, \tag{C.8}$$

where $\Delta\overline{c}^{\,\mathrm{e}}(T_\mathrm{I})$ denotes the concentration difference between the two electrodes at the current interruption time and $\overline{c}_0^{\,\mathrm{e}}$ the initial concentration without concentration gradients. The combination of Equ. (C.7) with Equ. (C.8) and $\delta_n = n\pi$ allows to determine the coefficients C_n as

$$C_n = \frac{2\Delta\overline{c}^{\,\mathrm{e}}(T_\mathrm{I})\,(\cos(n\pi)-1)}{\overline{c}_0^{\,\mathrm{e}} n^2\pi^2} \quad \Rightarrow \quad C_{(2n-1)} = \frac{-4\Delta\overline{c}^{\,\mathrm{e}}(T_\mathrm{I})}{\overline{c}_0^{\,\mathrm{e}}(2n-1)^2\pi^2},$$

where Equ. (C.5) is used again. The coefficients $C_{(2n-1)}$ can be inserted in Equ. (C.6), which gives the final expression for the concentration difference

$$\Delta\overline{c}^{\,\mathrm{e}}(t) = 8\frac{\Delta\overline{c}^{\,\mathrm{e}}(T_\mathrm{I})}{\pi^2}\sum_{n=1}^{\infty}\frac{1}{(2n-1)^2}\exp\left(-\frac{(2n-1)^2\pi^2 D^*_{\pm,\mathrm{eff}}}{l^2}t\right). \tag{C.9}$$

For $t = 0$, this formulation is verified by $\Delta\overline{c}^{\,\mathrm{e}}(0) = \Delta\overline{c}_0^{\,\mathrm{e}}$, where the relation

$$\sum_{n=1}^{\infty}\frac{1}{(2n-1)^2} = \frac{\pi^2}{8},$$

and $\exp(0) = 1$ is used.

C.2 Short-term relaxation from a steady-state concentration profile

The partial differential equation given in Equ. (5.35) with the boundary conditions given in Equ. (5.37) describe the short-term relaxation behavior from a steady-state concentration profile with respect to time t. The steady-state concentration profile given in Equ. (C.8) is considered as the initial condition for the concentration $\overline{c}^{\,\mathrm{e}}(x,T_\mathrm{I})$. This boundary value problem is solved by two Laplace transformations. A general introduction in solving partial differential equations by Laplace transformation is given, e.g., in Bard and Faulkner [14, chap. A.1].

The partial differential equation given in Equ. (5.35) is reformulated by a Laplace transformation in t

$$\frac{d^2\hat{\overline{c}}^{\,e}(x,s)}{dx^2} - \underbrace{\frac{s}{D^*_{\pm,\text{eff}}}}_{a^2}\hat{\overline{c}}^{\,e}(x,s) = -\underbrace{\frac{\overline{c}^{\,e}(x,T_\text{I})}{D^*_{\pm,\text{eff}}}}_{b}, \tag{C.10}$$

where $\hat{\overline{c}}^{\,e}(x,s)$ is the Laplace transform of the concentration $\overline{c}^{\,e}(x,t)$ in t. In the appendix, the zero order approximation $D^*_{\pm,\text{eff}}(c_0)$ of the concentration dependent diffusion coefficient $D^*_{\pm,\text{eff}}(c)$ is abbreviated by $D^*_{\pm,\text{eff}}$ to simplify the notation. According to the solution of an ordinary differential equation by an additional Laplace transformation in x (see, e.g., Bard and Faulkner [14, chap. A.1.4]), Equ. (C.10) can be written as

$$\hat{\overline{c}}^{\,e}(x,s) = \frac{\overline{c}^{\,e}(x,T_\text{I})}{s} + \hat{A}(s)\text{exp}(-ax) + \hat{B}(s)\text{exp}(ax). \tag{C.11}$$

The Laplace transformed boundary conditions given Equ. (5.37) can be evaluated at the cathode $x = 0$ and at the anode $x = l$

$$\frac{\partial\hat{\overline{c}}^{\,e}_\text{C}(0,s)}{\partial x} = \frac{1}{s}\frac{\partial\overline{c}^{\,e}(0,T_\text{I})}{\partial x} + \left(s/D^*_{\pm,\text{eff}}\right)^{1/2}\left[-\hat{A}(s) + \hat{B}(s)\right] \equiv 0, \tag{C.12}$$

$$\frac{\partial\hat{\overline{c}}^{\,e}_\text{A}(l,s)}{\partial x} = \frac{1}{s}\frac{\partial\overline{c}^{\,e}(l,T_\text{I})}{\partial x} + \left(s/D^*_{\pm,\text{eff}}\right)^{1/2}\Bigg[-\hat{A}(s)\text{exp}\Big(-\underbrace{\left(s/D^*_{\pm,\text{eff}}\right)^{1/2}l}_{2f(\sqrt{s})}\Big) + \hat{B}(s)\text{exp}\Big(\underbrace{\left(s/D^*_{\pm,\text{eff}}\right)^{1/2}l}_{2f(\sqrt{s})}\Big)\Bigg] \equiv 0. \tag{C.13}$$

Now, Equ. (C.12) can be reformulated to

$$\hat{B}(s) = \hat{A}(s) - \underbrace{\frac{\left(D^*_{\pm,\text{eff}}\right)^{1/2}\Delta\overline{c}^{\,e}(T_\text{I})}{l}}_{C_1}\frac{1}{s^{3/2}}, \tag{C.14}$$

where the initial condition for the concentration given in Equ. (C.8) is used. Based on Equ. (C.14) and Equ. (C.13) the coefficient $\hat{A}(s)$ can be determined as

$$\hat{A}(s) = \frac{C_1}{s^{3/2}}\left[\frac{\exp\left(2f(\sqrt{s})\right) - 1}{\exp\left(2f(\sqrt{s})\right) - \exp\left(-2f(\sqrt{s})\right)}\right], \tag{C.15}$$

and the coefficient $\hat{B}(s)$ as

$$\hat{B}(s) = \frac{C_1}{s^{3/2}}\left[\frac{\exp\left(-2f(\sqrt{s})\right) - 1}{\exp\left(2f(\sqrt{s})\right) - \exp\left(-2f(\sqrt{s})\right)}\right]. \tag{C.16}$$

As a result, the concentration $\hat{\bar{c}}^{\,e}_C(0,s)$ at the cathode is given as

$$\hat{\bar{c}}^{\,e}_C(0,s) = \frac{\bar{c}^{\,e}_0 - \frac{1}{2}\Delta\bar{c}^{\,e}(T_I)}{s} + \frac{C_1}{s^{3/2}}\tanh(2f(\sqrt{s})).$$

where Equ. (C.15), Equ. (C.16) and Equ. (C.8) are inserted in Equ. (C.11). In addition, the relation

$$\left[\frac{\exp(2f(\sqrt{s})) - 1}{\exp(2f(\sqrt{s})) - \exp(-2f(\sqrt{s}))}\right] + \left[\frac{\exp(-2f(\sqrt{s})) - 1}{\exp(2f(\sqrt{s})) - \exp(-2f(\sqrt{s}))}\right] = \tanh(f(\sqrt{s}))$$

is used to simplify the complex exponential function. The concentration $\hat{\bar{c}}^{\,e}_A(l,s)$ at the anode is given by

$$\begin{aligned}
\hat{\bar{c}}^{\,e}(l,s) =& \frac{\bar{c}^{\,e}_0 + \frac{1}{2}\Delta\bar{c}^{\,e}(T_I)}{s} + \hat{A}(s)\exp(-\underbrace{\left(s/D^*_{\pm,\text{eff}}\right)^{1/2} l}_{2f(\sqrt{s})}) + \hat{B}(s)\exp(\underbrace{\left(s/D^*_{\pm,\text{eff}}\right)^{1/2} l}_{2f(\sqrt{s})}),\\
\hat{\bar{c}}^{\,e}(l,s) =& \frac{\bar{c}^{\,e}_0 + \frac{1}{2}\Delta\bar{c}^{\,e}(T_I)}{s} + \frac{C_1}{s^{3/2}}\left[\frac{\exp(2f(\sqrt{s})) - 1}{\exp(2f(\sqrt{s})) - \exp(-2f(\sqrt{s}))}\right]\exp(-2f(\sqrt{s})),\\
&+ \frac{C_1}{s^{3/2}}\left[\frac{\exp(-2f(\sqrt{s})) - 1}{\exp(2f(\sqrt{s})) - \exp(-2f(\sqrt{s}))}\right]\exp(2f(\sqrt{s})),\\
\hat{\bar{c}}^{\,e}(l,s)) =& \frac{\bar{c}^{\,e}_0 + \frac{1}{2}\Delta\bar{c}^{\,e}(T_I)}{s} - \frac{C_1}{s^{3/2}}\tanh(2f(\sqrt{s})).
\end{aligned}$$

In a last step, the relations $\frac{1}{s^{3/2}} \to 2\left(\frac{t}{\pi}\right)^{1/2}$ and $\lim_{s\to\infty}\tanh(2f(\sqrt{s})) = 1$ are used to invert the Laplace transform:

$$\begin{aligned}
\bar{c}^{\,e}(0,t)) &= (\bar{c}^{\,e}_0 - \frac{1}{2}\Delta\bar{c}^{\,e}(T_I)) + \frac{2\sqrt{D^*_{\pm,\text{eff}}}\,\Delta\bar{c}^{\,e}_0}{l\sqrt{\pi}}\sqrt{t},\\
\bar{c}^{\,e}(l,t)) &= (\bar{c}^{\,e}_0 + \frac{1}{2}\Delta\bar{c}^{\,e}(T_I)) - \frac{2\sqrt{D^*_{\pm,\text{eff}}}\,\Delta\bar{c}^{\,e}_0}{l\sqrt{\pi}}\sqrt{t}.
\end{aligned}$$

Note that the limit $s \to \infty$ corresponds to $t \to 0$. As a result, the concentration difference $\Delta\bar{c}^{\,e}(t) = \bar{c}^{\,e}_A(l,t) - \bar{c}^{\,e}_C(0,t)$ is given by

$$\Delta\bar{c}^{\,e}(t) = \Delta\bar{c}^{\,e}(T_I) - \frac{4\sqrt{D^*_{\pm,\text{eff}}}\,\Delta\bar{c}^{\,e}_0}{l\sqrt{\pi}}\sqrt{t}.$$

C.3 Initial time behavior of a potentiostatic polarization experiment

The solution of the boundary value problem in section 5.5.2 is based on the Laplace transformation given in Equ. (C.11):

$$\hat{\bar{c}}(x,s) = \frac{\bar{c}_0}{s} + \hat{A}(s)\text{exp}(-ax) + \hat{B}(s)\text{exp}(ax). \tag{C.17}$$

Here, s denotes the Laplace transform of t and $\hat{\bar{c}}$ the Laplace transform of $\bar{c}$. The variable a is defined as $a = \left(s/D^*_{\pm,\text{eff}}\right)^{1/2}$ and b as $b = \bar{c}_0/D^*_{\pm,\text{eff}}$. In the appendix, the zero order approximation $D^*_{\pm,\text{eff}}(c_0)$ of the concentration dependent diffusion coefficient $D^*_{\pm,\text{eff}}(c)$ is abbreviated by $D^*_{\pm,\text{eff}}$ to simplify the notation. In contrast to the derivation presented in section C.2, the initial concentration field $\bar{c}_0$ is constant and the volumetric phase average of the concentration $\bar{c}$ is considered instead of the volumetric intrinsic phase average $\bar{c}^{\,\text{e}}$. Using the Laplace transformed semi-infinite limit for $x \to \infty$ defined in Equ. (5.62) as boundary condition

$$\lim_{x\to\infty}(\hat{\bar{c}}) = \frac{\bar{c}_0}{s},$$

Equ. (C.17) reads as

$$\hat{\bar{c}}(x\to\infty,s) = \frac{\bar{c}_0}{s} + \hat{A}(s)\underbrace{\text{exp}(-ax)}_{\to 0} + \hat{B}(s)\underbrace{\text{exp}(ax)}_{\to\infty} \equiv \frac{\bar{c}_0}{s}.$$

As a result of this equation, the constant $\hat{B}(s)$ has to be $\hat{B}(s) = 0$ to fulfill the semi-infinite limit. At the cathode $x = 0$, the spatial derivative of Equ. (C.17) is given by

$$\frac{\partial \hat{\bar{c}}_\text{C}(0,s)}{\partial x} = -a\hat{A}, \tag{C.18}$$

where $\hat{B}(s) = 0$ and $\text{exp}(0) = 1$ is used. Additionally, the concentration $\hat{\bar{c}}_\text{C}$ at the cathode is given as

$$\hat{\bar{c}}_\text{C}(0,s) = \frac{\bar{c}_0}{s} + \hat{A}(s). \tag{C.19}$$

During a SSPP experiment, the initial current I_0 decreases with time until the steady-state current I_S is reached. This means that the concentration gradient at anode and cathode are not constant over time but adjusted continuously. Therefore, it is necessary to find an analytical expression for the time dependent concentration gradient. In a second step, this time-dependent concentration gradient can be related to the current $I(t)$. Based on Equ. (5.26) and (5.27), the concentration gradient at the cathode can be expressed as a function of the current I:

$$-\frac{D^*_{\pm,\text{eff}}}{1-t_+}\frac{\partial\,\bar{c}_\text{C}(0,t)}{\partial x} = \frac{1}{z_+\nu_+F}\frac{I(t)}{A}, \tag{C.20}$$

where the porosity ε is shifted from the effective diffusion coefficient $D_{\pm,\text{eff}}$ to the concentration $\overline{c}^{\,\text{e}}$ and the normal n_x is given as $n_x = -1$. Note that according to the definition given in section 5.3 the current at the cathode is negative. Equ. (C.20) can be reformulated using the equivalent circuit model

$$R = \frac{U - \Delta\overline{\Phi}^{\,\text{e}}}{I_{\text{eq}}},$$

which gives

$$\frac{\partial\, \overline{c}_{\text{C}}(0,t)}{\partial x} = -\frac{1}{z_+\nu_+F}\,\frac{1-t_+}{D^*_{\pm,\text{eff}}}\,\frac{-I_{\text{eq}}}{A} = \frac{1}{z_+\nu_+F}\,\frac{1-t_+}{D^*_{\pm,\text{eff}}}\,\frac{1}{A}\,\frac{(U-\Delta\overline{\Phi}^{\,\text{e}})}{R_{\text{I}}}. \tag{C.21}$$

At this point, it has to be considered that the cell potential U and the current I_{eq} in a equivalent circuit model are not defined with respect to a coordinate system but relative to each other. Therefore, the current I_{eq} in the equivalent circuit model is positive in this setup whereas the current I in Equ. (C.21) has to be negative. To account for these different definitions, an additional negative sign is introduced in Equ. (C.21). As a result, Equ. (C.21) can be expressed as

$$\frac{\partial\, \overline{c}_{\text{C}}(0,t)}{\partial x} = \frac{1}{z_+\nu_+F}\frac{1-t_+}{D^*_{\pm,\text{eff}}}\frac{1}{A\,R_{\text{I}}}\left[U + R_{\text{el}}\,I(t) - \frac{\nu}{z_+\nu_+}\frac{RT}{F}\left(1+\frac{\mathrm{d}\ln f_\pm}{\mathrm{d}\ln c}\right)(1-t_+)\,\frac{\Delta\overline{c}^{\,\text{e}}(t)}{\overline{c}^{\,\text{e}}_0}\right],$$

where the integrated form Equ. (5.31) with the approximation for small concentration variations given in Equ. (5.33) is used. At this point, the concentration gradient in the concentration overpotential (second term on the rhs in Equ. (5.31)) is only considered as an absolute concentration difference $\Delta\overline{c}^{\,\text{e}}(t)$ but does not influence the concentration gradient directly. The current $I(t)$ in the term $R_{\text{el}}\,I(t)$ is given by Equ. (C.20) and the concentration difference $\Delta\overline{c}^{\,\text{e}}(t)$ between anode and cathode can be reformulated to

$$\frac{\Delta\overline{c}^{\,\text{e}}(t)}{\overline{c}^{\,\text{e}}_0} = \frac{2\frac{\Delta\overline{c}^{\,\text{e}}(t)}{2}}{\overline{c}^{\,\text{e}}_0} = \frac{2(\overline{c}^{\,\text{e}}_0 - \overline{c}^{\,\text{e}}_{\text{C}}(t))}{\overline{c}^{\,\text{e}}_0} = 2\left(1-\frac{\overline{c}^{\,\text{e}}_{\text{C}}(t)}{\overline{c}^{\,\text{e}}_0}\right) = 2\left(1-\frac{\overline{c}_{\text{C}}(0,t)}{\overline{c}_0}\right)$$

if the developing concentration profile is point symmetric to $x = l/2$. This is the case for constant transport parameters. As a result, the concentration gradient at the cathode reads as

$$\frac{\partial\overline{c}_{\text{C}}(0,t)}{\partial x} = \underbrace{\frac{1}{z_+\nu_+F}\,\frac{1-t_+}{D^*_{\pm,\text{eff}}}\,\frac{1}{A\,(R_{\text{I}}+R_{\text{El}})}}_{C_1}$$
$$\left[U - \frac{\nu}{z_+\nu_+}\frac{RT}{F}\left(1+\frac{\mathrm{d}\ln f_\pm}{\mathrm{d}\ln c}\right)(1-t_+)\,2\left(1-\frac{\overline{c}_{\text{C}}(0,t)}{\overline{c}_0}\right)\right],$$

where the constant C_1 is used to simplify the notation. The notation can be simplified further utilizing the constants C_2 and C_3

$$\begin{aligned}\frac{\partial \overline{c}_{\mathrm{C}}(0,t)}{\partial x} =& \underbrace{C_1\left[U - \frac{2\nu}{z_+\nu_+}\frac{RT}{F}\left(1+\frac{\mathrm{d}\ln f_\pm}{\mathrm{d}\ln c}\right)(1-t_+)\right]}_{C_2} \\ &+ \underbrace{C_1\frac{2\nu}{z_+\nu_+}\frac{RT}{F}\left(1+\frac{\mathrm{d}\ln f_\pm}{\mathrm{d}\ln c}\right)(1-t_+)\ \frac{1}{\overline{c}_0}}_{C_3}\overline{c}_{\mathrm{C}}(0,t),\end{aligned}$$

which results in

$$\frac{\partial \overline{c}_{\mathrm{C}}(0,t)}{\partial x} = C_2 + C_3\,\overline{c}_{\mathrm{C}}(0,t). \tag{C.22}$$

The Laplace transformation of Equ. (C.22) in t reads as

$$\frac{\partial \hat{\overline{c}}_{\mathrm{C}}(0,s)}{\partial x} = \frac{C_2}{s} + C_3\,\hat{\overline{c}}_{\mathrm{C}}(0,s). \tag{C.23}$$

Based on Equ. (C.18) and (C.19), Equ. (C.23) can also be formulated as

$$-a\hat{A}(s) = \frac{C_2}{s} + C_3\left(\frac{\overline{c}_0}{s} + \hat{A}(s)\right).$$

Utilizing the definition for a, the coefficient $\hat{A}$ is given by

$$\hat{A}(s) = -\sqrt{D^*_{\pm,\mathrm{eff}}}\,(C_2 + C_3\overline{c}_0)\,\frac{1}{s\left[\sqrt{s} + C_3\sqrt{D^*_{\pm,\mathrm{eff}}}\right]}.$$

As a result, the concentration $\hat{\overline{c}}_{\mathrm{C}}(0,s)$ at the cathode can be written as

$$\hat{\overline{c}}_{\mathrm{C}}(0,s) = \frac{\overline{c}_0}{s} - \sqrt{D^*_{\pm,\mathrm{eff}}}\,(C_2 + C_3\overline{c}_0)\,\frac{1}{s\left[\sqrt{s}+H\right]}$$

and the concentration gradient as

$$\frac{\partial \hat{\overline{c}}_{\mathrm{C}}(0,s)}{\partial x} = (C_2 + C_3\overline{c}_0)\,\frac{1}{s^{1/2}\left[s^{1/2}+H\right]},$$

where the relation $H = C_3\sqrt{D^*_{\pm,\mathrm{eff}}}$ is used. After inverting the Laplace transformation, the current $I(t)$ is given by

$$I(t) = -z_+\nu_+FA\frac{D^*_{\pm,\mathrm{eff}}}{1-t_+}\,(C_2 + C_3\overline{c}_0)\exp(H^2t)\left(1-\mathrm{erf}(Ht^{1/2})\right).$$

After insertion of the coefficients C_1, C_2 and C_3, the current $I(t)$ at the cathode reads as

$$I(t) = -\frac{U}{R_{\mathrm{LF}}} \exp(H^2 t) \left(1 - \mathrm{erf}(Ht^{1/2})\right), \tag{C.24}$$

where the constant H is defined as

$$H = \frac{2\nu}{z_+^2 \nu_+^2} \frac{RT}{F^2} \frac{1}{A\, R_{\mathrm{LF}}\, \varepsilon\, \overline{c}_0^{\mathrm{e}}} \left(1 + \frac{\mathrm{d}\ln f_\pm}{\mathrm{d}\ln c}\right) \frac{(1-t_+)^2}{(D^*_{\pm,\mathrm{eff}})^{1/2}}. \tag{C.25}$$

Here, the interface and the electrolyte resistance are already combined in the low frequency resistance $R_{\mathrm{LF}} = R_{\mathrm{I}} + R_{\mathrm{El}}$.

Bibliography

[1] https://en.wikipedia.org/wiki/lithium_perchlorate.

[2] P. M. Adler, *Porous media: geometry and transports*, Butterworth-Heinemann series in chemical engineering, Butterworth-Heinemann, 1992.

[3] P. Albertus, J. Christensen, and J. Newman, Modeling side reactions and nonisothermal effects in nickel metal-hybride batteries, *Journal of The Electrochemical Society* **155**, A48 – A60, 2008.

[4] P. Albertus, G. Girishkumar, B. McCloskey, R. S. Snchez-Carrera, B. Kozinsky, J. Christensen, and A. C. Luntz, Identifying capacity limitations in the lithium/oxygen battery using experiments and modeling, *Journal of The Electrochemical Society* **158**, A343 – A351, 2011.

[5] D. Andre, S.-J. Kim, P. Lamp, S. F. Lux, F. Maglia, O. Paschos, and B. Stiaszny, Future generations of cathode materials: An automotive industry perspective, *J. Mater. Chem. A* **3**, 6709 – 6732, 2015.

[6] G. E. Archie, The electrical resistivity log as an aid in determining some reservoir characteristics, *Transactions of the American Institute of Mining, Metallurgical, and Petroleum Engineers* **146**, 54 – 62, 1942.

[7] M. Armand and J. M. Tarascon, Building better batteries, *Nature* **451**, 652 – 657, 2008.

[8] P. Arora and Z. J. Zhang, Battery separators, *Chemical Reviews* **104**, 4419 – 4462, 2004.

[9] P. Atkins and J. de Paula, *Atkins' Physical Chemistry (9^{th} ed.)*, Oxford University Press, 2010.

[10] D. Aurbach, E. Zinigrad, Y. Cohen, and H. Teller, A short review of failure mechanisms of lithium metal and lithiated graphite anodes in liquid electrolyte solutions, *Solid State Ionics* **148**, 405 – 416, 2002.

[11] A. Awarke, M. Wittler, S. Pischinger, and J. Bockstette, A 3D mesoscale model of the collector-electrode interface in Li-ion batteries, *Journal of The Electrochemical Society* **159**, A798 – A808, 2012.

[12] A. Awarke, S. Pischinger, and J. Ogrzewalla, Pseudo 3D modeling and analysis of the SEI growth distribution in large format Li-ion polymer pouch cells, *Journal of The Electrochemical Society* **160**, A172 – A181, 2013.

[13] C. Barchasz, J.-C. Leprêtre, F. Alloin, and S. Patoux, New insights into the limiting parameters of the Li/S rechargeable cell, *Journal of Power Sources* **199**, 322 – 330, 2012.

[14] A. J. Bard and L. R. Faulkner, *Electrochemical methods, Fundamentals and Appliations (2nd ed.)*, John Wiley & Sons, Inc., 2001.

[15] M. Barrande, R. Bouchet, and R. Denoyel, Tortuosity of porous particles, *Analytical Chemistry* **79**, 9115 – 9121, 2007.

[16] J. Barthel, R. Neueder, H. Poepke, and H. Wittmann, Osmotic and activity coefficients of nonaqueous electrolyte solutions. Part 1. Lithium perchlorate in the protic solvents methanol, ethanol, and 2-propanol, *Journal of Solution Chemistry* **27**, 1055 – 1066, 1998.

[17] J. Barthel, R. Neueder, H. Poepke, and H. Wittmann, Osmotic coefficients and activity coefficients of nonaqueous electrolyte solutions. Part 2. Lithium perchlorate in the aprotic solvents acetone, acetonitrile, dimethoxyethane, and dimethylcarbonate, *Journal of Solution Chemistry* **28**, 489 – 503, 1999.

[18] G. Bauer, *A coupled finite element approach for electrochemical system*, PhD thesis, Technische Universität München, 2012.

[19] G. Bauer, V. Gravemeier, and W. A. Wall, A 3D finite element approach for the coupled numerical simulation of electrochemical systems and fluid flow, *International Journal for Numerical Methods in Engineering* **86**, 1339 – 1359, 2011.

[20] G. Bauer, V. Gravemeier, and W. A. Wall, A stabilized finite element method for the numerical simulation of multi-ion transport in electrochemical systems, *Computer Methods in Applied Mechanics and Engineering* **223 – 224**, 199 – 210, 2012.

[21] G. Bauer, P. Gamnitzer, V. Gravemeier, and W. A. Wall, An isogeometric variational multiscale method for large-eddy simulation of coupled multi-ion transport in turbulent flow, *Journal of Computational Physics* **251**, 194 – 208, 2013.

[22] M. Z. Bazant, M. S. Kilic, B. D. Storey, and A. Ajdari, Towards an understanding of induced-charge electrokinetics at large applied voltages in concentrated solutions, *Advances in Colloid and Interface Science* **152**, 48 – 88, 2009.

[23] J. Bear and Y. Bachmat, *Introduction to modeling of transport phenomena in porous media*, Kluwer Academic Publishers, 1990.

[24] J. Besenhard, *Handbook of Battery Materials*, Wiley & Son, 2008.

[25] P. M. Blonsky, D. F. Shriver, P. Austin, and H. R. Allcock, Complex formation and ionic conductivity of polyphosphazene solid electrolytes, *Solid State Ionics* **18 - 19**, 258 – 264, 1986.

[26] P. Bochev and R. B. Lehoucq, On the finite element solution of the pure Neumann problem, *Society for Industrial and Applied Mathematics review* **47**, 50 – 66, 2005.

[27] A. M. Bond, K. B. Oldham, and G. A. Snook, Use of the ferrocene oxidation process to provide both reference electrode potential calibration and a simple measurement (via semiintegration) of the uncompensated resistance in cyclic voltammetric studies in high-resistance organic solvents, *Analytical Chemistry* **72**, 3492 – 3496, 2000.

[28] G. G. Botte, B. A. Johnson, and R. E. White, Influence of some design variables on the thermal behavior of a lithium-ion cell, *Journal of The Electrochemical Society* **146**, 914 – 923, 1999.

[29] G. G. Botte, V. R. Subramanian, and R. E. White, Mathematical modeling of secondary lithium batteries, *Electrochimica Acta* **45**, 2595 – 2609, 2000.

[30] F. Brezzi and M. Fortin, *Mixed and hybrid finite element methods*, Springer-Verlag, 1991.

[31] P. G. Bruce and C. A. Vincent, Steady state current flow in solid binary electrolyte cells, *Journal of Electroanalytical Chemistry and Interfacial Electrochemistry* **225**, 1 – 17, 1987.

[32] P. G. Bruce, M. T. Hardgrave, and C. A. Vincent, The determination of transference numbers in solid polymer electrolytes using the Hittorf method, *Solid State Ionics* **53 – 56**, 1087 – 1094, 1992.

[33] D. A. G. Bruggeman, Berechnung verschiedener physikalischer Konstanten von heterogenen Substanzen I. Dielektrizitätskonstanten und Leitfähigkeiten der Mischkörper aus isotropen Substanzen, *Annalen der Physik* **416**, 636–664, 1935.

[34] L. Cai and R. E. White, Mathematical modeling of a lithium ion battery with thermal effects in COMSOL Inc. Multiphysics (MP) software, *Journal of Power Sources* **196**, 5985 – 5989, 2011.

[35] L. Cai and R. E. White, Lithium ion cell modeling using orthogonal collocation on finite elements, *Journal of Power Sources* **217**, 248 – 255, 2012.

[36] C. Capiglia, Y. Saito, H. Kageyama, P. Mustarelli, T. Iwamoto, T. Tabuchi, and H. Tukamoto, ^{7}Li and ^{19}F diffusion coefficients and thermal properties of non-aqueous electrolyte solutions for rechargeable lithium batteries, *Journal of Power Sources* **81 – 82**, 859 – 862, 1999.

[37] J. F. Casteel and E. S. Amis, Specific conductance of concentrated solutions of magnesium salts in water-ethanol systems, *Journal of Chemical & Engineering Data* **17**, 55 – 59, 1972.

[38] F. Castiglione, E. Ragg, A. Mele, G. B. Appetecchi, M. Montanino, and S. Passerini, Molecular environment and enhanced diffusivity of Li^+ ions in lithium-salt-doped ionic liquid electrolytes, *The Journal of Physical Chemistry Letters* **2**, 153 – 157, 2011.

[39] Cepheiden. Li-ion-zelle (CoO2-Carbon, Schema), *wikipedia*, 2008, https://commons.wikimedia.org/wiki/File:Li-Ion-Zelle_(CoO2-Carbon,_Schema).svg.

[40] J. Chakraborty, C. P. Please, A. Goriely, and S. J. Chapman, Combining mechanical and chemical effects in the deformation and failure of a cylindrical electrode particle in a Li-ion battery, *International Journal of Solids and Structures* **54**, 66 – 81, 2015.

[41] J. Christensen and J. Newman, Stress generation and fracture in lithium insertion materials, *Journal of Solid State Electrochemistry* **10**, 293 – 319, 2006.

[42] D.-W. Chung, M. Ebner, D. R. Ely, V. Wood, and R. E. Garca, Validity of the Bruggeman relation for porous electrodes, *Modelling and Simulation in Materials Science and Engineering* **21**, 074009, 2013.

[43] J. Chung and G. Hulbert, A time integration algorithm for structural dynamics with improved numerical dissipation: the generalized-α method, *Journal of Applied Mechanics* **60**, 371 – 375, 1993.

[44] F. Ciucci and W. Lai, Derivation of micro/macro lithium battery models from homogenization, *Transport in Porous Media* **88**, 249 – 270, 2011.

[45] M. B. Clennell, Tortuosity: a guide through the maze, *Geological Society, London, Special Publications* **122**, 299 – 344, 1997.

[46] S. J. Cooper, D. S. Eastwood, J. Gelb, G. Damblanc, D. J. L. Brett, R. S. Bradley, P. J. Withers, P. D. Lee, A. J. Marquis, N. P. Brandon, and P. R. Shearing, Image based modelling of microstructural heterogeneity in $LiFePO_4$ electrodes for Li-ion batteries, *Journal of Power Sources* **247**, 1033 – 1039, 2014.

[47] D. Cornell and D. L. Katz, Flow of gases through consolidated porous media, *Industrial & Engineering Chemistry* **45**, 2145 – 2152, 1953.

[48] D. Danilov and P. Notten, Mathematical modelling of ionic transport in the electrolyte of Li-ion batteries, *Electrochimica Acta* **53**, 5569 – 5578, 2008.

[49] M. S. Ding, Liquid phase boundaries, dielectric constant, and viscosity of PC-DEC and PC-EC binary carbonates, *Journal of The Electrochemical Society* **150**, A455 – A462, 2003.

[50] D. Djian, F. Alloin, S. Martinet, H. Lignier, and J. Sanchez, Lithium-ion batteries with high charge rate capacity: Influence of the porous separator, *Journal of Power Sources* **172**, 416 – 421, 2007.

[51] M. M. Doeff, P. Georn, J. Qiao, J. Kerr, and L. C. De Jonghe, Transport properties of a high molecular weight poly(propylene oxide)$LiCF_3SO_3$ system, *Journal of The Electrochemical Society* **146**, 2024 – 2028, 1999.

[52] J. Donea and A. Huerta, *Finite Element Methods for Flow Problems*, John Wiley & Sons Lts., 2004.

[53] M. Doyle, *Design and Simulation of Lithium Rechargeable Batteries*, PhD thesis, Lawrence Berkeley Laboratory University of California, 1995.

[54] M. Doyle, T. F. Fuller, and J. Newman, Modeling of galvanostatic charge and discharge of the lithium/polymer/insertion cell, *Journal of The Electrochemical Society* **140**, 1526 – 1533, 1993.

[55] M. Doyle, J. Newman, A. S. Gozdz, C. N. Schmutz, and J. M. Tarascon, Comparison of modeling predictions with experimental data from plastic lithium ion cells, *Journal of The Electrochemical Society* **143**, 1890 – 1903, 1996.

[56] A. Ehrl, J. Landesfeind, W. A. Wall, and H. A. Gasteiger, Determination of transport parameters in liquid binary electrolytes: Part II. Transference number, *Journal of The Electrochemical Society* **164**, A2716 – A2731, 2017.

[57] A. Ehrl, J. Landesfeind, W. A. Wall, and H. A. Gasteiger, Determination of transport parameters in liquid binary lithium ion battery electrolytes: I. Diffusion coefficient, *Journal of The Electrochemical Society* **164**, A826 – A836, 2017.

[58] A. Ehrl, G. Bauer, V. Gravemeier, and W. A. Wall, A computational approach for the simulation of natural convection in electrochemical cells, *Journal of Computational Physics* **235**, 764 – 785, 2013.

[59] S. Elul, Y. Cohen, and D. Aurbach, The influence of geometry in 2D simulation on the charge/discharge processes in Li-ion batteries, *Journal of Electroanalytical Chemistry* **682**, 53 – 65, 2012.

[60] M. Ender, J. Joos, T. Carraro, and E. Ivers-Tiffée, Three-dimensional reconstruction of a composite cathode for lithium-ion cells, *Electrochemistry Communications* **13**, 166 – 168, 2011.

[61] T. R. Ferguson and M. Z. Bazant, Nonequilibrium thermodynamics of porous electrodes, *Journal of The Electrochemical Society* **159**, A1967 – A1985, 2012.

[62] A. Ferry, M. M. Doeff, and L. C. De Jonghe, Transport property measurements of polymer electrolytes, *Electrochimica Acta* **43**, 1387 – 1393, 1998.

[63] T. F. Fuller, M. Doyle, and J. Newman, Relaxation phenomena in lithium-ion-insertion cells, *Journal of The Electrochemical Society* **141**, 982 – 990, 1994.

[64] T. F. Fuller, M. Doyle, and J. Newman, Simulation and optimization of the dual lithium ion insertion cell, *Journal of The Electrochemical Society* **141**, 1 – 10, 1994.

[65] P. Gamnitzer, *Residual-based variational multiscale method for turbulent flows and fluid-structure interaction*, PhD thesis, Technische Universität München, 2010.

[66] P. Georén and G. Lindbergh, Characterisation and modelling of the transport properties in lithium battery polymer electrolytes, *Electrochimica Acta* **47**, 577 – 587, 2001.

[67] P. Georén and G. Lindbergh, Characterisation and modelling of the transport properties in lithium battery gel electrolytes: Part I. the binary electrolyte PC/$LiClO_4$, *Electrochimica Acta* **49**, 3497 – 3505, 2004.

[68] G. Girishkumar, B. McCloskey, A. C. Luntz, S. Swanson, and W. Wilcke, Lithium – air battery: Promise and challenges, *The Journal of Physical Chemistry Letters* **1**, 2193 – 2203, 2010.

[69] S. Golmon, K. Maute, and M. L. Dunn, Numerical modeling of electrochemical-mechanical interactions in lithium polymer batteries, *Computers & Structures* **87**, 1567 – 1579, 2009.

[70] S. Golmon, K. Maute, and M. L. Dunn, Multiscale design optimization of lithium ion batteries using adjoint sensitivity analysis, *International Journal for Numerical Methods in Engineering* **92**, 475 – 494, 2012.

[71] J. B. Goodenough and Y. Kim, Challenges for rechargeable Li batteries, *Chemistry of Materials* **22**, 587 – 603, 2010.

[72] V. Gravemeier and W. A. Wall, An algebraic variational multiscale-multigrid method for large-eddy simulation of turbulent variable-density flow at low Mach number, *Journal of Computational Physics* **229**, 6047 – 6070, 2010.

[73] P. Gresho, R. Sani, and M. Engelman, *Incompressible Flow and the Finite Element Method, Incompressible Flow & the Finite Element Method - Advection-Diffusion & Isothermal Laminar Flow Combined Edition*, John Wiley & Sons, 1998.

[74] G. Gritzner and J. Kuta, Recommendations on reporting electrode potentials in nonaqueous solvents (provisional), *Pure and Applied Chemistry* **54**, 1527 – 1532, 1982.

[75] W. B. Gu and C. Y. Wang, Thermal-electrochemical modeling of battery systems, *Journal of The Electrochemical Society* **147**, 2910 – 2922, 2000.

[76] M. Gurtin, *An Introduction to Continuum Mechanics, 1st Edition*, Academic Press, 1982.

[77] H. Hafezi and J. Newman, Verification and analysis of transference number measurements by the galvanostatic polarization method, *Journal of The Electrochemical Society* **147**, 3036 – 3042, 2000.

[78] C. Hamann and W. Vielstich, *Elektrochemie*, John Wiley & Sons Australia, Limited, 2005.

[79] H. S. Harned and D. M. French, A conductance method for the determination of the diffusion coefficients of electrolytes, *Annals of the New York Academy of Sciences* **46**, 267 – 284, 1945.

[80] K. Henjes and M. Liu, Hydrodynamics of polarizable liquids, *Annals of Physics* **223**, 243 – 276, 1993.

[81] M. M. Hiller, M. Joost, H. J. Gores, S. Passerini, and H. D. Wiemhöfer, The influence of interface polarization on the determination of lithium transference numbers of salt in polyethylene oxide electrolytes, *Electrochimica Acta* **114**, 21 – 29, 2013.

[82] L. Holzer, D. Wiedenmann, B. Münch, L. Keller, M. Prestat, P. Gasser, I. Robertson, and B. Grobéty, The influence of constrictivity on the effective transport properties of porous layers in electrolysis and fuel cells, *Journal of Materials Science* **48**, 2934 – 2952, 2013.

[83] M. Hori and S. Nemat-Nasser, On two micromechanics theories for determining micro–macro relations in heterogeneous solids, *Mechanics of Materials* **31**, 667 – 682, 1999.

[84] X. Hu, S. Li, and H. Peng, A comparative study of equivalent circuit models for Li-ion batteries, *Journal of Power Sources* **198**, 359 – 367, 2012.

[85] R. Huggins, *Advanced Batteries: Materials Science Aspects*, Springer, 2008.

[86] J. Jackson, *Classical Electrodynamics Third Edition*, John Wiley & Sons Ltd, New York, 1998.

[87] K. E. Jansen, C. H. Whiting, and G. M. Hulbert, A generalized–α method for integrating the filtered Navier–Stokes equations with a stabilized finite element method, *Computer Methods in Applied Mechanics and Engineering* **190**, 305 – 319, 2000.

[88] J. Joos, T. Carraro, A. Weber, and E. Ivers-Tiffée, Reconstruction of porous electrodes by FIB/SEM for detailed microstructure modeling, *Journal of Power Sources* **196**, 7302 – 7307, 2011.

[89] V. V. Kharton, *Solid State Electrochemistry I: Fundamentals, Materials and their Applications*, Wiley-VCH Verlag GmbH & Co. KGaA, 2009.

[90] S. Kjelstrup and D. Bedeaux, *Non-Equilibrium Thermodynamics Of Heterogeneous Systems*, Volume 16 of *Series on Advances in Statistical Mechanics*, World Scientific Publishing Co. Pte. Ltd., 2008.

[91] K. Kontturi, L. Murtomäki, and J. A. Manzanares, *Ionic Transport Processes: In Electrochemistry and Membrane Science*, Oxford University Press, USA, 2008.

[92] G. Kreysa, K. Ota, and R. Savinell, *Encyclopedia of Applied Electrochemistry*, Encyclopedia of Applied Electrochemistry, Springer New York, 2014.

[93] W. Lai and F. Ciucci, Mathematical modeling of porous battery electrodes – revisit of newman's model, *Electrochimica Acta* **56**, 4369 – 4377, 2011.

[94] W. M. Lai, D. Rubin, and E. Krempl, *Introduction to Continuum Mechanics*, Butterworth-Heinemann, 2010.

[95] J. Landesfeind. Analysis and characterisation of olivine cathode materials for automotive lithium-ion batteries. Master's thesis, Technische Universität München, 2013.

[96] J. Landesfeind, A. Ehrl, M. Graf, W. A. Wall, and H. A. Gasteiger, Direct electrochemical determination of thermodynamic factors in aprotic binary electrolytes, *Journal of The Electrochemical Society* **163**, A1254 – A1264, 2016.

[97] J. Landesfeind, J. Hattendorff, A. Ehrl, W. A. Wall, and H. A. Gasteiger, Tortuosity determination of battery electrodes and separators by impedance spectroscopy, *Journal of The Electrochemical Society* **163**, A1373 – A1387, 2016.

[98] M. Landstorfer and T. Jacob, Mathematical modeling of intercalation batteries at the cell level and beyond, *Chemical Society Reviews* **42**, 3234 – 3252, 2013.

[99] A. Latz and J. Zausch, Thermodynamic consistent transport theory of Li-ion batteries, *Journal of Power Sources* **196**, 3296 – 3302, 2011.

[100] J. Liu and C. W. Monroe, Solute-volume effects in electrolyte transport, *Electrochimica Acta* **135**, 447 – 460, 2014.

[101] J. Liu and C. W. Monroe, On the characterization of battery electrolytes with polarization cells, *Electrochimica Acta* **167**, 357 – 363, 2015.

[102] H. Lundgren, M. Behm, and G. Lindbergh, Electrochemical characterization and temperature dependency of mass-transport properties of $LiPF_6$ in EC:DEC, *Journal of The Electrochemical Society* **162**, A413 – A420, 2015.

[103] Y. Ma, M. Doyle, T. F. Fuller, M. M. Doeff, L. C. De Jonghe, and J. Newman, The measurement of a complete set of transport properties for a concentrated solid polymer electrolyte solution, *Journal of The Electrochemical Society* **142**, 1859 – 1868, 1995.

[104] R. Marom, S. F. Amalraj, N. Leifer, D. Jacob, and D. Aurbach, A review of advanced and practical lithium battery materials, *J. Mater. Chem.* **21**, 9938 – 9954, 2011.

[105] V. Mauro, A. D Aprano, F. Croce, and M. Salomon, Direct determination of transference numbers of $LiClO_4$ solutions in propylene carbonate and acetonitrile, *Journal of Power Sources* **141**, 167 – 170, 2005.

[106] A. D. McNaught and A. Wilkinson, *IUPAC. Compendium of Chemical Terminology, 2nd ed. (the "Gold Book")*, Blackwell Scientific Publications, Oxford, 1997.

[107] R. N. Methekar, P. W. C. Northrop, K. Chen, R. D. Braatz, and V. R. Subramanian, Kinetic Monte Carlo simulation of surface heterogeneity in graphite anodes for lithium-ion batteries: Passive layer formation, *Journal of The Electrochemical Society* **158**, A363 – A370, 2011.

[108] G.-A. Nazri and G. Pistoia, *Lithium batteries Science and Technology*, Springer Science + Business Media, 2009.

[109] J. Newman and K. E. Thomas-Alyea, *Electrochemical Systems (3rd ed.)*, John Wiley & Sons, Inc., Hoboken; New Jersey, 2004.

[110] J. Newman and T. W. Chapman, Restricted diffusion in binary solutions, *American Institute of Chemical Engineers Journal* **19**, 343 – 348, 1973.

[111] J. Newman and W. Tiedemann, Porous-electrode theory with battery applications, *American Institute of Chemical Engineers Journal* **21**, 25 – 41, 1975.

[112] J. Newman, D. Bennion, and C. W. Tobias, Mass transfer in concentrated binary electrolytes, *Berichte der Bunsengesellschaft für physikalische Chemie* **69**, 608 – 612, 1965.

[113] T. Nishida, K. Nishikawa, and Y. Fukunaka, Diffusivity measurement of $LiPF_6$, LiTFSI, $LiBF_4$ in PC, *Electrochemical Society Transactions* **6**, 1 – 14, 2008.

[114] K. Nishikawa, Y. Fukunaka, T. Sakka, Y. H. Ogata, and J. R. Selman, Measurement of $LiClO_4$ diffusion coefficient in propylene carbonate by Moiré pattern, *Journal of The Electrochemical Society* **153**, A830 – A834, 2006.

[115] A. Nyman, M. Behm, and G. Lindbergh, Electrochemical characterisation and modelling of the mass transport phenomena in $LiPF_6$-EC-EMC electrolyte, *Electrochimica Acta* **53**, 6356 – 6365, 2008.

[116] M. Odziemkowski and D. E. Irish, An electrochemical study of the reactivity at the lithium electrolyte/bare lithium metal interface: II. Unpurified solvents, *Journal of The Electrochemical Society* **140**, 1546 – 1555, 1993.

[117] N. Ogihara, S. Kawauchi, C. Okuda, Y. Itou, Y. Takeuchi, and Y. Ukyo, Theoretical and experimental analysis of porous electrodes for lithium-ion batteries by electrochemical impedance spectroscopy using a symmetric cell, *Journal of The Electrochemical Society* **159**, A1034 – A1039, 2012.

[118] T. Osaka, T. Momma, Y. Matsumoto, and Y. Uchida, Surface characterization of electrodeposited lithium anode with enhanced cycleability obtained by CO_2 addition, *Journal of The Electrochemical Society* **144**, 1709 – 1713, 1997.

[119] K. K. Patel, J. M. Paulsen, and J. Desilvestro, Numerical simulation of porous networks in relation to battery electrodes and separators, *Journal of Power Sources* **122**, 144 – 152, 2003.

[120] L. Peter, W. Dürr, P. Bindra, and H. Gerischer, The influence of alkali metal cations on the rate of the $Fe(CN)_6^{4-}$ / $Fe(CN)_6^{3-}$ electrode process, *Journal of Electroanalytical Chemistry and Interfacial Electrochemistry* **71**, 31 – 50, 1976.

[121] W. Polifke and J. Kopitz, *Wärmeübertragung: Grundlagen, analytische und numerische Methoden*, Ing - Maschinenbau, Pearson Studium, 2009.

[122] P. Popov, Y. Vutov, S. Margenov, and O. Iliev, Finite volume discretization of equations describing nonlinear diffusion in Li-ion batteries, In *Numerical Methods and Applications*, Springer Berlin Heidelberg, 2011.

[123] W. S. Price, Pulsed-field gradient nuclear magnetic resonance as a tool for studying translational diffusion. Part 1: Basic theory, *Journal of Magnetic Resonance* **9**, 299 – 336, 1997.

[124] V. Ramadesigan, P. W. C. Northrop, S. De, S. Santhanagopalan, R. D. Braatz, and V. R. Subramanian, Modeling and simulation of lithium-ion batteries from a systems engineering perspective, *Journal of The Electrochemical Society* **159**, R31 – R45, 2012.

[125] J. Redepenning, E. Castro-Narro, G. Venkataraman, and E. Mechalke, Influence of supporting electrolyte activity on formal potentials measured for dissolved internal standards in acetonitrile, *Journal of Electroanalytical Chemistry* **498**, 192 – 200, 2001.

[126] J. N. Reimers, Algorithmic improvements and PDE decoupling for the simulation of porous electrode cells, *Journal of The Electrochemical Society* **160**, A811 – A818, 2013.

[127] J. C. Roth, A. Ehrl, T. Becher, S. J. Frerichs, I and, N. Weller, and W. W. A., Correlation between alveolar ventilation and electrical properties of lung parenchyma, *Physiological Measurement* **36**, 1211 – 1226, 2015.

[128] I. Ruff, V. J. Friedrich, K. Demeter, and K. Csillag, Transfer diffusion. II. Kinetics of electron exchange reaction between ferrocene and ferricinium ion in alcohols, *The Journal of Physical Chemistry* **75**, 3303 – 3309, 1971.

[129] Y. Saad, *Iterative Methods for Sparse Linear Systems, Second Edition*, 2 Edition, Society for Industrial and Applied Mathematics, 2003.

[130] A. Salvadori, E. Bosco, and D. Grazioli, A computational homogenization approach for Li-ion battery cells. Part 1 - Formulation, *Journal of the Mechanics and Physics of Solids* **65**, 114 – 137, 2014.

[131] B. Scrosati and J. Garche, Lithium batteries: Status, prospects and future, *Journal of Power Sources* **195**, 2419 – 2430, 2010.

[132] A. K. Sethurajan, S. A. Krachkovskiy, I. C. Halalay, G. R. Goward, and B. Protas, Accurate characterization of ion transport properties in binary symmetric electrolytes using in situ NMR imaging and inverse modeling, *The Journal of Physical Chemistry B* **119**, 12238–12248, 2015.

[133] L. Shen and Z. Chen, Critical review of the impact of tortuosity on diffusion, *Chemical Engineering Science* **62**, 3748 – 3755, 2007.

[134] L. Song and J. W. Evans, Electrochemical-thermal model of lithium polymer batteries, *Journal of The Electrochemical Society* **147**, 2086 – 2095, 2000.

[135] S. Stewart and J. Newman, Measuring the salt activity coefficient in lithium-battery electrolytes, *Journal of The Electrochemical Society* **155**, A458 – A463, 2008.

[136] S. G. Stewart and J. Newman, The use of UV/vis absorption to measure diffusion coefficients in $LiPF_6$ electrolytic solutions, *Journal of The Electrochemical Society* **155**, F13 – F16, 2008.

[137] J. Tarascon and M. Armand, Issues and challenges facing rechargeable lithium batteries, *Nature* **414**, 359 – 367, 2001.

[138] F. Tariq, V. Yufit, M. Kishimoto, P. Shearing, S. Menkin, D. Golodnitsky, J. Gelb, E. Peled, and N. Brandon, Three-dimensional high resolution X-ray imaging and quantification of lithium ion battery mesocarbon microbead anodes, *Journal of Power Sources* **248**, 1014 – 1020, 2014.

[139] S. D. Thompson and J. Newman, Differential diffusion coefficients of sodium polysulfide melts, *Journal of The Electrochemical Society* **136**, 3362 – 3369, 1989.

[140] I. V. Thorat, D. E. Stephenson, N. A. Zacharias, K. Zaghib, J. N. Harb, and D. R. Wheeler, Quantifying tortuosity in porous Li-ion battery materials, *Journal of Power Sources* **188**, 592 – 600, 2009.

[141] A. S. U. Trottenberg, Cornelis W. Oosterlee, *Multigrid*, Academic Press, 2001.

[142] L. O. Valøen and J. N. Reimers, Transport properties of $LiPF_6$–based Li-ion battery electrolytes, *Journal of The Electrochemical Society* **152**, A882 – A891, 2005.

[143] J. Vatamanu, O. Borodin, and G. D. Smith, Molecular dynamics simulation studies of the structure of a mixed carbonate / $LiPF_6$ electrolyte near graphite surface as a function of electrode potential, *The Journal of Physical Chemistry C* **116**, 1114 – 1121, 2012.

[144] M. Wagemaker, A. Van Der Ven, D. Morgan, G. Ceder, F. M. Mulder, and G. J. Kearley, Thermodynamics of spinel Li_xTiO_2 from first principles, *Chemical Physics* **317**, 130 – 136, 2005.

[145] F. T. Wagner, B. Lakshmanan, and M. F. Mathias, Electrochemistry and the future of the automobile, *The Journal of Physical Chemistry Letters* **1**, 2204 – 2219, 2010.

[146] R. Wagner, N. Preschitschek, S. Passerini, J. Leker, and M. Winter, Current research trends and prospects among the various materials and designs used in lithium-based batteries, *Journal of Applied Electrochemistry* **43**, 481 – 496, 2013.

[147] W. A. Wall and M. W. Gee, Baci - A multiphysics simulation environment, Technical report, Technische Universität München, 2010.

[148] Y. Wang, E. I. Rogers, and R. G. Compton, The measurement of the diffusion coefficients of ferrocene and ferrocenium and their temperature dependence in acetonitrile using double potential step microdisk electrode chronoamperometry, *Journal of Electroanalytical Chemistry* **648**, 15 – 19, 2010.

[149] S. Whitaker, *The Method of Volume Averaging*, Theory and Applications of Transport in Porous Media, Springer, 1999.

[150] D. Wiedenmann, L. Keller, L. Holzer, J. Stojadinovć, B. Münch, L. Suarez, B. Fumey, H. Hagendorfer, R. Brönnimann, P. Modregger, M. Gorbar, U. F. Vogt, A. Züttel, F. L. Mantia, R. Wepf, and B. Grobéty, Three-dimensional pore structure and ion conductivity of porous ceramic diaphragms, *American Institute of Chemical Engineers Journal* **59**, 1446 – 1457, 2013.

[151] H. Willman. Bestimmung der übergangszahl durch potentiostatische Polarisation. Master's thesis, TU München, 2013.

[152] D. Wittmann. Erweiterte Reaktionsmodelle fr die numerische Simulation von elektrochemischen Systemen. Master's thesis, TU München, 2011.

[153] M. R. Wright, *An Introduction to Aqueous Electrolyte Solution*, John Wiley & Sons Ltd, Chichester, 2007.

[154] M. Wyllie and W. D. Rose, Some theoretical considerations related to the quantitative evaluation of the physical characteristics of reservoir rock from electrical log data, *Society of Petroleum Engineers* **2**, SPE–950105–G, 1950.

[155] J. Xu and G. C. Farrington, A novel electrochemical method for measuring salt diffusion coefficients and ion transference numbers, *Journal of The Electrochemical Society* **143**, L44 – L47, 1996.

[156] K. Xu, Nonaqueous liquid electrolytes for lithium-based rechargeable batteries, *Chemical Reviews* **104**, 4303 – 4418, 2004.

[157] K.-H. Xue and G. L. Plett, A convective transport theory for high rate discharge in lithium ion cells, *Electrochimica Acta* **87**, 575 – 590, 2013.

[158] V. Zadin, D. Danilov, D. Brandell, P. H. Notten, and A. Aabloo, Finite element simulations of 3D ionic transportation properties in Li-ion electrolytes, *Electrochimica Acta* **65**, 165 – 173, 2012.

[159] J. M. Zalc, S. C. Reyes, and E. Iglesia, The effects of diffusion mechanism and void structure on transport rates and tortuosity factors in complex porous structures, *Chemical Engineering Science* **59**, 2947 – 2960, 2004.

[160] J. Zhao, L. Wang, X. He, C. Wan, and C. Jiang, Determination of lithium-ion transference numbers in $LiPF_6$-PC solutions based on electrochemical polarization and NMR measurements, *Journal of The Electrochemical Society* **155**, A292–A296, 2008.

[161] O. C. Zienkiewicz, R. L. Taylor, and J. Z. Zhu, *The Finite Element Method: Its Basis and Fundamentals (6^{th} Edition)*, Butterworth-Heinemann, 2005.

[162] O. C. Zienkiewicz, R. L. Taylor, and P. Nithiarasu, *The finite element method for fluid dynamics*, Elsevier Butterworth-Heinemann, Oxford, 2005.

[163] S. Zugmann, M. Fleischmann, M. Amereller, R. M. Gschwind, H. D. Wiemhöfer, and H. J. Gores, Measurement of transference numbers for lithium ion electrolytes via four different methods, a comparative study, *Electrochimica Acta* **56**, 3926 – 3933, 2011.